THE EFFECTS OF CURRENT BLOCKAGE ON OFFSHORE STRUCTURES

HARRIF SANTO

DEPARTMENT OF CIVIL AND ENVIRONMENTAL ENGINEERING

NATIONAL UNIVERSITY OF SINGAPORE

2014

THE EFFECTS OF CURRENT BLOCKAGE ON OFFSHORE STRUCTURES

HARRIF SANTO

B. Eng. (Hons) (NUS)

A THESIS SUBMITTED

FOR THE DEGREE OF DOCTOR OF PHILOSOPHY

DEPARTMENT OF CIVIL AND ENVIRONMENTAL ENGINEERING

NATIONAL UNIVERSITY OF SINGAPORE

2014

DECLARATION

I hereby declare that the thesis is my original work
and it has been written by me in its entirety.
I have duly acknowledged all the sources
of information which have been used in the thesis.

This thesis has also not been submitted for any
degree in any university previously.

Harrif Santo
15 May 2014

Acknowledgements

I would like to express my sincerest gratitude to my supervisor, Professor Choo Yoo Sang, who from day to day has given me invaluable support and guidance in every aspect of this thesis. His supervision and help rendered throughout my PhD are very much appreciated. Without him, this thesis would not have been completed. One simply could not wish for a better supervisor.

I would also like to thank my first co-supervisor, Professor Paul Howard Taylor, for his guidance and advice from the early stage of this thesis as well as extraordinary experiences through this collaborative work. It is an honour for me to be able to work and to learn from him; he has exceptionally inspired and enriched my growth as a PhD student.

I would also like to thank my second co-supervisor, Dr. Bai Wei, for his support and guidance throughout our weekly meetings. His advice helps me in developing comprehensive & delicate understanding in the numerical part of my work.

I gratefully acknowledge Professor Rodney William Eatock Taylor, Professor Peter William Marshall, and Dr. John Edwin Halkyard for their advice and support through group meetings and discussions. Their involvement undoubtedly motivated me in delivering a fine piece of work which I believe would not have been as good without them.

I sincerely thank Professor Charles Harvey Kaye Williamson for our fruitful collaboration in the Cornell experiments. With his support and that of the Cornell Fluid Dynamics Research Laboratory (FDRL) team, we produced a very fulfilling set of experimental results.

Special thanks to Mr. Trevor Mills and Dr. Carlos Llorente of McDermott International for their support to my PhD as well as MicroSAS implementation for the current blockage application. Their presences and involvements are greatly appreciated.

I would also like to thank Dr. Richard Willden of the University of Oxford and Dr. Jun Zang of Bath University for their helpful discussions in the numerical part of my work. Special acknowledgement to Dr. Richard Gibson of BP for his help and support to my PhD through a collaborative Andrew project in both numerical and experimental work.

I am also thankful for Professor Nigel Barltrop and Professor Sandy Day of the University of Strathclyde for their support and helpful discussions for a possible larger scale set of experiments to be conducted in Glasgow.

I am grateful for the support of The Lloyd's Register Foundation to the Centre for Offshore Research & Engineering, where most of my PhD work was completed. Many thanks to Mdm. Norela bte Buang for her administrative help in ensuring that my PhD is going smoothly without much hurdles.

In my daily work, I have been blessed with a friendly and cheerful group of fellow students, who are too many to be listed. It is my pleasure to enjoy their companionship through my PhD. Their friendly gestures and encouraging words are unequivocally appreciated.

Finally, I would like to thank my parents for supporting me emotionally, morally and financially throughout this thesis and my undergraduate and graduate studies at the university. Without them, this thesis certainly would not have existed.

Contents

Abstract

This thesis revisits the problem of hydrodynamic forces on fixed space-frame structures in combined waves and an in-line steady current. Because of current blockage, the actual drag force experienced by such structures is over-predicted by the standard Morison equation and the present industry standard practice. A set of analytical models of current blockage is formulated based on the actuator disc theory and proposed to represent the actual hydrodynamic drag force more accurately after taking into account the current blockage effects. This thesis tests and verifies the adequacy of the analytical model against series of experiments and full Computational Fluid Dynamics (CFD) numerical simulations, as well as demonstrating the novel use of a porous block as a simple representation for the complex geometry of real offshore structures in the numerical simulations.

Much of this thesis are devoted to validation of the proposed full current blockage model (FCB) for regular waves with an in-line current. For relatively small current speed (u_c) compared with wave velocity amplitude (u_w) with oscillation phase angle (ωt), the drag force time history on obstacle arrays with solid area (A) and projected frontal area (A_f) can be expressed as:

$$\text{Drag } = \frac{1}{2}\rho C_d A u_w^2 \cos\omega t|\cos\omega t| + \frac{\pi}{4}\rho A_f u_c^2|\cos\omega t|,$$

so there is no $u_w \times u_c$ cross term as commonly found in the Morison equation and the present practice, and the current squared (u_c^2) term is phase-locked to the oscillatory wave crests. The crest and trough peak values of the drag force is reduced to:

$$F_{peak} = \pm\frac{1}{2}\rho C_d A u_w^2 + \frac{\pi}{4}\rho A_f u_c^2.$$

The full model will be shown to fit the entire force time history as well as the peak force for a wide range of experiments and numerical simulations, requiring only calibration of the Morison type drag and inertia coefficients (C_d and C_m).

The FCB model and the use of a porous block model in numerical simulations in general work very well for statically-responding structures in regular waves. The drag force reduction is real and significant, and this has a direct implication and application to new-builds and reassessment of space–frame offshore structures, such as jackets and compliant towers.

List of Tables

List of Figures

Nomenclature

$\boldsymbol{\tau}$	The specific Reynolds stress tensor
Δp	The pressure drop
ϵ	The turbulent dissipation rate
γ	The scalar field used to represent the fraction of a cell volume filled with water
μ	The dynamic viscosity of fluid
ν_T	The turbulent eddy viscosity
ω	The angular frequency of wave or oscillation, or the turbulent specific dissipation rate
ϕ	The oscillation phase angle, also expressed as ωt
ρ	The fluid density, normally taken to be the water density
$\mathbf{g}$	The gravitational acceleration
$\mathbf{u}$	The fluid velocity field (u, v, w) in Cartesian coordinates
$\mathbf{u}_c$	The artificial compression velocity for interface modelling
$\mathbf{x}$	The local Cartesian coordinates (x, y, z)
θ	The incident angle of a flow to the normal vector of an obstacle array
A	The solid drag area of an obstacle array
a	The (linear) amplitude of wave or oscillation
A_f	The projected frontal area of an obstacle array
A_L	The maximum allowable limit of the hydrodynamic area on the first disc in the two-disc model

C'_m	The bulk Morison inertia coefficient equivalent to the standard C_m coefficient
C_dA	The total hydrodynamic area of an obstacle array
C_dA/A_f	The total hydrodynamic loading on an obstacle array
C_d	The Morison drag coefficient
C_m	The Morison inertia coefficient
C_γ	The intensity of the interface compression
D	The streamwise separation distance of two adjacent actuator discs, or the Darcy resistance parameter
d	The width of vertical strips in the perforated plates, which is related to the diameter of a jacket leg
F	The Forchheimer resistance parameter
I	The turbulent intensity
k	The turbulent kinetic energy
L	The downstream width of an actuator disc, or the downstream length of a porous block or tower
L_t	The turbulent mixing length scale
p	The fluid flow pressure
S	The total rate of volume addition on a source disc in actuator disc theory, or the momentum sink term in the Navier–Stokes equations to account for the effect of the porous block or tower
T	The period of wave or oscillation
u_c	The free stream current velocity
u_s	The shielded velocity, also known as u_{cs}
u_w	The wave velocity kinematics, or the oscillatory velocity amplitude
u_{cs}	The shielded current velocity

u_{cta}	The shielded steady flow velocity from time-averaged mean flow simulation
u_{Tb}	The total blocked (or shielded) flow velocity
u_{wake}	The flow velocity in the far wake region
V	The displaced volume of an offshore jacket or an obstacle array
v	The flow velocity deficit at upstream of an actuator disc
v_1	The total flow velocity deficit across an actuator disc
V_P	The total wetted volume of a porous block or tower
w_f	The frontal width of an obstacle array, commonly used in two-dimensional planar simulations

Chapter 1

Introduction

1.1 Background

The design of offshore structures for operation in harsh waters is largely governed by the extreme storm environmental loading. The ability to predict and represent accurately the extreme storm loading remains a crucial factor to ensure continuous safe and economic recovery of the hydrocarbon reserves. The phenomena which cause environmental loading are complex, which demand a huge amount of research effort. Continuous numerous studies and researches have been spent to explain the observed phenomena and to establish and refine appropriate models for predictive purposes. This thesis is confined to a sub-class of offshore structures, namely statically-responding fixed space-frame structures or jackets, which comprise slender members that do not affect the characteristics of the incident wave (no wave diffraction). Hence, only the fixed structures without any effects of flexibility or wake-induced oscillations are considered. The majority of fixed offshore structures fall in this category.

The most important metocean parameters pertinent to evaluating the extreme environmental loading are: significant wave height, mean zero crossing period, wind speed averaged over a suitable time interval, current speed and profile, storm surge and tidal range (Efthymiou and Graham, 1990). The accurate usage and representation of the actual current speed experienced by an offshore structure is thus one of the crucial factors for the platform survival.

The first generation of fixed offshore structures for Gulf of Mexico (GOM), which were designed in the 1950s, proved to have inadequate reliability mainly because of the underestimation of the magnitude of the environmental loading. These early designs were generally based on a wave height with return period of 25 years, Stokes V wave theory, a drag coefficient of 0.5, no allowance for the presence and contribution of currents nor for marine fouling of the members (Bea et al., 1988). Some of these structures collapsed during hurricanes. For this reason, the early practice was quickly replaced.

Through the 1960s and 1970s, the magnitude of the design environmental loads inclined to drift upwards. The environmental loads according to the present design practice are found to be about 2.5 - 3 times higher than those used in the early 1950s for nominally identical structures in the same geographical area (Bea et al., 1988). Prior to the 1960s, the first generation offshore structures must have been under-designed, but after the 1960s, the 'newer' structures could have been (grossly) over-designed instead. This thesis aims to provide a more accurate predictive model of the extreme environmental loading after taking into account the effects of current blockage.

Current blockage occurs when the velocity of an incident steady flow onto the members of an obstacle array is reduced over the whole array due to the presence of the obstacles. As the current flows past the obstacle array, it exerts a net drag force on it. The fluid experiences an equal and opposite force acting to locally reduce the speed of the flow. The flow field is complicated by the fact that each member of the obstacle array generates its own wake and the structure as a whole generates a less obvious global wake. This reduction in velocity translates into a reduction in the global hydrodynamic force experienced by the structure. This blockage effect is the result of fluid–structure interaction (confined to statically-responding fixed structures), in which the total force on a cluster of slender members is smaller than the sum of the individual forces on each member considered in isolation. Such an effect is obviously important for the design of offshore jacket-type structures used for oil and gas production, and more recently to support large wind turbines. A direct analogy to describe the effect is described in the following quote:

"On a windy day the force on a single tree in a forest is much smaller than the force on the same tree in isolation, and each tree bends rather than breaks"

The Morison equation (Morison et al., 1950) has been used for the last sixty years to estimate the hydrodynamic loading of a space-frame structure, and the standard practice had been to apply the formula on each individual member by taking the current and wave velocities from the undisturbed flow field, and sum the forces up individually as if the rest of the members were removed, thus neglecting any bulk fluid–structure interaction effect. This is a reasonable approach for a wave-induced motion. However, if the presence of the structure modifies the flow field, this approach leads to over-estimation of the peak hydrodynamic loading. The actual current velocity is reduced due to the flow divergence as a result of the presence of the structure as

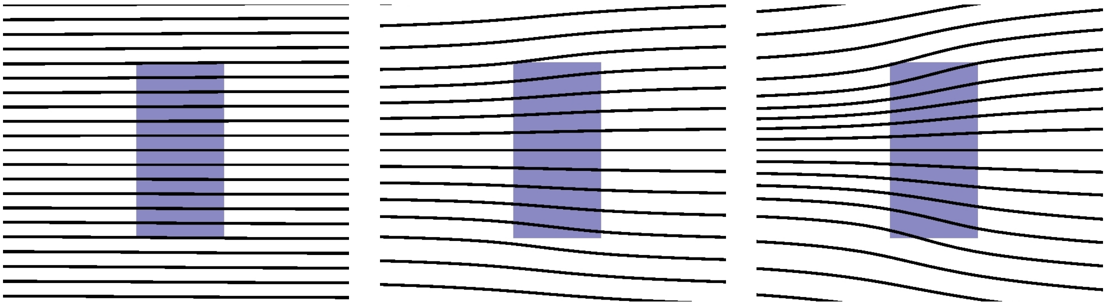

(a) (b) (c)

Figure 1.1: Three different flow representations of average streamlines for flow past a porous block: (a) standard Morison; (b) simple current blockage (SCB); (c) full current blockage (FCB).

obstacles. This study of current blockage is aimed at improving the Morison equation to better quantify the amount of loading experienced by statically-responding fixed space-frame offshore structures.

An early study of current blockage was reported by Taylor (1991). This simple approach was devised for a structure subjected to a pure steady flow, and has been used as a part of the standard design method after it was incorporated in the API design guidelines in 1994 (American Petroleum Institute, 2000). Here this is termed 'simple current blockage' or SCB, as it takes into account only current–structure interaction. However, there is strong evidence showing a much larger blockage for a structure subjected to combined waves and current, and a full current blockage model has been proposed for this combined problem (see Taylor, Santo and Choo (2013)). The 'full current blockage model', or FCB, accounts for wave–current–structure interaction, a more complete fluid–structure interaction process (confined to statically-responding fixed structures) which is responsible for the larger net flow and force reduction on an offshore structure. This full model is presently suited for steady flow plus regular waves.

Figure 1.1 illustrates the comparison of the three different flow representations of averaged streamlines, obtained from full Computational Fluid Dynamics (CFD) numerical simulation using OpenFOAM® (www.openfoam.org), of time-averaged mean flow past a porous block: the standard Morison representation without any blockage (Figure 1.1(a)), the simple current blockage model for steady current flow (Figure 1.1(b)), and the full current blockage model for oscillatory flow superimposed on the steady current flow (Figure 1.1(c)). Clearly, the evidence for a much larger blockage effect is reflected in the larger divergence experienced by the mean velocity flow field.

The amount of current blockage will depend on the number and size of members with respect to the frontal area of the platform. A re-examination of relevant experimental results (as described in Chapter 3) shows that the proposed blockage model is sufficiently accurate. For typical fixed offshore platforms, the effective current speed which flows through the platform is 10% - 25% lower than the free stream current speed. Once a hydrodynamic model of an offshore structure is available, application of this blockage model to establish the reduced current speed and the reduced hydrodynamic (drag) force is relatively straightforward.

1.2 Objectives

The main objective of this study is to observe and quantify the effect of current blockage on statically-responding fixed space-frame offshore structures such as jackets subjected to a combination of waves plus current loading. Two specific objectives are identified to satisfy the main objective. The first objective is to introduce an analytical model aimed to improve the Morison equation to better quantify the amount of loading experienced by offshore structures. The second objective is to introduce and demonstrate the novel use of a numerical porous block model as a simple representation for the complex geometry of real space-frame structures. This current blockage study is aimed at achieving a breakthrough and new insight into the dynamical physics of fluid loading on an obstacle array and delivering a state-of-the-art engineering formulation and methodology which could be adopted into the standard design guidelines for offshore structures such as API, DNV and ISO.

The motivation of this study arises partly due to the BP Macondo blow out, and partly due to the strong evidence in the literature of full current blockage phenomena. The Macondo blow out disaster was a result of human error in handling a subsea wellhead (wet tree). Surface wellheads (dry trees) are generally easier to control and thus safer. Subsea wellheads are mostly used on floating platforms, while surface wellheads on fixed platforms. Thus, there is a possibility of growing industrial interests on deepwater jackets and compliant towers in the near future.

One piece of strong evidence of full current blockage phenomenon was shown in the Allender & Petrauskas experiment on a scaled jacket subjected to regular waves and current loading discussed in Chapter 3.5 (Allender and Petrauskas, 1987). They reported a great deal of current blockage occurred when waves are present, shown in the following quote from their paper:

"The drop in C_d between wave alone and wave plus current cases found here (from a C_d of 1.3 - 1.6 for waves to a C_d of 0.7 - 0.8 for waves plus current) is much greater than expected ..." (Allender and Petrauskas, 1987)

The reduction in hydrodynamic force for a new-built structure means smaller or lighter members can be possibly used, which eventually leads to cost saving compared to the conventional design method which overestimates the force. Current typical jacket structures are over-designed, and conventional compliant towers are in fact grossly over-designed. Steele (1986) reported the response from the Exxon Lena guyed compliant tower to Loop Current eddies has been over-predicted by a factor of five to six, and it is all because the net current velocity at the tower is estimated to be only 40% of the far field velocity, a significant 60% flow reduction!

Apart from the advantage gained for new-built structures, the study of current blockage can also be applied in the area of reassessment of existing offshore structures and structural integrity management, particularly in life-extension of existing ageing platforms. If the hydrodynamic loading on an old platform turns out to be lower than the initial designed load, it is then possible to extend its design life after properly incorporating the current blockage effect. This benefit is of direct relevance to oil and gas operators. Energy companies, who own hundreds of old platforms all over the world, often would like to add additional processing or Enhanced Oil Recovery (EOR) modules as there are still much oil left to be recovered. Reduced environmental forces may allow them to add this extra equipment without overloading the structure.

1.3 Structure of thesis

This study of current blockage combines analytical work with numerical simulation (CFD) and experimental work. It starts from looking into the current blockage effect on planar flow for regular oscillations (waves) plus steady mean flow (current) application, both numerically (Chapter 4) and experimentally (Chapter 5). It then proceeds to account for wave kinematics depth-variation and free surface effects by including 3D free surface flow and/or real wave action for regular waves plus current, also numerically (Chapter 6) and experimentally (in-progress at the time of writing), for more realistic engineering applications. Analytically, the full current blockage model has been validated and can be applied to both planar and free surface flow for regular waves plus current only (Chapter 3). Eventually, the study aims to extend the full model to include random (irregular) waves plus current application (in-progress at the time of writing).

The layout of the thesis is arranged (not necessarily in chronological order) such that the flow of information is smooth and coherent. Chapter 2 that comes right after the introduction (Chapter 1) is the literature review on the previous study of current blockage. There are not many studies conducted in recent times to look into the blockage effect, mainly due to the shift of the industrial interest from fixed to floating platform in the 1990s. However, as the reassessment of old platforms has become of greater importance recently and there is still industrial interest in considering fixed structures (jackets and compliant towers) for deep water, the current blockage issue becomes a crucial design factor to account for.

Chapter 3 introduces the phenomenon of current blockage in offshore engineering. Standard current blockage theory was first developed by Taylor (1991) and is suited for grids of obstacles in steady flow when Morison drag is assumed locally. This is confirmed by analysis of the published experimental data on drag forces for several examples of multiple grids of obstacles in steady flow. A more complex analytical model is derived and elaborated in this chapter to account for the considerable extra blockage which occurs when a space-frame structure is exposed to regular waves and an in-line current. This new model is shown to be in excellent agreement with the experimental data of Allender and Petrauskas (1987) for steady current superimposed with regular waves, both incident on a model of a Gulf of Mexico jacket. In contrast, both the original unblocked version of the Morison equation and the Morison equation assuming just steady current blockage (as in API RP2A) over-estimate the measured forces. This chapter has been published in the journal Ocean Engineering as Taylor, Santo and Choo (2013). The new model at this stage (the full current blockage model) is only suited for regular waves plus current as the environment load. A complete full model incorporating random waves plus current is still under development.

Chapter 4 provides numerical evidence for reduced fluid loading on space-frame structures exposed to ocean waves and in-line current. Comparisons are made between the current blockage model presented previously (Taylor, Santo and Choo, 2013), Computational Fluid Dynamics (CFD) simulation and experimental data. Three different flow models are considered: steady flow, time-averaged mean flow and fully unsteady flow both for regular oscillations with an in-line steady flow. A porous block is used to model an obstacle array of cylinders. This is appropriate because of the global nature of current blockage, which has significant effects over distances of the order of the frontal width of the obstacle array. Good agreement is obtained between the numerical simulation, the experimental data and the previously published current blockage model, which lends support to the validity and applicability of the theoretical model in predicting the blockage effects. This chapter also demonstrates that, in general, the two-dimensional porous block model simulates the reduced flow better than the simple one-dimensional analytical current blockage model. This chapter has been submitted to the journal Ocean Engineering as Santo, Taylor, Bai and Choo (2013a).

Chapter 5 experimentally revisits the problem of forces on obstacle arrays in combined waves and an in-line steady current. A series of experiments are performed on planar grids moved in both steady and oscillatory motion through otherwise stationary water. Detailed comparisons are made to a wave–current–structure interaction model recently presented in Chapter 3 and Taylor et al. (2013). New features of the analytical model are presented and tested against the experimental data. All of the features are identified within the experimental data, and provide considerable support for the new current blockage model. The new model is also shown to fit the entire force time history well for a wide range of individual cases, with different blockage ratio (A/A_f) and number of grids, requiring only calibration of the Morison-type drag and inertia coefficients. In contrast, the industry-standard form of the Morison equation can only be matched at a single instant of the oscillation cycle, so present practice should be regarded as seriously inadequate for combined steady current and oscillatory flow acting on obstacle arrays. This chapter has been published in the Journal of Fluid Mechanics as Santo, Taylor, Williamson and Choo (2014b).

Chapter 6 introduces a new numerical approach for the estimation of the global hydrodynamic loads on space-frame offshore structures exposed to combined waves and current. This chapter provides numerical evidence for reduced fluid loading on offshore structures – current blockage, which serves as an extension to the analytical, computational and experimental work of Taylor, Santo, and Choo (2013), Santo, Taylor, Bai, and Choo (2013a) and Santo, Taylor, Williamson, and Choo (2014b) (as presented in Chapter 3, 4 and 6). A full three-dimensional free-surface turbulent flow is simulated for a porous tower in a numerical wave tank. This is intended to model waves and current through a jacket or compliant tower, both space-frame structures. Comparisons are made between the numerical simulations and experiments conducted by Allender and Petrauskas (1987) on a scale-model jacket structure from the Gulf of Mexico, and the current blockage model presented previously in Taylor et al. (2013). Three different flows are simulated: steady current flow, regular waves with no current and regular waves with an in-line current. Overall, good agreement in terms of peak total forces is achieved, showing that the force reduction on such structures due to current blockage effects is real and significant. Additional information on force time history and flow visualisation are presented from the numerical simulations. Flow visualisation for waves and current reveals that the form of the global mean wake is simple at the structure but becomes complex well downstream. The simple form of the flow at the tower is responsible for the global force reduction being predictable using a modified version of the Morison equation (Morison et al., 1950). This chapter also demonstrates the novel use of a porous tower as a simple representation for the complex geometry of real space-frame structures when exposed to combined large waves and significant in-line current, an approach which could be considered for possible incorporation into offshore design practice. This chapter has been submitted to the Journal of Fluids Mechanics as Santo, Taylor, Bai and Choo (2014a).

Chapter 7 ends with conclusions and recommendations for future work.

Chapter 2

Literature review

In the early 80s to 90s, the occurrence of current blockage was observed and investigated in field measurements and laboratory experiments, due to the increasing interest of the offshore industry towards deepwater drilling and production using deepwater space-frame structures. The idea of replacing the conventional jacket with a compliant tower was proposed if the water depth exceeds the operational limit of the jacket. If the occurrence of current blockage is real, and a design guideline to properly account for the blockage exists, then the benefit in terms of cost and/or material saving is enormous, especially for complaint tower which has densely packed structural members along the height of the tower. This motivation encouraged many researchers to develop current blockage or shielding theory on a group of multiple cylinders, which would lead to the development of analytical models on a whole structure to account for the current blockage or wake shielding effect.

Forristall (1996) analysed and reported his measurements of current blockage in the Bullwinkle platform in 1996 due to the Loop Current and the Hurricane Andrew. His analysis revealed that the average current speed inside the platform was approximately reduced by a factor of the order of 0.7 - 0.9, leading to a significant reduction in the environmental loads. Steele (1986) studied and described the performance of the Exxon Lena guyed tower in both waves and current in 1986, and concluded that the current-induced loading was massively over-estimated by a factor of 5 - 6 times without considering blockage effect. These field measurements confirmed that the current blockage phenomenon is real.

Further carefully-controlled laboratory experiments involved measuring peak fluid loading on scaled jacket models exposed to waves alone, current alone and combined regular waves with an in-line current. Experiments conducted by Allender and Petrauskas (1987), Finnigan (1992) and Mendes et al. (2000) generally reported bigger values of C_d for pure waves alone with no current, and smaller values of C_d for combined waves and current, in order to fit the measured peak forces with the standard Morison formulae. The same conclusion was also reached from the experiments on conductor pipe groups performed by Reed et al. (1990). Sterndorff et al. (1990) investigated pure wake shielding effect due to waves alone with no current for different conductor arrangements, and found that the shielding effects in waves are either small or constant for the tested jacket configuration. These laboratory findings coupled with the field measurement evidence demonstrated that the current blockage effect occurs at both full-scale and lab-scale, and become significant when the current is present on top of waves.

In 1991, Taylor (1991) derived a simple current blockage model based on the single actuator disc theory of Glauert (1983). Instead of looking into details of each cylinder forming a member of a space-frame structure, Taylor (1991) approximated and represented the global resistance of the entire structure as a single actuator disc, and sought for the reduced flow velocity inside the structure due to the presence of the structure as obstacles, by applying conservation of energy upstream and downstream the disc and conservation of momentum across the disc. This simple approach was devised for a structure subjected to a pure steady flow, and has been used as a part of the standard design method after it was incorporated in the API design guidelines in 1994 (American Petroleum Institute, 2000). The simple current blockage model considers current–structure interaction only, and serves as a foundation for the development of the more complex models, such as the multiple actuator disc model, and the full current blockage model which takes into account wave–current–structure interaction.

In 1992, Lambrakos and Beckmann (1992) presented an analytical model to account for shielding and blockage effect in steady flow. The model is not at all similar to Taylor's model as it is based on the idea of pure shielding - one cylinder is exactly in line with a second. They treated a space-frame offshore structure as porous body of variable porosity along the flow direction. Structural members are grouped together to form individual screens, which is termed porous 'screens'. The correlation between the screen drag coefficient, C_{ds}, and the drag coefficient of an individual screen member (i.e. cylinder), C_{do}, in the free stream is adopted from an earlier paper by Lock (1930):

$$C_{ds} = B_w(1.0 + 0.25B_w + 0.82B_s^2)^2$$

where B_s is the solidity ratio, defined as the ratio of the solid cylinder drag area, A_d, to the screen area, A_s, which is equivalent to the Taylor's model of A/A_f, and B_w is the 'wake blockage ratio', defined as $C_{do} \times B_s$.

Despite the difference in the basic assumption of the analytical models, the Lambrakos and Beckmann model reduces and becomes identical to Taylor's when the blockage is small, only when both B_s and B_w are assumed to be small in the correlation equation, which gives:

$$\frac{u_s}{u_c} = \frac{1}{1 + 0.25B_w}$$

$$F = \frac{1}{2}\rho C_{do} A_d u_s^2$$

in which u_s and u_c is the shielded and free stream velocity, respectively.

However, when it comes to the extend of multiple actuator disc or multiple screen theory, Lambrakos and Beckmann adopted a further empirical factor to account for flow divergence or leakage between two adjacent porous screens. As a result, after the correction on the single porous screen model, Lambrakos and Beckmann model contains two empirical factor: the drag coefficient C_{do} for individual screen members, and the new 'maximum' coefficient C_{dm}, which is not conventional and can only be obtained from model test data on groups of cylinders. Meanwhile, after the improvement on the single actuator disc model, Taylor's model contains only a single adjustable empirical parameter, i.e. the drag coefficient, C_d, for individual members of the structure, which needs to be estimated anyway for a conventional analysis of current loads (Standing and House, 1997). This shows how the Taylor's model is very attractive from a practical viewpoint.

In 1992, Finnigan (1992) presented comparison between analytical and experimental results of model tests on a 1:47 scale jacket model under wave plus current loadings. The development of the analytical model was motivated by the speculated high hydrodynamic blockage and shielding found in the experiment by Allender and Petrauskas in 1987, which led to a series of repeated tests in 1988. The paper proposed an analytical method of estimating the flow reduction based on wake theory of Schlichting (1979), and extended the method to develop their own current blockage prediction on a complex jacket structure. Essentially, the proposed formula based on member shielding was used to predict the amount of current blockage and shown to be consistent with the experimental results.

The Schlichting model looks into detail of the wakes of a cylinder. Finnigan then extended the model to multiple cylinders resembling a jacket structure. Thus, the drag force expression which takes into account the amount of blockage is shown to be dependent upon jacket's leg spacing, and the amount of member shielding, which is a function of the number of jacket's leg. The model also claimed that a group of well conductors contribute to a major source of blockage. However, as their proposed model takes into account the details of the wakes of each cylinder forming a jacket type structure, these details can possibly add on to higher degree of complexity encountered in real life jacket design application. We thus believe that a simpler yet accurate analytical model to account for current blockage is preferable.

The numerical study of current blockage is performed using porous block and tower to simulate the amount of current blockage experienced by a space-frame offshore structure exposed to waves and current. Based on the same argument used in the development of the analytical model of current blockage, we represent the bulk effect of the structure as a porous block and do not model the details of the individual cylinders: the dominant physical process we seek to model is the reduced mean flow within and near the obstacle array over distances of the order of the width of the obstacle array, not the individual cylinders within the array. Obviously modelling the complete flow over complex array of cylinders in both 2D and eventually 3D is very challenging and resource-expensive.

The numerical study is performed in OpenFOAM® (Open Field Operation and Manipulation), a free open-source Computational Fluid Dynamics (CFD) software package written in C++ which has gained popularity in recent years. It was originally developed in the late 1980s by a research group headed by Henry Weller in Imperial College, London. The objective was to develop a more powerful and flexible general simulation platform than the de facto standard at the time, FORTRAN, which led to the use of C++ due to its modularity and object-oriented programming features. OpenFOAM® is now part of the ESI group (since 2012), and the continuous updates and improvements of the source codes are distributed through the OpenFOAM® Foundation.

OpenFOAM® is basically a collection of C++ libraries which is used to create two main parts of the application: solvers – to solve specific problems in continuum mechanics, and utilities – to perform tasks that involve data manipulation. It has a wide range of features to solve complex fluid flows ranging from chemical reactions, turbulence and heat transfer, to solid dynamics and electromagnetics. It is essentially designed as a programmable toolbox, nicknamed "MATLAB for CFD" (OpenCFD, 2011).

Being an open source means users have complete freedom to create and/or modify new solvers and utilities to better suit their own needs, with some pre-requisite knowledge of the underlying method, physics and C++ programming technique. OpenFOAM® features a highly modular code design in which collections of functionality (for instance meshing, numerical methods, etc) are each compiled within their own shared library. Thus, the ability to alter part of a solver or utility is a desirable feature. Eventually, executable applications are created that are simply linked to the library functionality.

OpenFOAM® is supplied with third-party post-processing tools. Some of the tools are reader modules and data converters to interface with other third party products. The most commonly used reader module for flow visualisation is ParaView®. It uses the Visualisation Toolkit (VTK) format in processing data and rendering image and can therefore read any data in VTK format. All of the flow visualisations presented in this thesis are produced by ParaView®.

The porous media algorithms in OpenFOAM® were originally developed and intended to model flow over reservoir or rock formation, and flow over breakwater and other coastal defences, where the Darcy resistance term is more dominant than the Forchheimer, as the nature of the flow velocity is slow in general. Hence, the idea and numerical technique of using a porous block model as a representation for a complex offshore structure to simulate the current blockage effects appear to be a genuinely novel approach in offshore engineering.

Chapter 3

Current blockage: Reduced Morison forces on space frame structures with high hydrodynamic area, and in regular waves and current

3.1 Introduction

Generally, the extreme environmental loading on the steel-frame offshore platforms is dominated by fluid drag, due to waves and currents. Most of the loading estimations on tubular structures are based on a Morison type force calculation (Morison et al., 1950), which takes into account both waves and currents. The standard method of estimating the total wave and current force is by summing up the load on each individual member of the structure, as if the rest of the structure were not present. Historically, the flow velocity used in the force estimation was generally taken to be the free stream current measured or estimated for the open sea far away from the platform. This is a reasonable approach for a wave-induced motion. However, if the presence of the structure modifies the flow field, this estimation leads to overestimation of the peak loading. The actual current velocity is reduced due to the flow divergence as a result of the presence of the structure as obstacles. This phenomenon is described as current blockage.

With regular waves and a current incident onto a structure, there is additional blockage produced by the mean force averaged over a wave cycle. This chapter provides a model for this extra blockage and tests the model against the published data.

3.2 Actuator disc theory for current blockage - the analytical model

3.2.1 Theory for flow through a single row of obstacles: a single actuator disc

Taylor (1991) derived a simple current blockage model based on the single actuator disc theory of Glauert (1983) for a space-frame structure subjected to steady flow. The blocked current, u_s, can be expressed in terms of the product of the free stream current, u_c, and an offshore blockage factor. The blockage factor is expressed in terms of the total hydrodynamic area, C_dA, which we define as the product of the Morison drag coefficient, C_d, and the solid drag area of the obstacles, A, and the total frontal (projected) area of the obstacle array, A_f as:

$$u_s = u_c \left(\frac{1}{1 + \dfrac{C_dA}{4A_f}} \right) \tag{3.1}$$

This offshore blockage factor has already been incorporated into standard design codes, such as API. The citation can be found in the API RP2A WSD 21st Edition under Section 2.3 Design Loads, 2.3.1.b Static Wave Analysis point 4 (American Petroleum Institute, 2000). This simple formulation is adequate for estimating the total hydrodynamic loading on a typical offshore structure resulting from uniform steady flow current only, but we shall demonstrate that it is unduly conservative for waves + current.

Although the full derivation of the blockage factor can be found in Taylor (1991), we provide a short derivation highlighting key equations. Consider a single obstacle array in a flow with a steady current u_c. Instead of analysing in details the local flow around each obstacle, a global approximation is taken – the obstacle array is replaced by a porous actuator disc, which produces the same overall modification to the uniform current as the array, but without the local complications of real turbulent flow very close to each obstacle within the array. Several assumptions on the flow have been made. One dimensional streamtube idealisation is invoked and the flow is assumed to be irrotational throughout the domain, except at the vortex sheets which separate the wake from the external flow downstream. Figure 3.1 shows the schematic diagram of the idealisation.

Describing the flow condition globally, the approaching steady free stream flow velocity, u_c, is reduced to a shielded flow velocity, $u_s = u_c - v$, due to the presence

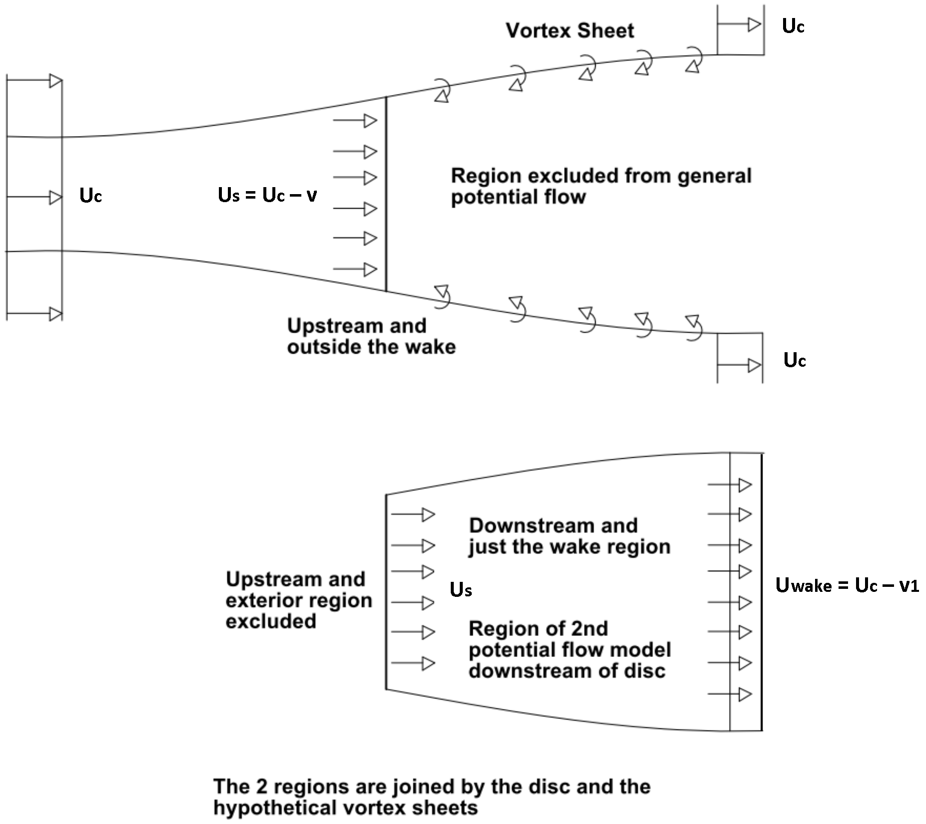

Figure 3.1: Representation of an obstacle array as an actuator disc in a free stream.

of the disc, or obstacles. v is defined as the flow velocity deficit at the upstream of the disc. The flow pressure increases from the far-field value, p_c, to p immediately in front of the disc, before dropping to $p - \Delta p$ across the disc, which results in a net drag force on the disc. Downstream of the disc, the flow velocity further drops to $u_{wake} = u_c - v_1$ in the far wake region, while the flow pressure slowly rises back to the ambient pressure, p_c. v_1 is defined as the total flow velocity deficit across the disc. Vortex sheets are present as a result of the velocity discontinuity between the streamtube and the outer flow.

Referring to Figure 3.1, conservation of mass holds between far upstream and far downstream of the disc. Thus, applying the Bernoulli equation from $-\infty$ to immediately upstream of the disc, and from downstream of the disc to $+\infty$, and subtracting these two equations, we obtain the pressure drop across the disc, Δp. Bernoulli's equation is not to be applied across the disc as there is energy into the wake downstream (implying the loss of energy is in the process of getting into the wake, i.e. across the disc).

Bernoulli's equation to both upstream and downstream:

$$\text{Upstream:} \quad p_c + \frac{1}{2}\rho u_c^2 = p + \frac{1}{2}\rho u_s^2$$
$$\text{Downstream:} \quad p_c + \frac{1}{2}\rho u_{wake}^2 = (p - \Delta p) + \frac{1}{2}\rho u_s^2$$

The pressure drop across the disc can be expressed as:

$$\Delta p = \frac{1}{2}\rho(2u_c v_1 - v_1^2)$$

Applying conservation of momentum: the rate of change in the axial momentum between the incoming and the outgoing flow through the disc corresponds to the net force on the flow, we obtain another equation for the pressure drop, Δp, expressed as:

$$\text{Force} = \rho A_f (u_c - v) v_1 = A_f \Delta p \tag{3.2}$$

where A_f = frontal area of the disc, defined as the area normal to the direction of flow enclosed by the cross-section of the structure.

Comparing these two expressions for Δp gives:

$$v = \frac{1}{2}v_1 \text{ and } u_s = \frac{1}{2}(u_c + u_{wake}) \tag{3.3}$$

This expression shows that half the total velocity deficit, v_1, due to the force on the flow occurs upstream of the disc and the remaining half occurs downstream.

Substituting the above expression into the net force on the disc derived from the momentum conservation (Equation 3.2), and equating it to the local Morison drag force, as expressed below:

$$\begin{aligned} F &= \Delta p A_f = 2A_f \rho u_s (u_c - u_s) \\ &= \frac{1}{2}\rho C_d A u_s^2 \end{aligned} \tag{3.4}$$

Then Equation 3.1 follows, where the blockage factor can be obtained.

3.2.2 The requirement for a streamwise structure: multiple actuator disc in-line

While a single actuator disc theory is sufficient for most calculations for the global forces on structures in steady flow, there are three main limitations on collapsing a whole structure into a single disc:

1. When the hydrodynamic loading on a structure is very high due to a compact layout of many densely packed structural members, for instance in a compliant tower,
2. When the structure has high aspect ratio; long in the streamwise direction yet rather narrow across the flow direction, here the wake mixing is an important factor which must be included,
3. When the structure is exposed to regular or random waves with a current, where the time-averaged wave–current interaction plays an important role in modifying the local flow field.

Of most importance to the second point, the simple single disc model does not provide any information on the variation of current velocity in a real structure in the streamwise direction. This additional limitation on a single disc model can be tackled using multiple actuator disc in-line model. These three main limitations will be addressed in this chapter.

The general expression for the wake velocity derived from a single actuator disc theory (referring to Equation 3.1) can be expressed as:

$$u_{wake} = 2u_s - u_c$$

$$u_{wake} = u_c \frac{\left(1 - \dfrac{C_d A}{4A_f}\right)}{\left(1 + \dfrac{C_d A}{4A_f}\right)} \tag{3.5}$$

There are various type of flow fields which correspond to the different values of u_s and u_{wake}:

- Normal actuator disc flow, whereby $u_s > u_c/2$ and $u_{wake} > 0$
- Flow through heavily loaded actuator disc, whereby $u_s = u_c/2$ and $u_{wake} = 0$
- Flow with eddy motion behind a bluff body, whereby $u_s < u_c/2$
- And flow with a bound vortex ring, whereby $u_s < 0$

It is worth stressing that not all types of flow field can be modelled using actuator disc theory. For the actuator disc theory to be valid, the flow field in the streamtube idealisation must remain approximately one dimensional. The limiting case for this is when the wake velocity is reduced to zero due to high hydrodynamic loading. This corresponds to the highest drag force achievable on the disc.

The wake velocity is reduced to zero, $u_{wake} = 0$, only when $C_d A = 4A_f$, which corresponds to the condition $u_s = u_c/2$. For a structure like a compliant tower with a very high hydrodynamic loading, a single disc approach may be unsuitable.

3.2.2.1 A source/sink model for the flow around an actuator disc

In describing the velocity variation across the flow around an actuator disc in the streamwise direction, potential flow theory is adopted. For a particle advected from far upstream towards the actuator disc, it is pushed outwards (diverged away) from the disc normal to the direction of the flow in the far field. This normal displacement of streamlines is permanent, they do not return towards the disc axis. Hence, the disc acts upstream as if it were a point source of fluid embedded in a steady uniform flow. The strength of the source is related to the net force on the structure. In modelling the actuator disc frontal area, the source of fluid may be assumed to be distributed uniformly over the disc cross section.

Although the upstream external effect of the actuator disc can be modelled a source, there is no injection of fluid at the disc: there is no discontinuity in the fluid velocity across the disc. Therefore, a different model is required for the wake region downstream of the flow. The main idea is that the mean approaching velocity in the wake zone drops from the plane of the disc to a lower value far downstream, which is denoted by the wake velocity, u_{wake}. This reduction is similar to that occurring upstream of the actuator disc. Hence, a reasonable model for the wake region is to use a fluid sink. The strength of the sink is equal and opposite to that of the source. The wake is assumed to be separated from the external irrotational flow by a vortex sheet which corresponds to a velocity discontinuity. The structure of the source/sink of the flow is shown in Figure 3.2. This source/sink model will be used to describe the global flow around an actuator disc, which is the building block to construct multiple source/sink models (to represent multiple actuator discs in-line) to obtain information on the variation of flow velocity in a real obstacle array where the flow structure changes in the streamwise direction. Note that in the modelling of the flow velocity on the axis of the actuator disc to be described next, the pressure boundary condition across the vortex sheet will be ignored. The analysis is then only approximate, in keeping with the one-dimensional modelling inherent in actuator disc theory.

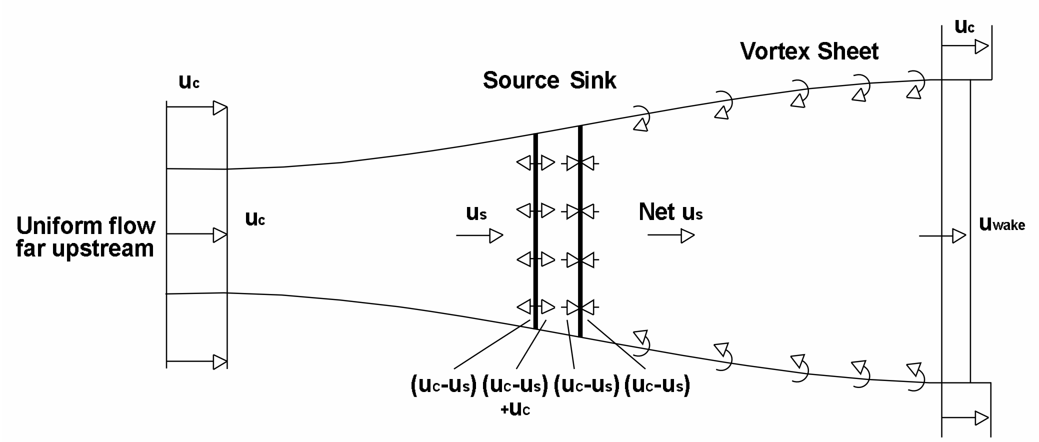

Figure 3.2: The source/sink model for the flow near an actuator disc in a free stream.

3.2.2.2 The flow velocity along the axis of an actuator disc in planar (2D) flow

The velocity distribution on the disc axis upstream can be derived from a case of point source embedded in a uniform stream in potential flow theory, see Milne-Thomson (1968).

Consider a source of strength m at the origin embedded in a uniform stream $U = u_c$ parallel to the x-axis illustrated in Fig 3.3. Combining the source with the uniform stream, the complex potentials for each can be added by superposition:

$$w = \phi + i\psi = -Uz - m \ln z$$
$$\frac{dw}{dz} = -u + iv = -U - \frac{m}{z}$$

u can be obtained by taking the real part of $\frac{dw}{dz} = -u + iv$:

$$\begin{aligned} u &= \mathrm{Re}\left(U + \frac{m}{z}\right); z = x + iy \\ u(x) &= \mathrm{Re}\left[U + m\frac{1}{x+iy}\frac{x-iy}{x-iy}\right] \\ u(x) &= U + m\frac{x}{x^2+y^2} \end{aligned}$$

where x is measured from the origin which is at the point source, thus the velocity expression on the upstream of the point source in a uniform stream is:

$$u(x) = u_c - m\frac{x}{x^2+y^2}$$

Assuming the total rate of volume addition on the source disc is $S = 2\pi m$, and the width of the disc is $2L$ which is also the frontal area A_f, the lateral position, y,

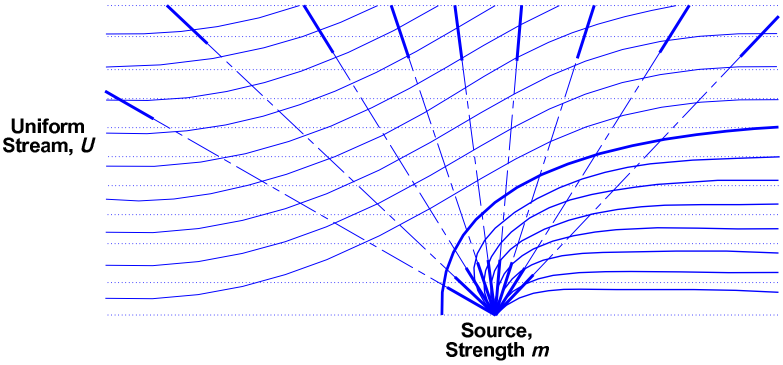

Figure 3.3: Representation of a point source in a uniform stream.

across the disc now ranges from $-L$ to L. Thus, integrating the above expression, and x is positive when measured downstream, yields:

$$u(x) = u_c - \frac{S}{2\pi L} \arctan\left(\frac{L}{|x|}\right) \tag{3.6}$$

The source strength is obtained by equating the two expressions for the shielded velocity at the disc (Equation 3.1 and Equation 3.6 with $x = 0$) as:

$$\frac{S}{4L} = u_c \left(\frac{\frac{C_d A}{4A_f}}{1 + \frac{C_d A}{4A_f}} \right) = u_s \left(\frac{C_d A}{4A_f} \right) \tag{3.7}$$

The velocity of the wake drops from u_s at the disc to u_{wake} far downstream. We assume this decay is similar to that upstream of the disc; the wake velocity can then be expressed as:

$$u(x) = u_c - \frac{S}{2L} + \frac{S}{2\pi L} \arctan\left(\frac{L}{|x|}\right) \tag{3.8}$$

Note the factor of two applies for the strength of the source as there is also a fluid sink inline with the source. These equations represent a double potential flow model consistent with one-dimensional actuator disc theory. However, we now have an estimate of the length scales over which the flow structure changes. Upstream of the disc, the flow slows down and diverges according to Equation 3.8, inversely with the distance (for $x \gg L$). Downstream of the disc, the wake relaxes fairly quickly to its far field state, $u_{wake} \to u_c - S/2L$ as $x \to \infty$ from Equation 3.8. It should be noted that this model ignores mixing out of the wake; the bounding vortex sheets are assumed to persist far downstream.

3.2.2.3 The flow velocity along the axis of an actuator disc in cylindrical (3D) flow

The assumption of planar flow is more appropriate for structures where the flow field divergence is constrained to occur on a plane, with no significant out-of-plane flow. One example is when a uniform current from seabed to the surface approaching a structure which is uniform in height. However, if the structural dimensions in both the transverse directions are comparable, if not equal, the use of a circular flow model using a circular actuator disc is more reasonable. With such circular flow model, divergence can occur in both transverse directions at the same time. The potential flow formulation in this case for both the external irrotational flow and the wake is the same as the planar flow; the only difference is that wake relaxation is faster with distance.

Consider a source disc of radius L which injects a total rate of volume addition S, the velocity on the disc axis upstream is given by:

$$u(x) = u_c - \frac{S}{2\pi L^2}\left(1 - \frac{x}{\sqrt{x^2 + L^2}}\right) \tag{3.9}$$

where x is the upstream distance from the disc. The source strength is again obtained by equating the two expressions for the shielded velocity at the disc surface, which total disc area $A = \pi L^2$:

$$\frac{S}{2\pi L^2} = u_c \left(\frac{\dfrac{C_d A}{4A_f}}{1 + \dfrac{C_d A}{4A_f}}\right) = u_s \left(\frac{C_d A}{4A_f}\right)$$

In the limit $x \to \infty$, the perturbation to the free–stream decays with the square of the distance, as follows:

$$\lim_{x\to\infty}\left[u_c - \frac{S}{2\pi L^2}\left(1 - \frac{x}{\sqrt{x^2 + L^2}}\right)\right] \to u_c - \frac{S}{4\pi x^2},$$

so the upstream influence decays more rapidly in three-dimensional cylindrical flow than in the two-dimensional planar flow. The three-dimensional potential flow model for the wake equivalent to that of the two-dimensional plane follows directly. The wake is assumed to relax very rapidly downstream of the disc as well.

Again, assuming that the decay of the downstream wake is similar to that upstream of the disc, the wake velocity can be written as:

$$u(x) = u_c - \frac{S}{\pi L^2} + \frac{S}{2\pi L^2}\left(1 - \frac{x}{\sqrt{x^2 + L^2}}\right)$$

There are two situations where the three-dimensional model is useful, despite the fact that the planar model is more appropriate for most of the current blockage applications. First is the analysis of the compliant tower towed longitudinally, be it a real structure or a tower model as discussed in Section 3.3.2. The second is in the application of finite current layer depth flows past a very tall structure, where the width of the structure and the depth of the current layer at the structure are comparable.

3.2.2.4 A two-disc model for planar flow through an obstacle array

To construct a two-disc model, consider a flow through two in-line actuator discs, which are separated by a distance D apart. Using the potential flow models derived earlier, it is easy to write down the velocity at each disc by combination of the perturbations to the mean flow introduced by each disc individually:

$$\begin{aligned} u_1 &= u_c - \frac{S_1}{4L} - \frac{S_2}{2\pi L}\arctan\left(\frac{L}{D}\right) \\ u_2 &= u_c - \frac{S_1}{2L} + \frac{S_1}{2\pi L}\arctan\left(\frac{L}{D}\right) - \frac{S_2}{4L} \end{aligned} \tag{3.10}$$

The velocity at the plane of the upstream disc, u_1, is equal to the upstream current, u_c, reduced by two components: the first is due to the blockage at the first disc itself, the second term is due to the upstream influence of the blockage at the second disc. This upstream influence of the second disc is much weaker, decaying as the streamwise separation distance of the two discs, D, is increased.

Likewise, the reduction in the velocity at the downstream disc comprises two components: a self-induced blockage and the effect of the wake of the first disc. It is worth noticing that the wake term in this equation rapidly rises to a limit when the disc spacing is increased. So long as the global wake mixing effect with the surrounding fluid is ignored, this downstream wake effect lasts for ever, while the upstream flow divergence is a much localised effect in nature.

Substituting the expressions for the strength of sources into Equation 3.10, the two-disc formulation of the actuator disc theory in planar flow becomes:

$$\begin{aligned} u_1 &= u_c - u_1\left(\frac{C_d A_1}{4A_f}\right) - u_2\left(\frac{C_d A_2}{4A_f}\right)\frac{2}{\pi}\arctan\left(\frac{L}{D}\right) \\ u_2 &= u_c - u_1\left(\frac{C_d A_1}{4A_f}\right)\left[2 - \frac{2}{\pi}\arctan\left(\frac{L}{D}\right)\right] - u_2\left(\frac{C_d A_2}{4A_f}\right) \end{aligned} \tag{3.11}$$

The only unknowns are u_1 and u_2. Consequently, the above formulation becomes a pair of simultaneous equations for the velocities at each disc. Solving these equations, the force on each disc can be obtained by the local Morison equation:

$$F_1 = \frac{1}{2}\rho C_d A_1 u_1^2 \quad \text{and} \quad F_2 = \frac{1}{2}\rho C_d A_2 u_2^2$$

In the event of analysing N number of discs, the above formulations become a set of $N \times N$ matrix of linear simultaneous equations. Unless wake mixing is important to consider, only one or two discs are necessary if only the total force on an entire structure is required.

3.2.2.5 A two-disc model for cylindrical flow through an obstacle array

Similar to the planar flow model, to construct a two-disc model, consider a flow through two in-line actuator discs, which are separated by a distance D apart. The velocity at each disc, as a combination of the perturbations to the mean flow introduced by each disc individually, can be expressed as:

$$\begin{aligned} u_1 &= u_c - u_1\left(\frac{C_d A_1}{4A_f}\right) - u_2\left(\frac{C_d A_2}{4A_f}\right)\left(1 - \frac{D}{\sqrt{D^2+L^2}}\right) \\ u_2 &= u_c - u_1\left(\frac{C_d A_1}{4A_f}\right)\left(1 + \frac{D}{\sqrt{D^2+L^2}}\right) - u_2\left(\frac{C_d A_2}{4A_f}\right) \end{aligned}$$

3.2.3 Improvements to the single actuator disc model

This section provides ways around the limitations encountered by a single actuator disc theory. Due to the importance of the improvement on the third limitation, i.e. steady flow in the presence of regular waves, it will be presented in a separate stand-alone section instead.

3.2.3.1 A switching model for high hydrodynamic loading

As mentioned above in describing the first limitation encountered by the single actuator disc theory, when the hydrodynamic loading on a structure is very high: $C_d A > 4A_f$, the simple current blockage theory becomes inconsistent. The total drag formulation based on this theory predicts that the drag decreases (slowly) as the loading is further increased, instead of the other way round. This slight inconsistency can be observed from the formulation as such:

$$\text{Drag on a single disc} = \frac{1}{2}\rho C_d A u_c^2 \left(1 + \frac{C_d A}{4A_f}\right)^{-2}$$

If $\dfrac{C_d A}{A_f} > 4$, the total force on the higher loaded disc is reduced for the single disc model as the hydrodynamic loading $C_d A$ is increased - an implausible result.

However, it ought to be possible to model a structure as an infinite array of infinitely sparse discs, considering an extreme case of a structure under very high hydrodynamic loading.

The total drag formulation for many sparse discs can be formulated as (derivation in Appendix A):

$$\text{Drag on many sparse discs} = \frac{1}{2}\rho C_d \frac{A}{N} u_c^2 \sum_{n=1}^{N} u_n^2 = \frac{1}{2}\rho A_f u_c^2 \left\{1 - \exp\left[-\left(\frac{C_d A}{A_f}\right)\right]\right\}$$

This formulation shows that the drag increases with the total hydrodynamic area to an asymptotic value of the product of the frontal area of the array and the dynamic head of the free stream flow.

This result should be compared to the previous expression which is for a single disc with the same total hydrodynamic loading. The two expressions for the drag look different. However, numerical calculations (see Figure 3.4) reveal that these two expressions are virtually indistinguishable even for the loadings greater than the limit for the single disc model, although the two expressions are apparently very different.

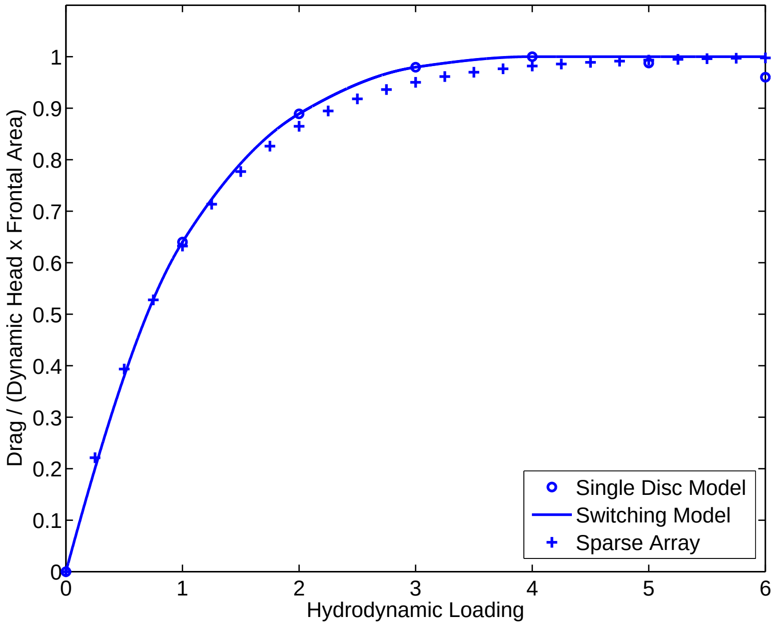

Figure 3.4: The comparison of single disc, sparse array and switching model.

Thus, it can be safely concluded that the total drag on the array does not depend significantly on the structural layout along the flow direction. This leads to the conclusion that the simplest actuator disc model valid for all sorts of hydrodynamic values is actually the switching model:

For $C_d A < 4A_f$, a single disc model is used.

For $C_d A > 4A_f$, a two-disc model is used.

The assumption for a two-disc model is that, due to the nature of the high hydrodynamic loading, it is convenient mathematically to have the upstream disc carry as much loading as possible for an isolated disc ($u_{wake} = 0$). The downstream disc is placed in the fully expanded wake region of the first disc where the wake flow velocity is zero. Thus, it carries no load. This approach is consistently used in the improvement made to tackle the third limitation, which will be presented in Section 3.4.2.

Most realistic examples of the current blockage in entirely steady flow do not require the use of the switching model. Generally, a single disc model approach suffices. However, the switching model becomes important for the assessment of current blockage in the event of regular or random waves.

3.2.3.2 The inclusion of wake mixing

Previously, the actuator disc model for current blockage was derived assuming that the wake is separated by the vortex sheets from the external irrotational flow. However, in reality, these vortex sheets are rather unstable and mixing between the free stream and the wake occurs downstream of the structure. Yet, this process takes place at approximately constant pressure and hence the actuator disc model remains applicable. The main effect of this wake mixing is that the mean flow velocity on the wake axis rises slowly back to the free stream current velocity as the width of the wake increases as a result of the wake divergence.

Reference is made to Tennekes and Lumley (1972) in establishing the following relationships on the simple decay rates for the mean velocity perturbations:

In 2D planar flow, mean velocity deficit $\propto$ (distance)$^{-1/2}$

In 3D cylindrical flow, mean velocity deficit $\propto$ (distance)$^{-2/3}$

These decay rates are established for the wakes far downstream of single obstacles. In formulating the wake flow from obstacle arrays, it will be assumed that these decay rates are applicable to the wakes of arrays at downstream distances greater than one array width, because the length scale of the interaction between the global mean wake and the obstacle arrays scales approximately as the frontal width of the arrays.

For planar wake flow:

$$u(x) = u_c - \left[\frac{S}{2L} - \frac{S}{2\pi L}\arctan\left(\frac{L}{x}\right)\right] \cdot \sqrt{\frac{2L}{x}}, \qquad \text{for } x > 2L$$

where the width of the disc is $A_f = 2L$.

For cylindrical wake flow:

$$u(x) = u_c - \left[\frac{S}{\pi L^2} - \frac{S}{2\pi L^2}\left(1 - \frac{x}{\sqrt{x^2 + L^2}}\right)\right] \times \sqrt[3]{\left(\frac{2L}{x}\right)^2}, \qquad \text{for } x > 2L$$

For some cases which require more than 2 actuator discs, there is a difficulty with how to treat the effect of the second disc on the third disc due to the decay of the wake of the first disc, as there would be additional interference. In this actuator disc analysis, such interference effects are ignored. The decay of the wake of the first disc up to the third disc is treated as though the second disc was absent.

3.3 Experimental evidence for current blockage in steady flow

3.3.1 Lattice frames in turbulent flow

Georgiou and Vickery (1980) conducted experiments intended to measure the shielding effects which are present for flows through configurations of multiple building frames. Hence, they conducted experiments in a wind tunnel with multiple biplanar lattice frames aligned in-line, by varying the direction of approaching wind flow, frame solidity ratio, frame spacing, frame aspect ratio and the number of frames.

Among all the various different experiments, one experimental result is used to compare with the load prediction based on the current blockage theory. The chosen set has an aspect ratio (height, H / breadth, B) of 4.0, spacing, S / breadth, B ratio of 0.186, breadth dimension, B, of 1.239 m (or 4.063 ft), and frame solidity ratio of 0.136. The frame solidity ratio is defined as the effective solid area of a single frame divided by the total area enclosed by a single frame, the A/A_f ratio in the current blockage theory. The loads were recorded by a rotatable strain-gauge plate as shown in Figure 3.5. Wind tunnel blockage corrections were applied by repeating another series of tests in a much bigger tunnel with presumed zero blockage effect. The measured forces on the frames in the wind tunnel are estimated to be within 10% of the forces to be expected in unconstrained flow.

The experimental results are in the form C_d, which Georgiou and Vickery refer to as a force coefficient on a group of N frames compared to the force predicted on a single frame with the flow normally incident and C_d taken to be 1. These were plotted for a combination of N = 2, 3, 4, 5 and 7 frames exposed to various angles of attack, θ, ranging from 0 to 60°. The total frontal (projected) area, A_f, will inevitably be a

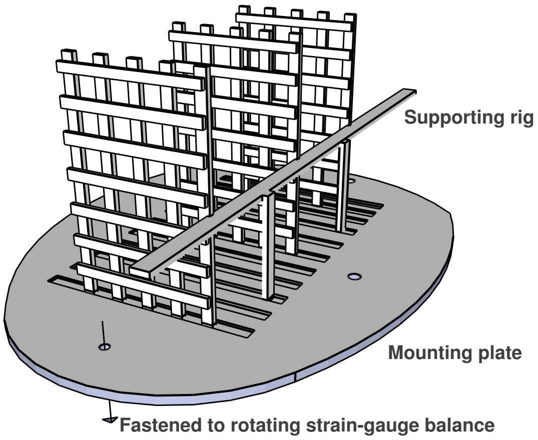

Figure 3.5: The model test setup.

Table 3.1: Summary of the drag coefficient as a function of number of frames and angle of attack.

Number of Frames	Angle between Frame Normal and Mean Flow (deg) 0	15	30	45	60
2	2.20	2.50	2.40	2.00	1.30
3	3.09	3.53	3.41	2.90	1.91
4	3.87	4.45	4.36	3.76	2.52
5	4.55	5.29	5.26	4.59	3.13
7	5.64	6.78	6.94	6.21	4.32
True C_d	1.30	1.52	1.46	1.21	0.76

function of θ, i.e. $A_f(\theta) = [B\cos(\theta) + S\sin(\theta)] \times H$. In this comparison, the force coefficient is treated much like an effective drag coefficient for a group of N frames.

Since the experiment did not provide information on the true drag coefficient, C_d, the result for two frames is used as C_d calibration to obtain the true C_d. The true drag coefficient is defined as the actual drag coefficient for flow velocity in the event of zero blockage. Meanwhile, the effective drag coefficient is the drag coefficient which has taken into account the reduced (correction) factor due to the shielded flow velocity. Having found the true C_d for each angle of attack, the subsequent effective drag coefficients for $N = 3$, 4, 5 and 7 frames are sought. The results are tabulated in Table 3.1 and plotted in Figure 3.6.

In Figure 3.6, the measured data are the symbols, while the current blockage results are plotted as solid curves. Generally, the agreement between the theory and

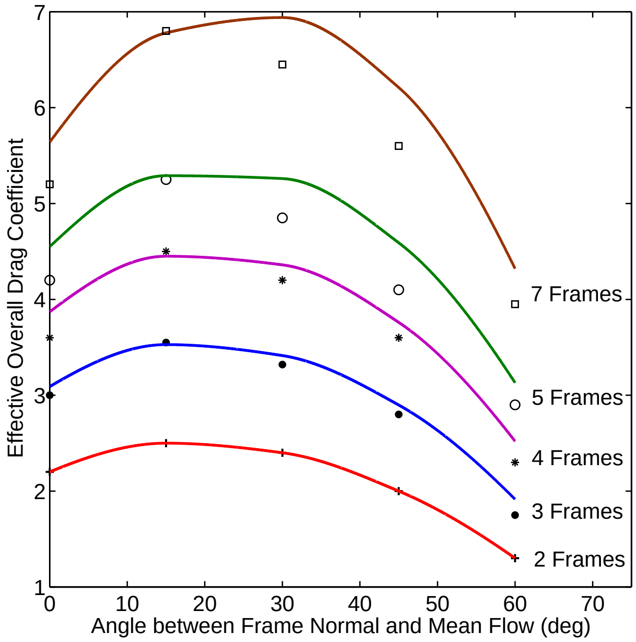

Figure 3.6: The effect of the number of frames and the flow approach angle - data points from Georgiou and Vickery (1980).

the experiment is good.

3.3.2 Model tow test of an Exxon compliant tower design

Monopolis and Danaczko (1989) reported a series of scaled model tests and numerical simulations of the transport of a hypothetical deepwater Gulf of Mexico compliant tower. The in-water towing test results are analysed in terms of the current blockage theory. The 1:48 scale compliant tower model was used in their experiment, with a cross section at full scale of 61 m by 82 m (200 ft by 270 ft), and a height of 781 m (2560 ft). Supposedly, the assembly procedure requires the tower be constructed in two separate sections, mated in shallow water and then towed into final position with virtually the whole structure completely beneath the sea surface, before being upended on the installation site. Since the aspect ratio (the length of the structure over the maximum dimension across the flow) of the structure is 9.5, this comparison serves as an extreme test of the current blockage theory.

Two sets of towing tests were conducted at speeds ranging from 0 to 2.5 m/s: towing both the completely mated and, separately, the lower section of the scaled model. The lower section represents the rear 4/7ths of the total length of the scaled model (446 m or 1464 ft). Measurements were reported for the total drag on the whole tower and also the net force on the lower section of the whole tower, which is shielded by the front section, as well as the total drag on the lower section tower only. The results were plotted in terms of drag forces, as functions of the towing speed. In this comparison, only the total drag and the drag on the lower section of the entire tower are analysed.

The geometry is shown in Figure 3.7. The whole tower is divided into seven actuator discs, and hence the total hydrodynamic area is distributed equally onto each of them. Due to its extreme geometry, wake mixing must be considered. The simple correction based on the decay of an axisymmetric wake is applied when the aspect ratio (the length of the disc separation distance / half the width of the disc) > 2. Note that this aspect ratio is defined in terms of the actuator disc geometry, not to be confused with the aspect ratio defined in terms of the tower geometry.

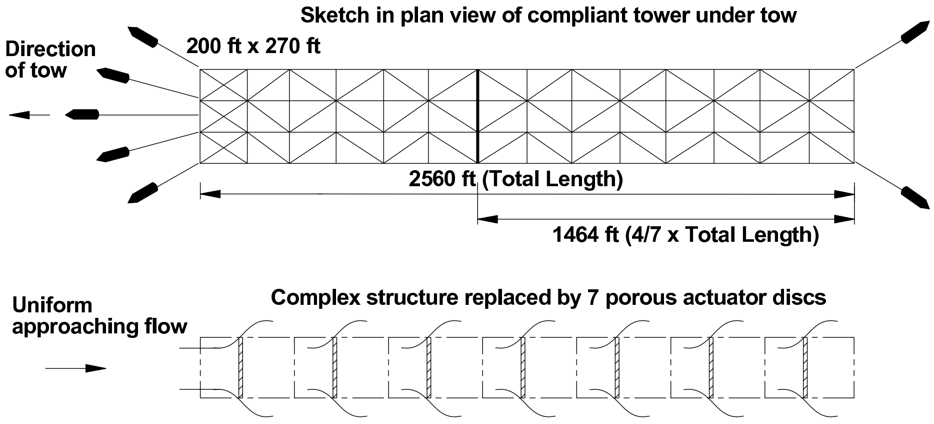

Figure 3.7: Generic towed compliant tower modelled as a series of in-line actuator discs.

As there is no information on the value of the drag coefficient, a calibration is performed on the drag value at the towing speed of 0.5 m/s by assuming a drag coefficient of 1.2, in order to obtain the estimate of the drag area, A. Having found the drag area, the drag estimate based on the current blockage theory can be obtained for the subsequent towing speed, up to 2.5 m/s. Another comparison is also performed using a drag coefficient of 0.9, with the same drag area. The ratio A/A_f for the whole tower is found to be 3.46. Thus, the hydrodynamic loading $(C_d A/A_f)$ for the whole tower when $C_d = 1.2$ and 0.9 is 4.152 and 3.114, respectively.

The comparisons are shown in Figure 3.8, in which the drag for $C_d = 1.2$ is slightly higher than for $C_d = 0.9$ for both mated and rear tower. The top lines represent the drag on the complete mated tower, while the bottom curves are for the rear section

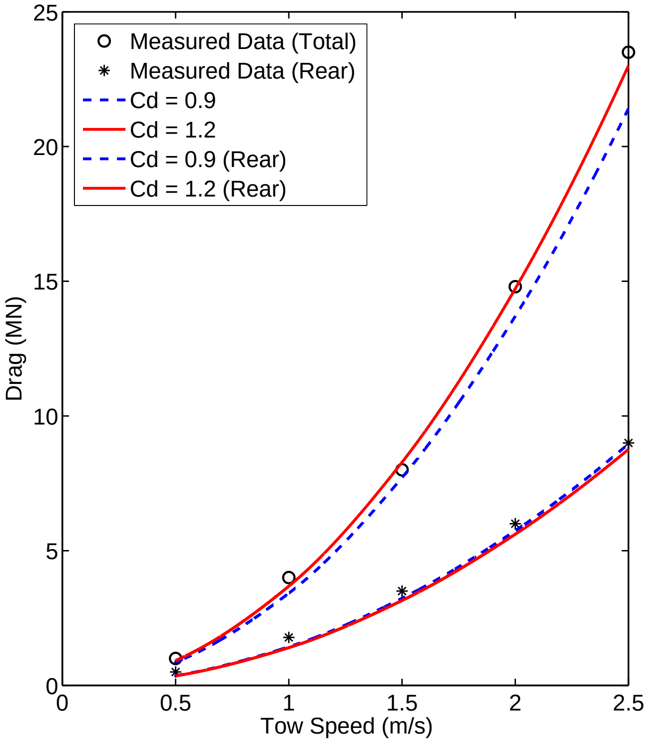

Figure 3.8: Predicted and measured drag on the scaled compliant tower model under tow - data points from Monopolis and Danaczko (1989).

only of the mated tower. This extreme case of comparison demonstrates one additional feature of the current blockage model predictions, that for high hydrodynamic loading the total drag does not depend strongly on the structural layout along the flow direction (in this case the value of the drag coefficient C_d keeping A/A_f fixed), as illustrated in Figure 3.4. Overall, the analytical results from the current blockage theory agree reasonably with the experimental results.

3.4 Current blockage with regular waves

3.4.1 Background

So far, the theory of current blockage has been applied to steady flow problems only. Comparisons made so far show generally good agreement between the theory and experiments involving steady flow, the model towed at constant speed, and the frames loaded at constant wind speed in a wind tunnel.

However, in reality, the environmental loading on a steel offshore platform can be regarded as being dominated by the drag force which contains large unsteady flow components: driven by either regular or random waves, and a generally smaller steady flow: the current. As presented below, the theory for steady current flow over-predicts the offshore loading on a platform as a combination of both wave and current forces. Physically, the time averaged mean force due to waves is larger than that due to the current alone. This larger averaged mean force should be reflected in a larger reduction in the current close to the platform. Such a greater force reduction corresponds to a genuine physical difference in the local flows around the structure resulting from the presence of waves. It is therefore highly desirable to obtain a formulation which is applicable in the presence of regular waves, propagating on an in-line current.

It should be stressed that the material in this chapter is aimed at the prediction of peak loads in regular waves and a current. It is clear that an isolated large wave (group) on a steady current, or a large wave within a random wave background on a current, would require a different model. This is necessary because the wave–current–structure interaction requires a large-scale wake, which is responsible for the global blockage effect. With regular waves, this wake has reached a steady-state structure downstream whereas for isolated wave packets it will not have reached steady-state during the time taken for the packet to dynamically load the structure. An extension of our formulation to account for the time-dependent evolution of this large-scale wake in random waves is in development.

3.4.1.1 Analysis of Chevron model tests suggests the steady current blockage model is inadequate

Comparison between the standard practice of peak force estimation, i.e. the standard Morison model and the Morison model with simple current blockage, and the experimental measurements of the peak forces on a Chevron model in regular waves with a current is shown in Figure 3.9. The experimental tests were conducted by Allender and Petrauskas (1987) on a realistic scale model of a Gulf of Mexico offshore platform. The aim was to examine the wave and current loading on the scaled jacket in a wave tank using a range of wave heights and current speeds. The details of these experiments will be discussed in the next section.

Figure 3.9 shows a comparison of the measured and predicted peak base shear force on the model, for a 2.5 m/s current and a wide range of regular wave heights. The point data are the measured forces scaled up to full scale, while the solid curves are two models for the estimated peak forces. The top solid line represents the standard Morison equation for estimating the environmental forces on a stick model, without any allowance for blockage effects. As seen from the figure, the peak force

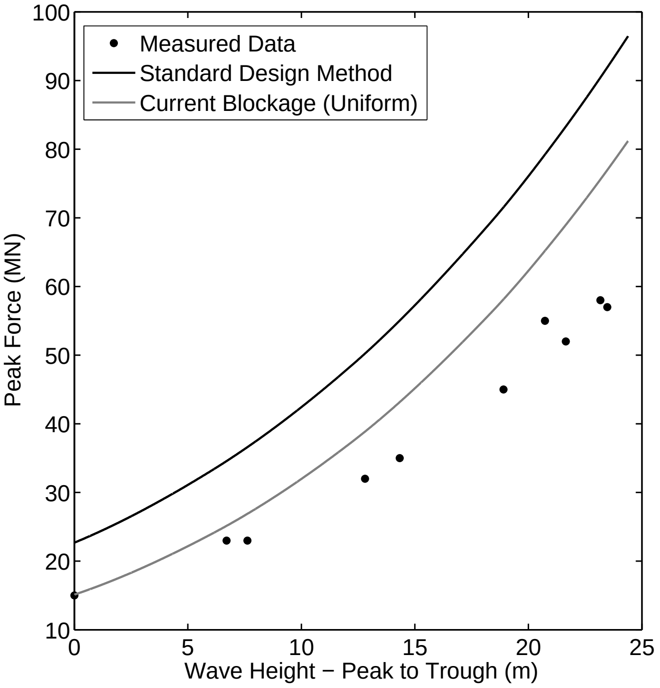

Figure 3.9: Discrepancy between the predicted and measured forces on space-frame model with waves and 2.5 m/s in-line current.

on the structure is massively overestimated. The lower line allows for simple current blockage (refer to Equation 3.1), which reduces the mean current by the factor:

$$\left(\frac{1}{1 + \dfrac{hydrodynamic\ area}{4 \times frontal\ area}} \right)$$

and corresponds to a reduction in terms of the peak force by order of 20%. It is observed that the steady current blockage formula predicts the correct drag force regime for zero and small waves. However, for large waves, the estimated peak forces on the structure are apparently considerably overestimated. Therefore, an improvement to the simple current blockage theory is desirable.

3.4.2 A theory for the peak force on a structure in regular waves and a current

In describing the theory for full current blockage model for regular waves with in-line current, an assumption of scale separation is made. The current blockage model is formulated by assuming that the diameter of individual cylinders is very much smaller than the frontal width of an obstacle array, and that the sweep distance of the wave oscillation is smaller than the frontal width of the array, and hence the sweep distance is much larger than the individual cylinders. This gives the scale separation necessary for the modelling to work. These assumptions hold for a typical big offshore jacket exposed to waves in a severe storm. As such, wake shielding (or blockage from pure wave oscillation with no current) is expected not to occur in this case, even though in big waves with no current wake shielding is known to occur as there is a mean force resulting from the average over a wave cycle (since the wave crest and trough kinematics and free surface effects are different for crests vs. troughs for nonlinear waves). For a structure such as an offshore jack-up leg, the leg width could be equal to the wave sweep distance, so there would be some wake shielding – a problem left for future work.

3.4.2.1 Why a one-actuator disc model fails in the presence of sufficiently large waves

Consider a single obstacle disc in a flow with both a steady current u_{cs} (the extra subscript s denotes that this is the shielded current at the disc, not the free stream current u_c), and an oscillating component u_w. We assume that the Morison equation can be used to describe the force on the obstacles over the wave cycle and further assume that there are no Keulegan-Carpenter number effects; the drag coefficient is constant throughout. The averaged force over a complete flow oscillation can be expressed as:

$$\frac{F_{av}}{\frac{1}{2}\rho C_d A} = \frac{1}{2\pi}\int_0^{2\pi} (u_w \cos\phi + u_{cs}) \cdot |u_w \cos\phi + u_{cs}| d\phi \tag{3.12}$$

where ϕ is the oscillation phase angle. Note that there is no contribution from the inertia term in the Morison equation as it does no work on the flow over a complete oscillation cycle. This integral has an exact solution as:

$$\text{for } (u_{cs} > u_w) : \frac{F_{av}}{\frac{1}{2}\rho C_d A} = \left(u_{cs}^2 + \frac{1}{2}u_w^2\right) \tag{3.13}$$

$$\text{for } (u_w > u_{cs}) : \frac{F_{av}}{\frac{1}{2}\rho C_d A} = \left(u_{cs}^2 + \frac{1}{2}u_w^2\right) \cdot \left[1 - \frac{2}{\pi}\arccos\left(\frac{u_{cs}}{u_w}\right)\right] + \frac{3}{\pi}u_{cs}u_w\sqrt{1 - \left(\frac{u_{cs}}{u_w}\right)^2} \tag{3.14}$$

In the limit when the current is small relative to the oscillation velocity amplitude, the second expression for the averaged force can be reduced to:

$$\frac{F_{av}}{\frac{1}{2}\rho C_d A} \rightarrow \frac{4}{\pi} u_{cs} u_w \quad \text{for } (u_w >> u_{cs}) \tag{3.15}$$

Notice that this expression for the averaged force is defined in terms of the flow velocity at the disc; the relationship is local in nature.

In order to relate these expressions to the global reduction in the free stream current at the disc, the result from the actuator disc theory for the structure of the time averaged mean flow is used. From the analysis of the mean flow external to the disc, the net force on the disc can be written in terms of the free stream current u_c, and the mean shielded current at the disc, u_{cs}, as:

$$F_{av} = 2A_f \rho u_{cs}(u_c - u_{cs}) \tag{3.16}$$

where A_f is the frontal area of the disc. Note that the above actuator disc model is for steady flow, yet it is applicable in this case since it is assumed that the structure of the mean flow near the disc is dominated by the global wake. This global wake consists of vorticity shed from the obstacles and advected downstream by the mean flow. In the high frequency limit when the oscillation amplitude is small relative to the disc geometry, the net vorticity in the wake reflects the averaged force on the disc.

Equating these last two expressions for the time averaged force on the actuator disc, whereby one is local while the other is global in nature, the reduction in the free stream current at the disc due to the upstream flow divergence can be written as:

$$(u_c - u_{cs}) = \frac{C_d A}{4A_f} \frac{4}{\pi} u_w \quad \text{valid in the limit } (u_w >> u_{cs}) \tag{3.17}$$

This expression shows how a single disc model actually fails. The expression predicts strong blockage of the current at the structure in the absence of the free stream current, and depends only on the strength of the oscillating flow term in the limit of large regular waves. We compare this with the general blockage factor of a single disc model under steady flow, which is dependent on the strength of the free stream current:

$$(u_c - u_{cs}) = u_c \left[1 - \left(1 + \frac{C_d A}{4A_f} \right)^{-1} \right]$$

Of course, in the limit of zero or very small current, there is only one possible solution, which is zero blockage. With no mean flow there is no net force on the structure, with no net force on the structure there is no global wake, and with no global wake there can be no blockage taking place.

This discrepancy can be actually related to the problem of a heavily loaded actuator disc in steady flow, and can be resolved in a similar manner. For the time averaged actuator disc model to be self consistent, and the one-dimensional basis of the analysis not to fail, the mean velocity of the flow in the fully expanded wake far downstream must be greater than zero.

From the previous actuator disc analysis, the flowfield is found to have an important symmetry property: half the reduction in the mean flow velocity due to the blockage occurs upstream of the disc and half downstream in the expansion of the wake. If the wake velocity is to be greater than zero, the minimum value of the shielded current at the disc is simply:

$$u_{cs} \geq u_c/2$$

Substituting this limiting value into Equation 3.17, the maximum possible value for the hydrodynamic loading on a single actuator disc model for the one dimensional model to be valid:

$$C_d A \leq \frac{\pi}{2} \frac{u_c}{u_w} A_f \quad \text{valid in the limit } (u_w >> u_{cs}) \tag{3.18}$$

This loading limit (denoted by $C_d A_L$) depends on the frontal area of the disc and the ratio of the free stream current velocity to the oscillation velocity. If this limit is satisfied, then the structure can be modelled by constraining it into a single actuator disc and the reduction of the free stream current can be obtained from the Equations 3.13 or 3.14 and 3.16 in a straightforward manner.

If this limit is violated, then the single actuator disc model fails. As the space-frame of a typical offshore structure is three dimensions, it is up to the analyst to choose the number of in-line actuator discs to model the structure. From the previous steady flow analysis, the predicted total force is only weakly dependent on the arrangement and distribution of the discs, so long as the global wake spreading is not significant. Hence, two discs are assumed to be sufficient to model structures in a mean flow on top of an oscillation flow.

3.4.2.2 Force on a structure modelled as two actuator discs

Similar to the concept proposed for the switching model, the first disc is assumed to be loaded as highly as possible. The loading of that upstream disc is thus limited to $C_d A_L$, and the current at the disc is one half of that far upstream ($u_{cs} = u_c/2$).

The hypothetical second disc is assumed to be located in the far wake of the first disc, so that the mean current is reduced to zero, and the remainder of the total hydrodynamic loading area $C_d(A - A_L)$ is attributed to this downstream disc.

This is a slightly modified switching model described earlier. Notice that the assumption that the second disc is placed far downstream is made only for convenience. In general, discs can be of any distance apart. There is always a downstream influence of the first disc on the second disc due to the wake of the first disc. However, the influence of the second disc on the first disc due to the upstream divergence of the flow as it approaches the second disc becomes negligible once the disc spacing is increased.

Due to the wave horizontal velocity profile which decays hyperbolically from the mean sea level towards the seabed, there exist three distinct regions for the variation between the wave and the current velocities. These three regions are as follows.

Case (i): when $u_w > u_{cs}$ and $u_{cs} \leq u_c/2$

In general for larger values of the free stream current, the condition $u_w >> u_{cs}$ is no longer satisfied. Hence, the asymptotic expression for the averaged force (Equation 3.15) is no longer valid. Thus, the full solution (Equation 3.14) is required, and the structure is modelled as two discs. The blocked current, u_{cs}, is obtained by equating Equation 3.14 with 3.16, which is shown in Equation 3.19. Due to the degree of complexity in Equation 3.14, a solution for u_{cs} by trial and error is required.

$$\begin{aligned}\frac{2A_f u_{cs}(u_c - u_{cs})}{\frac{1}{2}C_d A} &= \left(u_{cs}^2 + \frac{1}{2}u_w^2\right) \cdot \left[1 - \frac{2}{\pi}\arccos\left(\frac{u_{cs}}{u_w}\right)\right] + \\ &\quad \frac{3}{\pi}u_{cs}u_w\sqrt{1 - \left(\frac{u_{cs}}{u_w}\right)^2}\end{aligned} \tag{3.19}$$

Once u_{cs} is obtained, a further check is necessary for $u_{cs} \leq u_c/2$. If so, then we may proceed with the two-disc model, with the allowable loading on the first disc written as:

$$\frac{C_d A_L}{A_f} = u_c^2 \left\{\frac{1}{4}(u_c^2 + 2u_w^2)\left[1 - \frac{2}{\pi}\arccos\left(\frac{u_c}{2u_w}\right)\right] + \frac{3}{2\pi}u_c u_w\sqrt{1 - \left(\frac{u_c}{2u_w}\right)^2}\right\}^{-1}$$

This expression is obtained by rearranging Equation 3.19, and the current at the first disc is taken to be $u_{cs} = u_c/2$, as the limiting case.

The second actuator disc thus carries the remainder of the hydrodynamic loading of the structure $C_d(A - A_L)/A_f$. The current at this second disc is taken to be zero, $u_{cs} = 0$.

The peak force on the structure can then be written as:

$$\text{Peak drag} \; = \frac{1}{2}\rho C_d A_L (u_w + \frac{1}{2}u_c)^2 + \frac{1}{2}\rho C_d (A - A_L) u_w^2 \tag{3.20}$$

The first disc is loaded heavily by both the oscillation and the current flow. On the other hand, the second disc is loaded only by the oscillatory flow. It is assumed to be completely shielded from the mean flow.

Case (ii): when $u_w > u_{cs}$ and $u_{cs} \geq u_c/2$

If the current is sufficiently large, the flow oscillation is small, and the hydrodynamic loading of the entire structure, $C_d A/A_f$, is less than 4, then the peak loading on the structure can be estimated by contracting the structure into a single actuator disc. The blocked current, u_{cs}, can be obtained in a similar fashion as in case (i) Equation 3.19, but u_{cs} is checked against u_w and $u_c/2$. If both these conditions are satisfied, this case can be modelled by a single actuator disc.

The peak force on the structure can then be written as:

$$\text{Peak drag} \; = \frac{1}{2}\rho C_d A (u_w + u_{cs})^2 \tag{3.21}$$

Case (iii): when $u_w < u_{cs}$ and $u_{cs} > u_c/2$

The blocked current, u_{cs}, can be obtained by equating Equation 3.13 with 3.16, which is shown below:

$$\frac{4A_f u_{cs}(u_c - u_{cs})}{C_d A} = \left(u_{cs}^2 + \frac{1}{2}u_w^2\right)$$

Rearranging in terms of u_{cs}:

$$\left(1 + \frac{C_d A}{4A_f}\right) u_{cs}^2 - u_c u_{cs} + \frac{1}{2}\left(\frac{C_d A}{4A_f}\right) u_w^2 = 0$$

Solving for u_{cs}:

$$u_{cs} = \frac{u_c \pm \sqrt{u_c^2 - 4\left(1 + \frac{C_d A}{4A_f}\right)\left(\frac{C_d A}{8A_f}\right) u_w^2}}{2\left(1 + \frac{C_d A}{4A_f}\right)}$$

Further simplification leads to:

$$u_{cs} = \frac{u_c + \sqrt{u_c^2 - 2\left(1 + \frac{C_d A}{4A_f}\right)\left(\frac{C_d A}{4A_f}\right) u_w^2}}{2\left(1 + \frac{C_d A}{4A_f}\right)} \tag{3.22}$$

while the ± operator has been changed to +, since the $u_{cs} > u_c/2$ requirement is imposed.

The peak force on the structure can then be written as:

$$\text{Peak drag } = \frac{1}{2}\rho C_d A(u_w + u_{cs})^2 \tag{3.23}$$

Although this procedure may seem to be rather convoluted, it reveals that there is considerably more reduction in the current within a structure if the flowfield is combined with a regular oscillatory flow, along the direction of the current. The next section will show how this calculation method can be readily implemented for a structure exposed to regular waves and current. The flowfield is cut into horizontal slices, each slice represented by a disc. Within each slice, the free stream current and the wave induced motion can be found. The peak drag for each slice through the structure can then be calculated using the method presented in this section. The total force on the structure is then obtained by summing up the forces on each individual slice. Note that this procedure works best when the current profile is uniform throughout the water depth. Otherwise, the downwards divergence of the current layer should be considered.

For the sake of illustrating the behaviour of the analytical models of current blockage with regular waves, the following diagrams from the Allender and Petrauskas case (with the associated parameters) are presented. The three distinct regions (or submodels) can be summarised in a schematic diagram shown in Figure 3.10. The peak drag is plotted as a solid line with data points for various wave velocities under a constant current at 2.5 m/s. The three submodels switch very smoothly among each other at two separate switching limits, as if the peak drag was obtained from a single force expression.

A typical velocity and drag profile for a structure under waves and current loadings is shown in Figure 3.11. Note that the free stream current is recorded at 2.5 m/s. The extra blockage due to wave–current interaction is also reflected in the same figure. The blocked current profile, u_{cs}, slowly decays from approximately one-third of the water depth up to the mean sea level (region where wave kinematics are more prominent) as opposed to the steady flow case whereby the blocked current profile is uniform throughout the water depth. Again, the peak drag profile plotted as a function of water depth varies smoothly.

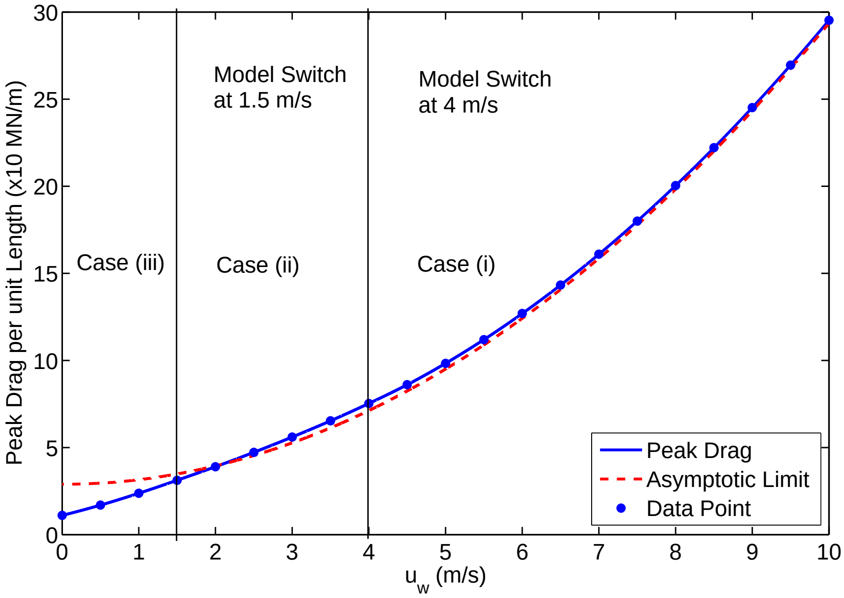

Figure 3.10: The variation of peak drag with wave kinematics velocity under 2.5 m/s constant current.

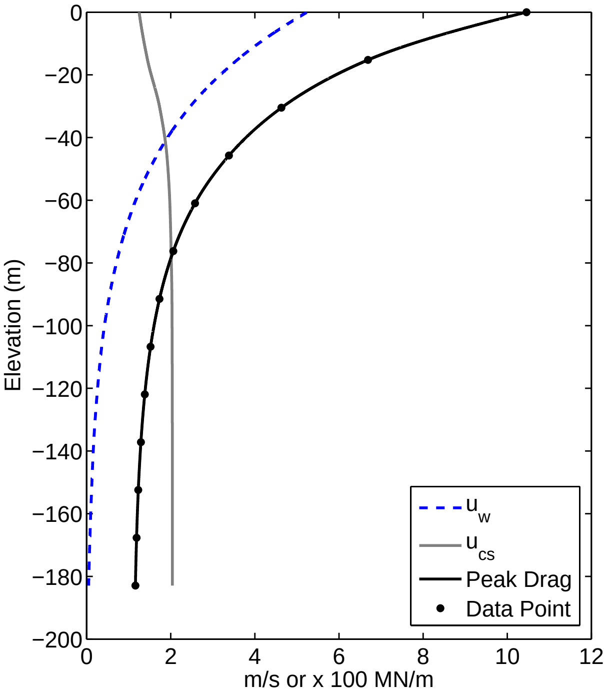

Figure 3.11: The profile of waves and current velocity, and drag force for a structure under waves and 2.5 m/s current loadings.

3.4.2.3 Asymptotic limit for regular waves and a small current

In a typical storm driven sea-state in the Gulf of Mexico or the northern North Sea, the oscillating wave induced component close to the water surface is much stronger than the current. With a wave height of about 25 m and a wave period of 12.8 sec, the surface wave induced flow speed is $u_w = 6$ m/s, whereas a typical current speed might be $u_c < 1$ m/s. Thus, it is of some interest to derive an analytical form for the drag force on a structure in the limit of large regular wave over small current.

From Equation 3.20, the two-disc model predicts the force per unit height of the structure as:

$$\text{Peak drag } = \frac{1}{2}\rho C_d A_L(\pm u_w + \frac{1}{2}u_c)|\pm u_w + \frac{1}{2}u_c| + \frac{1}{2}\rho C_d(A - A_L)(\pm u_w)|u_w| \tag{3.24}$$

where the loading on the front actuator disc is $C_d A_L = \frac{\pi}{2}\frac{u_c}{u_w}A_f$. The total structural properties are $C_d A$, the hydrodynamic area, and A_f, the frontal area of the structure. Invoking the limit $u_w >> u_{cs}$, the expression for the peak drag in regular waves can be simplified into:

$$\text{Peak drag } = \frac{1}{2}\rho\frac{\pi}{2}\frac{u_c}{u_w}A_f(u_w u_c + \frac{1}{4}u_c^2) + \frac{1}{2}\rho C_d A(\pm u_w)|u_w|$$

$$\text{Peak drag } \cong \pm\frac{1}{2}\rho C_d A u_w^2 + \frac{\pi}{4}\rho A_f u_c^2 \tag{3.25}$$

Notice the absence of the wave × current term, $(u_w u_c)$, in the approximate form. The additional blockage in regular waves removes this term.

Figure 3.12 shows this expression integrated up to the full height of the structure compared to the full numerical calculations for two different wave heights using the three submodels discussed earlier (shown as the data points). The asymptotic form is reasonable even for relatively high currents. Clearly in regular waves, the peak force increases very slowly with current (only as current squared).

Likewise, Figure 3.10 shows a similar comparison between the asymptotic and the full calculations for a constant current obtained by varying the wave velocity. Notice that the asymptotic limit works very well even for the case of the local wave velocity only slightly larger than the current.

In contrast, the equivalent expression for the simple current blockage is:

$$\text{Peak drag } = \frac{1}{2}\rho C_d A\left[u_w + \frac{u_c}{\left(1 + \frac{C_d A}{4A_f}\right)}\right]^2$$

The wave squared term is identical to the regular wave case but there is a substantial wave × blocked current term. This case is perhaps more appropriate to the variation in the peak force on a structure with a mean current and a single large

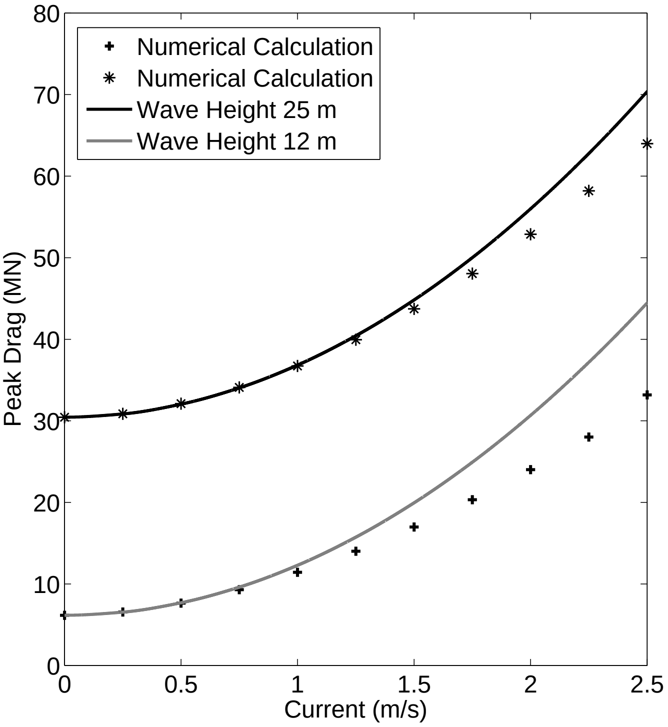

Figure 3.12: Asymptotic de-coupled form for peak drag on Chevron space-frame model in regular waves with in-line current.

wave. The peak drag force (force increases linearly with current, see Figure 3.9) is much larger than in regular waves.

3.5 Comparison with the forces measured by Allender and Petrauskas

Allender and Petrauskas (1987) carried out a set of experiments for a 1:47 scale jacket model of a Gulf of Mexico type for a 138 m (450 ft) water depth in the OTC wave / towing basin at Escondido, California. The scaled model as shown in Figure 3.13 was commissioned by Chevron, and therefore the model is described as the Chevron model subsequently. The objective of the experiments was to evaluate the use of the Morison equation in predicting the force in the presence of regular waves and current. Hence, the results are reported in terms of total wave force and current (by towing) for a wide range of environmental conditions; wave heights from 0 - 25 m (0 - 80 ft), and current speeds from 0 - 2.5 m/s (0 - 5 knot), while the wave period is fixed at 12.8 sec.

Unfortunately, Allender and Petrauskas did not present sufficient information about their model to allow direct analysis of their measured forces in their OTC paper. However, it is still possible to infer all the important parameters based on what they published.

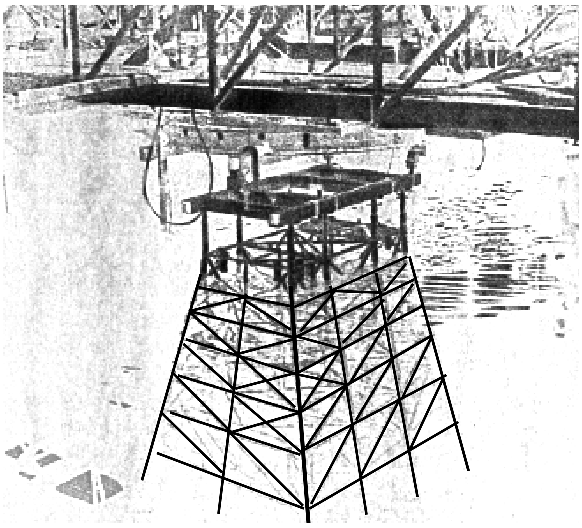

Figure 3.13: Layout of the scaled jacket model (adapted from Allender and Petrauskas Figure 1 (1987)).

The only definitely known important parameters are the water depth - 138 m, and the wave period fixed at 12.8 sec. The effective overall drag coefficient for tow tests with no waves is given in the paper. From these tests, it is reported that the steady state drag coefficient is 0.6 for the 2.5 m/s towing speed, and 0.7 for the 1.25 m/s case. Each drag coefficient is associated with its own measured drag. This enables direct comparison using the standard drag formula to extract information on the drag area, A, and the actuator disc loading parameter C_dA/A_f from the simple current blockage model for steady flow. Combined with the information on the towing speed (free stream current) as well as the wave height and wave period, this is adequate to predict the peak force on the structure as the wave crest passes by using the current blockage model. The drag area, A, is found to be 7871.7 m^2, and the frontal area, A_f is estimated to be 8115.2 m^2, giving $A/A_f = 0.97$.

Further we assume an individual value of the drag coefficient of $C_d = 1.0$. It is reasonable given the size of the individual elements within the Chevron model. Note that using this value of C_d, the area ratio of the drag area of the structure to its frontal area is $A/A_f = 0.97$ for the Chevron structure. This is smaller than that for a typical northern North Sea jacket. This is expected as the Chevron platform is of comparable size as one for the North Sea but made of smaller diameter members.

Even though the dominant forces on any space frame structure, such as a conventional jacket, are drag forces, the inertia force component of the Morison equation can be quite significant for small waves. Hence, there is a need to approximate the parameters involved in the inertia component, which is the estimate of the displaced volume and the inertia coefficient. Given the drag area, A, obtained earlier, we assume 1 m average as the best representation for the diameter of circular cylinder members within the structure. With the knowledge of a typical diameter and the drag area, an estimate of the displaced volume (V) can further be made, which is 6170.87 m^3. In terms of the inertia coefficient, a value of $C_m = 2.0$ is used throughout the analysis in this section.

One last set of assumptions is regarding the flow kinematics at the wave crests. It is worth mentioning that even though the experiment by Allender and Petrauskas was conducted in regular waves in a wave tank, it is by no means clear whether the Stokes wave model is appropriate for regular waves artificially created. To minimise the degree of complexity in the implementation of the current blockage model, simplifications have been made. Here, linear Airy wave theory is used to describe the flow kinematics below mean sea level, while vertical extrapolation at the wave crests (assuming the kinematics value to be the same as those at the mean sea level) is utilised for the free surface kinematics. Although this procedure is crude, it gives sensible values for the overall forces on the structure.

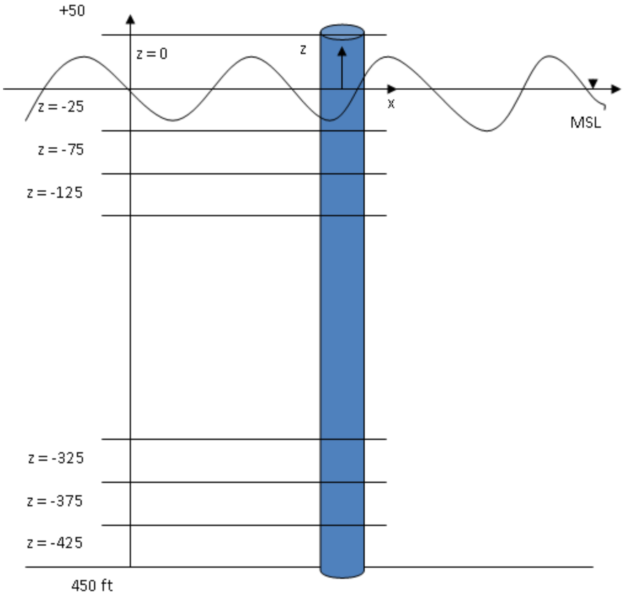

Figure 3.14: The layout of the stick model.

The next step is to construct a stick model as representative of the Chevron jacket model. We assume that the Chevron model is uniform along its height, so is the stick model. The analysis is then carried out by slicing the model or structure into N horizontal sections and the flow in each section is calculated using the various versions of the actuator disc theory (in the presence of regular waves). This procedure further assumes that the flowfield is planar (2D) and that each horizontal section is independent. Figure 3.14 illustrates the layout of the stick model.

Since no information on the jacket height is provided, the height of the stick model is assumed to be 152 m (500 ft). Thus, in calculating the wave forces on the stick model using the current blockage formulation, the drag area, A, and the volume, V, are divided by the number of the horizontal sections, $N = 20$ in this case, assuming uniform distribution along the height of the structure.

Three different formulations are compared with the experimental results from Allender and Petrauskas, namely the standard Morison force equation, the Morison model with the simple current blockage theory (steady flow), and the Morison model with the full current blockage theory with regular waves. The comparisons are shown in the following sections.

3.5.1 Forces on the Chevron structure with waves but no current

Figure 3.15 shows a comparison of the peak horizontal force (base shear) predicted in regular waves by the standard Morison equation and those measured by Allender and Petrauskas. The top solid line is the total predicted Morison force, while the bottom solid line is the Morison drag force only. For these zero current (towing) tests, the comparison suggests that the peak forces are reasonably well predicted using the Morison equation with a drag coefficient of $C_d = 1.0$ and inertia coefficient of $C_m = 2.0$. These values have been retained for all the calculations in this section.

There is no account of any significant wake shielding (wave blockage) in these zero current wave tests, nor are there any indications of Keulegan–Carpenter number effects for the peak force on the entire structure in the overall peak force measurements. The good agreement between the predicted peak forces and the measurements for this zero current case justifies the validity of the linear wave theory with the exponential decay of the wave kinematics below mean sea level (MSL) and vertical extrapolation above MSL to the wave crest.

It is worth noting that the gradient of the total force vs. the wave height is finite for the small wave regime. This shows the importance of the inertia component in

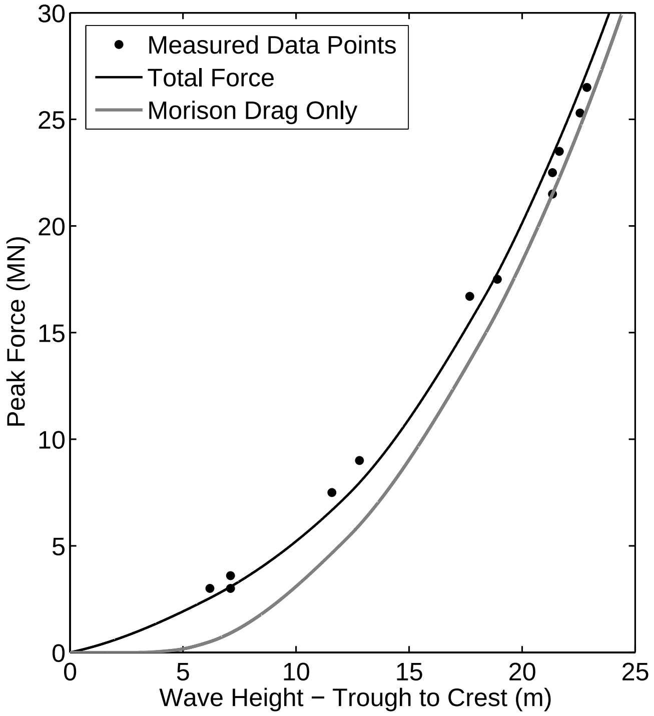

Figure 3.15: Comparison of the predicted and measured forces on space-frame model with waves and zero current.

the Morison equation for small waves. The inertia term is proportional to the fluid particle acceleration, and this acceleration is proportional to the wave height. For bigger waves, the drag term dominates, being proportional to the square of the fluid particle velocity, thus to the square of the wave height.

3.5.2 Forces on the Chevron structure for both waves and current

Allender and Petrauskas recorded the measured peak forces in terms of an effective drag coefficient, C_{de}. This C_{de} can be used as a direct representative of the drag force, because when combined with the values of current and the wave induced velocities together with the exposed area, it yields the measured force. Allender and Petrauskas stated that:

"The drop in C_d between wave alone and wave plus current cases found here (from a C_d of 1.3 - 1.6 for waves to a C_d of 0.7 - 0.8 for waves plus current) is much greater than expected ..." (Allender and Petrauskas, 1987)

They speculated that significant flow blockage occurred in their tests but had no theory to explain it. This section attempts to reproduce their force measurements with the new current blockage theory.

Figures 3.16 and 3.17 present the comparison of the peak forces (base shear) predicted in regular waves in two current (towing) speeds, i.e. 1.25 m/s and 2.5 m/s. Three different methods of prediction are provided, namely the standard Morison equation, the Morison model with the simple current blockage formulation, and the Morison model with the current blockage with regular waves formulation. These figures show that the new theoretical model of the current blockage for regular waves generally fits well to the measured forces for both values of the current. In each case, the standard Morison equation, equivalent to ignoring any blockage effect, massively overestimates the peak forces on the structure. Meanwhile, the simple current blockage theory, suited for steady flow with a single large wave passing by, predicts the peak forces well in the region of small waves. However, as the waves grow bigger, the predictions from the simple current blockage theory deviate considerably from the measurements. The model for regular waves predicts the peak forces significantly lower than the rest, and the predictions from this model are in good agreement with the measurements for both towing speeds, as well as for zero current (Figure 3.15).

Overall, it should be emphasised that the methods of estimating the peak forces are solely based on the physics of the flowfield and contain no adjustable parameters. It is only the drag coefficient, C_d, which needs to be estimated beforehand. This comparison shows that the agreement between the theory for regular waves and the model tests is good and no variation in the value of the drag coefficient, C_d, is needed over the wide range of wave heights and current speeds.

3.5.3 The peak forces for small currents and regular big waves

An analytical expression for the force on a structure in the large regular waves and small current limit was derived in Section 3.4. This section attempts to compare the decoupled peak drag expression of the asymptotic limit with Allender and Petrauskas' data.

In order to demonstrate clearly this extra reduction in the effective current within a structure for regular waves, Allender and Petrauskas should have measured the peak force on their model as a function of tow speed (current) for fixed large wave height in regular waves. If the force increased quadratically, this regular wave model would be validated qualitatively. Unfortunately, this was not done.

However, a crude comparison is possible using their data for 0, 1.25 and 2.5 m/s currents and a wave height of 21 m. The measurements closest to 21 m wave height have been used but some of the scatter represents the variation of wave height in

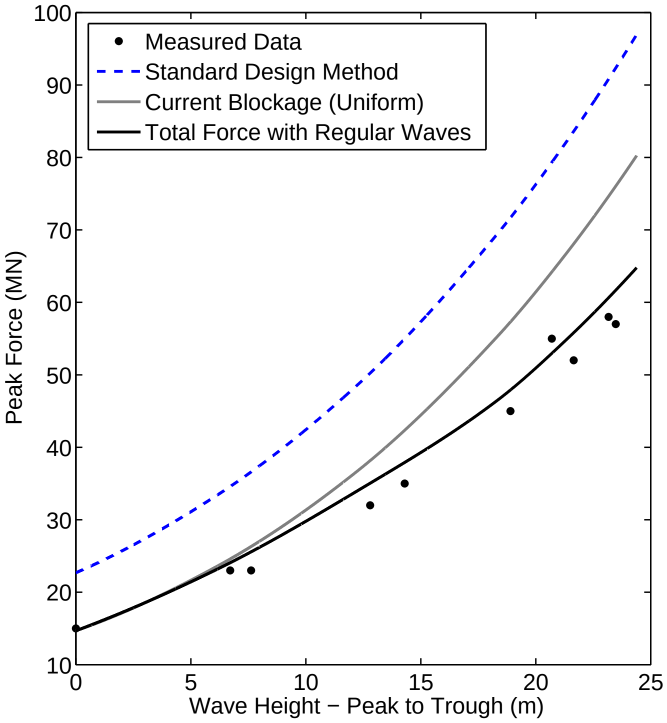

Figure 3.16: Comparison of the predicted and measured forces on space-frame model with waves and 2.5 m/s in-line current.

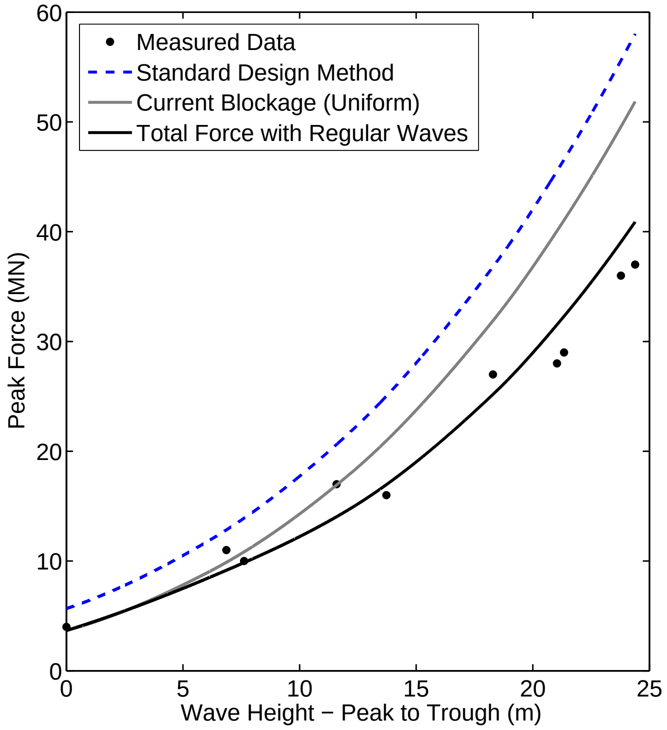

Figure 3.17: Comparison of the predicted and measured forces on space-frame model with waves and 1.25 m/s in-line current.

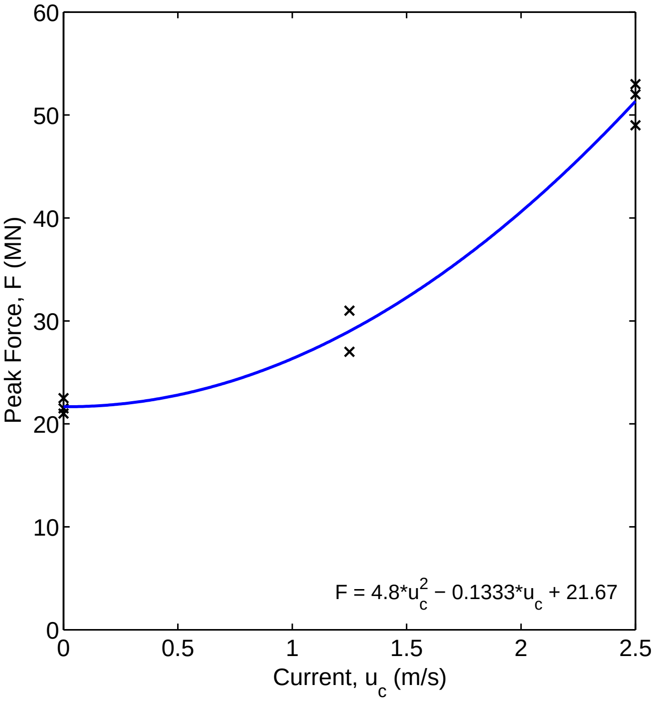

Figure 3.18: Asymptotic peak drag profile with various current.

the available data - there is not enough information available for all the three tow speeds for any other wave height. These experimental points are shown in Figure 3.18 together with a parabolic polynomial in current fitted to the measured peak forces. This parabola fits the data well, and we note that the term in the force polynomial proportional to the current (the wave × current coupling term) is insignificant.

Hence, the extensive force measurements by Allender and Petrauskas give considerable support to the idea of the de-coupling of the wave and current contributions to the peak load. This qualitative feature of the analysis is robust, being independent on the assumptions made for the wave kinematics.

3.6 Chapter summary & conclusions

The simple current blockage model was first developed almost 20 years ago. It consists of two parts, single and multiple actuator disc models, and both are valid for steady flow. The single disc model yields the offshore blockage factor, which is presently used as a standard method in estimating the amount of blockage induced by current–structure interaction. In order to improve on the single disc model to account for high hydrodynamic loading and wake mixing effects, the multiple actuator disc model has been developed. The multiple disc model also gives some information on the distribution of blocked current velocity along the discs. This simple current blockage model is valid for steady flow, and possibly for a single large wave superimposed on the top of steady flow. As presented in Section 3.3, there is a considerable experimental evidence for blockage in steady flow consistent with the simple model.

For flow of a current and regular waves, an improved version of the simple model, termed the full current blockage model, is required to account for extra blockage from wave–current interaction. The full model is more complex and it consists of three submodels to account for different flow regimes. The transitions between the three sub-models are smooth, depending on the magnitude of wave, free stream and shielded current velocities. For the special case of large waves in a small current flow, the full model reduces to an asymptotic expression for peak drag which contains no wave × current term, unlike the standard Morison drag which has the coupling term due to $u|u|$.

The new current blockage model accounting for wave–current effects is validated against the experimental data from Allender and Petrauskas. Despite the fact that there are several assumptions made about the model geometry, using a single C_d value of 1.0 associated with $A/A_f \approx 0.97$ and C_m value of 2.0, we successfully match all of their experimental results using the new current blockage theory, with and without large waves, with and without current.

This chapter has been published in the journal Ocean Engineering as Taylor et al. (2013).

Chapter 4

Blockage effects in wave and current: Two-dimensional planar simulations of combined regular oscillations and steady flow through porous blocks

4.1 Introduction

The material in the previous chapter, and published as Taylor et al. (2013), reveal strong evidence that a much larger blockage occurs for a structure subjected to combined regular waves and current, and propose a full current blockage model for this combined problem to improve the Morison equation (Morison et al., 1950) in quantifying the loading experienced by fixed space-frame offshore structures. This chapter serves as a follow-up study and provides direct comparison between Computational Fluid Dynamics (CFD) simulation and the theoretical analysis; comparisons are also made with the experimental data where this is available.

The first idea for investigating the effects of current blockage on an offshore structure numerically was to model a structure in the simulation as closely as possible to an existing real-life structure. Thus, the closest possible structure is inevitably a group of cylinders, positioned vertically, horizontally and diagonally, to represent the geometric complexity encountered in the framing patterns of an actual jacket or a compliant tower. Numerical simulation of flow over such complex multiple cylinders would be very challenging. Recently, Nicolle and Eames (2011) have published a study of two-dimensional flow through a complex array of cylinders, which resolved individual elements. However, it may not be necessary to model the details of each cylinder. The dominant physical process we seek to model is the reduced mean flow within and near the obstacle array over distances of the order of the width of the obstacle array, not the local flow around individual cylinders within the array. To approximate the bulk effect of the structure and the fluid–structure interaction as a whole, a porous block can be used instead as a reasonable assumption when modelling the flow around a jacket or compliant tower. Thus, flow through a porous block with a specified level of resistance can be used to model the global flow reduction effect on a typical offshore structure.

This chapter will present results based on modelling the complex geometry of a space-frame offshore structure as a porous block, and analysing the effects of current blockage on the overall hydrodynamic loading. The resistance can be calibrated from the current blockage model in the form of drag coefficient, C_d, and drag area, A, while maintaining the same frontal area, A_f, of the obstacle array. The reduced velocity and the corresponding reduced drag force on the array can then be approximately obtained from the Navier–Stokes equations in a CFD simulation. This chapter will demonstrate that, in general, the porous block model (which models the flow in two- or three-dimensional space) is better than the current blockage model (which models the flow in one-dimensional space), which was derived based on potential flow approach (conservation of mass and momentum via actuator disc theory). Apart from being able to model the simple case of flow over a compact porous block resembling a space-frame structure in steady flow, the numerical porous block model does better in modelling flow over series of blocks subjected to skewed incident angle, and also in a long array of blocks where lateral mixing (side leakage) is important, as compared to the current blockage model, all in steady flow as described in Section 4.3. The porous block model also performs better in time-averaged mean flow and fully unsteady flow: regular oscillations plus mean flow, where the flow is resolved on a planar level, and it is able to model high hydrodynamic loading case, as demonstrated in Section 4.5. The theoretical model, in contrast, requires an ad-hoc assumption of a hypothetical split into two-disc model or more when the loading gets high as the one-disc model would break down due to the limitation of a one-dimensional model. Moreover, the porous block model is more generally applicable than the analytical current blockage model: it can be applied to irregular (or random) oscillations, so the effects of current blockage in random sea can be investigated. In contrast, the theoretical model (FCB) is presently suited for regular waves only.

Although the analysis in this chapter is for two-dimensional planar flow, it provides a building block towards a more complete CFD simulation where the porous block model can be extended to a porous tower, and the current blockage problem can be investigated in a finite water depth with free surface effects of combined waves and in-line current, all obtained by solving the Navier–Stokes equations in three-dimensional space. In this way, more realistic water particle kinematics could be simulated, and the integrated effect of current blockage across water depth could be analysed.

4.2 Numerical methods

In this section, we first present the numerical methods necessary to simulate ranges of planar flow through a porous block.

4.2.1 Governing equations

To account for the effect of porous block in the numerical simulation, the conventional Navier–Stokes equation needs to be modified by adding a momentum sink term, such as:

$$\frac{\partial}{\partial t}(\rho \mathbf{u}) + \mathbf{u}\frac{\partial}{\partial \mathbf{x}}(\rho \mathbf{u}) = -\frac{\partial p}{\partial \mathbf{x}} + \mu \frac{\partial \boldsymbol{\tau}}{\partial x} + \mathbf{S} \tag{4.1}$$

where ρ is the fluid density, $\mathbf{u} = (u, v, w)$ is the fluid velocity field in Cartesian coordinates, p is the fluid pressure, $\boldsymbol{\tau}$ is the shear stress, μ is the dynamic viscosity, and $\mathbf{x} = (x, y, z)$ is the local Cartesian coordinates. Here we account for momentum lost from the flow via a sink term. The sink term, S, commonly consists of two parts, a linear and a nonlinear drag loss term, which create pressure drops proportional to the velocity and velocity squared respectively, so in the case of simple homogeneous porous block:

$$\mathbf{S} = -\left(\mu D + \frac{1}{2}\rho|\mathbf{u}|F\right)\mathbf{u} \tag{4.2}$$

Equation 4.2 is known as the Darcy–Forchheimer equation, containing both Darcy and Forchheimer pressure gradients, where D and F are the associated resistance parameters. The original application of the equation is to model flow over reservoir or rock formation, where the Darcy resistance term is more important than the Forchheimer term, as the velocity is slow. In this porous block simulation, only the non-linear component proportional to $\mathbf{u}|\mathbf{u}|$ is retained, as it is directly equivalent to the drag component of the Morison equation. Thus, the coefficient D of the Darcy linear term is set to be zero throughout the analysis.

It is necessary to relate the F parameter of the Forchheimer non-linear term to the C_dA/A_f from the actuator disc theory (Taylor et al., 2013). The relationship can be shown as follows. Consider a steady flow through a porous block spanning a channel. In this case, the Navier–Stokes equations reduce to pressure drop gradient term + momentum sink term (see Equation 4.1).

Setting $D = 0$ at the sink term, S, the local pressure drop gradient is simplified to:

$$\frac{\partial p}{\partial \mathbf{x}} = \frac{1}{2}\rho F|\mathbf{u}|\mathbf{u}$$

Assuming the porous block has a finite length L in downstream direction, the total pressure difference across the porous block is:

$$\Delta p = \frac{1}{2}\rho F L|\mathbf{u}|\mathbf{u}$$

Assuming frontal area of A_f for the block, the net drag on it is:

$$\Delta F = \Delta p \cdot A_f = \frac{1}{2}\rho A_f F L|\mathbf{u}|\mathbf{u}$$

Meanwhile, the standard Morison drag term on an obstacle array can be written as:

$$\Delta F = \frac{1}{2}\rho C_d A|\mathbf{u}|\mathbf{u}$$

where C_d is the drag coefficient on the obstacles within the grid and A is the total solid area of these obstacles.

Thus, by matching (or calibrating):

$$\frac{C_d A}{A_f} = FL \tag{4.3}$$

F can be obtained. Hence, the porous block modelled numerically is directly comparable to the representation of simple current blockage model (SCB) from the actuator disc theory.

The steady-state, incompressible equations of motion are solved with the finite volume method using OpenFOAM$^{®}$ (www.openfoam.org). The pressure-velocity coupling is solved with the SIMPLE (Semi-Implicit Method for Pressure-Linked Equations) iterative algorithm (see Patankar (1980) & Patankar and Spalding (1972)). In the fully unsteady flow simulation, an implicit Euler time stepping is used for the time derivative term (Ferziger and Perić, 2002), but the whole scheme remains explicit due to the treatment of the Forchheimer drag term. The results in the present work are all obtained by using OpenFOAM$^{®}$ version 1.7.1.

4.2.2 Turbulence models

Turbulence is generated by locally unsteady flow occurring at high Reynolds number, characterised by a large range of eddy scales within the flow, with considerable wake mixing taking place. The resulting bounding shear layers are unstable, marked by eddy mixing with the outer flow which causes the mean wake velocity to slowly rise back to the ambient velocity. Turbulent flow modelling is more realistic than laminar flow modelling, and it becomes essential for this work when the structure is long in the downstream direction, or when wake mixing is crucial.

4.2.2.1 $k - \omega$ turbulence model

The widely used turbulence model incorporated into this porous block flow simulation is the two-equation: Wilcox's $k - \omega$ model (Wilcox, 1988). The transport equations for this two equation model for the turbulent kinetic energy, k, and specific dissipation rate, ω, are as follows:

$$\frac{\partial k}{\partial t} + u_j \frac{\partial k}{\partial x_j} = \tau_{ij} \frac{\partial u_i}{\partial x_j} - \beta^* k\omega + \frac{\partial}{\partial x_j}\left[(\nu + \sigma^* \nu_T)\frac{\partial k}{\partial x_j}\right] \tag{4.4}$$

$$\frac{\partial \omega}{\partial t} + u_j \frac{\partial \omega}{\partial x_j} = \alpha \frac{\omega}{k} \tau_{ij} \frac{\partial u_i}{\partial x_j} - \beta \omega^2 + \frac{\partial}{\partial x_j}\left[(\nu + \sigma \nu_T)\frac{\partial \omega}{\partial x_j}\right] \tag{4.5}$$

and the turbulent eddy viscosity is defined by:

$$\nu_T = \frac{k}{\omega}$$

The closure coefficients and auxiliary relations are taken to be the standard values of:

$$\alpha = 0.52$$
$$\beta = 0.072$$
$$\beta^* = 0.09$$
$$\sigma = 0.5$$
$$\sigma^* = 0.5$$

Often, the initial values of both k and ω are needed for simulation with the turbulent flow model. Their initial values in the simulation are usually specified in free–stream boundary condition (inlet - outlet), and also in near-wall modelling. The following relationships provide the first estimates of the k and ω for the free–stream boundary condition:

The turbulent kinetic energy, k, is computed as:

$$k = \frac{3}{2}(uI)^2 \tag{4.6}$$

in which u is the mean flow velocity and I is the turbulent intensity. This relationship assumes that the initial turbulence is isotropic, i.e. the fluctuating components of the velocity are equal in the x, y, and z directions.

The specific dissipation rate, ω, can be obtained as:

$$\omega = \frac{\sqrt{k}}{L_t} \tag{4.7}$$

in which L_t is the turbulent mixing length scale. It describes the size of the largest energy-containing eddies in a turbulent flow. In porous block flow simulation, L_t governs the characteristics of the wake mixing scale. The bigger the specified L_t, the faster the turbulence mixes out into the surrounding flow, and vice versa. It is normally taken to be a fraction of a typical dimension of the problem, e.g. characteristic length. It should not be larger than the dimension of the problem, as the turbulent eddies cannot be larger than the computational domain. In this work, $I = 5\%$ and $L_t = 0.07 \times w_f$ are chosen as the initial estimates, where w_f is the frontal width of an obstacle array.

4.2.2.2 Obstacle-induced turbulence model

To assess the effect of internal turbulent mixing representing wake interaction among individual jacket members (legs and braces), additional turbulence is injected within the porous block. An obstacle-induced turbulence model based on $k - \epsilon$ as introduced by Nishino and Willden (2012) is adopted. Their application was to blade-induced turbulence in the large scale simulation of marine current turbines. The blade-induced turbulence characteristics used in their actuator disc simulation are taken to be somewhat comparable to the obstacle wake-induced turbulence in the porous block simulation of our problem.

To account for the effect of additional injection of turbulence, additional source terms of k and ϵ are added to the right-hand side of the transport equations of the standard two-equation $k - \epsilon$ turbulence model (not shown), respectively, at the location of the porous block. Nishino and Willden introduce two model variables as additional inputs for the simulation which directly represent physically meaningful quantities, namely the ratio of the energy dissipated to turbulence to the energy removed from the mean flow at the porous block, β, and a representative length scale for the equivalent of obstacle-induced turbulence, L_b, which in this case is at most the length scale of internal structural member spacing or smaller. These two variables are further assumed to be described by turbulent kinetic energy from the internal members, k_b, and dissipation rate, ϵ_b, expressed as:

$$\begin{aligned} k_b &= \beta K \frac{1}{2} u_d^2 \\ \epsilon_b &= \frac{C_\mu^{0.75} k_b^{1.5}}{L_b} \end{aligned} \tag{4.8}$$

where u_d is the local streamwise velocity at the disc plane and K is a momentum loss factor (parameter to determine the load or thrust acting on the disc), which equals to C_d.

Nishino and Willden further assume their blade-induced turbulence of k_b and ϵ_b is instantly mixed with the incoming ambient turbulence of k_a and ϵ_a at the disk plane. This results in the mixed turbulence being described by its turbulent kinetic energy, $k_m = k_a + k_b$, its effective dissipation rate, $\epsilon_m = k_m/\tau_m$, and τ_m is the eddy turnover time that may be determined from consideration of turbulence kinetic energy decay over time. We simply adopt their additional source terms for k and ϵ:

$$\begin{aligned} S_k &= u_d(k_m - k_a) = u_d k_b \\ S_\epsilon &= u_d(\epsilon_m - \epsilon_a) \\ &= u_d \left(\frac{(k_a + k_b)^2}{(k_a^2/\epsilon_a) + (k_b^2 + \epsilon_b)} - \epsilon_a \right) \end{aligned} \tag{4.9}$$

4.3 Steady current flow

For steady flow, the simple current blockage model (SCB) with blocked current velocity as described in Equation 3.1 is used, and comparisons between the analytical results from the actuator disc theory and experiments have been previously described in Taylor et al. (2013). This section provides further comparisons between the porous block flow simulation results, the same theoretical analysis and the same set of experiments.

It is worth emphasising that the porous block simulation and the actuator disc theory are of entirely different flow representations, the former from the complex Navier-Stokes equations and the latter from the conservation of mass and momentum in simple quasi one-dimensional flow. Thus, there are major differences between the two flow representations, and the range of output information available from each differs greatly. One major difference between the theory and the simulation is that the simulation provides additional information on the lateral flow profile (divergence flow), which the actuator disc theory cannot provide simply because it is a one-dimensional model. One practical advantage of having such additional information is the ability to model a non-spatially-uniform porosity distribution across the structural layout, one that more closely resembles the positioning of clustered arrays of conductors usually at one side of a real-life jacket-type offshore platform. At least a two-dimensional model is necessary for that.

4.3.1 Comparison with the experiment by Georgiou and Vickery

Georgiou and Vickery (1980) conducted experiments intended to measure the shielding effects which are present for flows through configurations of multiple building frames. Hence, they conducted experiments in a wind tunnel with multiple biplanar lattice frames aligned in-line, by varying the direction of approaching wind flow, frame solidity ratio, frame spacing, frame aspect ratio and the number of frames. A summary of the details of the experiments and the comparison between the measured effective drag coefficient and the theoretical analysis is given in Chapter 3.3.1 and Taylor et al. (2013). The loads were recorded by a rotatable strain-gauge plate with configuration as shown in Figure 3.5.

Among all the various different experiments, one experimental result was used to compare with the load prediction based on the current blockage theory. The chosen set had an aspect ratio (height to breadth ratio) of 4.0, spacing to breadth ratio of 0.186, breadth dimension of 1.239 m, and frame solidity ratio of 0.136. The frame solidity ratio is defined as the effective solid area of a single frame divided by the total area enclosed by a single frame, the A/A_f ratio in the current blockage theory.

4.3.1.1 Computational domain layout

We now compare experimental results from Georgiou and Vickery, the theoretical analysis and the numerical simulation, taking into account various incident flow angles for $N = 2$ up to 7 multiple porous blocks, with each block represents a frame. To simulate various incident flow angles, each porous block is rotated according to the incident angle, and the grids are meshed accordingly.

The dimension of each porous block is designed in accordance with the actual size of the frames. The frontal width (w_f, or A_f per unit depth) of each porous block is

1.24 m, and the thickness (downstream width or L) of each is 0.1035 m. A single size of computational domain is used throughout the simulation, with the number of cells about 370,000. A typical layout for a 7 grid porous block configuration subjected to 0° incident angle is illustrated in Figure 4.1. The array of black strips represents the array of porous blocks.

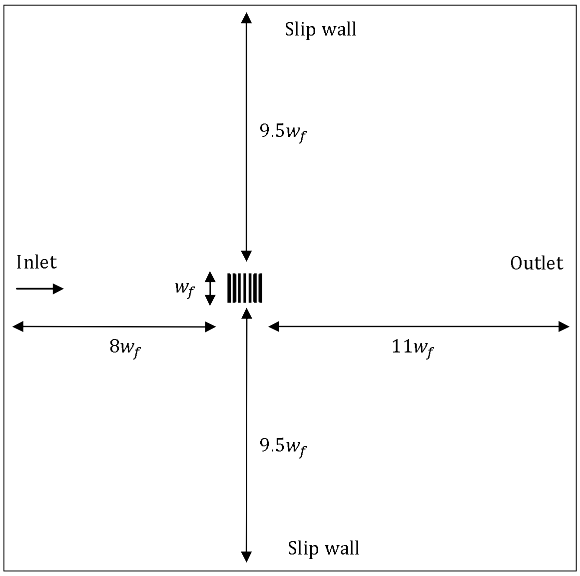

Figure 4.1: Arrangement and computational domain for a 7 porous block configuration, 0° incident angle.

4.3.1.2 Boundary and initial conditions

A steady fixed uniform velocity of 1 m/s is applied at the inlet with flow from left to right, with outlet boundary condition ($\partial \mathbf{u}/\partial n = 0$). A slip boundary condition is applied to the two channel side walls. The pressure, p, is kept uniform at the outlet and $\partial p/\partial n = 0$ at the inlet. The initial and boundary conditions for k and ω are similar to those of $\mathbf{u}$, with a fixed uniform k value of $3.75 \times 10^{-3}\text{m}^2/\text{s}^2$ at the inlet assuming an initial turbulence intensity of 5%. No information on the exact turbulent intensity was available from the Georgiou and Vickery test, but Sykes (1981) reported similar wind tunnel measurements with turbulent intensity ranging from 3.9 to 13.6%, so 5% is perhaps a customary turbulence level in large wind tunnels. A fixed uniform ω value of 3.402 s^{-1} assuming the turbulent mixing length, L_t, of $0.07 \times w_f = 0.0868$ m. The obstacles were likely to be of the order of this scale, with $\sim$ 7 obstacles in each Georgiou and Vickery's lattice frame grid. We take the integral length scale to be approximately one half of the gap spacing. Sensitivity test analysis on the choice of turbulent mixing length has been performed and it is found that the exact value of the turbulent mixing length is not significant as the aspect ratio of the array of porous blocks (or actual frames) is not high (ratio of the length of the structure along the flow to the maximum dimension across the flow).

The experimental result for 2 frames is used as C_d calibration in actuator disc theory to obtain the true (zero blockage) C_d for each incident angle, since there is no information on the true C_d from the experiment. This estimate of the true C_d is used here to calibrate the Forchheimer parameter, F, together with ratio of A/A_f for each incident angle. The frontal area, A_f, takes into account the projection effect of different incident angle, is expressed as a function of incident angle, θ, i.e. $A_f(\theta) = [B\cos(\theta) + S\sin(\theta)] \times H$. The resulting Forchheimer parameter, F, is tabulated in Table 4.1.

Table 4.1: The calibrated F parameter for varying incident angle.

Field	Incident Angle				
Parameter	0°	15°	30°	45°	60°
$C_d A/A_f$	0.18	0.20	0.21	0.20	0.16
$F(\mathrm{m}^{-1})$	1.71	1.97	2.00	1.89	1.50
True C_d	1.30	1.52	1.46	1.21	0.76

4.3.1.3 Simulation results

Figure 4.2 provides the spatial structure of pressure, velocity and vorticity for flow incident at 30°. The porous blocks are represented by white-coloured cells. Clearly the resulting flow field is not exactly symmetric about the centreline of the mean flow. However, no significant lift forces are produced and the wake asymmetry will eventually mix out. The simulation time for each case is about 8,000 sec ($\sim$ 2 hours) in serial mode on a Dell workstation.

The velocity distribution profiles on each porous block can be compared with the theoretical analysis and experimental data, by taking the average of the horizontal velocity profile across the width of the block (in transverse direction). Subsequently, the effective overall drag coefficient obtained from flow past porous block simulation can be computed in a similar manner as in the theoretical analysis. The results from numerical simulation are shown in Figure 4.3 as solid lines, plotted against incident angle, together with the theoretical predictions (dashed lines) and the experimental data from Georgiou and Vickery (data points). The data points along the solid lines

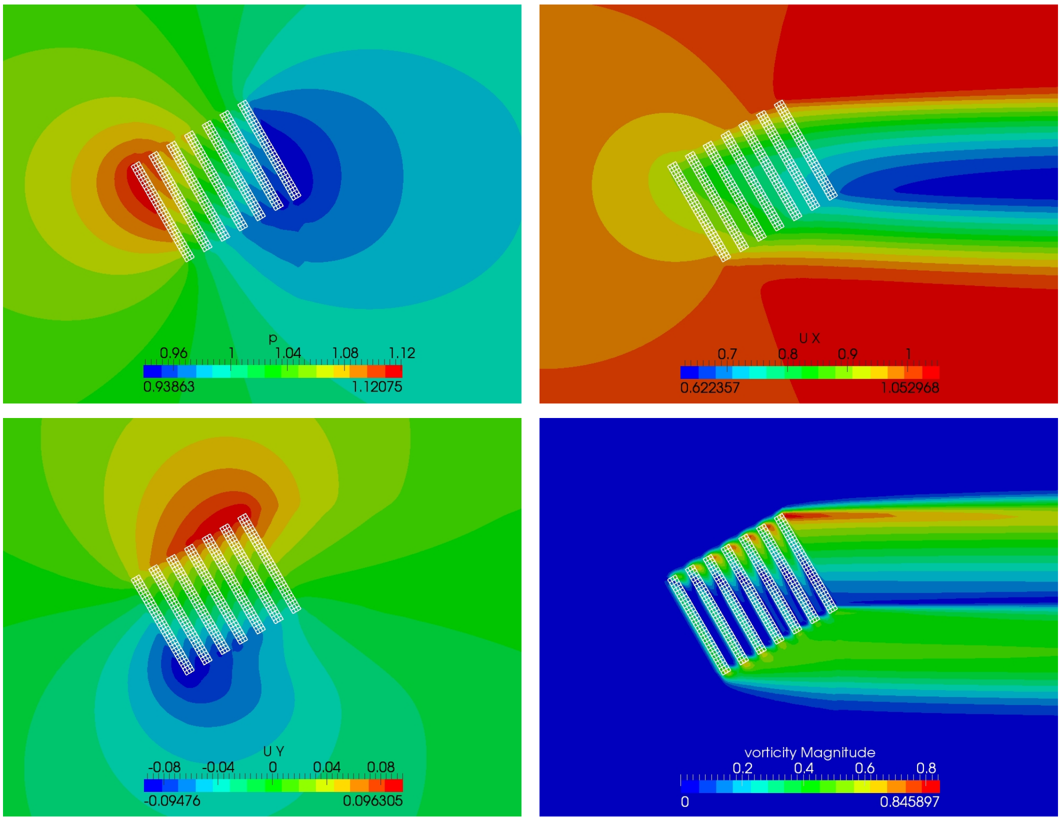

Figure 4.2: Turbulent flow results for the 30° incident angle. Clockwise from the top left figure: pressure, longitudinal velocity, vorticity (magnitude), and lateral velocity distribution.

represent the cases simulated on each specific incident angle, and interpolation is performed to connect the data points to form a solid line for each number of frame.

The agreement between the numerical simulation and the experimental data is very good. It is clear that the numerical porous block model is able to simulate the skewed flow in a better manner than the theoretical model. The difference is likely to be due to the choice of the appropriate frontal area for the skew grids, where the theoretical analysis simply used the maximum projected frontal area for each incident angle, $A_f(\theta)$, which underestimated the amount of blockage for a large number of frames and large approach angles.

4.3.2 Comparison with the experiment by Monopolis and Danaczko

Monopolis and Danaczko (1989) reported a series of scaled model tests and numerical simulations of the wet tow before installation of a hypothetical deepwater Gulf of Mexico compliant tower. A 1:48 scale compliant tower model was used in their

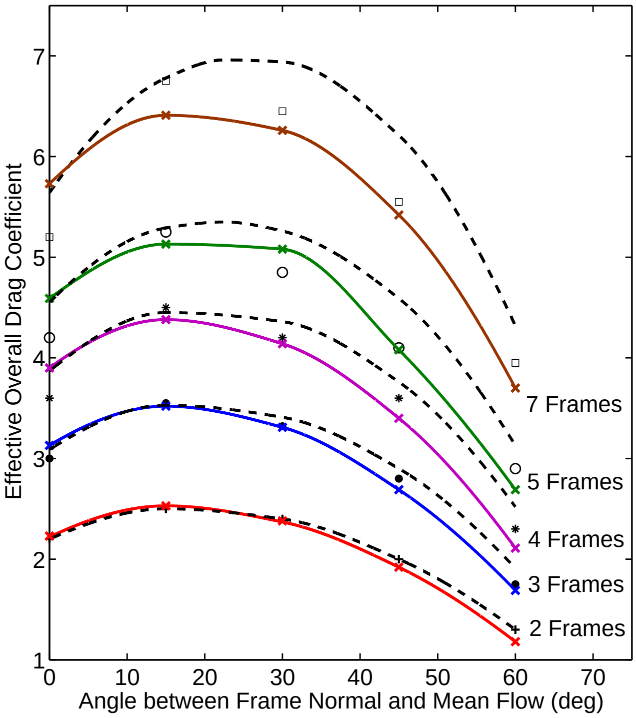

Figure 4.3: Comparison of the effective overall drag coefficient - data points from Georgiou and Vickery (1980).

experiment, with a cross section at full scale of 61 m by 82 m (200 ft by 270 ft), and a height of 781 m (2560 ft). The geometry is shown in Figure 3.7. Two sets of towing tests were conducted at speeds ranging from 0 to 2.5 m/s: towing both the completely mated tower and, separately, the lower section of the scaled model. The lower section represents the rear 4/7ths of the total length of the scaled model (446 m or 1464 ft).

The in-water towing test results were analysed using the simple current blockage model (SCB). The whole tower was divided into seven actuator discs in the theoretical analysis, and hence the total hydrodynamic area was distributed equally onto each of them. The comparison between their experimental results and the theoretical analysis is given in Chapter 3.3.2 and Taylor et al. (2013).

This towed compliant tower model test serves as an extreme case for the lateral turbulent wake mixing due to its high aspect ratio. This lateral wake mixing is responsible for re-energising the longitudinal flow into the grids through the injection of momentum from the external flow. More discussion on lateral wake mixing is presented in Section 4.4.2.

Here, it is essential to have a three-dimensional computational domain, as flow divergence can occur in any direction away from the flow direction and the estimate of the velocity profile by the actuator disc theory was obtained based on a three-dimensional cylindrical flow model, with its assumed axisymmetric wake mixing model. We follow this simplification by treating the grids as axisymmetric in the numerical simulations.

4.3.2.1 Computational domain layout

Only one quadrant of the entire domain is needed as the flow has 2 planes of symmetry, with symmetry boundary conditions invoked along the side walls. The layout of the one quadrant of the three-dimensional computational domain is shown in Figure 4.4. The porous block is attached on the smaller cylinder along the centreline of the whole domain. A total of 7 porous blocks are formed, shown clearly by the finer mesh grading along the whole domain. There are about 500,000 cells for the one quadrant of the domain, and the simulation time is about 36,000 sec (10 hours) in serial mode on a Dell workstation.

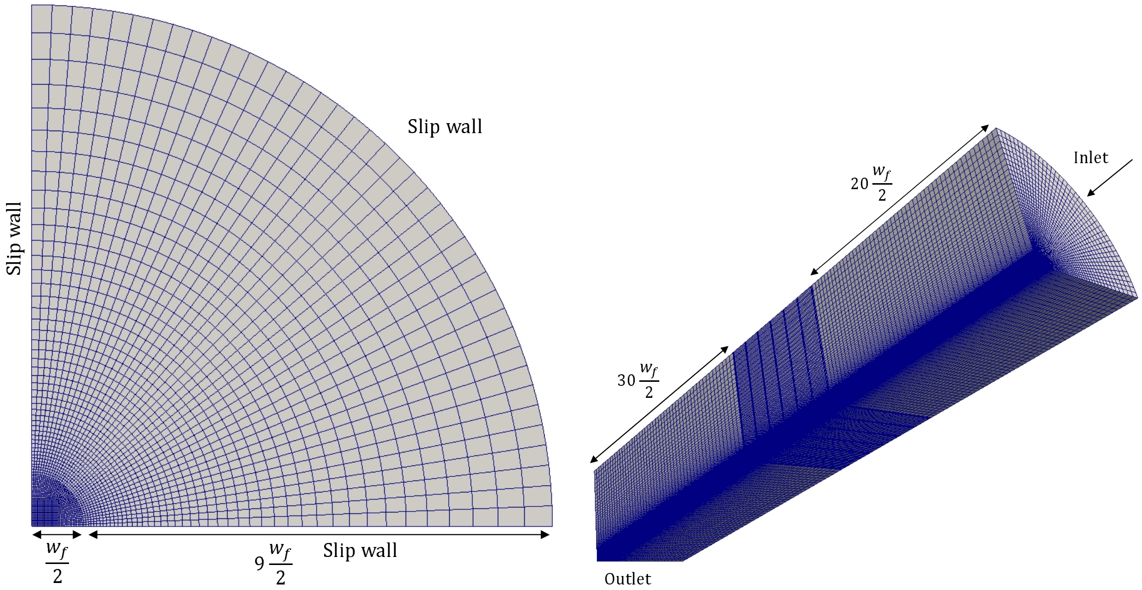

Figure 4.4: Layout of the one quadrant of the entire three-dimensional computational domain.

There is an interesting question as to whether the quarter model with two planes of symmetry is adequate for the compliant tower simulation. Clearly for a single solid obstacle such as a sphere in a flow, the large-scale features of the wake are not axisymmetric, just as the wake of a cylinder across the flow does not have a single plane of symmetry. In each case, the wake evolution downstream but close to the body is not symmetric. However, this asymmetry can be pushed much further downstream by introducing ‘base bleed’ for a bluff body (Wood, 1964). We believe that the flow through the grids will have the same bulk effect as base bleed, implying that locally symmetric flow model will be adequate at least close to the structure.

The domain consists of a doubled-tower configuration, by reflecting the mirror image of the original compliant tower over the undisturbed water surface, because in reality the flow spreading is suppressed on the upper boundary due to the presence of water free–surface. The resultant diameter, w_f, of the axisymmetric porous block (derived from $2A_f$ as in Figure 4.4) is 113.06 m, and the diameter to spacing ratio of the assumed seven grids is taken to be 1.016. The thickness (L) of each block is 14.13 m. The size of each axisymmetric porous block (A_f) is modelled with the same physical dimension in the numerical simulation.

4.3.2.2 Boundary and initial conditions

The same set of boundary and initial conditions as in Section 4.3.1 are used. The only difference lies on the choice of turbulent mixing length, which in this case becomes more important. It is found that, $L_t = 4.85$ m (assuming average mixing length $\sim 0.04 \times w_f$) provides velocity distribution profiles on each porous block closest to the theoretical prediction.

Calibration for the Forchheimer parameter, F, is made by equating $C_d A/A_f = FL$, with $C_d A/A_f = 0.59$ for each disc for $C_d = 1.2$, and $C_d A/A_f = 0.44$ for each disc for $C_d = 0.9$, and $L = 14.13$ m. Thus, F for each porous block is 0.0417 m^{-1} and 0.031 m^{-1}, respectively.

4.3.2.3 Simulation results

Figure 4.5 provides the spatial distribution of the field parameters: velocity, vorticity, k and ω.

The drag reduction factor, which yields the effective drag coefficient when multiplied by the free-field unblocked drag coefficient, can be obtained from the simulation for both cases. The resultant drag forces for both the cases as a function of tow speed are plotted in Figure 4.6. The simulations results are shown as lines: black lines for $C_d = 1.2$, grey lines for $C_d = 0.9$, solid lines for the total tower configuration, and dashed lines for the rear 4/7ths of the total tower. The experimental results of Monopolis and Danaczko are shown as data points. The analytical prediction is not shown for clarity but is similar (and given in Chapter 3.3.2 and Taylor et al. (2013)).

It is noted that for this extreme case with such a long aspect ratio, the turbulent mixing length becomes an important parameter as it determines the rate of the lateral

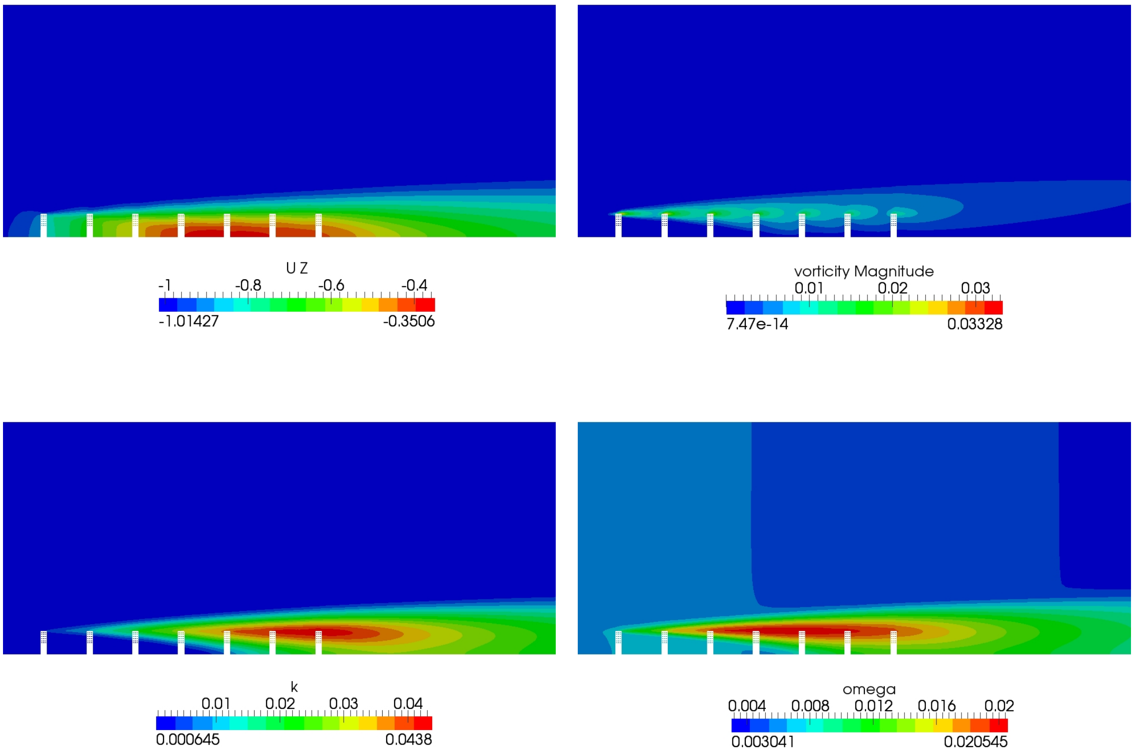

Figure 4.5: Three-dimensional turbulent flow results. Clockwise from the top left figure: longitudinal velocity, vorticity (magnitude), specific dissipation rate and turbulent kinetic energy distribution.

mixing. Different choices of mixing length will produce different velocity distribution across each porous disc. Fortunately however, all of the practical important cases of offshore installed structure will only have typical aspect ratios of at most 2.5:1 (jacket), or even 1:1 (compliant tower); none of the real life bottom-fixed offshore structures once installed would have such an extreme aspect ratio as the Monopolis and Danaczko tow case. Hence, the choice of turbulent mixing length in our subsequent analysis is not critical.

Thus, we see reasonable agreement between the measurements from Monopolis and Danaczko, the results from the numerical simulation and the theoretical analysis. For very long arrays, the choice of the C_d coefficient, or equivalently the Forchheimer F parameter, is less crucial.

For steady flow past a single cylinder, the Reynolds number plays an important role in determining the drag force, as does the level of free-stream turbulence. Both affect boundary layer separation. It seems likely that neither effect is as important for current blockage as most of the cylinders within the array are exposed to the wakes of other cylinders with the locally high levels of turbulence that this implies.

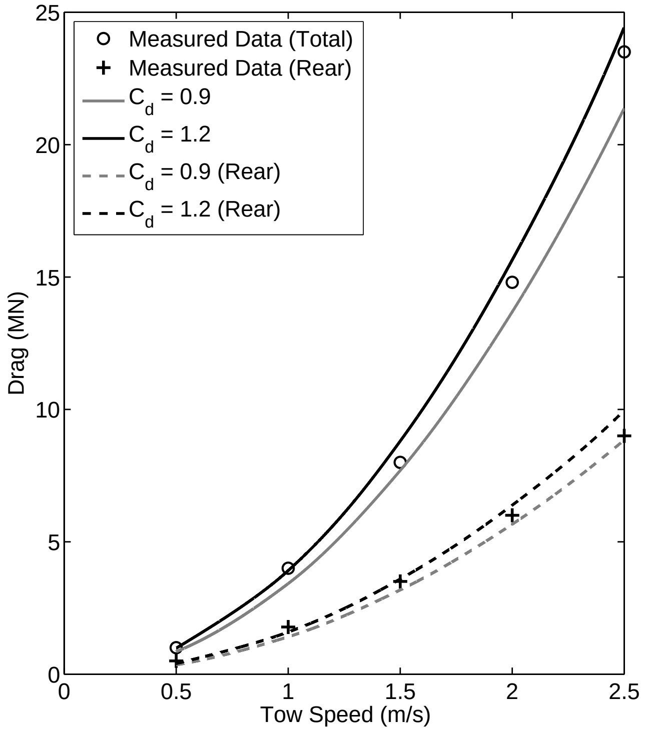

Figure 4.6: Comparison of the drag forces as a function of tow speed - data points from Monopolis and Danaczko (1989).

In the Monopolis and Danaczko compliant tower tests, the individual obstacles were $\sim$ 1 cm across and the flow speed was $\sim$ 1 m/s, giving a Reynolds number $\sim$ 10,000. This is large enough to give significant vortex structures in the wakes and turbulence incident on downstream cylinders.

4.4 Numerical study of steady flow

This section provides several key numerical studies for the steady flow analysis: grid independence, lateral mixing and the importance of additional turbulence injection to account for the local obstacle-induced turbulence not generated by standard porous block simulations.

4.4.1 Grid independence

The grid independence study investigates the influence of the number of cells used to form a porous block on the resultant field parameter, such as pressure gradient and velocity profile. The aim is to achieve a grid independent solution, that is a consistent solution which does not vary significantly when one alters the number of cells forming the porous block.

Three different levels of mesh forming the porous block are considered, shown in Figure 4.7.

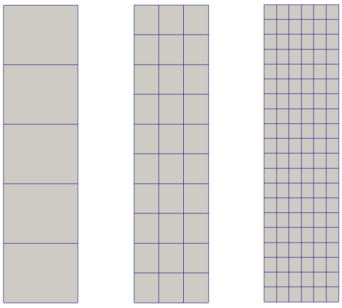

Figure 4.7: Three different mesh resolutions: level 1, level 2 and level 3.

The velocity profile on the block of three different levels is provided in Table 4.2. The velocity magnitude for each level is taken by averaging the velocity profile across the height of the porous block. Richardson extrapolation indicates that the longitudinal velocity (u_x) converges faster than quadratically as the mesh is refined.

Table 4.2: The velocity distribution profile for the three different levels of mesh.

Configuration Type	Field Parameter (m/s) u_x	u_y
Level 1	0.712	0.072
Level 2	0.671	0.083
Level 3	0.669	0.085

The velocity distribution profiles of levels 2 and 3 are sufficiently close that both choices of the finer levels are usable. Of course, to have a more precise solution, the finest is recommended. For Georgiou and Vickery comparison in Section 4.3.1, level 2 meshes were used.

4.4.2 Lateral mixing

One substantial advantage of numerical simulation as compared to the actuator disc theory is the ability to simulate proper lateral momentum exchange between the inner blocked flow and the outer free-field flow. This lateral mixing (due to side leakage) accelerates the blocked flow which results in slightly less blockage compared to the actuator disc theory, thus higher overall drag force. The amount of lateral mixing is dependent on the downstream spacing distance between two adjacent grids,

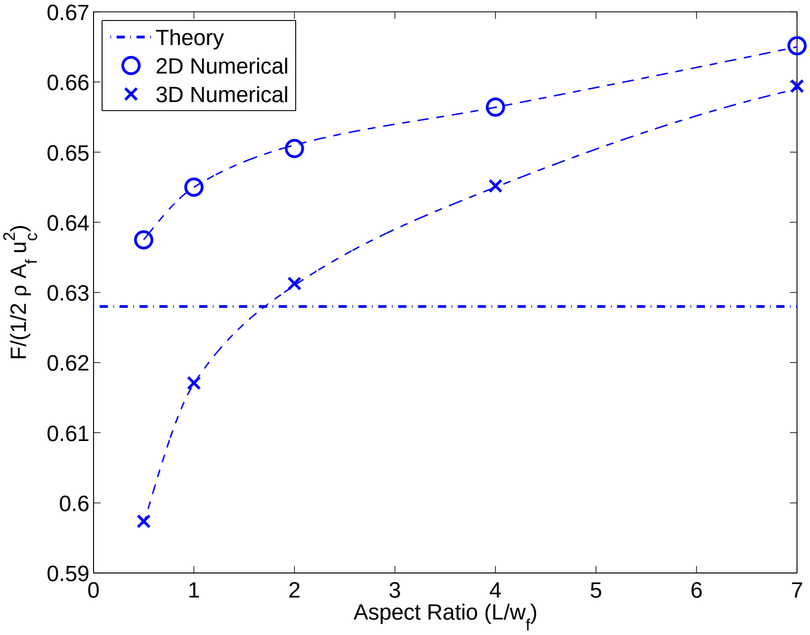

Figure 4.8: Variation of drag (or blocked current) against aspect ratio.

and (possibly) also on the resistance level (or amount of blockage). The further the downstream spacing distance and/or the higher the resistance, the more prominent the lateral mixing effect.

For the extreme case of Monopolis and Danaczko towed compliant tower, the numerical simulation results are generally slightly larger than the theoretical analysis, in terms of drag or effective drag coefficient, but both the theoretical and numerical simulation results match the experimental data well. The numerical simulation is able to simulate the lateral mixing effect which in this case is governed by the downstream spacing distance in a more robust manner, as compared to the theory which invokes a very simple wake mixing model when the spacing is greater than the width of the frontal grid (see Chapter 3.2.3.2 and Taylor et al. (2013)).

Figure 4.8 provides variation of normalised mean force as a function of aspect ratio: length to width (L/w_f) on a porous block in two-dimensional (denoted as circles) and three-dimensional steady flow simulations (denoted as crosses). The analysis uses the same computational domain and boundary conditions as the Geogiou and Vickery single grid under 0° incident angle test case for the two-dimensional simulation and the Monopolis and Danaczko single block test case for the three-dimensional simulation. Also included in the figure the analytical results from the actuator disc theory (shown as a dashed line) without wake mixing model. All cases are run for $C_d A/A_f = 0.97$ and $u_c = 2.5$ m/s.

One can observe the slight effect of lateral mixing which re-energises the blocked flow as the aspect ratio of the porous block gets larger. There is more distance for the lateral momentum exchange to take place along the edges of the porous block, which results in higher drag or blocked velocity (or lesser blockage). The three-dimensional porous block simulation allows lateral mixing to occur in two-dimensional space (both lateral and vertical), while the two-dimensional simulation only allows it to occur in one-dimensional space (lateral), thus the lateral mixing effect is larger in the three-dimensional case compared to the two-dimensional. Overall, the lateral mixing effect is more prominent when the aspect ratio of the grid is roughly larger than 1:1, or when $L > w_f$, as observed in the Monopolis and Danaczko towed compliant tower test.

4.4.3 Obstacle-induced turbulent injection

A test comparison between the standard $k - \omega$ and $k - \epsilon$ turbulence model for the Georgiou and Vickery wind tunnel test of 7 frames under 0° incident angle has been conducted previously to ensure no significant differences between the two models, and it is indeed found that there is a very slight reduction in the averaged velocity profile from $k - \omega$ to $k - \epsilon$ turbulence model, yet this variation is not significant. We now proceed to investigate the effect of injecting additional turbulence, with the obstacle-induced turbulence model based on $k - \epsilon$ formulation described previously in Section 4.2.2.2. The same steady flow case of Georgiou and Vickery is chosen for the turbulent injection study.

4.4.3.1 Comparison of $k - \epsilon$ with injected turbulence for fixed β

This subsection compares the standard $k - \epsilon$ with the obstacle-induced turbulent model for fixed β which is taken to be 0.05 and for varying L_b from 0.025 to 0.1 $\times w_f$. The resultant averaged velocity u_i measure and Σu_i^2 are shown in Table 4.3.

Table 4.3: Comparison of u_i and Σu_i^2 between $k - \epsilon$ and injected turbulence for fixed β.

$k - \epsilon$	u_1	u_2	u_3	u_4	u_5	u_6	u_7	Σu_i^2
Standard	0.885	0.851	0.815	0.781	0.749	0.720	0.696	4.344
$L_b = 0.025 w_f$	0.884	0.850	0.817	0.785	0.756	0.730	0.708	4.392
$L_b = 0.05 w_f$	0.888	0.857	0.826	0.799	0.776	0.757	0.743	4.571
$L_b = 0.1 w_f$	0.895	0.868	0.844	0.824	0.809	0.799	0.795	4.871

Here we demonstrate that for reasonable values of L_b which represent the length scale of internal structural member spacing (note the turbulent mixing length, L_t, is taken to be 0.07 $\times w_f$), no significant variation is observed in terms of the average velocity measure in each grid.

4.4.3.2 Comparison of $k - \epsilon$ with injected turbulence for fixed L_b

This subsection compares the standard $k - \epsilon$ with the obstacle-induced turbulent model for fixed L_b which is taken to be $0.05 \times w_f$ and for varying β from 0.025 to 0.1. The resultant averaged velocity u_i profile and Σu_i^2 is shown in Table 4.4. The close up views of the velocity distribution profile for each case is illustrated in Figure 4.9.

Table 4.4: Comparison of u_i and Σu_i^2 between $k - \epsilon$ and injected turbulence for fixed L_b.

$k - \epsilon$	u_1	u_2	u_3	u_4	u_5	u_6	u_7	Σu_i^2
Standard	0.885	0.851	0.815	0.781	0.749	0.720	0.696	4.344
$\beta = 0.025$	0.886	0.853	0.820	0.790	0.763	0.740	0.721	4.461
$\beta = 0.05$	0.888	0.857	0.826	0.799	0.776	0.757	0.743	4.571
$\beta = 0.1$	0.891	0.862	0.835	0.813	0.796	0.783	0.775	4.742

Again, for reasonable values of β, no significant difference is observed between the obstacle-injected turbulent and the standard turbulent results.

We conclude that the presence of additional injected turbulence does not significantly affect the velocity and pressure distribution of the global blocked flow. The injected turbulence eventually is averaged out when global blockage prevails, i.e. when steady-state condition has been reached. Here we demonstrate that only the global (bulk) effect of the wake mixing of the whole structure matters for current blockage, and not the detailed (smaller scale) wake mixing of individual cylinders within the structure.

4.5 Regular oscillations plus current flow

Here we are interested in modelling the combination of regular oscillations and steady current flow past a porous block. With the extra loading contribution from waves superimposed on top of the current, extra resistance thus extra blockage is expected. A full current blockage model (FCB) has been introduced to account for the extra blockage as described in Chapter 3 and published in Taylor et al. (2013). This model

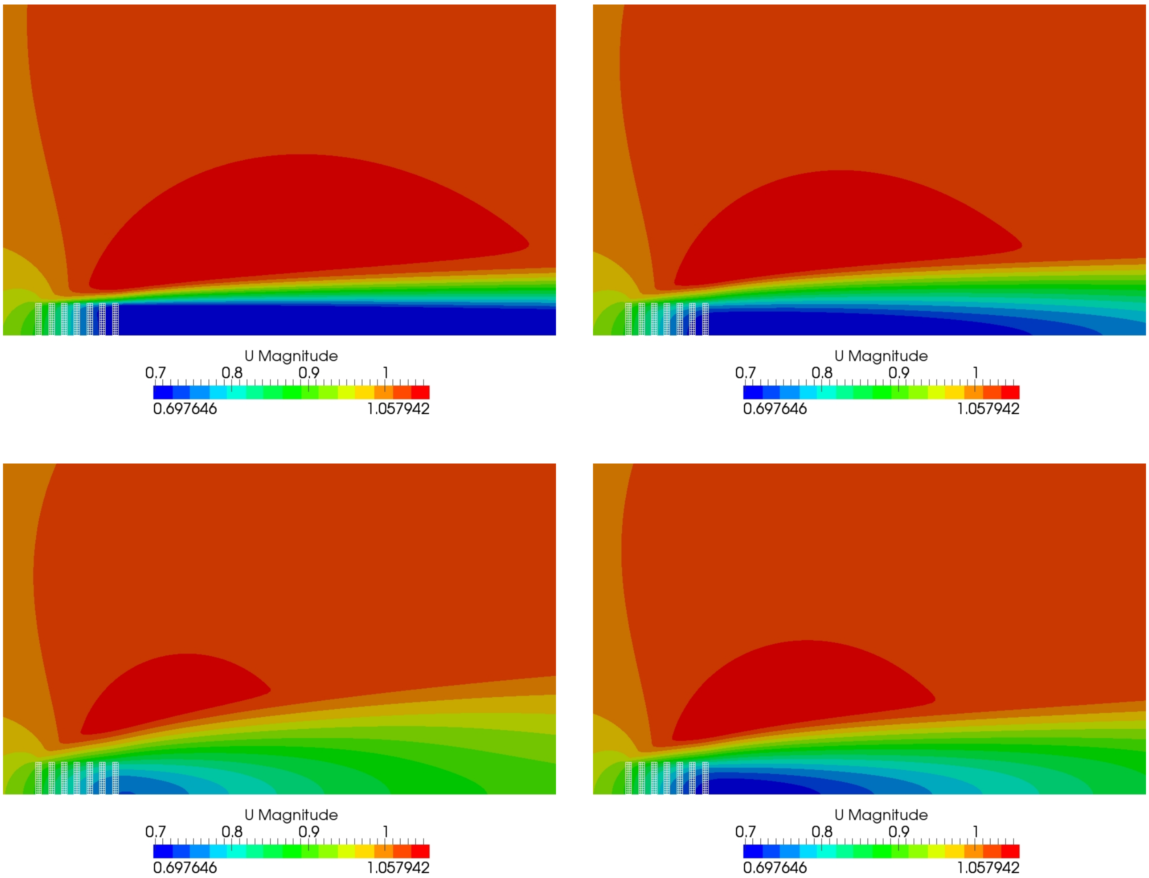

Figure 4.9: Velocity distribution profile for standard $k-\epsilon$, $\beta = 0.025$, $\beta = 0.05$ and $\beta = 0.1$ when $L_b = 0.05 \times w_f$ (clockwise from the top left figure).

is presently suited for regular waves plus current. Here the FCB model is summarised briefly.

Consider a grid in a flow with both a steady blocked current u_{cs} and a regular oscillating wave component u_w. Assuming that the Morison equation can be used to describe the force on the obstacles over the wave cycle and there are no Keulegan-Carpenter number effects, the averaged force over a complete flow oscillation, which forms the underlying principle for the FCB model, can be expressed as:

$$\frac{F_{av}}{\frac{1}{2}\rho C_d A} = \frac{1}{2\pi}\int_{0}^{2\pi} (u_w cos\phi + u_{cs})|u_w cos\phi + u_{cs}|d\phi \qquad (4.10)$$

where ϕ is the oscillation phase angle. The integral has two exact solutions for $u_{cs} > u_w$ and for $u_{cs} < u_w$, and a simple asymptotic form for $u_w >> u_{cs}$. Equating each of the two exact solutions to the net force on the actuator disc for the grid of the time averaged mean flow eventually yields three submodels depending on the relative magnitude of the wave and current velocities. Likewise, equating the asymptotic solution to the same net force expression yields an asymptotic two disc model which forms the main feature of the full model, expressed as (Taylor et al., 2013):

$$\text{Peak drag } \cong \pm\frac{1}{2}\rho C_d A u_w^2 + \frac{\pi}{4}\rho A_f u_c^2 \tag{4.11}$$

Notice the absence of the wave × current term, $(u_w \times u_c)$, in the approximate form. The additional blockage in regular waves removes this term.

For the comparison with numerical simulation in terms of the peak drag values, Equation 4.11 is used for the theoretical analysis (FCB). For the comparison in terms of the complete drag force time history, the asymptotic drag force time history solution described in Chapter 5 and Santo et al. (2014b) is used instead, which is expressed as:

$$\text{Drag} = \frac{1}{2}\rho C_d A(u_w \cos\phi)|u_w \cos\phi| + \frac{\pi}{4}\rho A_f u_c^2 |\cos\phi| \tag{4.12}$$

We now compare the validity of the full analytical model with the numerical simulations in regular oscillations plus steady current flow. One available experimental data set for the case of regular waves plus current is the Allender & Petrauskas experiment analysed in Chapter 3 and Taylor et al. (2013). That study compares the experiment data with the FCB model, and the agreement is shown to be very good. It could also be compared with the numerical simulation when one moves from a planar flow simulation to a three-dimensional porous tower with free surface effect implemented (this is covered in Chapter 6 and in Santo et al. (2014a)). However, as the present simulation only considers two-dimensional planar flow without a free surface, a more appropriate comparison would be between the FCB model and the numerical simulation by looking at a slice of a jacket or tower with varying relative magnitude of wave oscillation to current velocity (u_w/u_c) and $C_dA/A_f = 0.97$. Thus, the flow motion considered is regular oscillations plus steady flow (or current). This is provided in Figure 3.10 (which is also Figure 8 of Taylor et al. (2013)).

We note that the same C_d value for steady flow (inferred from the steady tow tests of Allender and Petrauskas (1987)) is used for unsteady flow simulation in Chapter 3 and Taylor et al. (2013) and in this study. We are neglecting Keulegan–Carpenter number effects because the sweep of the oscillations is much bigger than the size of the individual obstacles and the wave-induced oscillatory flow is assumed to be large compared to the current. No large variation in C_d between steady and unsteady flow is expected, because of the nature of obstacle array and large turbulent intensity within the array. This will massively disrupt the coherent nature of the vortex wake behind a single cylinder in ‘clean’ flow. The disruption of the vortex induced local reversed flow is likely to reduce or eliminate KC number effects.

Two different types of simulations are performed, namely time-averaged mean flow and fully unsteady flow simulations.

4.5.1 Time-averaged mean flow modelling

Before proceeding to fully unsteady flow simulations, it is possible to account for regular oscillation with current in a time-averaged manner in numerical simulation. The time-averaged mean flow case still runs as a steady flow simulation, but with enhanced mean resistance due to an externally embedded averaged Morison force over a wave cycle. This accounts for additional blockage from the wave contribution, which is the governing principal equation of the FCB model. The major assumption in this case is that the extra resistance is assumed to behave as the mean Morison force averaged over a cycle, which may not be realistic in the event of irregular waves. Nevertheless, the time-averaged mean flow case provides an intermediate stage for comparison with the analytical theory, as the rest of the blockage calculation can be solved numerically using the now time-averaged Navier-Stokes equations.

The time-averaged mean flow simulation attempts to answer the question on how well the one-dimensional FCB model would perform when an actual flow problem cannot be reduced to a simple one-dimensional flow problem. With such simulation, the difference between the one-dimensional analytical model and two-dimensional numerical simulation model can be addressed, and any important features not able to be captured in the one-dimensional model can be identified. Thus, the time-averaged mean flow simulation serves as a bridge to link the gap from the one-dimensional analytical model to the two-dimensional numerical porous block model.

4.5.1.1 Lateral resistance

The first requirement is to embed the local averaged one-dimensional Morison expression according to the closed-form solutions obtained from Equation 4.10. However, a question arises on what to specify for the lateral resistance, as now we move from one-dimensional analysis (actuator disc theory) to two-dimensional numerical simulation. It is by no means clear what to prescribe laterally as the above expression and its associated closed form solutions are purely in one-dimensional form. The solution is to invoke a local averaged two-dimensional Morison force over a wave cycle, expressed as:

$$\left[\frac{F_{av}}{\frac{1}{2}\rho C_d A}\right]_x = \frac{1}{2\pi}\int_0^{2\pi} (u_w \cos\phi + u_{cs}) \cdot \left[(u_w \cos\phi + u_{cs})^2 + v^2\right]^{1/2} d\phi \tag{4.13}$$

$$\left[\frac{F_{av}}{\frac{1}{2}\rho C_d A}\right]_y = \frac{1}{2\pi}\int_0^{2\pi} v \cdot \left[(u_w \cos\phi + u_{cs})^2 + v^2\right]^{1/2} d\phi \tag{4.14}$$

where v is now the lateral velocity flow component, u_w is the amplitude of the wave oscillation, and u_{cta} is the ambient blocked current velocity component of the time-averaged mean flow simulation. The key assumption here is that the current velocity is reduced due to blockage but the wave velocity is unaltered. Equation 4.13 and 4.14 describe the porous block resistance in x- (along the mean flow) and y- (lateral) direction, respectively. They are solved by numerical integration (trapezoidal rule), as no closed form solutions are available.

The above averaged Morison relationship applies for two-dimensional case, but it can also be extended to three-dimensional time-averaged mean flow when both v and w (lateral velocity in z-direction) are assumed to be constant in time.

4.5.1.2 Comparison with the analytical model

The time-averaged mean flow simulation makes use of the same computational domain as the Georgiou & Vickery wind tunnel simulation domain, same mesh grading, same boundary and initial condition, and a 1:1 aspect ratio of a porous block representing a slice of a typical compliant tower section. The simulation ranges for various relative magnitude of horizontal wave oscillatory velocity to the free stream current velocity (u_w/u_c), while u_c is fixed at 2.5 m/s. The simulation time is about 7,500 sec (2 hours) in serial mode on a Dell workstation.

A typical result from the time-averaged mean flow simulation of a free stream current which flows through a porous block (from left to right) is plotted in Figure 4.10 in terms of the velocity streamline profile. Here the porous block is represented by a black-coloured grid. The extra blockage is captured by the larger flow divergence away from the core of the porous block and bigger flow reduction downstream of the block.

The horizontal wave oscillatory velocity (u_w) is internally imposed in the governing equation of the enhanced resistance of the porous block in this time-averaged mean

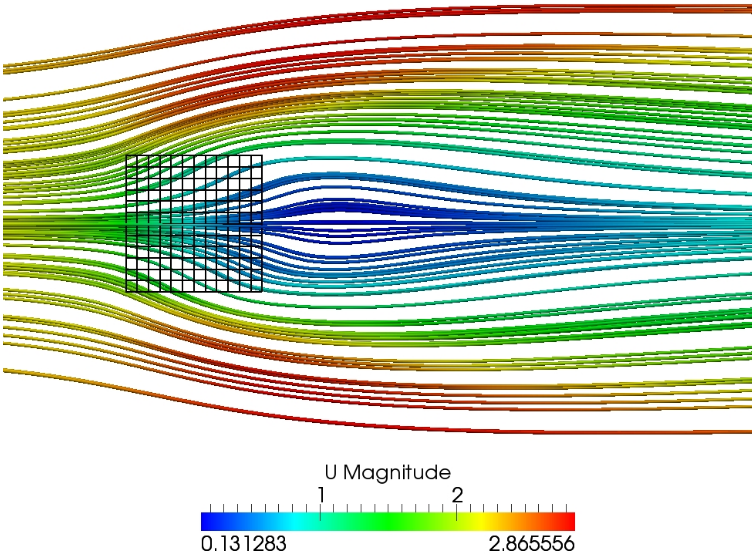

Figure 4.10: Typical velocity streamline profile of a time-averaged mean flow simulation.

flow simulation. Thus, the velocity that the porous block model solves for is the blocked steady flow velocity (u_{cta}). Here the advantage of the porous block model being a two-dimensional model in this planar flow simulation over the FCB model being a one-dimensional model is described.

The FCB model solves the predicted drag based on three submodels which switch smoothly, and for the case of big oscillations and small steady flow (case (i) flow regime in Taylor et al. (2013)), the model splits the loading into two discs with the minimum blocked steady flow velocity, $u_{cs} = u_c/2$ at the front disc and zero at the rear. The peak drag then follows Equation 4.11. This ad-hoc approach is imposed due to the limitation of the theory being a one-dimensional model. In contrast, the blocked steady flow velocity from the time-averaged mean flow simulation, u_{cta}, could be possibly less than $u_c/2$ in the numerical porous block model as it is a two-dimensional planar flow model (actually a three-dimensional model but out-of-plane flow is not considered here).

The peak drag of the numerical simulation is expressed as $1/2\rho C_d A(u_w + u_{cta})$ $\sqrt{(u_w + u_{cta})^2 + v^2}$, with u_{cta} supplied directly from the time-averaged mean flow simulation, and the drag formulation is consistent with Equation 4.13. It can be normalised by dividing with $1/2\rho C_d A u_c^2$, and plotted against u_w/u_c as shown in Figure 4.11.

The complete drag force time history of the time-averaged mean flow simulation is expressed as $1/2\rho C_d A(u_w \cos\phi + u_{cta})$ $\sqrt{(u_w cos\phi + u_{cta})^2 + v^2}$. Figure 4.12 shows the drag force time history for the extreme case of $u_w/u_c = 4$, i.e. when $u_w = 10$ m/s

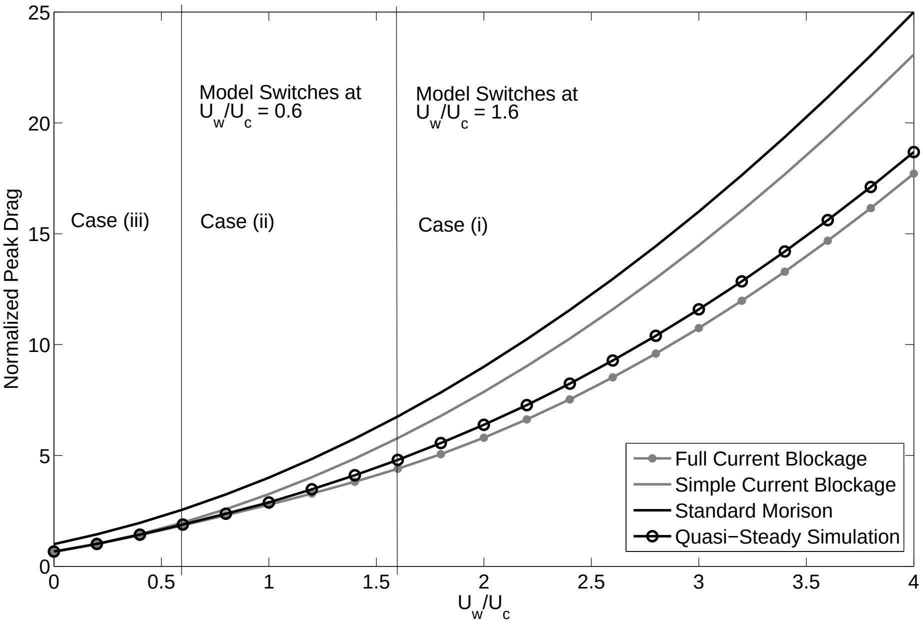

Figure 4.11: Normalised peak drag comparison between time-averaged mean flow simulation and theoretical analysis for ranges of u_w/u_c.

and $u_c = 2.5$ m/s, plotted in terms of the velocity term $u_x|u|$, where $u_x = u_w + u_{cta}$ and $u = u_w + u_{cta} + v$ (in vector form). To compare the drag force time history of the numerical simulation with the theoretical analysis, the predicted velocity term of the theory is required. Here we divide the asymptotic drag force time history of the theoretical analysis (Equation 4.12) with $1/2\rho C_d A$ to obtain the equivalent velocity term of the theory. The numerical result is plotted as solid grey line, and the theoretical result as solid black line.

It is interesting to note the relatively good agreement between the theoretical analysis and the numerical simulation for the case (i) flow regime, where the theory arbitrarily splits the loading into two discs for mathematical convenience, while the numerical simulation solves the case based on Navier-Stokes formulation which is supposed to be more realistic. This indicates that the ad-hoc approach of the FCB model works. The good agreement supports the theoretical prediction that there is no $u_w \times u_c$ term.

The slight offset of the simulation result from the theoretical analysis in case (i) flow regime is due to the difference in the governing equation of the two models. The full current blockage model invokes a local averaged one-dimensional Morison force over a wave cycle, and hence it is a one-dimensional model. In contrast, the porous block model in time-averaged mean flow simulation is a two-dimensional model, which takes into account the spatial variation (both longitudinal and lateral) of all the flow

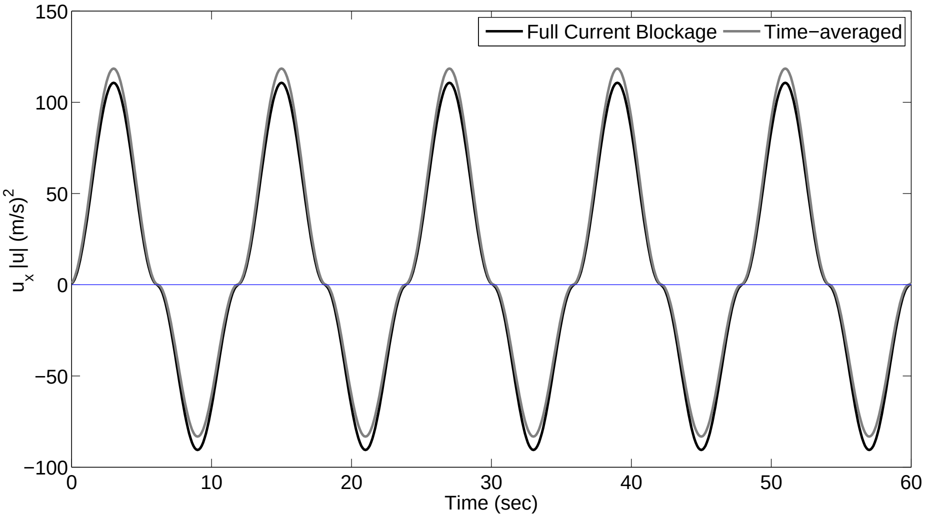

Figure 4.12: Reduced velocity time history comparison between time-averaged mean flow simulation and theoretical analysis for $u_w/u_c = 4$.

components, and hence it is more complete and realistic than the one-dimensional model.

Even though the numerical simulation predictions are a little higher than the theoretical analysis, the difference is insignificant compared to the difference in the peak drag between the FCB model and the SCB model (as well as the standard Morison formulation). Note that Figure 4.11 shows a load reduction for a section of a tower only - the reduction is more significant when it is integrated throughout the entire tower. Note also that the choice of $C_d A/A_f \sim 1$ is for a typical jacket type structure. For a compliant tower, $C_d A/A_f$ could be > 2, thus higher resistance (or blockage factor) which contributes to even higher load reduction.

Cautious attention needs to be drawn for the asymptotic limit of $u_w >> u_c$ of Figure 4.11. The result is obtained from the local Morison force average by assuming that a finite size of steady current, u_c, is always present ($u_c \neq 0$). Thus, when extrapolating the plot for the limit of $u_w/u_c \to \infty$, there is always a force reduction (blockage) compared to the other two methods. However, $u_w/u_c \to \infty$ could also mean $u_c \to 0$ i.e. the current is tiny compared to the wave oscillations, in which we obtain a slight incompatibility from Figure 4.11. This will be the case of wave oscillation with no steady mean flow, and there will be no blockage occurs - wave (without current) blockage is assumed not to occur.

Hence, we conclude that the predicted drag of the time-averaged mean flow simulation agrees well with the full current blockage model (FCB). The two-dimensional numerical porous block model, however, is more complete than the one-dimensional analytical model as it is able to model and resolve properly the reduced flow in all directions when subjected to high hydrodynamic loading (high u_w/u_c or C_dA/A_f), without invoking further assumptions other than the Forchheimer resistance calibration and the turbulence model.

4.5.2 Fully unsteady flow modelling

A fully unsteady flow case simulates regular oscillations plus steady flow on a stationary porous block, in which the porous resistance is defined by the standard Darcy-Forchheimer equation (refer to Equation 4.2). Thus, there is no additional resistance embedded into the solver, unlike the case of time-averaged mean flow simulation. The additional unsteady term accounts only for the inertia of the fluid undisturbed by the presence of the obstacles. No allowance is incorporated in these calculations for the Morison inertia term.

One obvious advantage of simulating a fully unsteady flow case is the ability to simulate random oscillation (to mimic random waves) plus current and resolve the time varying blocked current - a big leap ahead from the state-of-the-art FCB model which at present is only suitable for regular waves plus current. This feature can be used to provide essential information needed for the theory to account for the effect of random waves analytically, for instance the time-dependent evolution of the the global large-scale wake needed to build up to steady-state structure downstream in random waves.

4.5.2.1 Computational domain layout

The layout of the computational domain of the fully unsteady flow simulation is similar to that of time-averaged mean flow simulation, except the extent of the numerical domain away from the porous block has been greatly reduced to limit the computational times. It is known that typical drag calculations (such as for steady/unsteady flow around a cylinder) are generally very sensitive to the truncated domain distances from inlet and outlet boundaries. Fortunately in this porous block simulation, the drag calculation is less sensitive as fluid is allowed to flow through the porous body with certain porosity, thus the effect of flow separation is reduced and vortex shedding is suppressed, for most of the cases of interest. This flow condition is akin to high base bleed for a single body (Bearman, 1967; Wood, 1967).

Numerical wind tunnel blockage effect is investigated for two different widths of domain characterised by the distance of the slip wall to the porous block: $2.83w_f$

and $4.5w_f$, and the resultant blocked velocity profiles are identical. Thus, all the fully unsteady flow simulations are performed in $6.67w_f$ domain width configuration, with the mesh size of about 10,000 cells. The layout of the domain is illustrated in Figure 4.13.

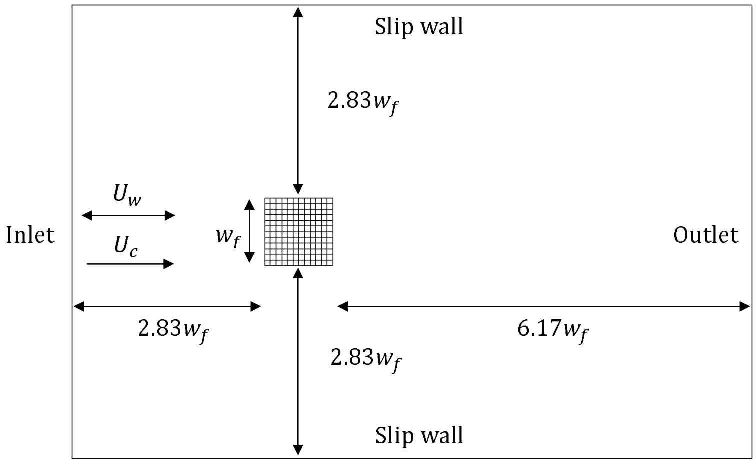

Figure 4.13: Layout of the computational domain for fully unsteady flow simulation.

The boundary condition for velocity at both inlet and outlet switches according to the direction of the oscillating flow, which means that the inlet and outlet of u switch to outlet and inlet whenever the oscillating flow reverses its direction and opposes the steady flow which flows at a fixed direction. The outlet boundary condition ($\partial p/\partial n = 0$) for pressure is applied to both inlet and outlet.

One advantage of using the SIMPLE algorithm is that the simulation remains stable even for Courant number > 1, permitting the use of an implicit solver in time. However, to produce smooth and clean oscillating flow, the simulation time step must be kept sufficiently small. The fully unsteady flow simulation requires much longer runs than the time-averaged mean flow simulation, because the Forchheimer resistance term is treated explicitly in time. A typical simulation time required for the fully unsteady flow simulation of 10 oscillation periods is about 360,000 sec (or 100 hours) in serial mode on a Dell workstation.

4.5.2.2 Comparison with the analytical model

Similar to Section 4.5.1.2, the fully unsteady flow simulation compares the theoretical analysis and the simulation results based on a slice of a structure subjected to two-dimensional planar regular oscillations plus steady flow (for a wide range of u_w/u_c).

In contrast to the time-averaged mean flow simulation where the horizontal wave oscillatory velocity (u_w) is externally imposed, the velocity that the porous block model solves in this fully unsteady flow simulation without enhanced resistance is the total reduced velocity, which consists of the combination of the reduced velocity of current, regular wave oscillation and lateral flow, denoted simply as u. The peak drag and the drag force time history of the fully unsteady flow simulation is obtained directly by integrating the velocity components over the entire porous cells as $1/2\rho C_d A/V \int u_x|u|dV$, where V is the volume of each porous cell.

A comparison of the drag force time history in terms of the velocity term between the fully unsteady flow simulation and the theoretical analysis, similar to Figure 4.12, is shown in Figure 4.14 for the extreme case of $u_w = 10$ m/s, $u_c = 2.5$ m/s ($u_w/u_c = 4$), with regular oscillation period of 12 sec. The numerical result is plotted as solid grey line, and the theoretical result as solid black line.

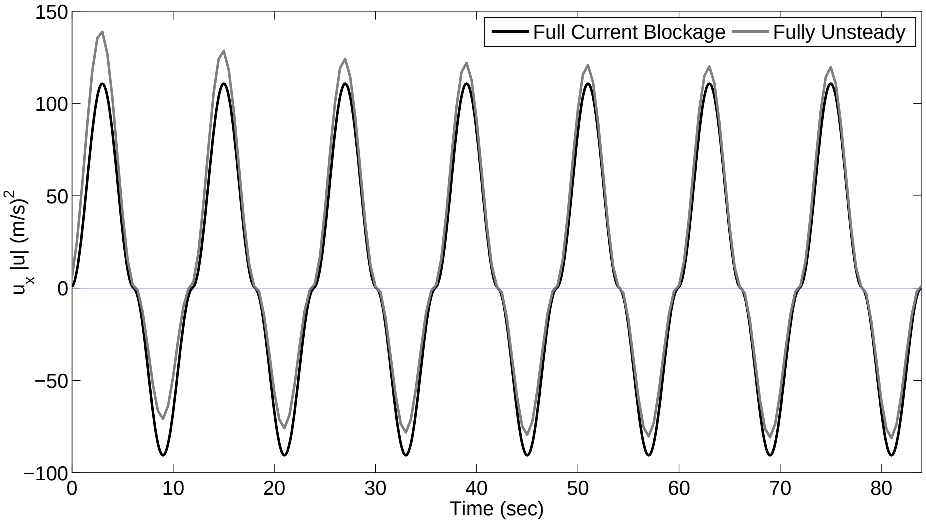

Figure 4.14: Reduced velocity time history comparison between fully unsteady flow simulation and theoretical analysis for $u_w/u_c = 4$.

It can be observed that the $u_x|u|$ term of the numerical simulation has converged to the steady-state periodic condition after about 5 oscillation cycles. Even though the porous block simulation does not resolve each individual wake from the internal structural members of a grid, the build up effect of the global wake structure is clearly represented. The $u_x|u|$ time history of the simulation at the steady-state has a slightly higher mean force compared to the that of the FCB model, but the overall periodic shape is similar. The slight difference in the peak crest and trough values follows the same argument as in the time-averaged mean flow simulation. The agreement in overall, however, is shown to be good.

Comparing Figure 4.12 and Figure 4.14, it is obvious that the time-averaged mean flow simulation yields an identical result as the fully unsteady flow simulation, even though the two simulations are of different types. This good agreement justifies the time-averaged two-dimensional Morison resistance approach presented in Section 4.5.1, which is a convenient approximation for the case of regular oscillations plus mean flow, as it runs much faster than a fully unsteady flow simulation.

To summarise the results so far, all the five hierarchy models are tabulated in Table 4.5: standard Morison with no blockage, simple current blockage model (SCB), full current blockage model (FCB), time-averaged mean flow simulation (TA) and full unsteady flow simulation (FU).

Table 4.5: Hierarchy of current blockage models.

Morison	$\frac{1}{2}\rho C_d A(u_w \cos\phi + u_c)\lvert u_w \cos\phi + u_c\rvert$
SCB	$\frac{1}{2}\rho C_d A(u_w \cos\phi + u_{cs})\lvert u_w \cos\phi + u_{cs}\rvert$ where u_{cs} is obtained from Equation 3.1
FCB	$\frac{1}{2}\rho C_d A(u_w \cos\phi)\lvert u_w \cos\phi\rvert + \frac{\pi}{4}\rho A_f u_c^2 \lvert\cos\phi\rvert$ (Santo et al., 2014b)
TA	$\frac{1}{2}\rho C_d A(u_w \cos\phi + u_{cta})\sqrt{(u_w \cos\phi + u_{cta})^2 + v^2}$
FU	$\frac{1}{2}\rho C_d \frac{A}{V}\int u_x \lvert u\rvert dV$

The normalised force time history comparisons for all the five models are plotted in Figure 4.15 for $u_w/u_c = 4$. The legend is sorted in decreasing force peaks, from the standard Morison being the highest to the FCB being the smallest.

Overall, both the TA and FU numerical simulation agree well with the FCB model, despite the very slight mean offset. Meanwhile, both the standard Morison and the SCB model greatly over-estimate the drag force peaks and under-estimate the drag force troughs, as there is no account made for any additional blockage effect, under the same hydrodynamic input parameters such as C_dA/A_f, u_w and u_c. This numerical evidence of load reduction in regular oscillations plus steady flow is consistent with the extensive experimental evidence of current blockage described in Chapter 5 and Santo et al. (2014b).

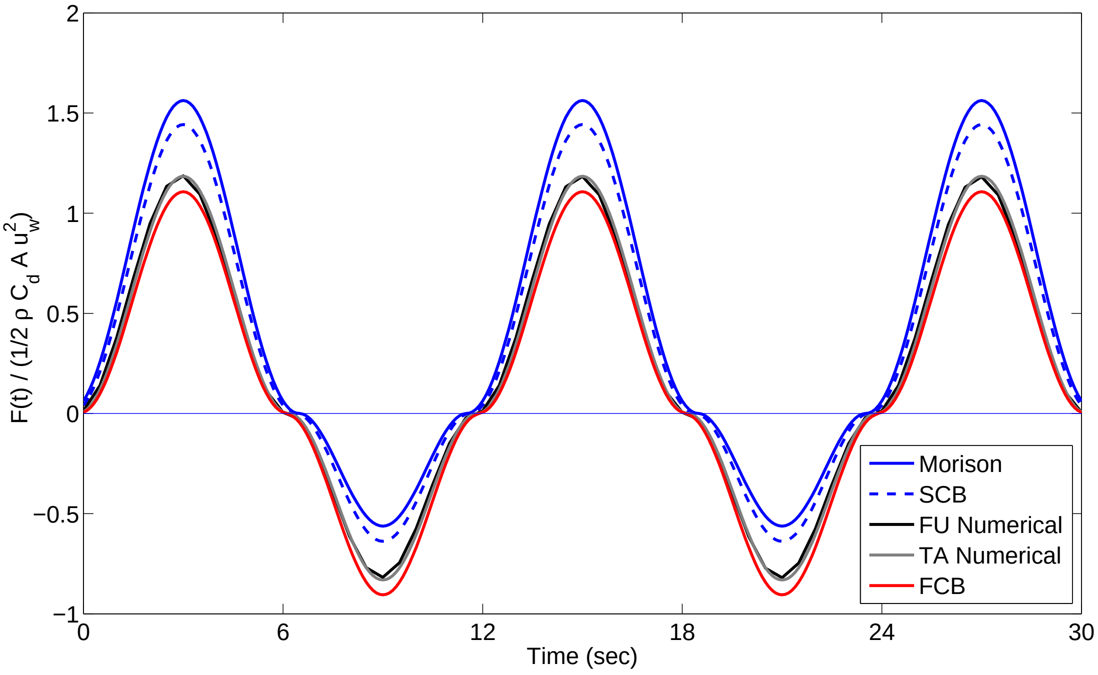

Figure 4.15: Normalised force time history comparison between the theoretical analysis and the numerical simulation for $u_w/u_c = 4$.

The good agreement demonstrates the viability of the novel use of a porous block in representing the complex geometry of a section of a statically-responding fixed space-frame offshore structure, where the drag resistance can be calibrated and modelled. The two-dimensional numerical porous block model, apart from being able to model and resolve high hydrodynamic loading case more properly than the one-dimensional analytical model, is also able to simulate irregular oscillations to mimic random waves for a more complete investigation of current blockage effects on offshore structures.

4.6 Chapter summary & conclusions

This chapter demonstrates that the use of CFD numerical simulation is a viable approach for investigating current blockage effects, and that any array of obstacles or grids can be replaced by Morison-type quadratic resistance porous blocks with a single calibration on the Forchheimer resistance term. The effect of injecting additional turbulence to produce smaller wake mixing effect compared to the dominant shear layer mixing has been investigated, and the global flow results are not significantly affected.

Good agreement is obtained between the flow simulation, the experimental data points and the simple current blockage model (SCB), for the steady flow comparisons:

the Georgiou & Vickery lattice frame test and the Monopolis & Danaczko compliant tower tow test. Skewed grids of multiple frames in the Georgiou & Vickery test case can be adequately modelled in the numerical simulation, and the exact value of the assumed turbulent mixing length is not critical. For structures with very high aspect ratio (very extended obstacle arrays in the downstream direction), considerable wake mixing occurs through the lateral edges of the porous blocks, which mixes low momentum flow within the array with higher momentum flow from outside and has the effect of partially re-energising the flow through the blocks. This leads to a more important role for the assumed turbulent mixing length, as demonstrated in the Monopolis & Danaczko compliant tower tow test case.

Time-averaged mean flow simulation internally imposes enhanced resistance on a porous block under the same underlying governing assumptions as the full current blockage model (FCB), i.e. the local Morison average over a wave cycle for regular waves. The time-averaged mean flow simulation agrees well with the FCB model, particularly in the region of large regular oscillations and small steady flow, and it is a convenient approximation for the case of regular oscillations plus steady flow as it runs much faster than a fully unsteady flow simulation.

Fully unsteady flow simulation models regular oscillating flows superimposed with a steady flow on a porous block without any enhanced resistance in contrast to the time-averaged mean flow simulation. The fully unsteady flow simulation agrees well with the FCB model and the time-averaged flow simulation. Also, it is a more general approach compared to the others as it is also capable of modelling irregular oscillation plus steady flow.

The good agreement between the two different flow representations (one by the actuator disc theory, the other by the Navier-Stokes equations) justifies the validity and applicability of the FCB model in predicting the amount of blockage experienced by a structure in the event of regular wave oscillations plus steady flow. Particularly for the case of big wave oscillations in a small steady flow, the good agreement between the theory and the numerical simulation lends support to the FCB prediction that $u_w \times u_c$ contribution to the force peaks vanishes due to the extra blockage contribution from waves. This chapter provides numerical evidence that there is more load reduction to be gained by accounting for wave–current–structure interaction for the case of steady current in regular oscillations, an essential feature that the standard Morison and the present offshore industry guideline (SCB) do not capture.

This chapter also demonstrates that the two-dimensional numerical porous block model is more general and complete than the one-dimensional analytical model for both steady and oscillatory flow applications to simulate steady current and waves. The two-dimensional numerical porous block model has been shown to better model array of obstacles under skewed incident angle, with lateral mixing, high hydrodynamic loading and a non-spatially-uniform porosity distribution across a structural layout. All the velocity components longer than individual obstacle scale can be properly resolved by solving the Navier–Stokes equations without invoking any assumptions other than the Forchheimer resistance calibration and the turbulence model. The numerical porous block model serves as a starting point for a more complete CFD investigation of current blockage effects: a three-dimensional porous tower model in a finite water depth with free surface effects of combined waves and in-line current.

This chapter has been submitted to the journal Ocean Engineering as Santo et al. (2013a).

Chapter 5

Current blockage experiments: Force time histories on obstacle arrays in combined steady and oscillatory motion

5.1 Introduction

This chapter attempts to test the validity and applicability of the full current blockage model, by looking into the complete total force time history and drawing comparisons from a series of experiments conducted at Cornell University. The motions performed in the experiments are for steady flow and steady flow plus regular oscillation to mimic motion of current alone and current plus regular waves acting on simple grids. We contrast the full time history of the drag loading, studied experimentally in this chapter, to the peak forces analysed by Taylor et al. (2013) and in Chapter 3. In this earlier analysis, only values for the peak forces were available from the experiments on a model structure in regular waves and current by Allender and Petrauskas (1987), not the entire time history of the force.

The experiments look at the fundamentals of current blockage by moving a series of perforated flat plates with square holes along a towing tank. The grid configuration is chosen to be simple to better understand the physics of the complete flow and the resulting blockage effects. Thus, rectangular bars instead of cylinders are used to force the flow separation to occur right at the edges, square holes instead of long slits are used to produce more efficient three-dimensional vortex shedding and mixing downstream of the grid. The grids are moved through otherwise stationary water to minimise variation of the flow and wake structure with depth below the free surface which would occur if real water waves were produced. In summary, this experiment is intended to be a novel and particularly clean investigation of fluid-structure interaction producing blockage.

The measured forces are first analysed in terms of the full blockage model (FCB) based on the Morison equation. The peaks and troughs of the force time history are well captured by the full model, but we note that the shoulders (inflexion regions) of the Morison-based equation, where the velocity crosses through zero, are too distinct. We then characterise the shape of the oscillation-generated component of the drag force as a Fourier series and show that this is preserved as an offsetting mean current is introduced. Also, as well as a mean force arising from the current, there is a coupling of the oscillation to the current component in that the drag term proportional to the square of the current shows oscillations in phase with the unsteady motion.

A common feature to all laboratory scale experimental studies is that the real world applications of Reynolds number cannot possibly be matched. In these experiments, we are short by a factor of $\sim 10^4$. Thus, the Reynolds number of these experiments is much lower than full scale offshore flow structures, and various issues which characterise wave-driven flows are not fully represented, which warrant further investigation. However, the present experiments are intended to constitute a basis for reference.

5.2 The complete time-dependent form of the full current blockage model

Here we are interested in exploring the validity of the asymptotic two-disc time-dependent drag force of the full current blockage model (FCB), in which previously the asymptotic drag force is expressed <u>only</u> in terms of peak drag (refer to Equation 3.25 in Section 3.4.2.3) and has been shown to contain clear separation of the wave × current term, $(u_w \times u_c)$, in the approximate form.

The full time-dependent asymptotic two-disc drag force expression can be obtained from a complete two-disc drag force of Equation 3.20 in time-dependent form as shown below:

$$\begin{aligned} \text{Drag } &= \frac{1}{2}\rho C_d A_L (u_w \cos\omega t + \frac{1}{2}u_c)|u_w \cos\omega t + \frac{1}{2}u_c| \\ &+ \frac{1}{2}\rho C_d (A - A_L) u_w^2 \cos\omega t |\cos\omega t| \end{aligned} \tag{5.1}$$

by expanding the modulus term of $(u_w \cos\omega t + u_c/2)$ and $\cos\omega t$, which gives:

$$\text{Drag } = \frac{1}{2}\rho C_d A u_w^2 \cos\omega t |\cos\omega t| + \frac{\pi}{4}\rho A_f u_c^2 |\cos\omega t| \tag{5.2}$$

Note that the current term contains a time-dependent $|\cos\omega t|$, which is in phase with the wave velocity field yet it scales with the current velocity squared.

Equation 5.2 becomes the prediction from a Morison-type model for the time-dependent drag loading on the entire structure. This model of the force time history makes very specific predictions on both the magnitude and time history of components within the total force, which are tested experimentally.

The asymptotic effect of the current is to produce a shift in the peak wave crest and trough forces by an equal amount of $\pi/4\rho A_f u_c^2$. In contrast, the mean (cycle-averaged) drag force is predicted to be smaller:

$$\text{Mean drag } = \frac{1}{2}\rho A_f u_c^2 \tag{5.3}$$

for high hydrodynamic loading when the two-disc switching model is required. If only a single disc is needed, the mean force is:

$$\text{Mean drag } = 2\rho A_f u_{cs}(u_c - u_{cs}) \tag{5.4}$$

where u_{cs} is the current at the plane of the single disc, and $u_{cs} > u_c/2$, so the mean drag is smaller than for the highly loaded disc.

5.3 Experimental setup

The experiments involve towing grids of perforated plates with four different values of the blockage ratio (A/A_f). These were conducted in a large computer-controlled XY towing tank in Cornell University. The towing tank has a length of about 6 m, with limit switches near both ends to stop the carriage from moving too far. Allowing for a safety margin, the maximum distance of motion for the carriage is 4 m. The width of the tank is 1 m, and the water depth is 0.5 m. Previous forced motion and force measurements on a single cylinder using this setup were conducted by Stallard et al. (2009).

The experimental arrangement is illustrated in Figure 5.1. It consists of grids of perforated thin plates (three are shown) mounted on a force transducer which is aligned in the x-direction. These are then supported on a stiff plate and mounted on a

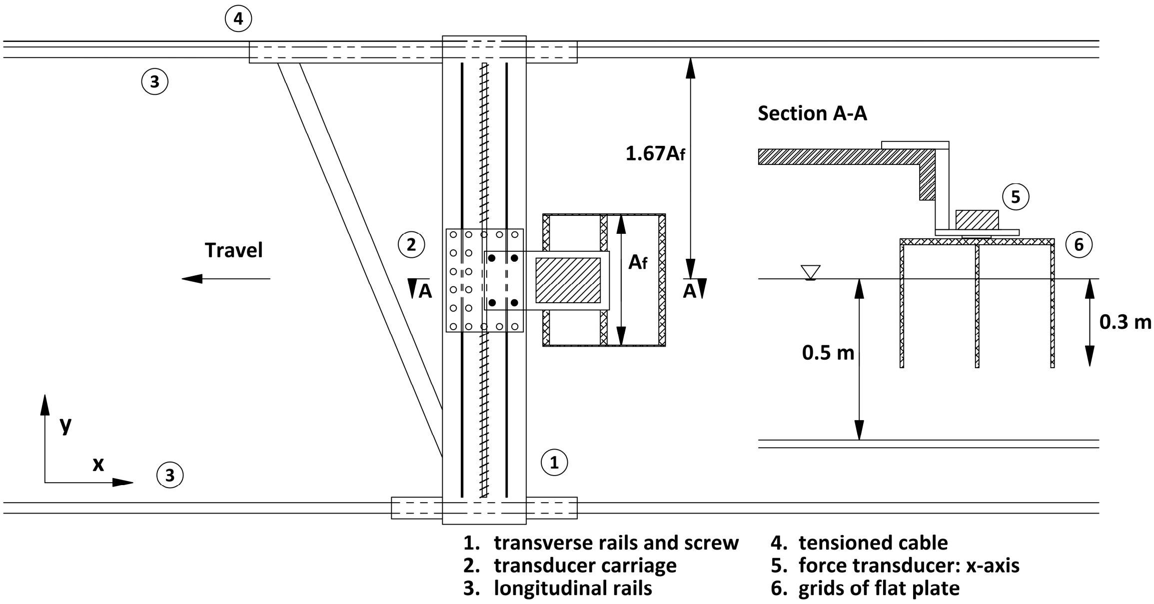

Figure 5.1: Schematic diagram of the XY towing tank, shown in plan and elevation view.

carriage. The support plate and the carriage are mounted within a triangulated cross-beam which is moved on rails by a motion-controlled tension cable in the x-direction. The speed of the carriage is limited to 20 cm/s.

A waiting time of 20 minutes between each test was chosen to allow settling of the water in the tank as the vorticity field generated by the previous test dissipated. Motion of the grids was coordinated from a LabView interface installed on a PC. The input data permit the input of a programmable velocity - time history. The interface sends a voltage signal to each motor to produce the required carriage motion. Both the commanded velocity and resulting load signals measured from the force transducer were recorded on the same interface, and the voltage signal was converted to an actual measured force in Newtons. This requires an *in situ* calibration of the force transducer in the x-direction by recording the voltage corresponding to a range of applied forces. When the recorded voltage was plotted against the applied forces, the slope corresponds the conversion factor from Newtons to voltage, and the inverse of that factor is the conversion factor from voltage to Newtons.

The grid layouts are shown in Figure 5.2. Up to three grids could be installed in a total of four configurations as shown in Figure 5.2(a). The geometric details of the grids are shown in Figure 5.2(b) and Table 5.1. Blockage ratios from 0.15 to 0.60 were tested. We present results across the entire range of the blockage but concentrate our analysis on blockage ratios from 0.15 up to 0.45. The grids were carefully designed and mounted in such a way that there was no horizontal bar at the still water level

(SWL), so that wave generation in the tank caused by grid motion was minimised.

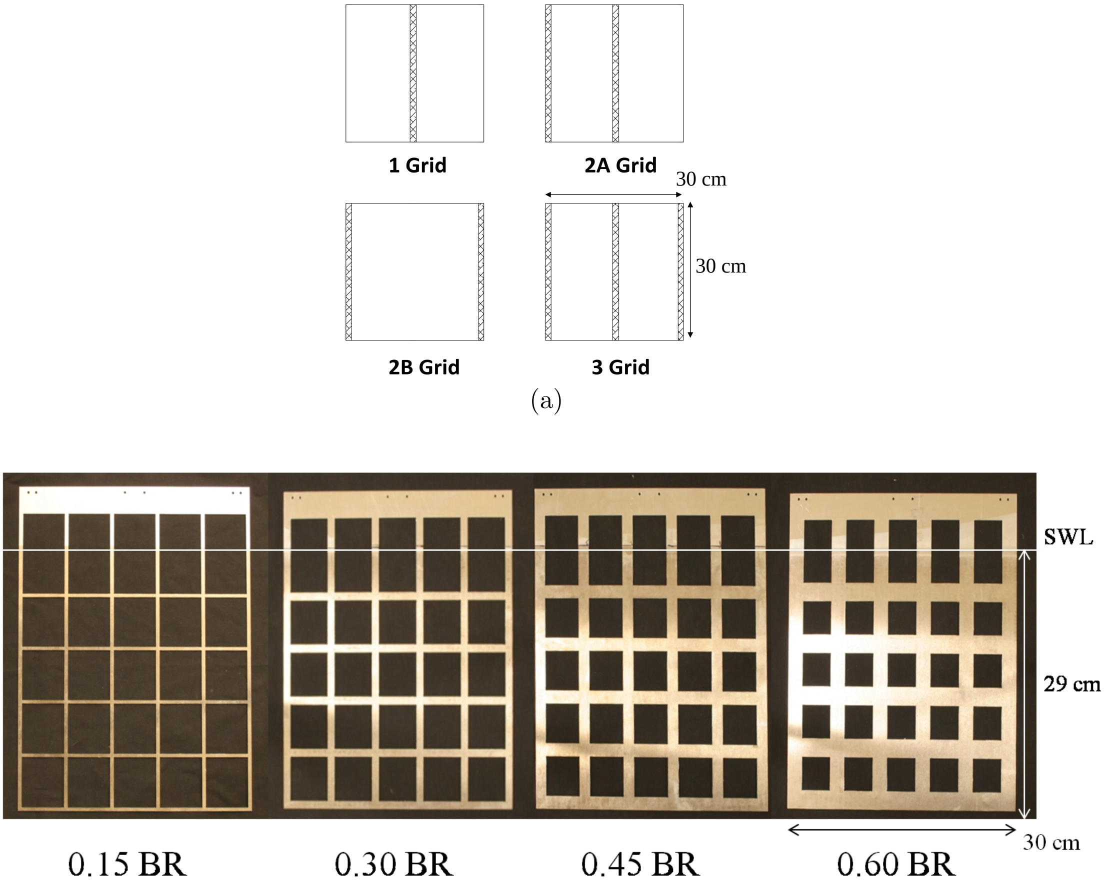

(a)

(b)

Figure 5.2: Layouts of the grids of perforated plates. (a) Plan view of the grids showing the four grid configurations. (b) Elevation view of the grids showing the four blockage ratio analysed.

The sampling rate of the force data is 1000 Hz. Thus, the raw data recorded through the force transducer and transmitted to the computer contains some electronic interference at frequencies well above those in the measured force signal. The records were low-pass filtered to cut off the irrelevant portion of the raw data to produce a clean and smooth filtered dataset.

The cut-off frequency was chosen to be 12 times the period of the oscillation, with a smooth ramp down to zero of the frequency component at the top end of the band pass range. For steady flow, the cut-off frequency is kept at 12 × 0.278 Hz (matching the 3.6 sec oscillation period of the base case of unsteady flow). A smooth ramp down is used instead of a sudden discontinuity at the cut-off frequency. We checked that different cut-off frequencies (6, 12 and 18 times) and number of Fourier components

Table 5.1: Grid dimensions for 4 different blockage ratios.

Parameter	Grid Type			
	I	II	III	IV
Width of the vertical strips (cm)	0.4677	0.887	1.354	1.891
Width of the horizontal strips (cm)	0.3613	0.864	1.425	2.069
Width of the square holes (cm)	5.439	4.936	4.375	3.731
Solid area, A (each, cm^2)	130.5	261	391.5	522
Frontal area, A_f (cm^2)	870	870	870	870
Plate thickness (cm)	0.16	0.16	0.16	0.16
Blockage ratio (A/A_f)	0.15	0.30	0.45	0.60
Porosity ratio ($1 - A/A_f$)	0.85	0.70	0.55	0.40

(interval width), which defines the frequency band of the ramp down (e.g. for 12 × 0.278 Hz cut-off frequency: 3.29 - 3.39 Hz, 3.24 - 3.45 Hz and 3.12 - 3.56 Hz), did not affect the results. All the filtering was done as post-processing in MATLAB. In the electronics in the measurement system, no filters were incorporated.

5.4 Steady flow blockage

Steady flow blockage is observed by towing grids of perforated plates along the tank at a constant velocity (u_c) with smoothed ramp up-and-down motions incorporated at the start and the end of the towing, respectively. Preliminary observations of types of grids of perforated flat plates similar to those used here revealed that a Reynolds-number-independent flow regime can be achieved from $u_c = 10$ cm/s upwards as shown in Figure 5.3(a), in which the inferred drag coefficient (C_d) is observed to be constant from there on. Thus, $u_c = 10$ cm/s is set to be the base case of the steady flow for all types of grids with different A/A_f ratio. For a velocity of 10 cm/s and a typical strip width of 0.9 cm, the Reynolds number is ~ 900.

Figure 5.3(b) demonstrates Reynolds number independence for unsteady flow through 3 grids with $A/A_f = 0.45$. Four different combinations of $[u_w\ ,\ u_c]$ for the same oscillation amplitude were tested (with u_w and u_c in cm/s), and the measured drag forces were plotted on top of each other with a normalised time axis and normalised drag. It is obvious that the [6 , 3] case is the sole outlier, implying that the requirement of Reynolds number independence for the unsteady flow is that the net forward velocity should be greater than 10 cm/s. Here, $u_w = 10$ cm/s plus the

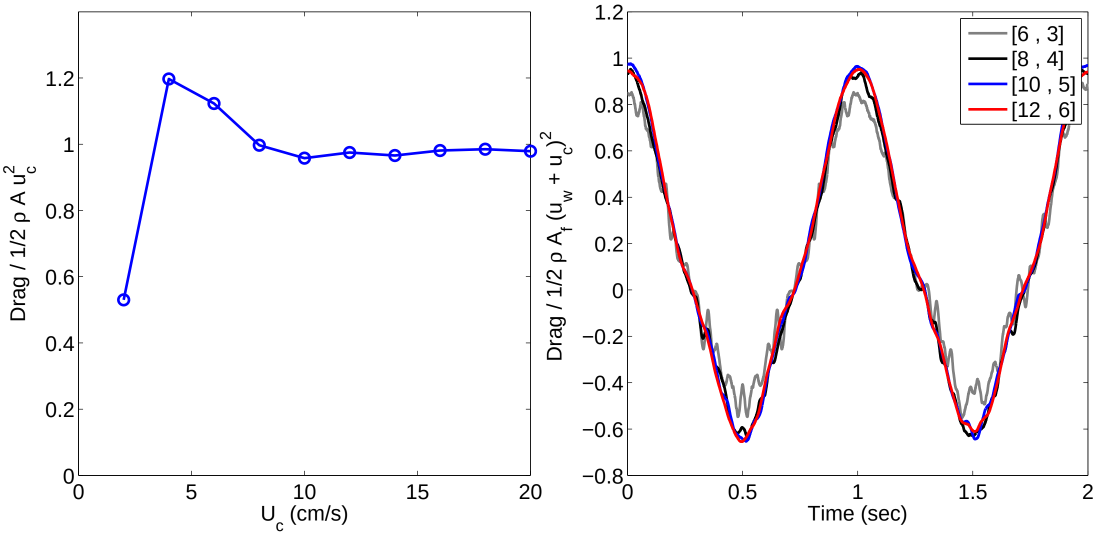

(a) (b)

Figure 5.3: Plot of test for Reynolds number independence for (a) steady flow of 3 grids, and (b) oscillatory plus steady flow $[u_w\ ,\ u_c]$ of 1 grid, $A/A_f = 0.45$; u_w and u_c in cm/s.

mean current $u_c = 5$ cm/s is set to be the base case of the unsteady flow. More discussion on the unsteady flow is provided in Section 5.5.

A typical force time history profile of steady flow is shown in Figure 5.4 for the 1, 2A, 2B and 3 grid configurations with $u_c = 10$ cm/s. The acceleration transient of the towing motion contributes to the initial sharp peak in the measured load. This is subsequently followed by steady decline to a constant drag condition from 10 sec onwards until the end of the steady flow phase at $\sim$ 36 sec. The effect of steady flow blockage is obvious: from 1 grid to 2A/2B and 3 grid configurations, the measured drag force does not increase by a simple multiplication of 2 and 3 − the increase is much smaller. This simple observation demonstrates the occurrence of current blockage in steady flow.

The effect of the downstream spacing of the grids is clearly visible: the measured drag of the 2B grid is slightly larger than that of the 2A grid. Side leakage enhances lateral mixing between the blocked flow after the first grid and the outer faster flow. This mixing results in an increase in the blocked flow velocity reaching the second grid, thus causing a slight increase in the associated measured drag. The spacing between the grids in the 2B configuration is twice that in the 2A configuration.

The large initial transient peak illustrates the build-up of current blockage as well as the inertial transients. Blockage occurs when the mean flow interacts strongly with each individual member and its wake containing vortices, and achieves the full saturation only when the steady-state wake condition has been reached. The larger

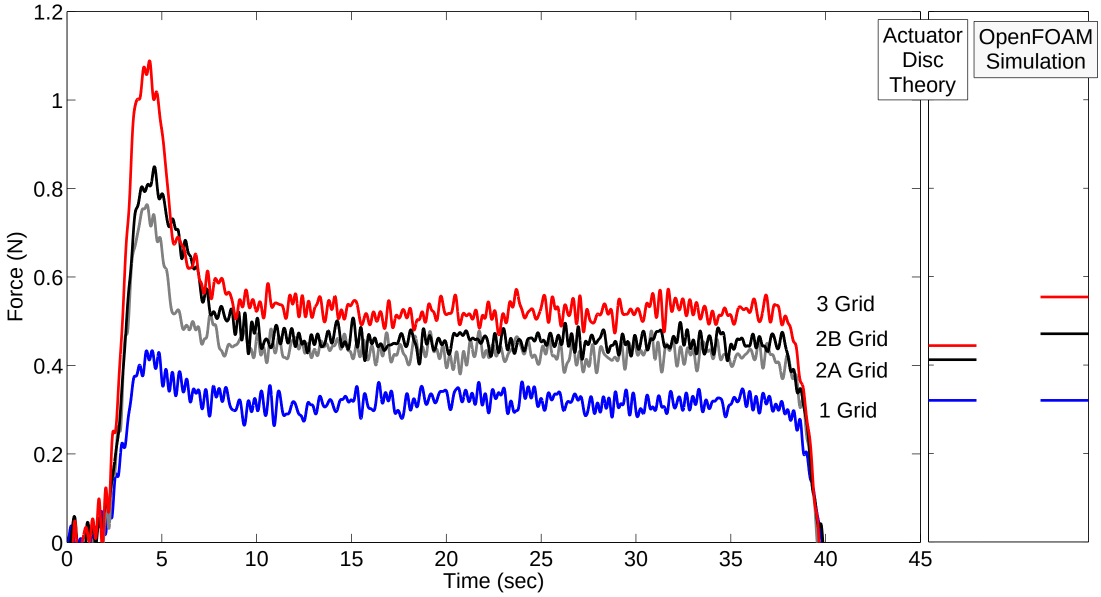

Figure 5.4: Plot of force time history of steady flow of $u_c = 10$ cm/s for $A/A_f = 0.45$.

the hydrodynamic area (C_dA), the higher the initial transients and the more blockage that ultimately results.

On the right hand side of Figure 5.4, the small horizontal bars show the predictions for the 2 and 3 grid tests based on the drag measured with only one grid present. The simple current blockage steady-flow model is used (see Equation 5.5 and Taylor et al. (2013)). The load on the 3 grid case is underpredicted, because leakage between the grids is not properly accounted for. In contrast, full CFD simulations using OpenFOAM® properly account for leakage and accurately predict the forces in 2 and 3 grids given the drag on a single grid. The grids are modelled as porous blocks, there is no attempt to resolve flow around individual structural elements within each grid. We note in passing that the CFD results clearly show the differences between 1, 2 and 3 grids. However, they are unable to distinguish the 2A & 2B cases with the grid resolution used.

Figure 5.5 summarises the measured drags for all four different A/A_f and grid configurations as data points, plotted in terms of normalised drag against hydrodynamic loading, (C_dA/A_f). The drag coefficients, C_d, for each A/A_f are obtained by calibrating the measured drag results of the 1 grid configuration with the simple current blockage model. The C_d values are provided in table B.1 in the Appendix B. The solid and dot-dashed lines are obtained from the drag on the switching model of current blockage theory based on A_f. The simple current blockage model predicts the total drag force on an obstacle array of frontal area (A_f) in terms of the hydrodynamic area ($C_d A$) of all the obstacles as:

$$F = \frac{1}{2}\rho u_c^2 \frac{C_d A}{\left(1 + \dfrac{C_d A}{4A_f}\right)^2} \tag{5.5}$$

This assumes that the velocity of the wake downstream is greater than zero, which requires $C_d A/(4A_f) \leq 1$. If the hydrodynamic area is larger, the idea of the switching model is that the hydrodynamic area is split into two discs $[C_d A = C_d A_L + C_d(A - A_L)]$, the first disc with as large an area as possible, $C_d A_L = 4A_f$, and the second disc containing the remainder of the area in the far wake where the velocity is zero, $C_d(A - A_L) = 0$. The total maximum force then becomes:

$$F_{max} = \frac{1}{2}\rho u_c^2 \frac{C_d A_L}{\left(1 + \dfrac{C_d A_L}{4A_f}\right)^2} = \frac{1}{2}\rho A_f u_c^2 \tag{5.6}$$

Although this split of the hydrodynamic area is somewhat *ad hoc*, the idea underlies the analysis of the loading on obstacles from combined current and regular waves. For further details, see Taylor et al. (2013).

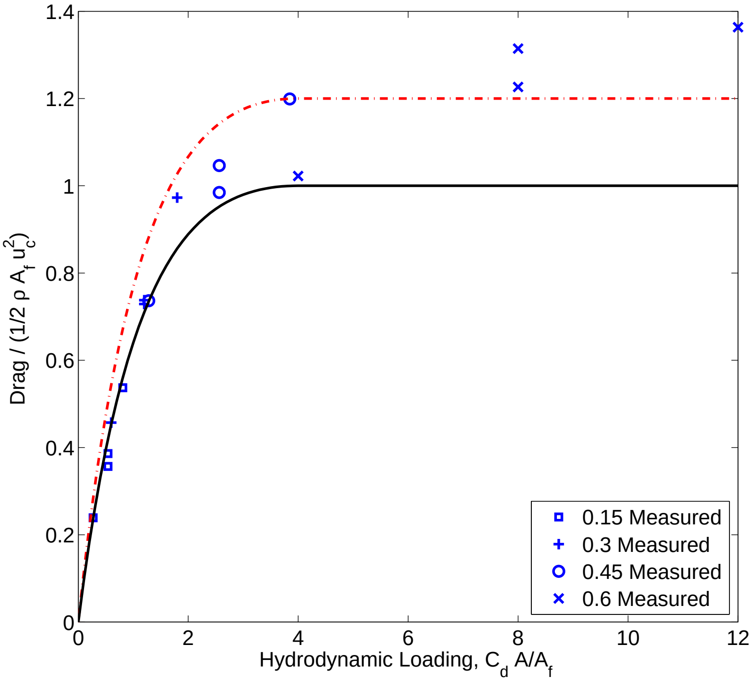

Figure 5.5: Asymptotic relationship of drag with hydrodynamic loading. The data points are the measured drag for four different A/A_f and grid configurations; the lines are the predictions.

For a grid with a continuous solid plate, the definition of A_f is obvious. However, each bar within the grid can be regarded as associated with part of a hole. Should this also be true for a bar on the perimeter? Is the 'effective' frontal area slightly larger? We test this hypothesis in Figure 5.5 with two versions of the switching model using the 'effective' frontal area A_f and $1.2 \times A_f$, plotted as solid and dot-dotted lines, respectively. We return to this increase in the effective frontal area in Section 5.5.7, 5.5.8 and 5.5.11, where we consider the current-induced component of drag in oscillatory plus steady motion.

The switching model of the theory postulates that the total drag on the array of grids does not depend significantly on the structural layout or the details of the distribution of hydrodynamic area (C_dA) along the flow direction, demonstrated from the two lines which behave asymptotically (flat) as the hydrodynamic loading (C_dA/A_f) increases. Whether or not the theory works can be observed from the same figure. The data points clearly show asymptotic behaviour as hydrodynamic loading increases. The majority of the data points lie close to the theoretical solid line. However, there is some offset particularly for $A/A_f = 0.6$, due to the leakage effect. Higher A/A_f values lead to more severe side leakage. This comparison shows rough agreement between the measured drag behaviour and the theoretical prediction, that the total drag experienced by an array of grids is independent of the hydrodynamic loading for the case of high C_dA/A_f.

5.5 Unsteady flow blockage

5.5.1 Choice of parameters

In order to obtain somewhat comparable flow regimes to those encountered in actual offshore conditions, separation of flow length scale effects need to be taken into account carefully. There are three different length scales involved: width of the vertical strips, d (related to the diameter of a jacket leg, e.g. 1 - 2 m), oscillation amplitude of waves, a (large waves could have a motion amplitude of 12 m near to the crest level), and the frontal width of the grid (or frontal width of a typical offshore jacket, e.g. a 60 m x 60 m platform has a width of 60 m). Table 5.2 shows the comparison of the scale parameters.

It is important to carefully match the relative magnitude of oscillation amplitude to the frontal width of the grids to closely resemble the flow regime in offshore conditions, simply because if the oscillation amplitude is too large everything will become blocked, and this will not be a good representation of the actual offshore conditions. We consider this length scale as important as the Keulegan–Carpenter ($KC = 2\pi a/d$) number scaling on individual elements (each plate), as the presence of steady flow

Table 5.2: Comparison of scale parameters between experiment and actual.

Parameter	Experiment	Actual
Physical dimension	30 cm × 30 cm	60 m × 60 m
Oscillation amplitude (a)	5.7 cm	$\sim$ 12 m
Width of vertical strips (d)	1 cm	2 m
Peak oscillation velocity	12 cm/s	6 m/s
Oscillation period (T)	3 sec	12 sec

will transport the vortices and wakes generated by the sharp corners of the plates in the downstream direction. Of course, this length scale can be regarded as giving a KC-type scaling on the entire grid. Obviously KC number effects may be expected to become more important for individual grid elements in the case of pure oscillation ($u_c/u_w = 0$) as there will be stronger wake encounter as a result, and the effect is well known to produce variation in the value of the Morison drag coefficient, C_d, on cylinders.

However, in sizing the width of the vertical strips, we choose the amplitude of oscillation and strip width to give a KC value in the range of 10 - 40, as would occur for the main structural components of an offshore platform in large waves.

Based on preliminary observations, we define a criterion above which we hope to achieve some degree of Reynolds number independence for the unsteady flow corresponding to the requirement that the net forward velocity is greater than 10 cm/s. We pick the magnitude of the oscillation velocity, u_w, as 10 cm/s and the mean current, u_c, as 5 cm/s as the base case to be modified to achieve different u_c/u_w values.

Table 5.3 lists the values of u_c/u_w used in the experiments. Moving vertically up and down the u_c/u_w columns within the table has the same effect as moving up and down through the water column in regular waves in which the kinematics vary hyperbolically with water depth. On the other hand, moving across the same u_c/u_w horizontally across the table has an effect of increasing the Reynolds number, but as the parameters have been shown to lie in the Reynolds-number-independent flow regime, the horizontal shift across the table is required to keep the maximum speed in the tank at or below 20 cm/s. The oscillation amplitude is kept constant by varying the oscillation period. As a result, two additional sets of regular waves and constant current are introduced to capture a wide range of u_c/u_w. There are two comparable cases for u_c/u_w of 1 and 3 of which the results can be used as a conformity check when one changes the Reynolds number of the flow (horizontal movement across columns of the same row).

Table 5.3: Experimental parameters (a = oscillation amplitude, T = oscillation period) with range of u_c/u_w; u_w and u_c in cm/s.

u_c/u_w	(a, T)	$[u_w\ ,\ u_c]$	(a, T)	$[u_w\ ,\ u_c]$
1/4			(11.5 cm, 4.5 sec)	[16 , 4]
1/3	(8.6 cm, 3.6 sec)	[15 , 5]	(8.6 cm, 4.5 sec)	[12 , 4]
1/2	(5.7 cm, 3.6 sec)	[10 , 5]		
1	(2.9 cm, 3.6 sec)	[5 , 5]	(2.9 cm, 1.8 sec)	[10 , 10]
2			(1.4 cm, 1.8 sec)	[5 , 10]
∞			-	[0 , 10]

All u_c/u_w cases are measured for four grid configurations: 1, 2A, 2B and 3. Additional pure oscillations ($u_c/u_w = 0$) are conducted for each u_c/u_w case but only for the 2B grid configuration.

5.5.2 Data analysis method

For unsteady flow, the measured force from each individual test is the total hydrodynamic force on the grids, which needs to be decomposed into drag and inertia components. Obviously, for steady flow there is only drag, no inertia loading. Here we present a simple technique to decompose the total force into drag and inertia. This requires knowledge of the input velocity profile to the carriage.

The total measured force, $F(t)$, is extracted after the starting transients, when the motion is sinusoidal with a mean component, and the total force is periodic - repeating every wave cycle. We choose a record of length 4 - 5 wave cycles and shift the time so that the input velocity is maximum at the zero time. The force record is then time-reversed to produce a reflected total measured force, $F_R(t)$, with $F_R(t) = F(-t)$. The two profiles are then combined, and both the drag and the inertia components can be extracted by the following relationship:

$$\begin{aligned} \text{Inertia} &= \frac{1}{2}[F(t) - F_R(t)] \text{ assumed to be } \rho C_m V \dot{u} \\ \text{Drag} &= \frac{1}{2}[F(t) + F_R(t)] \text{ assumed to be } \frac{1}{2}\rho C_d A u|u| \end{aligned} \qquad (5.7)$$

Whether this clearly extracts these two Morison-type load components is demonstrated next. A plot of the decomposition result is shown in Figure 5.6. The input velocity profile is included for reference. The extracted drag and inertia are shown to be smooth, except when the velocity is close to zero (also the drag force) when the inertia component is dominant.

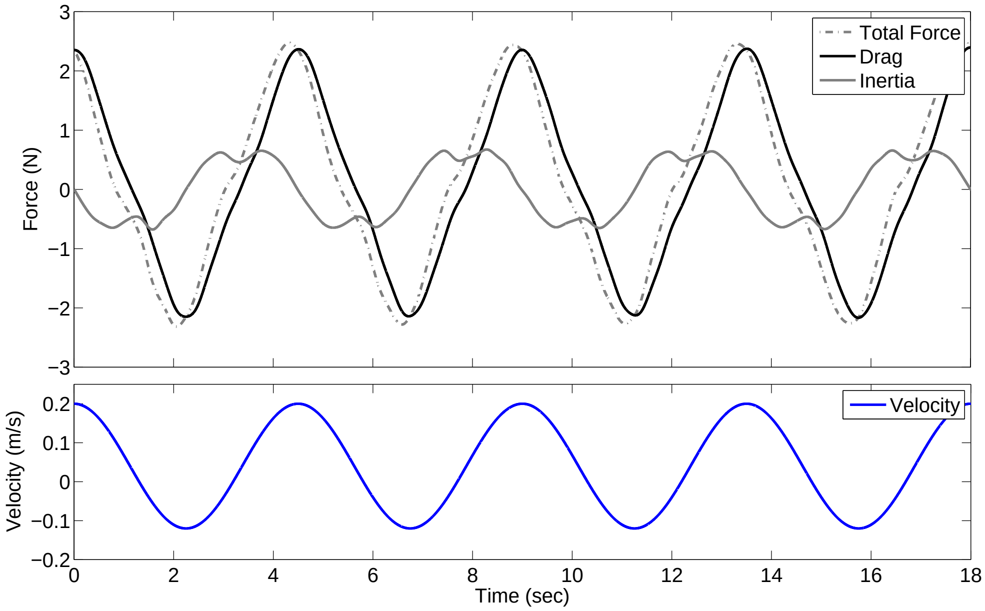

Figure 5.6: Plot of total force decomposition result. Top figure shows total force in dot-dashed grey line, drag in solid black line and inertia in solid grey line. Bottom figure shows input velocity profile.

This simple relationship (Equation 5.7) shows that it is possible to extract from the total force drag (which is assumed to be in phase with the velocity profile) and inertia (which is out of phase by 90° from the drag). Note that there are no assumptions in the decomposition process that the drag term is actually proportional to $\cos|\cos|$ and the inertia term to $-\sin$ according to the Morison equation (Morison et al., 1950). The simple decomposition method works well. The secondary wiggle at the peak crests and troughs of the assumed inertia term probably arises from the lack of perfect symmetry of the drag term. We explore this later in Section 5.5.11. We assume symmetry around the velocity peak because this is consistent with a Morison formulation - our new model for blockage is still based on the assumption of a Morison-type model for drag on the actuator discs.

5.5.3 Forms of the drag plots and the effect of blockage ratio, A/A_f

The measured drag forces are now compared with the new blockage theory for regular waves and current. In order to obtain the C_d coefficient for each case, mean square error minimisation by curve fitting is performed on each measured drag - time history, assuming the full current blockage model is correct. Since the measured drag contains much less of a shoulder at the zero crossing as compared to the full Morison-based theory, a weighting function of $cos^{10}(\omega t)$ is introduced to force the minimisation to occur only at both crests and troughs. The C_d coefficient can then be inferred for each case from this minimisation exercise.

A range of different cases is shown in Figure 5.7. In all cases, the grid layout 2B is used, with the downstream spacing equal to the grid width. The left side of each sub-plot shows the separated drag and inertia time histories for each experimental case. The right side shows the equivalent best fit with constant in time C_d and C_m coefficients based on the full wave–current–structure blockage model. For each case, the only adjustable parameters are the 'bare' unblocked C_d value and the inertia coefficient, C_m. The estimated C_d value for each experimental drag force time history is used to give the model prediction of the drag time history on the right hand side of each sub-plot. Moving vertically down the figure, the blockage ratio (A/A_f) of each of the two grids increases from 0.15, to 0.30 and 0.45 at the bottom. The left column is for a larger current to wave ratio ($u_c/u_w = 1/2$), and the right column is for $u_c/u_w = 1/4$.

Overall, we conclude that the full blockage model works well in reproducing much of the structure of the oscillating motion experiments both with (black) and without (grey) an imposed mean current. The equivalent assumed inertia load contributions are denoted by the dashed lines. The legend in each sub-plot shows $[u_w\ ,\ u_c]$ for each case, the velocities in cm/s. The relative importance of the current reduces as the blockage ratio (A/A_f) is increased. The only case for which the model fit is less good is shown at bottom right of Figure 5.7. This corresponds to $u_w = 16$ cm/s, $u_c = 4$ cm/s, and 2 grids of blockage ratio 0.45. Here, on the left, the peak crest and trough values in the measured time histories with and without the small current are virtually indistinguishable. There is, however, a difference in the shapes of the crests and troughs experimentally, with the crests being slightly broader in time. In contrast, there is a shift for the crest and trough peak values in the model but the local shapes are virtually identical.

A mean square error minimisation is also performed to fit the measured drag peaks with the standard Morison force formulation with no allowance for blockage. Here the weighting function is also $cos^{10}(\omega t)$, but it is applied to crests only. Comparisons between the measured drag, the standard Morison formulation for the drag term and the full model (FCB) are illustrated in Figure 5.8(a) and Figure 5.8(b).

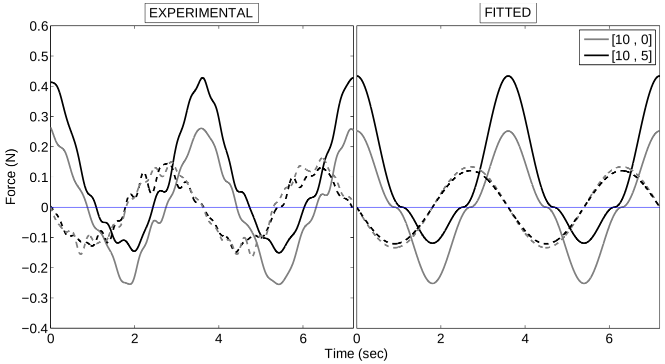

(a) $A/A_f = 0.15$

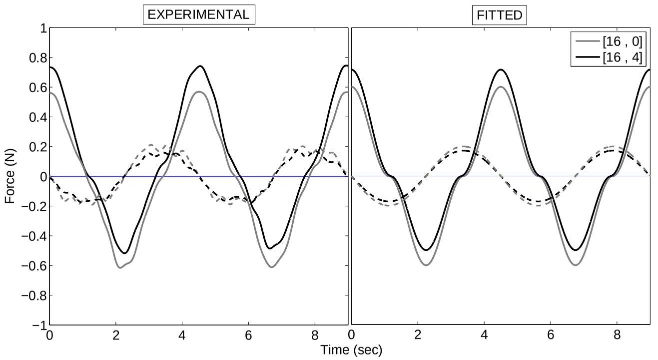

(b) $A/A_f = 0.15$

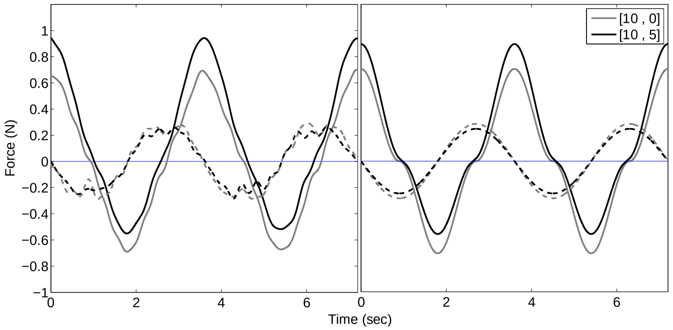

(c) $A/A_f = 0.30$

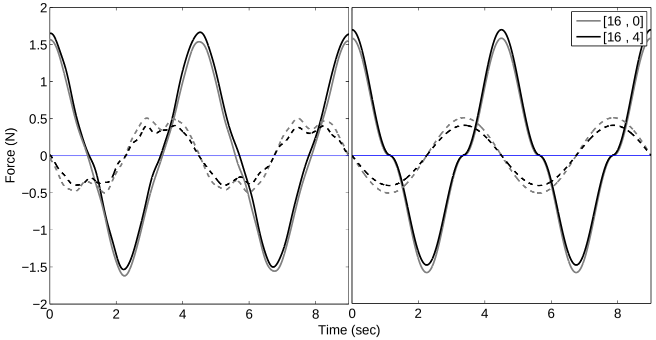

(d) $A/A_f = 0.30$

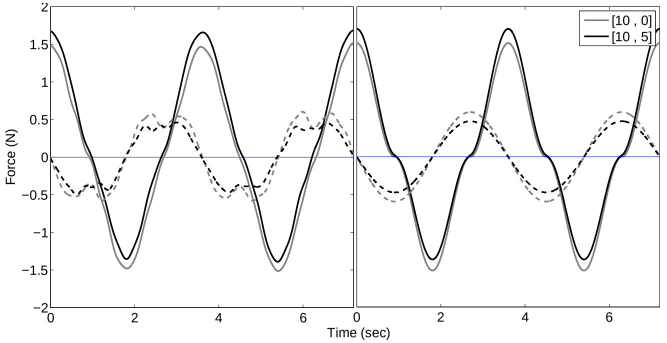

(e) $A/A_f = 0.45$

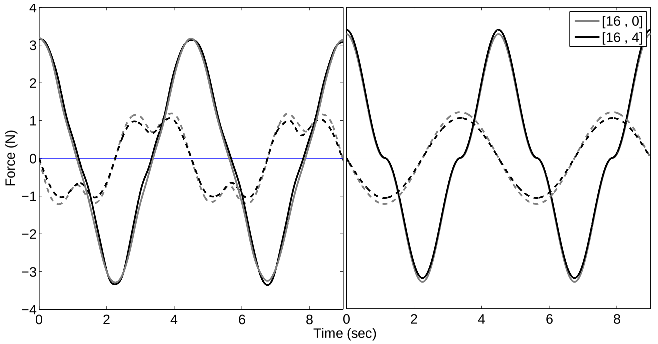

(f) $A/A_f = 0.45$

Figure 5.7: General structure of the drag (solid lines) and inertia (dashed lines) force time histories for 2B grid configuration, experimental vs. fitted data, $u_c/u_w = 0.5$ on left, 0.25 on right and 0 on both.

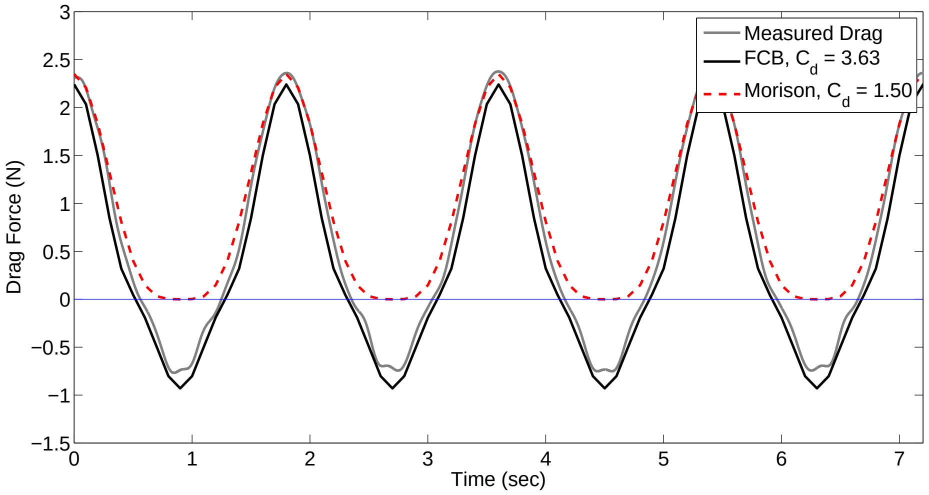

(a) u_w = 10 cm/s, u_c = 10 cm/s

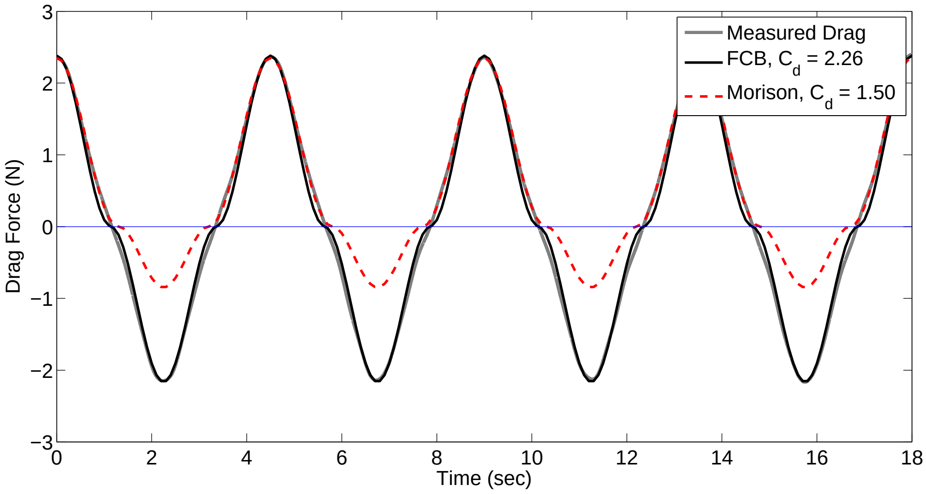

(b) u_w = 16 cm/s, u_c = 4 cm/s

Figure 5.8: Comparisons of the measured drag (solid grey lines) to predictions from the new full current blockage model (FCB, solid black lines) and the original Morison equation (fitted to the peak crests only, dashed (red) lines), 3 grids, $A/A_f = 0.30$, for $u_c/u_w = 1$ and 1/4.

Figure 5.8(a) shows a drag comparison for the case of [10 , 10]. In the standard Morison force formulation with no current blockage, there is a positive crest force (associated with the peak velocity of 20 cm/s) and a flat plateau (or zero trough). However, there is actually a significant negative trough force due to the physical blockage effects, and this effect is well captured by the full current blockage model. Figure 5.8(b) demonstrates a drag comparison for a large oscillation in a small current, [16 , 4], and the agreement between the measured drag and the new model is shown to be very good, except at the zero crossing where the measured drag exhibits no shoulder. The resulting force profile is very close to a pure wave oscillation (without any imposed mean current) with a slight vertical offset of the peaks contributed from the mean current contribution. This is discussed in detail later but provides the first indication that the asymptotic two-disc expression of the full current blockage model which contains no $u_w \times u_c$ term is working well.

It is obvious that neither the original form of the Morison equation for the drag force with no blockage nor the modified form described in the API design guidelines (which accounts for the reduction in the effective mean current within the structure but ignores wave–current–structure effects) can be matched to the whole force time history with a single constant C_d coefficient. In contrast, the new blockage model will be shown to be able to reproduce the whole measured drag force - time history well for all flow regimes. Although the peak force is usually one of the most important structural design parameters, a correct representation of the entire force - time history is essential for dynamically responding structures.

5.5.4 Inertia curve fit

A similar mean square error minimisation by curve fitting is also performed for the inertia component for each case, but now the weighting function is purely sinusoidal: $-\sin(\omega t)$. The associated C_m coefficients can then be inferred. Note that the inertia component considered is the fluid inertia loading component only, the structural inertia contribution of the grids and support frame has been removed. It is interesting to note that there are wiggles found at the peaks of the measured inertia component whenever the towing motion reverses its direction, as shown in Figure 5.7. These are discussed in Section 5.5.9.

5.5.5 The effects of u_c/u_w and demonstration of no $u_w \times u_c$ contribution to drag

We examine the effect of introducing a current into a regular oscillation for a fixed grid geometry, the 2B configuration for two grids, each with a blockage ratio (A/A_f) = 0.30. Figure 5.9 shows the experimentally measured drag and inertia force time histories (left) and the new current blockage predictions (right), within each sub-plot, for four different current to oscillation velocity ratios. As in Figure 5.7, the solid grey curve is for regular oscillation, the solid black for oscillation and current. The legend within each sub-plot shows the relevant u_c and u_w values (in cm/s). The important u_c/u_w ratios reduce from 1 (top left), clockwise to 1/2, 1/3 and 1/4 (bottom left).

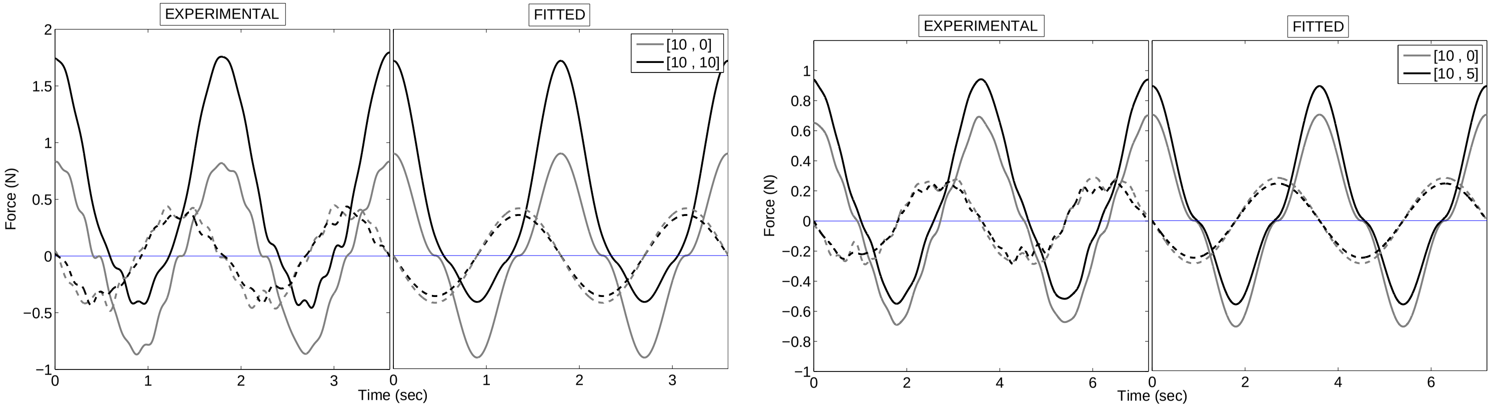

(a) $u_c/u_w = 1$ (b) $u_c/u_w = 1/2$

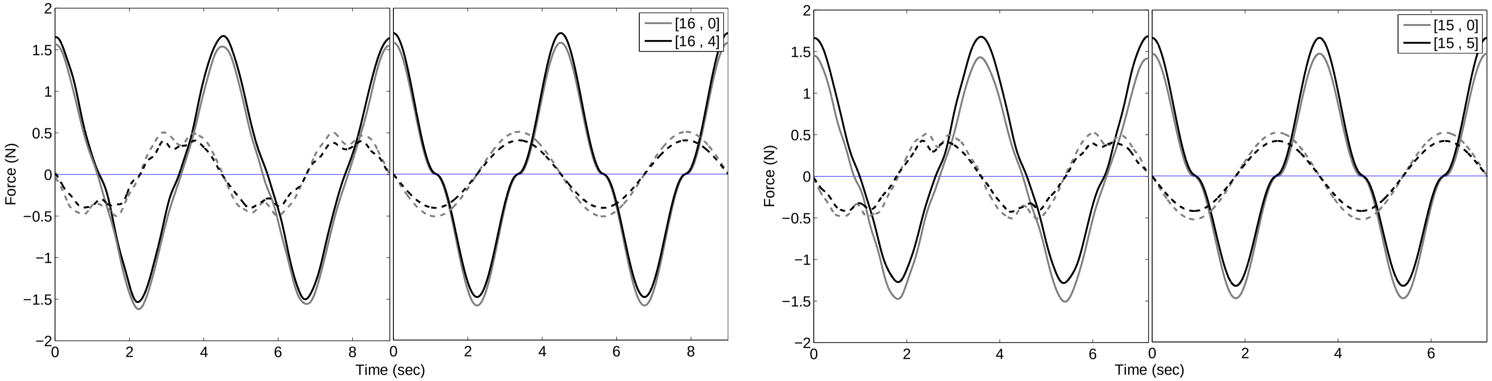

(d) $u_c/u_w = 1/4$ (c) $u_c/u_w = 1/3$

Figure 5.9: Effect of varying the mean current to oscillation velocity ratio (u_c/u_w) for the 2B grid, $A/A_f = 0.30$, experimental vs. fitted data, drag forces as solid lines, inertia forces as dashed lines

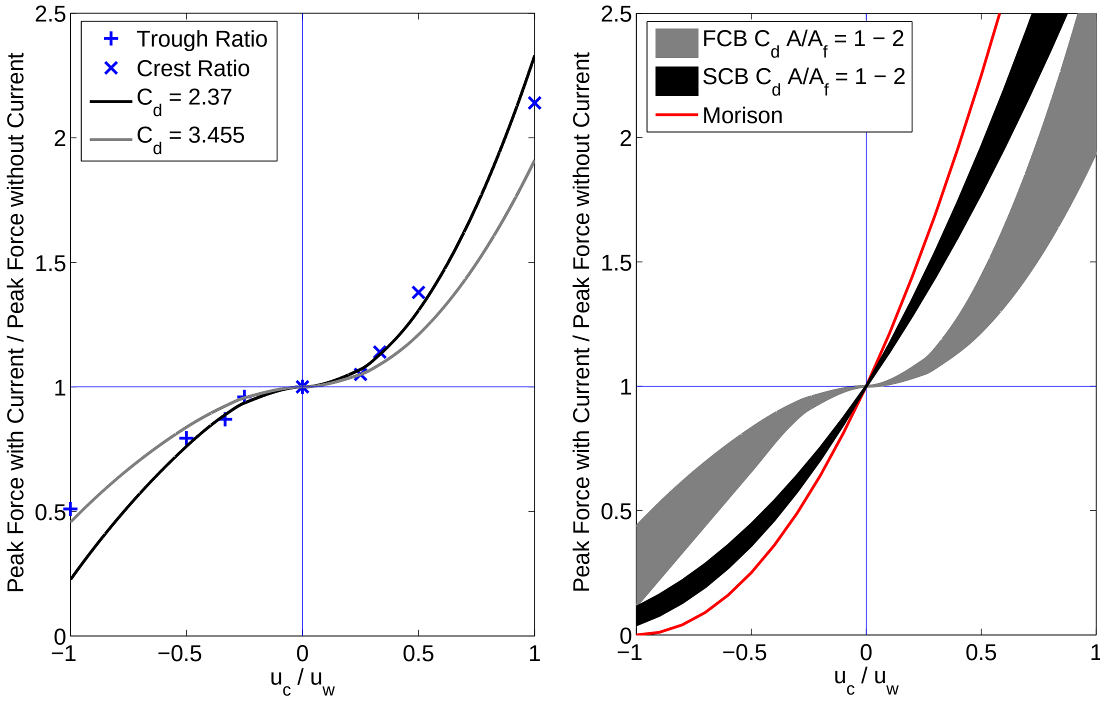

(a) (b)

Figure 5.10: Plot of peak crest and trough ratios of drag forces for the 2B grid, $A/A_f = 0.30$. (a) Comparison between measured crest and trough ratios (data points) and the full theory (solid lines). (b) Comparison between the blockage theories: FCB = full current blockage model (grey band), SCB = simple current blockage model (black band), and the standard Morison (solid line).

Apart from some discrepancy for the Morison 'shoulder' as the drag force crosses through zero, the full current blockage model works remarkably well for all cases.

One of the striking predictions of the full theory is that the predicted drag force time history and the associated peak crest and trough values contain no $u_w \times u_c$ component, when the magnitude of the regular oscillation (u_w) is large compared to the mean current (u_c). Figure 5.10(a) shows the peak crest and trough force values from the data in Figure 5.9, plotted as the strength of the current is varied so $-1 \leq u_c/u_w \leq 1$. The magnitude of the peak forces with current are non-dimensionalised by the peak forces in the same oscillation without current.

The data points on the right-hand half of Figure 5.10(a) correspond to the force peaks for the oscillation and current velocities being in the same direction, the data points on the left correspond to the force troughs for the oscillation and current velocities being opposed. The two solid lines in Figure 5.10(a) correspond to the full current blockage theory for two values of C_d. These values correspond to the two extremes of the averaged C_d values from the fits to each of the force time histories.

Averaged C_d values are used to account for the slight difference in the inferred C_d values between regular oscillations with and without current. The individual C_d value can be inferred from Table B.3 for regular oscillations with steady flow and Table B.5 for pure regular oscillations without steady flow, both in the Appendix B. The solid lines for the full current blockage theory are expressed as:

$$\frac{\text{Peak Force with Current}}{\text{Peak Force without Current}} = 1 \pm \frac{\pi A_f}{2C_d A}\left(\frac{u_c}{u_w}\right)^2$$

Both the experimental data and the full theory show an inflexion in the force ratio (with and without current) as the current passes through zero.

The major qualitative feature of this absence of any $u_w \times u_c$ contribution to the magnitude of the crest and trough forces is illustrated in Figure 5.10(b). The grey band shows the behaviour of the full current blockage theory for a range of values of the hydrodynamic loading, $C_d A/A_f$ (the range 1 - 2 captures the effects of waves and in-line current on a typical deep water offshore jacket structure).

In all cases, the full theory shows an inflexion. In contrast, the black band corresponds to a Morison force prediction for the same range of hydrodynamic loading when only the current is blocked – 'simple blockage' or SCB as in the present API design guidelines (American Petroleum Institute, 2000). The single line shows the Morison prediction with no account taken for blockage. Neither the black band ('simple blockage') or the Morison without blockage show the inflexion which is consistent with the experimental data for low (u_c/u_w) ratio. This can be observed from the force ratio expression of the Morison without blockage:

$$\frac{\text{Peak Force with Current}}{\text{Peak Force without Current}} = \frac{(u_w \pm u_c)^2}{u_w^2} = 1 \pm 2\left(\frac{u_c}{u_w}\right) + \left(\frac{u_c}{u_w}\right)^2$$

while the force ratio expression of the simple current blockage model can be obtained by simply substituting u_c with $u_{cs} = u_c/[1 + C_d A/(4A_f)]$. Both expressions yield a finite gradient as the current passes through zero, unlike the experimental data and the full current blockage model.

The theoretical prediction of the absence of any $u_w \times u_c$ term within the prediction of peak crests and troughs is then a major piece of evidence in support of the new full blockage model, irrespective of the calibration of drag coefficients, C_d. When the C_d values are calibrated for each case, a good representation of the entire drag time history over the oscillation cycle is achieved.

5.5.6 The effects of hydrodynamic loading (C_dA/A_f) on drag time history

Having examined the effect of varying the current relative to the oscillation for fixed grid geometry, we now fix the flow regime ($u_w = 15$ cm/s, $u_c = 5$ cm/s, so $u_c/u_w = 1/3$), and investigate the effects of changing the number and spacing of the grids, each with blockage ratio $A/A_f = 0.30$. This is shown in Figure 5.11.

The same structure for the composite sub-plots is used: the left side of each shows processed measured forces (drag - continuous line, inertia - dashed line), on the right the full blockage model best fit with C_d and C_m coefficients. Moving clockwise from top left we start with the 1 grid, then the two grids in the closer spacing (the 2A configuration), bottom right is the the two grid case with doubled downstream spacing (the 2B configuration), and finally the bottom left is the 3 grid configurations. As previously, we see immediately that the full current blockage model does an excellent job at reproducing the measured drag time histories. Also shown in each sub-plot is the inferred inertia contribution.

According to the asymptotic model, the shift (offset) component of the unsteady drag peaks and troughs (the current component) is independent of C_dA, and simply proportional to the frontal area, A_f. This concept is consistent with the switching model in Section 5.4: as C_dA/A_f increases, the peak steady force is independent of the details of the hydrodynamic area, C_dA, and only the frontal area, A_f, matters. As more blockage develops, the rear disc is assumed to be effectively within the stationary wake from the front disc and the fluid is forced to diverge out of the frontal area of the obstacle array, hence the associated drag force is dependent on the geometry of the frontal area only.

We investigate the adequacy of Equation 5.2 for the case of regular oscillations in steady flow as the number and spacing of the grids is changed. First we remove the shift from the measured and fitted drag force peaks so that the peak values are equal in magnitude but opposite in sign. Next we divide by the total blockage ratio for all the grids in the flow ($\Sigma A/A_f$), the summation being over the number of grids. The resulting measured and modelled drag force time histories are shown in Figure 5.12, in which the top part of this figure shows the measured drag in black and the modelled drag in grey. The resulting fluctuating parts of the measured records are shown to be virtually identical and independent of the number of grids, and shown to match well with the predicted forms. This is reinforced in the lower plots in the figure: on the left the four measured shifted and grid area-scaled drag histories are plotted together, and on the right the four corresponding predictions from the full blockage model. It

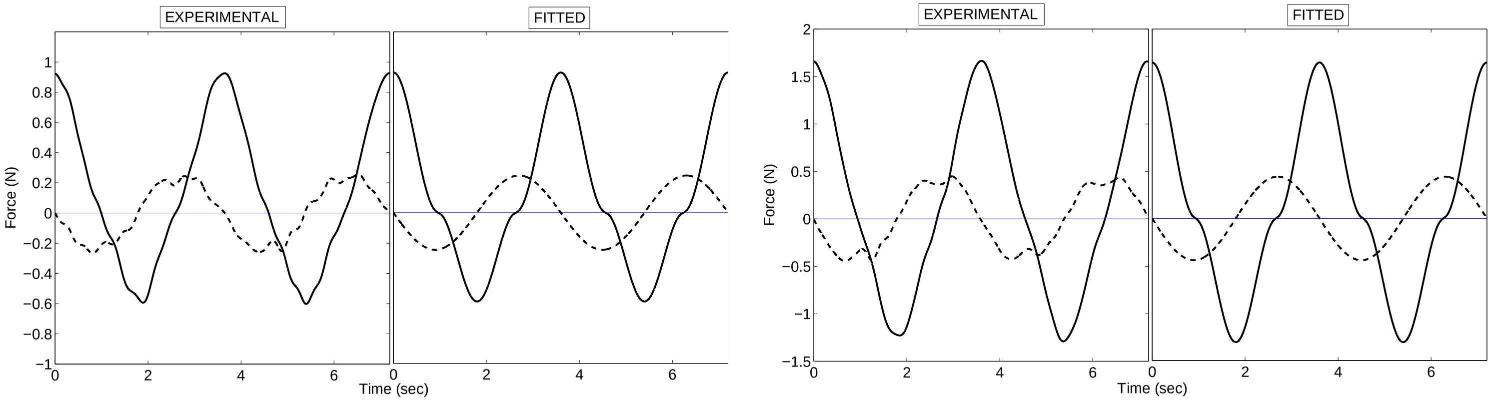

(a) 1 grid

(b) 2A grid

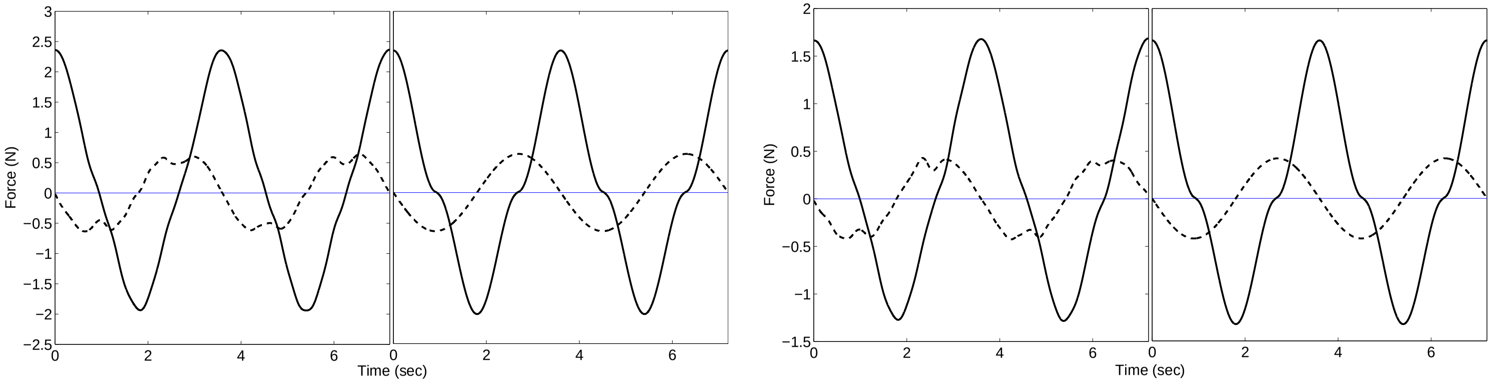

(d) 3 grid

(c) 2B grid

Figure 5.11: Experimental and fitted drag (solid lines) and inertia (dashed lines) forces for different arrangements of grids for [15 , 5], $A/A_f = 0.30$.

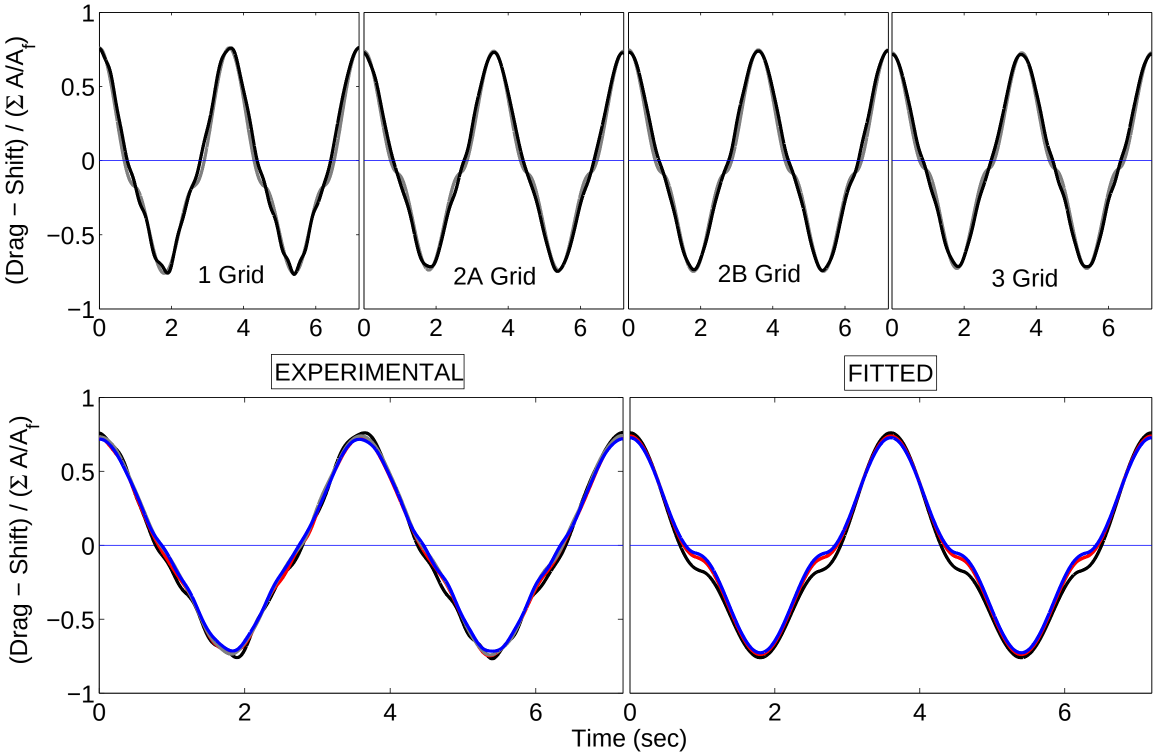

Figure 5.12: Oscillatory part of the drag force for the various grid arrangements, all for [15 , 5], $A/A_f = 0.30$. Top figure shows the experimental drag in black and the fitted drag in grey. Bottom figure shows the top four subplots plotted together as experimental vs. fitted drag.

should be noted that the full current blockage model fitted C_d values across the different grids vary by $< 2\%$ for the [15 , 5] flow case, so it is unnecessary to allow for C_d variation as the number of grids is changed (see Table B.3 in the Appendix B).

Overall, this collapse for the four different grid geometries is remarkably good for the oscillating part of the total drag force on the complete obstacle array. The sole outlier on the right hand lower plot occurs because the flow regime for the single grid is not quite asymptotic (which requires $C_d A/A_f$ large and u_c/u_w small). Although the shifted peak values of the forces scale, the shape of the Morison-derived drag force waveform is slightly different, with the Morison 'shoulders' shifted downwards slightly compared to the asymptotic result.

5.5.7 The shift of force crests and troughs of the drag time history

The asymptotic form of the two-disc model (Equation 3.25) has a shift for the force crests and troughs of:

$$F_{shift} = \pi/4\rho A_f u_c^2$$

Thus, it is predicted to scale with the frontal area but is independent of the number of grids, the blockage ratio of each grid (A/A_f), the drag coefficient (C_d) and the oscillatory motion (u_w).

In contrast, the crest / trough shift for the original Morison equation in a combined oscillation and steady current is:

$$F_{shift} = 1/2\rho C_d A(2u_w u_c)$$

This scales with the hydrodynamic area, C_dA and the product of the amplitude of the wave oscillation velocity and the steady current - a completely different form.

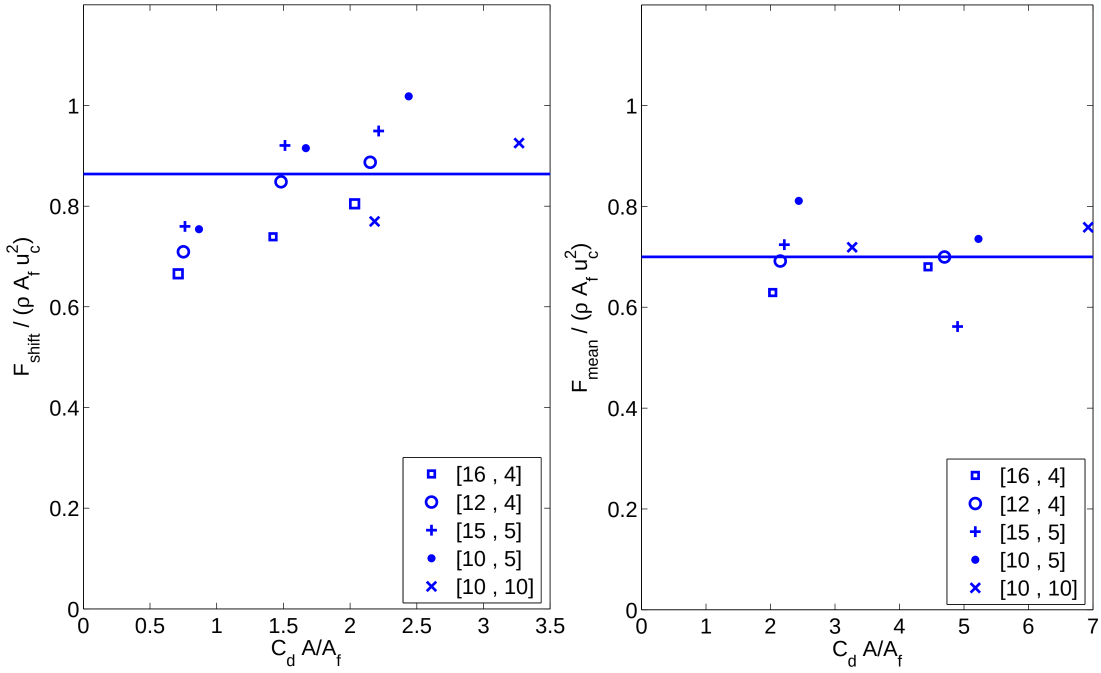

(a) (b)

Figure 5.13: Plot of (a) shift of peak crest and trough of drag forces, (b) time-averaged mean drag force, as the total hydrodynamic loading (C_dA/A_f) is altered.

Figure 5.13(a) shows the experimentally derived shift of peak forces as a function of the hydrodynamic loading (C_dA/A_f) for a wide range of grids and [u_w , u_c] combinations. There is some scatter but there is no significant variation with C_dA/A_f or with the magnitude of the oscillation velocity, u_w. The mean of the ratio, $F_{shift}/(\rho A_f u_c^2)$, is slightly greater than the theoretical numerical coefficient $\pi/4 \sim 0.785$. As for the steady flow asymptotic result (Section 5.4), a slightly increased frontal area may be appropriate, hence $1.1 \times A_f$ could be used and this is shown in the figure as the solid horizontal line.

5.5.8 The mean (time-averaged) force in regular oscillations and mean flow

The net retardation of the approach current depends on the mean force acting on the fluid over the oscillation cycle, and this controls the total blockage. The derivation of the two-disc model makes use of this mean force in apportioning the total hydrodynamic area across the two discs. Thus, it is of some interest to compare the measured and predicted mean forces.

Once the two-disc model is appropriate (for small u_c/u_w and at least moderate hydrodynamic loading $C_d A/A_f$), the asymptotic form of the mean force is predicted by:

$$F_{mean} = 1/2 \rho A_f u_c^2$$

which is independent of the oscillation magnitude, u_w, and the hydrodynamic area, $C_d A$. Note the different numerical coefficient compared to the shift of the peak forces (1/2 compared to $\pi/4$).

Figure 5.13(b) shows the good collapse of a range of experimental cases to the theoretical mean drag force. Again, the magnitude of the appropriate frontal area appears to be slightly larger than the actual frontal cross-sectional area of the grids (A_f), here a factor of $\sim 1.4\times$ seems appropriate. However, given that the data for both the shift (a) and the mean (b) are small fractions of the magnitude of the peak forces within the wave cycle, we view this level of consistency with theoretical predictions based on the full wave–current–structure blockage model as satisfactory.

5.5.9 Discussion of the inferred C_d and C_m coefficients

Table B.2, B.3 and B.4 in the Appendix B list the C_d and C_m coefficients inferred from curve fit minimisation of the full current blockage model for each u_c/u_w case and each grid configuration. A column containing the averaged C_d value is provided for each table of C_d by taking the average C_d value across the number of grids for each u_c/u_w. Since the Morison coefficients C_d and C_m are usually defined for an obstacle in isolation in a mean flow, we could correct for the presence of all the other obstacles within the same grid by multiplying the drag coefficient, C_d, by $(1-A/A_f)^2$ and the inertia coefficient, C_m, by $(1-A/A_f)$. This accounts for the reduction in the open area for the flows at the plane of the grid due to the presence of all the obstacle bars and the local speed up of the flow. This yields modified C_d values more in keeping with what might be expected for single rectangular bars in a uniform mean flow ($C_d \sim 1-2$) for the grids with higher blockage ratio (A/A_f).

It can be observed that the C_d coefficients of the full model are quite consistent across a varying number of grids of the same blockage ratio (A/A_f). There are, however, some discrepancies in the observed pattern, which are largely attributed to some residual effects. The C_d and C_m coefficients are observed to vary with varying blockage ratio (A/A_f) probably due to KC number effects on each individual flat bar.

The C_m coefficients are found to be very large for obstacles in the form of a perforated thin plate. There are significant variations of the C_m coefficients across different numbers of grids of the same blockage ratio (A/A_f). We are currently seeking an explanation for the high C_m values. It is likely that each grid itself should have a contribution to the inertial loading due to large-scale modification of the flow field, as well as the local modifications over length-scales comparable to each bar within each grid.

Our method of separating drag and inertia relies on the drag term being in phase with and symmetric about the velocity peaks. Although this is consistent with the basic form of the Morison equation with $u|u|$ being in phase with u and $\dot{u}$ being in quadrature, there is some evidence that the separation process applied to the measured force records is not perfect.

Figure 5.14 shows the inferred measured inertia time history for [16 , 4] of 3 grids of $A/A_f = 0.30$ and the sinusoidal fitted form, both skew in time relative to the velocity peaks. There is a notable third harmonic present in the measured signal (although the drag peak force is $\sim$ 2.4 N, the linear inertia fit $\sim$ 0.6 N and the residual 3rd harmonic $\sim$ 0.2 N). We believe this may arise from the 'shoulders' on the quadratic drag term. Although these are much less marked in the measured data than in the Morison-based fits, they are still present. If the timing of the shoulders is slightly different depending on whether the velocity increases towards the maximum (crest) or decreases towards the minimum (trough), this would account for a small degree of leakage from the drag term into what we expect to be the linear inertia term. Since

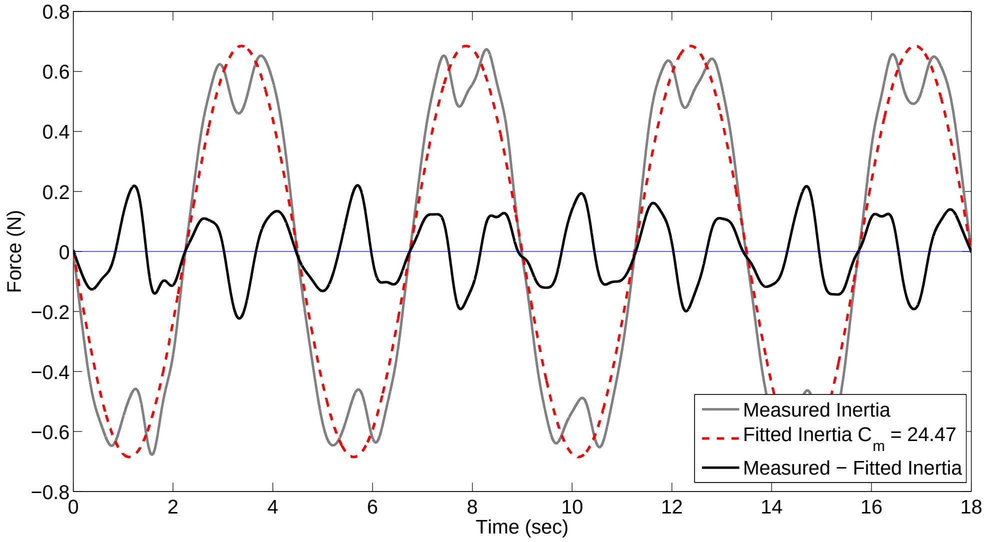

Figure 5.14: Plot of skew-in time force components including linear inertia for [16 , 4], 3 grid, $A/A_f = 0.30$. The measured data in solid grey line, the fitted data in dashed (red) line, and the difference between the measured and the fitted data in solid black line.

much of the focus in this work is on force peaks and troughs, a small degree of leakage as the drag force goes through zero up- and down-crossing is acceptable.

5.5.10 Reconstruction of complete force time history using the Morison-based FCB formulation

With the inferred C_d and C_m coefficients from the mean square error minimisation exercise, a reconstruction of a complete total force time history is made possible. Figure 5.15 provides at the top a comparison between the measured total force (grey line) and the reconstructed total force (black line), together with the fitted drag and inertia terms in the centre and the difference between the measured and the Morison-based FCB reconstructed total force at the bottom, for the case of [16 , 4] of the 3 grid configuration with 0.30 blockage ratio.

It is clear that the reconstructed total force closely resembles the measured total force, with small differences attributed to a third harmonic contribution and the fact that the measured force contains less distinct shoulders at the zero crossings than any Morison-based FCB model. In general, the root-mean-square (rms) error on the force time histories is about 20%. However, the values of peaks and troughs are much better modelled, with an rms error of 6%.

Having presented the amplitude prediction of total force, in the next subsection we use Fourier series to characterise the shape of the total force in time.

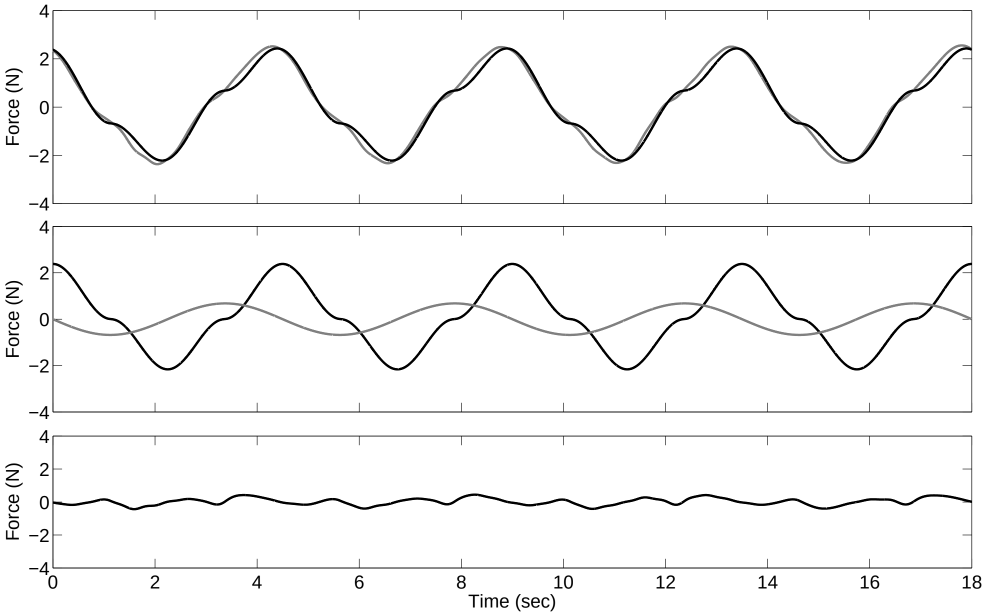

Figure 5.15: Plot of Morison-based FCB reconstruction of total force time history for u_w = 16 cm/s, u_c = 4 cm/s, 3 grid, A/A_f = 0.30. Top figure shows the measured total force in grey line and the fitted force in black line, middle figure shows the fitted drag in black line and inertia in grey line, bottom figure shows the difference between the measured and fitted total force in black line.

5.5.11 Total force decomposition using Fourier representations

Here we investigate the shape of the force components relative to the imposed velocity peaks by using a Fourier representation fitted to experimental data over 6 - 8 oscillation periods. We present decomposition results including components up to the fifth harmonic of the sinusoidal component of grid motion.

We observe that the time dependence of the asymptotic force ($u_w >> u_c$) derived using the Morison-based FCB equation can be broken down into three types of term, i.e.:

$$\begin{aligned} \cos\omega t|\cos\omega t| &= ()\cos(\omega t) + ()\cos(3\omega t) + \ldots && \text{odd harmonics} \\ |\cos\omega t| &= () + ()\cos(2\omega t) + ()\cos(4\omega t) + \ldots && \text{even harmonics} \\ \text{Morison inertia} &= -()\sin(\omega t) && \text{linear} \end{aligned}$$

The Morison-based FCB total force can then be further regrouped into odd and even frequency harmonic contributions with the odd harmonics originating from the u_w^2 term and the even harmonics from the time-varying u_c^2 term.

Motivated by the form of the Fourier series from the model, we perform Fourier fits to the experimental data sets $[u_w\ ,\ u_c] = [16\ ,\ 4]$, $[12\ ,\ 4]$, $[15\ ,\ 5]$ and the 3 grid configuration with $A/A_f = 0.30$, and also $[15\ ,\ 5]$ and the 2A and 2B grid configurations with $A/A_f = 0.30$. We also present Fourier fits for the pure oscillation [16 , 0], [12 , 0], [15 , 0] and the 2B grid configuration for comparison to the loading for oscillations plus mean motion. The results of Fourier fits to the first five harmonics are shown in Table 5.4.

We find that there is little variation in the mean and standard deviation of each coefficient across the five cases considered. In table 5.4, the upper figure within each set of brackets is the mean value of the fitted coefficient, and the lower figure is the standard deviation. The same format is used for the small shifts in phase used for the each super-harmonic. No phase shift is included within the cos term corresponding to the first term in the expansion of the Morison-based FCB drag, as we consider that the sin term component should more properly be treated as part of the Morison inertia coefficient.

It is observed that the theoretical total Morison-based FCB drag associated with the oscillating motion (i.e. total odd harmonics with the fundamental sin term removed) results in a shift of the shoulders. We group the higher harmonic odd sin components with the drag term as they scale with u_w^2, rather than u_w. The comparison of the shape in time of the odd harmonic Fourier representation and the theoretical Morison-based FCB term is provided in Figure 5.16.

Figure 5.17 shows that the fits of the time drag signals $[u_w\ ,\ u_c]$ and $[u_w\ ,\ 0]$ are very similar, with very similar shifts of shoulders and strength of the harmonics. Removal of the extra linear component, believed to be residual linear Morison inertia and taken to be a sin form leads to a virtually perfect match for with and without current time histories.

We now turn to the even harmonic contribution of the total force, and compare the shape with the theoretical Morison-based FCB formulation. The comparison of the shape in time of the mean (zero) and even harmonic force components (after an increase of A_f by 20%) and the theoretical Morison-based FCB term ($|\cos \omega t|$) is provided in Figure 5.18, each up to the fifth harmonic.

It is clear that the oscillations in 'current' loading are driven by the waves, with the force phase locked to oscillating velocity crests. However, the magnitude scales as u_c^2, so this is a current term. For the zeroth (steady) and second harmonic (and others), we find that the theoretical Morison-based FCB model fits better if the frontal area,

Table 5.4: Fourier representations of elements of the total drag-based hydrodynamic force.

Morison-based wave component (theoretical, both pure wave and wave part of FCB)

$$\cos\omega t|\cos\omega t| = (0.849)\cos(\omega t) + (0.170)\cos 3(\omega t) + (\text{-}0.025)\cos 5(\omega t) + \ldots$$

Odd frequency harmonic components (experimental)

For $[u_w\ ,\ u_c]$

$$\frac{\text{Wave drag}}{\frac{1}{2}\rho C_d A u_w^2} = \begin{pmatrix}0.904\\0.008\end{pmatrix}\cos(\omega t) + \begin{pmatrix}0.106\\0.011\end{pmatrix}\cos 3\left[\omega t + \begin{pmatrix}8.2^\circ\\2.2^\circ\end{pmatrix}\right] + \begin{pmatrix}0.018\\0.001\end{pmatrix}\cos 5\left[\omega t + \begin{pmatrix}-19.7^\circ\\4.1^\circ\end{pmatrix}\right] + \ldots$$

For $[u_w\ ,\ 0]$

$$\frac{\text{Wave drag}}{\frac{1}{2}\rho C_d A u_w^2} = \begin{pmatrix}0.881\\0.016\end{pmatrix}\cos(\omega t) + \begin{pmatrix}0.119\\0.005\end{pmatrix}\cos 3\left[\omega t + \begin{pmatrix}12.5^\circ\\2.1^\circ\end{pmatrix}\right] + \begin{pmatrix}0.023\\0.003\end{pmatrix}\cos 5\left[\omega t + \begin{pmatrix}-16.8^\circ\\1.6^\circ\end{pmatrix}\right] + \ldots$$

Morison-based current component (theoretical FCB)

$$|\cos\omega t| = (0.637) + (0.424)\cos 2(\omega t) + (\text{-}0.085)\cos 4(\omega t) + \ldots$$

Even frequency harmonics for the current component (experimental)

$$\frac{\text{Current drag}}{\frac{\pi}{4}\rho\,(1.2\times A_f)\,u_c^2} = \begin{pmatrix}0.743\\0.055\end{pmatrix} + \begin{pmatrix}0.262\\0.055\end{pmatrix}\cos 2\left[\omega t + \begin{pmatrix}7.4^\circ\\1.7^\circ\end{pmatrix}\right] + \begin{pmatrix}0.124\\0.017\end{pmatrix}\cos 4\left[\omega t + \begin{pmatrix}-30.7^\circ\\4.1^\circ\end{pmatrix}\right] + \ldots$$

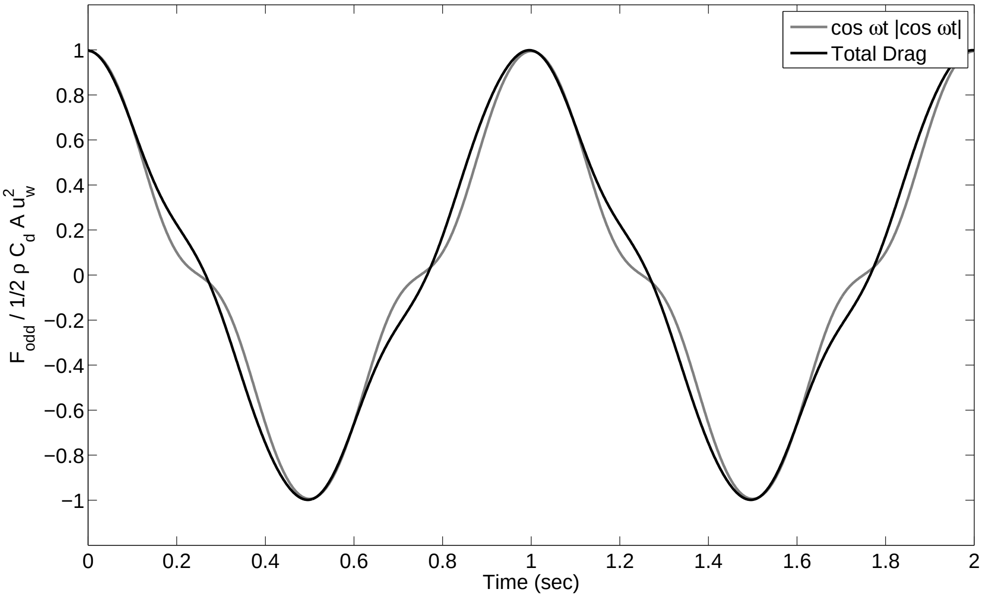

Figure 5.16: Shape comparison of the odd harmonic components of the wave-induced drag in time between the Morison-based FCB term (grey line) and the Fourier representation of the experimental data (black line).

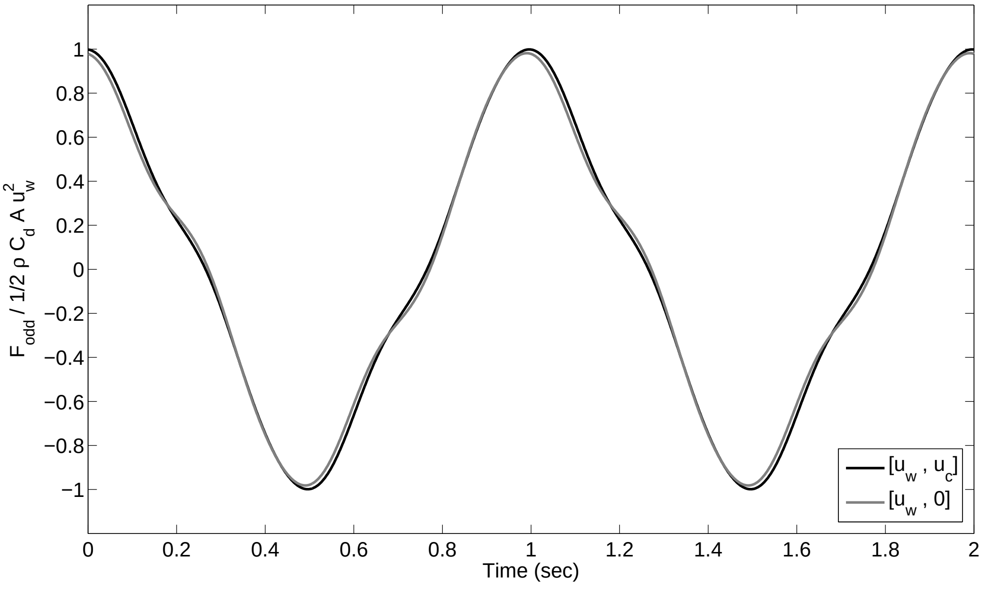

Figure 5.17: Shape comparison of the odd harmonic components of the wave-induced drag in time between $[u_w\ ,\ u_c]$ (black line) and $[u_w\ ,\ 0]$ (grey line).

A_f, is replaced by $1.2 \times A_f$. The cusps in $|\cos \omega t|$ are notably observed in the experimental data though their amplitudes are smaller than those in the theoretical form. Also observed in the data is a higher-frequency oscillating component which occurs as the motion of the grids passes through zero. This is out of phase with the velocity

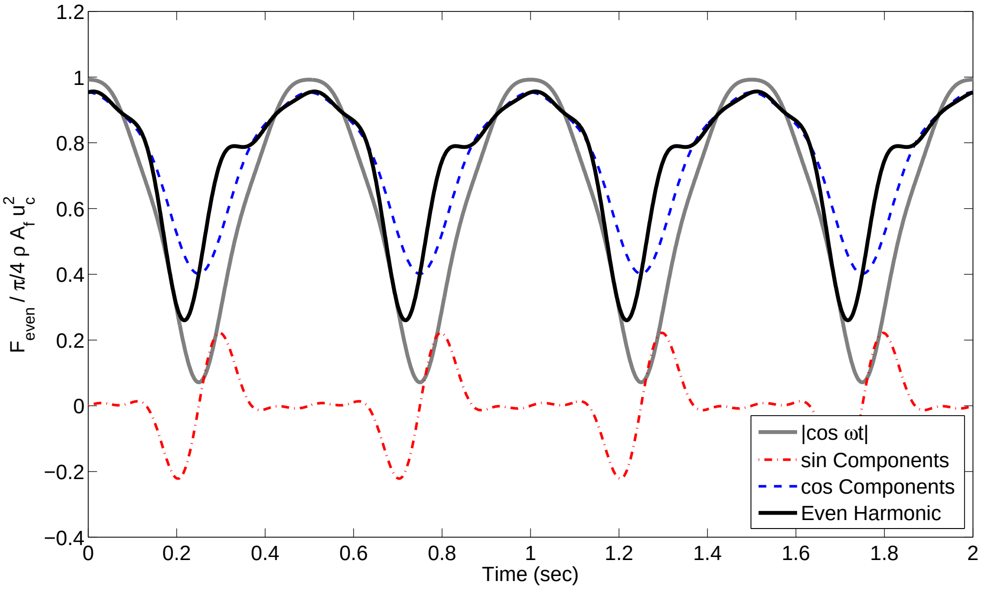

Figure 5.18: Shape comparison of the even harmonic components of the current-induced drag in time between the Morison-based FCB term (solid grey line) and the Fourier representation (solid black line). The cos and sin terms of the total even harmonic contribution are shown by the dashed (blue) line and the dot-dashed (red) line, respectively.

field.

We note that this decomposition method using Fourier representations strongly supports the generic split of total hydrodynamic force into drag and inertia, as well as the idea of an asymptotic split of drag force into separate components driven by the wave kinematics and the current individually, rather than in a complex combination. The observed shapes in terms of Fourier harmonics are close to but do not exactly match those of the Morison-based full current blockage model: there are interesting phase shifts for both odd and even harmonics.

5.5.12 Reconstruction of complete force time history using the Fourier representations

The reconstruction of the complete force time history using the Fourier representations is provided in Figure 5.19. The top part of the figure shows the measured total force in grey and the fitted force using the best Fourier representation in black (using the mean coefficients given in Table 5.4), the bottom part shows the comparison of the theoretical Morison-based residual (rms 20%) and the Fourier-based residual (rms 5%), with respect to the measured total force. It is clear that the agreement between the measured total force and the fitted force is much better using the Fourier representation of the shape of the force time history.

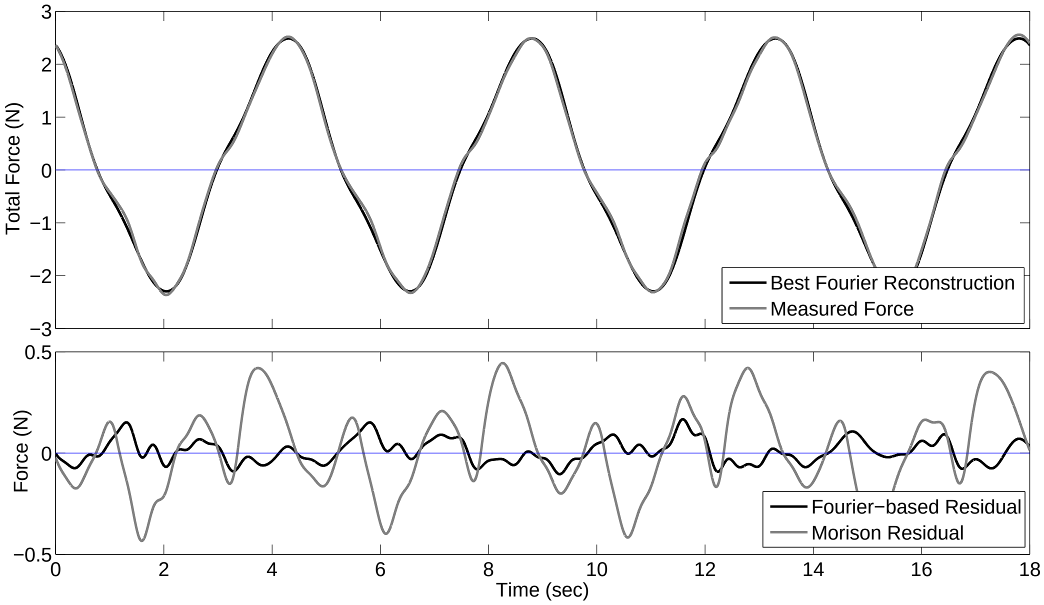

Figure 5.19: Plot of reconstruction of total force time history for $u_w = 16$ cm/s, $u_c = 4$ cm/s, 3 grid, $A/A_f = 0.30$. Top figure shows the measured total force in grey line and the fitted force using the best Fourier representation in black line, bottom figure shows the comparison of the theoretical Morison-based residual (grey line) and the Fourier-based residual (black line), with respect to the measured total force.

5.5.13 Possible applications of the revised force prediction methodology to offshore engineering

Implementation of the proposed force equation of the Morison-based full current blockage model:

$$F(t) = \frac{1}{2}\rho C_d A u_w^2 \cos(\omega t)|\cos(\omega t)| + \frac{\pi}{4}\rho A_f u_c^2 |\cos(\omega t)|$$

or its Fourier-based representation would require a major revision in the design guidelines for offshore platforms, and large changes in the design software used at present, such as USFOS® (www.usfos.no). In contrast, a cruder version with the correct force peaks and troughs:

$$F_{design} \approx \frac{1}{2}\rho C_d A u_w^2 \cos(\omega t)|\cos(\omega t)| + \frac{\pi}{4}\rho A_f u_c^2$$

would be simple - being the addition of the time history for pure waves but no in-line current with a steady mean force arising from a mean flow. The total current loading would be apportioned over the actual structural elements. Whether this would be an adequate representation would depend on the type of structure: statically responding jacket, dynamically responding jacket, compliant tower, etc.

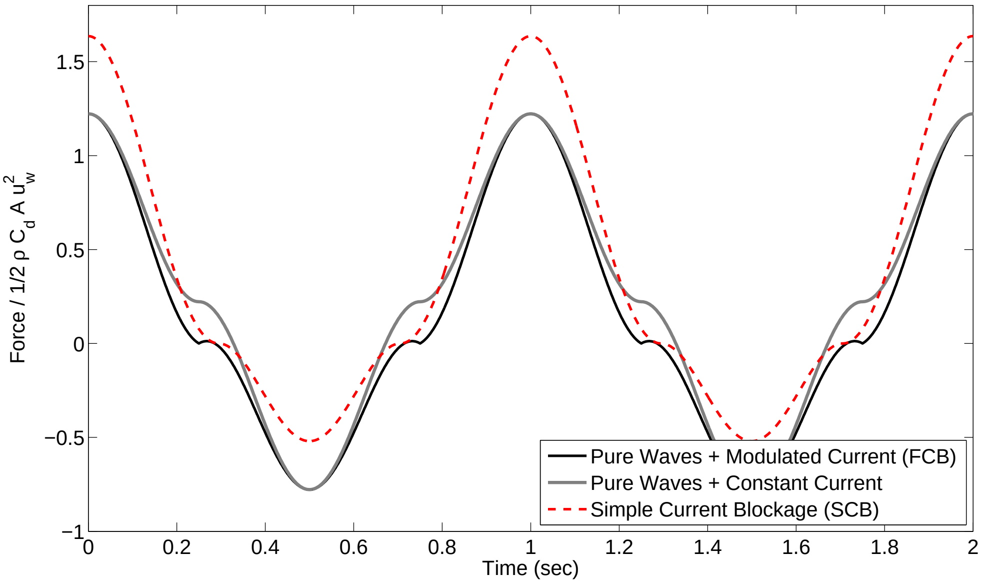

Figure 5.20: Shape comparison of three possible models in time: the full current blockage model (pure waves + modulated current) in black solid line, the F_{design} model (pure waves + constant current) in solid grey line and the simple current blockage model in dashed line.

Figure 5.20 shows the shape comparison of all the possible models: the full current blockage model shown by the solid black line, the F_{design} model by the solid grey line and the simple current blockage model by the dashed (red) line. It can be observed that the F_{design} model does match at drag force crests and troughs of the full model, but the shoulders would be wrong. Whether such an approximation would be sufficiently accurate to be useful in design would depend on the application.

5.6 Chapter summary & conclusions

In this extensive set of experiments, blockage effects have been investigated for 2D planar steady and steady plus regular oscillatory flows on grids of perforated flat plates. Comparisons between the measured forces and the new full current blockage theory have been made to test the validity of the theory.

In steady flow, the measured drag forces exhibit close to asymptotic behaviour as the hydrodynamic loading (C_dA/A_f) is increased. This is consistent with the switching model behaviour assumed by the theory: that for sufficiently high loading the drag force is independent of the structural layout and the details of the hydrodynamic area (C_dA) along the flow direction. This reasonable level of agreement lends support to the fundamental concept of a switching model used in the derivation of the full current blockage theory.

For the analysis of unsteady but periodic drag forces produced by regular oscillations with a steady current, the full current blockage model has been shown to reproduce the measured drag time histories well for all cases. In particular, the asymptotic two-disc model works well, from $u_w > u_c$ (fully blocked) to $u_w = u_c$ (lightly loaded), with a single adjustable parameter C_d. The good agreement also demonstrates the absence of any $u_w \times u_c$ term as would be predicted using the industry-standard form of the Morison equation: the total blockage effect simply removes such a term. The mean force in large-amplitude oscillatory plus steady flow has been demonstrated to depend only on the frontal area, A_f, and not on the hydrodynamic area, $C_d A$, again in direct contrast to the standard Morison expression. For high loading cases, the hypothetical front grid is assumed to take all the current loading and the fluid is forced to diverge out of the frontal area of the grids, hence only the frontal area is important. The standard Morison form is inappropriate in reproducing the drag force - time history.

The proposed method of separating drag and inertia terms from the measured total force has been shown to be simple and robust. The method only requires the information on the undisturbed incoming flow velocity. There is no assumption in the whole decomposition process that the drag term is proportional to a $\cos \omega t \; |\cos \omega t|$ and the inertia term to $\sin \omega t$ according to the standard Morison equation. The inferred inertia term is found to contain a third harmonic (3× frequency) component, which we believe actually arises from asymmetry in the drag term as the fluctuating velocity passed through zero.

With the full current blockage model, the residual C_d variations required to fit a range of experimental cases are relatively small as the number of grids is varied as compared to the standard Morison equation. The reconstructed total force based on the full model has been demonstrated to resemble closely the measured total force, with small differences due to the third harmonic effect, consistent with the observed weak shoulders as the measured force crosses zero.

As well as a simple decomposition of force components symmetric and skew in time about the velocity peaks and troughs, a full Fourier representation of the forces is presented. With up to the fifth harmonic of the oscillating motion included, we demonstrate that the wave-induced force component is unaltered by the addition of a current to the oscillation, and that the shoulders of the time history are slightly skew and much weaker than the Morison form. The other contribution to the drag force scales with the square of the current and the experiments confirm that this is a rectified signal close to in phase with the motion crests, and containing harmonics similar to but less pronounced than the theoretical $|\cos \omega t|$.

There are two main contributions of this chapter. Firstly, the previously published theoretical model (Taylor et al., 2013) is extended to predict the complete time history of the drag force on an obstacle array with very high fluid loading in oscillations and mean flow. This result for the total force over the oscillation cycle is entirely new. Secondly, we present detailed comparisons over the complete oscillation cycle between this new theoretical model and extensive laboratory experiments on moving grids.

The model also predicts the total force time histories well, including the peak drag crest and trough values and the time-averaged drag, after calibration of the Morison coefficients C_d and C_m. Neither the original Morison form (with no account made for blockage) nor the simple blockage model in the API design guidelines (where only the steady current is reduced by blockage) can reproduce realistic (drag) force time histories, so the present practice should be regarded as seriously inadequate for combined waves and steady current acting on obstacle arrays.

Overall, we conclude that this systematic and wide ranging series of tests on the unsteady drag forces arising on obstacle arrays in combined steady and sinusoidal approach flows provides strong support for the full wave–current–structure interaction blockage model.

This chapter has been published in the Journal of Fluid Mechanics as Santo et al. (2014b).

Chapter 6

Current blockage in a numerical wave tank: Three-dimensional simulations of regular waves and current through a porous tower

6.1 Introduction

This chapter further investigates the effect of current blockage on a typical space-frame offshore structure by simulating three-dimensional regular wave flow through a porous tower in a numerical wave tank via CFD simulations. In this way, more realistic water particle kinematics could be included, and the integrated effect of current blockage through the water column could be analysed. The aim is to test the modelled global forces on space-frame structures by reproduction of Allender and Petrauskas experimental results (Allender and Petrauskas, 1987). With the extra loading contribution from the waves superimposed on top of the steady current flow over a structure, extra resistance thus extra blockage is expected. Allender and Petrauskas observed significant flow blockage occurred in their tests, which they reported "requiring the use of a lower C_d of 0.7 to 0.8 for waves plus current from a C_d of 1.3 to 1.6 for waves alone to fit the peak forces of the standard Morison theory with the measured results" (Allender and Petrauskas, 1987). Unfortunately, they did not publish any plots of force time histories for the experimental model, only the *peak* values.

This chapter will attempt to reproduce their reported peak forces with a single and consistent set of Morison coefficient $C_d = 0.9$ for drag and $C_m = 2.0$ for inertia for regular waves with and without current over a wide range of wave heights and current speeds. We also provide additional information on the force time histories and the visualisation of the flows. Direct comparisons between the numerical simulation and the measured peak forces will be made, as well as between the numerical simulation and the FCB model presented previously in Chapter 3 and by Taylor et al. (2013) for peak force. We will demonstrate that good agreement can be achieved between the numerical simulations and the measured data.

One novel part of this chapter is the demonstration of the use of a quadratic resistance porous tower (or block) as a simple model for the complex geometry of a real space-frame offshore structure, where the drag resistance and the inertia contribution could be calibrated and modelled. Even though the local flow structures are not modelled at the scale of the individual structural elements within a jacket-type platform, the global flow behaviour is reasonably well represented. This technique could potentially be incorporated into a standard offshore design practice to investigate current blockage effects.

Real world applications have very high Reynolds number; none of the laboratory scale experimental studies can match that important non-dimensional parameter. The Reynolds number effects can only be investigated from full-scale field measurement, which can then be compared with numerical simulation. The issue of what C_d to choose is perhaps more relevant, which needs to account for the effects of surface roughness and marine growth, and fully submerged drag area vs. area fluctuations in the wave trough/crest zone. We believe that the complications mentioned above warrant further investigation. Here, a single value of $C_d = 0.9$ is applied uniformly over a porous tower across the water depth as a first approximation to constitute a basis for reference.

6.2 Numerical methods

In this section, we first present the numerical methods necessary to simulate ranges of three-dimensional regular wave flow through a porous tower in a numerical wave tank.

6.2.1 Governing equations

The governing equations for the two-phase combined flow of water and air are the Reynolds-averaged Navier–Stokes equations coupled with the continuity equation for incompressible flows, with an additional momentum sink term to account for the effect of the porous tower in the numerical simulation:

$$\nabla \cdot \mathbf{u} = 0 \tag{6.1}$$

$$\begin{aligned}\frac{\partial \rho \mathbf{u}}{\partial t} + \nabla \cdot [\rho \mathbf{u}\mathbf{u}^T] = & - \nabla p^* + \nabla \cdot [\mu \nabla \mathbf{u} + \rho \boldsymbol{\tau}] - \mathbf{S} \\ & + [-(\mathbf{g} \cdot \mathbf{x}) \nabla \rho + \sigma_T \kappa_\gamma \nabla \gamma]\end{aligned} \tag{6.2}$$

where ρ is the fluid density, $\mathbf{g}$ is the acceleration due to gravity, $\mathbf{u} = (u, v, w)$ is the fluid velocity field in Cartesian coordinates, p^* is the pressure in excess of hydrostatic pressure, μ is the dynamic viscosity, $\mathbf{x} = (x, y, z)$ is the local Cartesian coordinates, and $\boldsymbol{\tau}$ is the specific Reynolds stress tensor.

Here, momentum lost from the flow is accounted for via a sink term, which is proportional to a nonlinear drag loss term (a Morison-type quadratic resistance with the $\mathbf{u}|\mathbf{u}|$ form, so that the flow can be in any direction) and a bulk inertia term which models the local Morison inertia contribution due to potential flow-type distortions over scales of the order of the width of the individual cylinders in a real space-frame offshore structure. Hence, in the case of a simple homogeneous porous tower:

$$\mathbf{S} = \frac{1}{2} \rho F \mathbf{u}|\mathbf{u}| + C'_m \frac{\partial \rho \mathbf{u}}{\partial t} \tag{6.3}$$

where F is the Forchheimer resistance parameter and C'_m is the equivalent of the standard Morison inertia coefficient, C_m, but here defined in the porous tower context. The nonlinear drag loss term is treated explicitly as an additional sink term in the momentum equation, while the bulk inertia term is grouped together with the unsteady term and solved implicitly in time.

Both F and C'_m can be calibrated by matching $\int \mathbf{S} \; dV_P$ with the vector form of the Morison force equation:

$$F(t) = \frac{1}{2} \rho C_d A \mathbf{u}|\mathbf{u}| + C_m V \frac{\partial \rho \mathbf{u}}{\partial t} \tag{6.4}$$

where C_d is the Morison drag coefficient, A is the solid drag area of the components comprising space-frame offshore structure (jacket or compliant tower), V is the volume of the structural components within the structure, and $V_P = A_f \times L$ is the volume of the modelled porous tower, where A_f is the frontal area of the structure represented in the porous tower and L is the width of the porous tower in downstream direction.

Thus, F can be calibrated by matching $C_d A / A_f = FL$, where $C_d A / A_f$ is termed the hydrodynamic loading in the actuator disc theory (Taylor et al., 2013). Note that the theoretical model is concentrated in a disc, while the numerical porous model is distributed over a volume. See Chapter 3 and Taylor et al. (2013) for the details of the actuator disc theory and Chapter 4 and Santo et al. (2013a) for the F parameter calibration. C'_m can be calibrated by equating $C'_m V_P = C_m V$, giving $C'_m << C_m$ as $V_P >> V$. In this porous tower approximation, the total volume of an actual structure is distributed across a number of cells while maintaining the same cross-sectional area and height, forming a three-dimensional porous block, or a porous tower.

The last two terms in Equation 6.2 in square brackets are for numerical convenience for volume of fluid (VOF) method, and only active in the region where cell is partially filled with air, elsewhere these terms are zero. The $\sigma_T \kappa_\gamma \nabla\gamma$ term describes the surface tension effect using the CSF (Continuum Surface Force) model of Brackbill et al. (1992), where σ_T is the surface tension coefficient, and κ_γ is the surface curvature. γ is a scalar field used to represent the fraction of a cell volume filled with water, with $0 \leq \gamma \leq 1$; 0 for air, and 1 for water.

The equations are solved simultaneously for the two immiscible fluids together with the transport equation used to track the fluids. The transport equation is similar to the volume of fluid (VOF) method of Hirt and Nichols (1981), but with an additional compression technique to limit the numerical diffusion of the interface profile. The compression technique is developed by OpenCFD®, and the documentation can be found in Berberović et al. (2009).

The unsteady, incompressible and three-dimensional two-phase flow equations of motion are solved with the finite volume method (Ferziger and Perić, 2002) using the open-source code OpenFOAM® (http://www.openfoam.com). This study uses the numerical wave tank developed and released by Jacobsen et al. (2012). The momentum–pressure coupling is solved with the PISO (Pressure-implicit Split-Operator) iterative algorithm (Issa, 1986).

This study uses an LES (Large Eddy Simulation) k-equation eddy-viscosity turbulence model. The one-equation eddy viscosity subgrid scale (SGS) model for incompressible flows using a modelled balance equation to simulate the behaviour of k is based on Fureby et al. (1997), but with modification to the dimensionless model coefficients. The dimensionless model coefficients are given the default OpenFOAM® values $c_k = 0.094$ and $c_\epsilon = 1.048$.

The drag and inertia force in the porous tower is obtained by integration over the volume of the tower (a post-processing technique), with a cutoff γ value of 0.5 and greater to be treated as the water phase. The drag contribution in the mean flow direction is summed up by taking all three velocity flow components for the modulus term at each wetted cell, according to a full (three-dimensional) Morison force formulation: $1/2\rho A_f F L u_x \sqrt{(u_x^2 + u_y^2 + u_z^2)}$, and the inertia contribution by $\rho C'_m V_P \partial u_x/\partial t$, both over the tower volume. u_x and u_y are the longitudinal and lateral velocity components, respectively, in a horizontal plane, and u_z is the vertical velocity component, according to the computational domain layout described in Section 6.2.2.

6.2.2 Computational domain layout

The simulation case is set up to replicate as closely as possible the experimental wave tests conducted by Allender and Petrauskas (1987) in OTRC, Escondido, California. They conducted a series of experiments in which they measured the total fluid loading on a 1:47 scaled model of a Gulf of Mexico jacket structure exposed to regular waves of various sizes with no current, then with the same set of waves with two values of in-line current. Figure 6.1 shows the layout of their scaled jacket model. The taper on the structure is exaggerated by refraction at the water surface in the original photo.

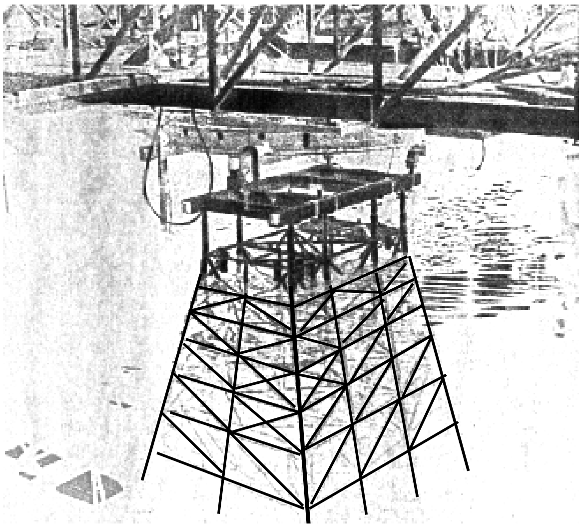

Figure 6.1: Layout of the scaled jacket model (adapted from Allender and Petrauskas (1987) Figure 1).

Figure 6.2 shows the layout of the three-dimensional numerical wave tank with a porous tower. The length of the domain is set at 2000 m at full-scale or $\sim 7.1\lambda$, where λ is the wavelength taken to be about 280 m, the maximum wavelength to be simulated in Section 6.4, with regular waves of 12.8 sec period and 25 m wave height in 135 m water depth. The tower is placed at 500 m downstream from the inlet. Two relaxation zones are created: one at the inlet for wave generation ($\sim 1\lambda$) and the other at the outlet for wave absorption ($\sim 2\lambda$). Hence, the central zone of most interest is of length $\sim 4\lambda$. From the inlet to the middle of the tank ($\sim 3\lambda$), a uniform mesh distribution is used. Mesh coarsening is introduced gradually from there in the downstream direction to reduce computational effort. Also shown are the boundary conditions associated with each patch of the wave tank. The x coordinate runs horizontally in the direction of wave propagation, the y coordinate

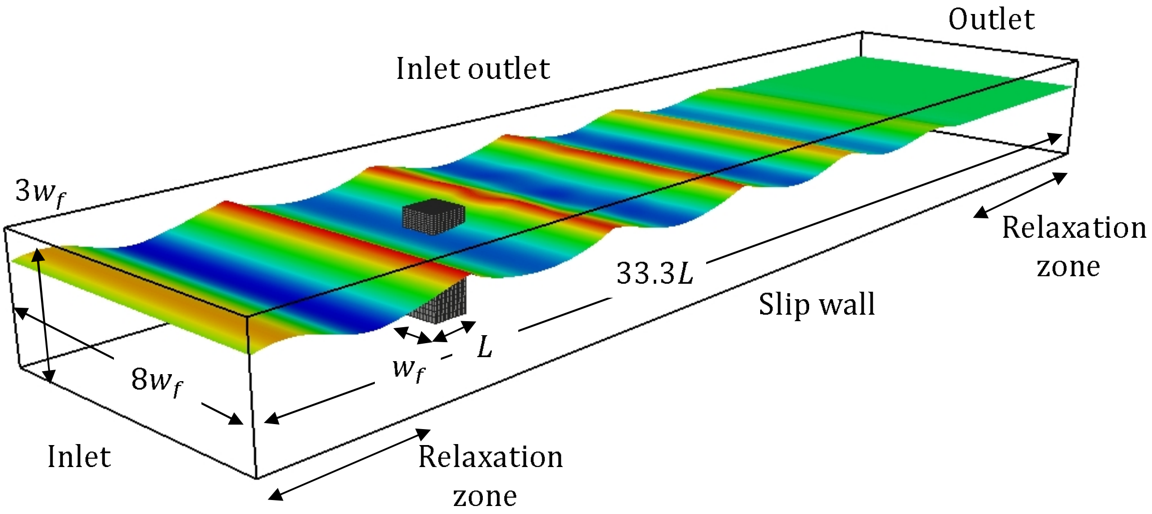

Figure 6.2: Layout of the computational domain. The location of a porous tower is indicated as a black rectangular block. A regular wave is shown propagating from the inlet to the outlet. Red colour represents wave crests, blue colour represents wave troughs, and green colour represents water surface close to mean sea level. Also shown is the key physical dimensions and the boundary conditions of the tank.

runs horizontally in the orthogonal direction of wave propagation (or laterally) and the z coordinate runs vertically (+ve upwards).

The wave elevation profile is coloured in such a way that red colour represents wave crests, blue colour represents wave troughs and green colour represents water surface close to mean sea level. It is apparent from the figure that there is a decay of the simulated regular wave height in space in the downstream direction towards the outlet due to numerical diffusion. Thus it is important to position the porous tower nearer to the inlet and to specify the wave amplitude at the model structure.

The detailed dimensions of the wave tank and the porous tower are provided in Table 6.1. The key dimensions of the numerical wave tank are modelled at full-scale according to the actual depth of the full-size jacket corresponding to the Allender and Petrauskas model. The porous tower is modelled as square in cross-section in this case – symmetric in broadside and end-on, with no taper. Hence, it differs from the actual Allender and Petrauskas model which had a (plan) aspect ratio of $\sim$ 2:1 and typical taper when viewed from end-on. Unfortunately, there is no geometric information reported in Allender and Petrauskas (1987) other than the water depth, so a 60 m × 60 m plan cross-section is simply used to represent the structure. Our aim is to examine the loads from waves and waves with various in-line currents in the light of their experimental results.

Table 6.1: Physical dimension of the wave tank and the porous tower.

Parameter		Value
Tank:	Length	2000 m
	Width	480 m
	Height	185 m
Tower:	Length (L)	60 m
	Width (w_f)	60 m
	Height	155 m
Relaxation Zone:	Inlet Length	300 m
Relaxation Zone:	Outlet Length	600 m
Mean sea level:	Water depth (h)	135 m

6.2.3 Boundary and initial conditions

For regular waves, waves are generated at the inlet and absorbed at the outlet, both by a relaxation technique implemented in relaxation zones (Jacobsen et al., 2012). The waves are generated according to the specified wave theory, which updates the corresponding velocity ($\mathbf{u}$), surface elevation and pressure (p) initial and boundary conditions at the inlet. Linear wave theory (Airy wave) is fed into the inlet, and the generated waves remain 1st order as imposed by (and along) the relaxation zone at the inlet. Once the waves propagate out of the relaxation zone into the main domain of interest, the waves become non linear (well modelled using Stokes 3rd order theory) after solving for the complete Navier–Stokes equations. Likewise for pure current, a steady fixed uniform current velocity is applied at the inlet, and the same magnitude of velocity is applied at the outlet to ensure mass continuity, and both are specified by theory and imposed in the relaxation zones.

A slip boundary condition is applied at the bottom and the two side walls. An atmospheric boundary condition is introduced at the top boundary, in which water and air are allowed to flow out but only air is allowed to flow in. As suggested by Jacobsen et al. (2012), the top lid of the domain has to be an adequate distance from the water crest level to avoid loss of water during the simulation. In this simulation, a clearance of 50 m from the mean sea level to the top lid of the domain is provided, and this is adequate because the largest scaled wave height tested by Allender and Petrauskas (1987) is about 25 m. For pressure, p, a total pressure boundary condition is imposed at the top boundary.

The boundary and initial conditions for turbulent kinetic energy, k, is specified as $\partial k/\partial n = 0$ at both inlet and outlet, and on the slip planes at the bottom and side walls. At the top boundary, an inlet-outlet boundary condition is applied, which acts as an inlet if the velocity vector points into the domain and as an outlet if the velocity vector points out of the domain. The initial value of k is taken to be a fixed uniform $3.75 \times 10^{-3}\mathrm{m}^2/\mathrm{s}^2$ assuming an initial turbulence intensity of 5% and root-mean-square velocity of 1 m/s. We note that this is quite large relative to the current, but of course not compared to the surface wave kinematics.

Calibration of the Forchheimer resistance parameter, F, is made by equating $C_d A/A_f = FL$, with $A = 7871.7$ m^2, $A_f = 8115.2$ m^2 and hence $C_d A/A_f = 0.9 \times 0.97 = 0.873$ for the full-size jacket corresponding to the Allender and Petrauskas model. Thus, with $L = 60$ m, F parameter for the modelled porous tower is 0.01455 m^{-1}, assuming isotropy in all x, y and z flow directions for the Morison drag term. We base this estimate of the hydrodynamic area on the constant current, no wave cases were reported by Allender and Petrauskas (1987). It is noted that the C_d value of 1.0 previously used in the 1D analytical stick model in Chapter 3 and Taylor et al. (2013) was obtained by assigning the areas and the volume of the stick model (A, A_f and V) up the peak wave crest level, while the correct distribution should be up to the still water line, since the areas and the volume of the stick model were inferred from their steady towing tests with no wave. The suitable C_d value after minor correction to the stick model is 0.9.

The local Morison inertia coefficient for porous tower, C'_m, is calibrated by equating $C'_m = C_m V/V_P$. The C_m coefficient used in the one-dimensional analytical stick model to reproduce the experimental results in Taylor et al. (2013) is the potential flow-based value of 2.0 for cylinders. The inferred total volume of the full-size jacket model up to the still water line (V) is 6170.87 m^3, and the wetted volume of the porous tower up to the still water line (V_P) is 60 m × 60 m × 135 m = 4.86×10^5 m^3. Thus, the C'_m coefficient is 0.0254, with the assumption that the porous tower is to be built entirely of 1 m diameter cylinders arranged within the tower evenly and isotropically to give a total length of this equivalent pipe of 7871.7 m. For a 1970s type Gulf of Mexico space-frame structure such as that tested by Allender and Petrauskas, the choice of an average member diameter of 1 m is reasonable.

The calibration of F and C'_m parameters assumes that the density of the drag (area) and inertia (volume) effects are uniformly distributed over the porous tower and that there is no change in properties above mean sea level (as there typically would be in a real design of a space-frame offshore structure, where the amount of metal exposed to the most severe wave crests is reduced). Both $F = 0.01455$ m^{-1}

and $C'_m = 0.0254$ are used throughout the simulations, which correspond to standard Morison values of $C_d = 0.9$ and $C_m = 2.0$.

6.3 Numerical study

In this section, various numerical studies are conducted to ensure that the numerical wave tank with the free-surface capturing VOF technique and the relaxation zone technique works adequately.

6.3.1 Length of the tank domain

The optimal length of the numerical wave tank domain is investigated next in order to minimise interference due to any potential reflections from the inlet and also from the downstream outlet. The total wavelength ($N\lambda$) is used to describe the length of the domain as it directly relates to the number of waves propagating along the tank at an instant. Three different lengths of tank are considered: 1000 m ($\sim 3.5\lambda$), 2000 m ($\sim 7.1\lambda$) and 3000 m ($\sim 10.7\lambda$), where λ is about 280 m, the maximum wavelength to be simulated in Section 6.4 which is for 25 m regular waves with 12.8 sec period in 135 m water depth. Table 6.2 outlines the distribution of the zone of interest, the inlet and the outlet relaxation zones for each tank. Two variations of the length of the outlet relaxation zone are considered for the 7.1λ length of tank.

Table 6.2: The distribution of the zone of interest, inlet and outlet relaxation zones for three different lengths of tank.

Length of tank (λ)	Length of (λ) Inlet relaxation zone	Zone of interest	Outlet relaxation zone
3.5	1	1	1
7.1	1	5	1
7.1	1	4	2
10.7	1	8	1

All simulations are run on mesh with resolution 2 m horizontal size × 2 m vertical size at free-surface zone to capture the wave fluctuations effectively (termed Mesh 2 in Section 6.3.2), with subsequent mesh coarsening introduced from the middle of the tank towards the outlet to reduce the computational requirements. A regular wave of height 15 m with 12.8 sec period in 135 m water depth is simulated for all cases, and the comparison is made based on the depth-averaged wave horizontal

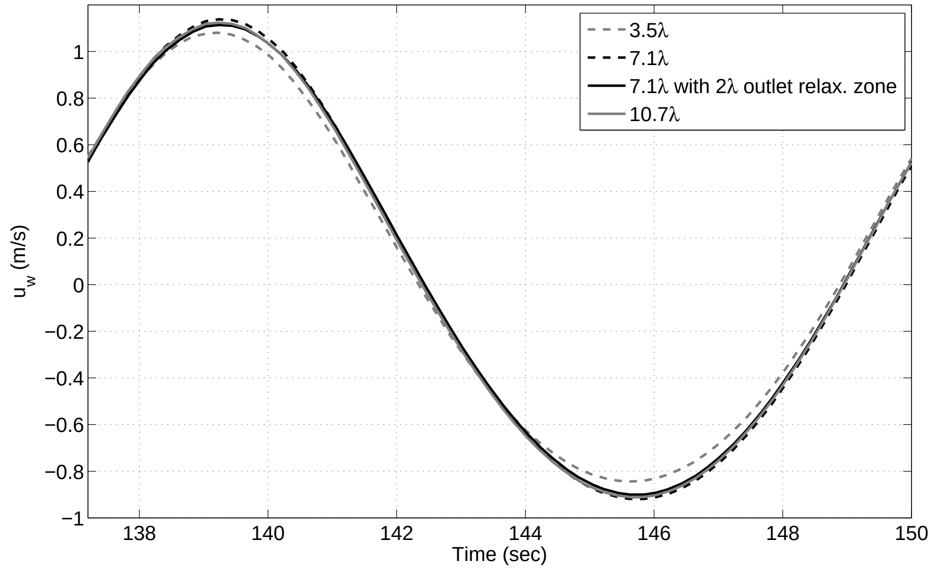

Figure 6.3: Comparison of different lengths of the tank domain for 15 m regular waves with 12.8 sec period in 135 m water depth in terms of depth-averaged wave horizontal velocity time history over a tower volume. The result for 1000 m ($\sim 3.5\lambda$) long domain is shown as dashed grey line, the 2000 m ($\sim 7.1\lambda$) long domain with 1λ length of the outlet relaxation zone as dashed black line, the same 2000 m long domain but with 2λ length of the outlet relaxation zone as solid black line, and the 3000 m ($\sim 10.7\lambda$) long domain as solid grey line.

velocity time history over the tower volume, without the presence of the porous tower. This is shown in Figure 6.3. The 3.5λ long domain (dashed grey line) suffers from a reflection effect from the outlet: it is different from the rest of the domains. The simulated wave velocity time histories for the two types of 7.1λ long domains (dashed and solid black lines) and the 10.7λ long domain (solid grey line) are very close to each other, but better agreement with the 10.7λ long domain can be obtained for the 7.1λ long domain with 2λ length of the outlet relaxation zone.

In this study, a 7.1λ long wave tank with 2λ length of outlet relaxation zone is used throughout. The lateral width is kept at eight times the frontal width of the tower ($8 \times w_f$), following the previous fully unsteady planar oscillation plus mean flow simulations in Section 4.5.2.1 and Santo et al. (2013a). Having determined the optimal length of the domain, the next stage is to check that the results are properly resolved, that is they are independent of the mesh size used.

6.3.2 Grid independence

The grid independence study investigates the influence of the number of cells of a computational domain to simulate free-surface fluctuations. The aim is to achieve a

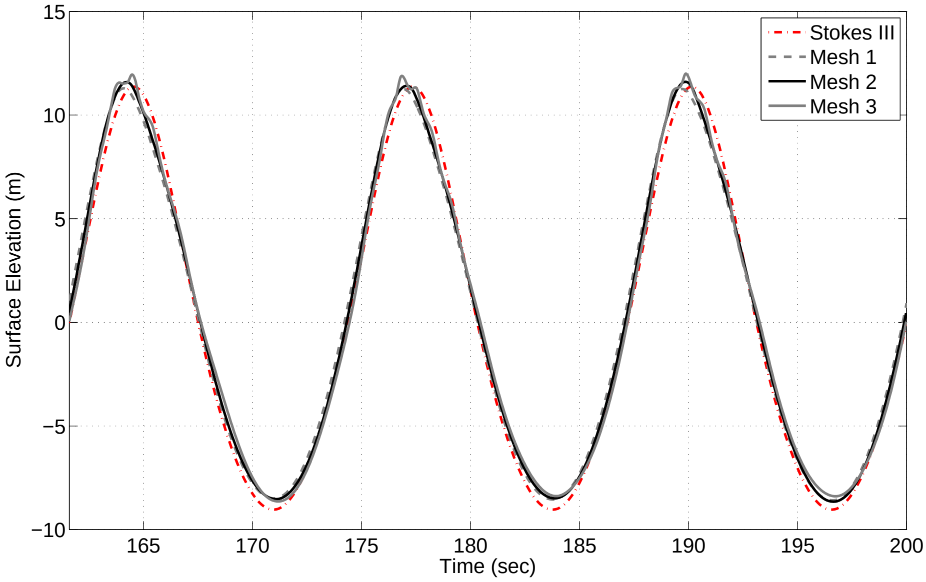

Figure 6.4: Grid independence study in terms of the surface elevation-time history for regular waves of 20 m height with period of 12.8 sec in 135 m water depth. The result of the theoretical 3rd order Stokes wave is plotted as dot-dashed (red) line, the result of Mesh 1 as dashed grey line, the result of Mesh 2 as solid black line, and the result of Mesh 3 as solid grey line.

grid independent solution which does not vary significantly when one alters the number of cells and also agrees well with the theoretical wave formulation. Comparable wave kinematics such as water particle velocity and dynamic pressure can then be obtained between the theory and the numerical simulation.

Figure 6.4 shows the grid independence study of three different mesh sizes in terms of surface elevation in time, benchmarked with the theoretical 3rd order Stokes wave (dot-dashed (red) line). The three mesh sizes are Mesh 1 (dashed grey line) of about 740,000 cells with minimum 3 m × 3 m mesh resolution at the free-surface zone to capture the wave fluctuation horizontally and vertically, Mesh 2 (solid black line) of about 2.6 million cells with 2 m × 2 m resolution, and Mesh 3 (solid grey line) of about 20 million cells with 1 m × 1 m resolution. For all mesh sizes, mesh coarsening in the horizontal direction has to be introduced gradually from the middle of the tank towards outlet to minimise excessive computational effort required, especially for Mesh 3.

Regular waves of 20 m height with period of 12.8 seconds in 135 m water depth are generated at the inlet, and the surface elevation is probed at the tower location. It is apparent that the surface elevation profile of Mesh 2 is closer to that of Mesh 3, as compared to from Mesh 1 to Mesh 2. Due to numerical diffusion, perfect agreement

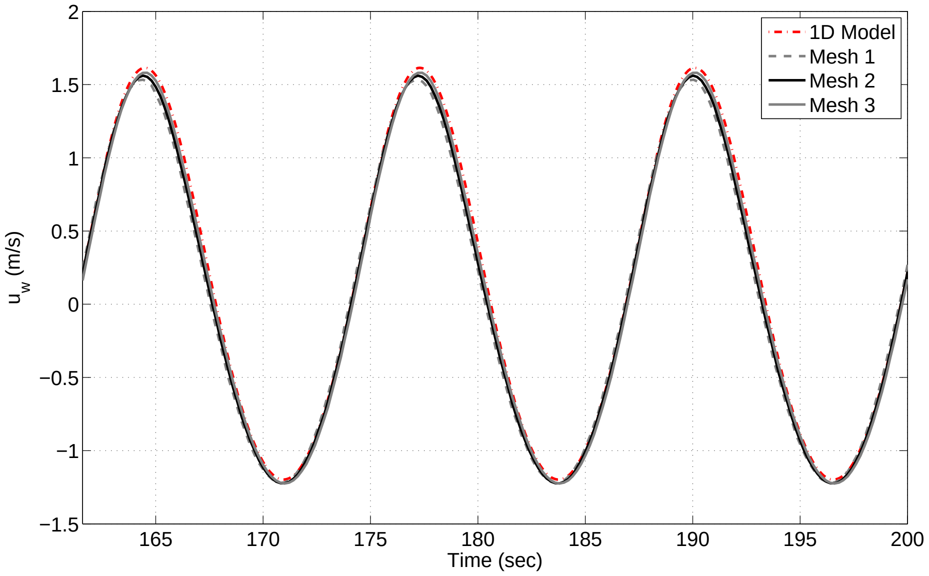

Figure 6.5: Grid independence study in terms of depth-averaged velocity u_w time history for regular waves of 20 m height with period of 12.8 sec in 135 m water depth. The result of the theoretical 3rd order Stokes wave kinematics is plotted as dot-dashed (red) line, the result of Mesh 1 as dashed grey line, the result of Mesh 2 as solid black line, and the result of Mesh 3 as solid grey line.

between the simulated surface elevation and the theoretical 3rd order Stokes wave cannot be achieved.

Figure 6.5 shows a similar study but now in terms of the velocity (u_w) time history. The velocity time history is depth-averaged over the tower volume at the tower location, without the presence of the porous tower, i.e. the drag and inertia coefficients (F and C'_m) are set to zero to yield an undisturbed wave field. This depth-resolved velocity will be substituted into the porous tower force model and then volume integrated to obtain the simulated Morison drag and inertia type of result for comparison. The same three mesh sizes are compared: Mesh 1 (dashed black line), Mesh 2 (solid black line) and Mesh 3 (solid grey line). Also, the one-dimensional model based on 3rd order Stokes wave kinematics is provided as a benchmark (dot-dashed (red) line). The theoretical model takes into account the horizontal and vertical profile of the wave velocity kinematics over the tower volume. Similar to Figure 6.5, Figure 6.6 shows the depth-integrated velocity in terms of velocity term $u_w|u_w|$ time history, which is directly proportional to the undisturbed drag force contribution on the tower.

From both Figures 6.5 and 6.6, it is apparent that the velocity time history of Mesh 2 is closer to that of Mesh 3, as compared to from Mesh 1 to Mesh 2. Here, the grid convergence is more satisfactorily demonstrated for Meshes 2 and 3, which agree

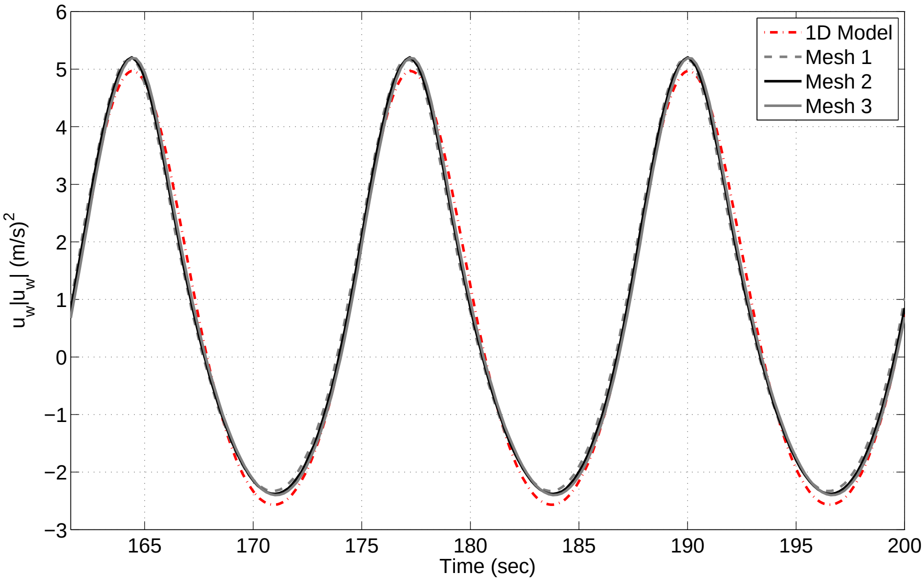

Figure 6.6: Grid independence study in terms of velocity term $u_w|u_w|$ time history for regular waves of 20 m height with period of 12.8 sec in 135 m water depth. The result of the theoretical 3rd order Stokes wave kinematics is plotted as dot-dashed (red) line, the result of Mesh 1 as dashed grey line, the result of Mesh 2 as solid black line, and the result of Mesh 3 as solid grey line.

with the Stokes kinematics better than Mesh 1. The slight discrepancy in the peaks of the $u_w|u_w|$ time history in Figure 6.6 between the numerical and the theoretical results is probably due to the treatment of the wave kinematics above mean sea level, where the theoretical model uses a vertical extrapolation approximation.

Mesh 2 is used in the subsequent simulations, but now with uniform mesh distribution in the dominant flow direction (x-axis) to minimise numerical diffusion which arises due to the mesh coarsening along the main flow direction and has an effect of reducing the flow velocity in steady current flow simulation. As a result, the mesh size is increased from 2.6 million to 5.3 million cells. The aspect ratio (defined as $\Delta x/\Delta z$) of the numerical cell in the region around mean sea level which contains most of the wave action is kept at 1.0, and the resolution of both Δx and Δz in that region is 2 m. The resolution of Δy is kept at 4 m in the lateral direction along the tower frontal area (A_f), and mesh coarsening is introduced gradually away from the frontal area towards the two side boundaries.

It is worth stressing that given the mesh resolution of 2 m by 2 m at the wave action zone, the simulation is running in unresolved LES or perhaps in the RANS model by transporting the averaged turbulent kinetic energy (the energy containing large eddies are not captured in the inertial range). However, in this free-surface flow over porous tower simulation, no violent flow perturbations are observed, so we hope that there is no requirement to resolve fine-scale flow structures.

6.3.3 The use of the Morison form

Here, a comparison between a two-dimensional Morison drag form and a full three-dimensional form is investigated. The Morison drag resistance is integrated over the volume of the porous tower to obtain the total drag force contribution on the tower exposed to combination of waves and current.

The original implementation of the porous resistance is based on the full Morison drag form, i.e. $\mathbf{u}|\mathbf{u}|$ (see Equation 6.3), which is the general form where the reduced three-dimensional flow is free to diverge in three directions, and the obstacles (or cylinders) are distributed horizontally, vertically and diagonally also in three directions, so the porous tower is not just a representation of a single stick model. The drag force in the direction of wave propagation is obtained by integrating $1/2\rho A_f F L$ $u_x\sqrt{u_x^2+u_y^2+u_z^2}$ over the tower volume.

The two-dimensional Morison drag form, however, assumes that the obstacles all run vertically, and that the cross-flow principle holds: that the axial (or vertical) flow components have negligible effect, as described by Garrison (1985). For comparison, the original resistance implementation is modified to $(u_x, u_y, 0)\sqrt{u_x^2+u_y^2}$, where the modulus term of the resistance is now acting based on cross-flow or planar flow (horizontal longitudinal and lateral flow only). The two-dimensional Morison drag force is subsequently obtained by integrating $1/2\rho A_f F L$ $u_x\sqrt{u_x^2+u_y^2}$ over the tower volume.

Figure 6.7 shows the comparison of the two different Morison force formulations for a porous tower in 15 m height of regular waves with 12.8 sec period in 135 m water depth. It can be observed that because of the additional vertical velocity flow component in the full Morison drag formulation, the tower experiences slightly larger drag forces in terms of the force peaks and troughs, as compared to the two-dimensional Morison drag formulation. Also, because of the same reason, the Morison 'shoulder' is observed to be less distinct in the full Morison drag form than the two-dimensional form. This slight discrepancy is reasonable, as the axial (vertical) flow component within the tower is expected to be less important than the cross-flow velocity components. The full Morison isotropic drag formulation is used throughout the subsequent simulations.

The maximum simulation time is about 520,000 sec (144 hours or 6 days), which is for the largest wave height (25 m) case. All simulations are run in parallel mode

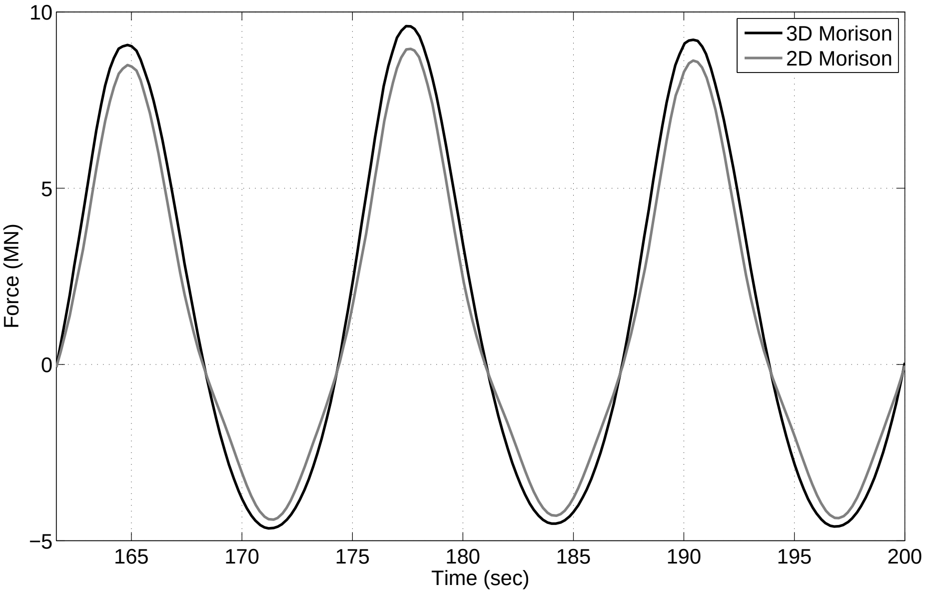

Figure 6.7: Comparison between two-dimensional (solid grey line) and three-dimensional (solid black line) Morison drag formulation for 15 m regular waves in terms of drag force time history on a porous tower.

on 8 processors at the High Performance Computing (HPC) facilities of the National University of Singapore.

6.4 Simulations of regular waves

In this section, simulation results for regular waves with and without current are presented and compared with the experimental peak forces measured by Allender and Petrauskas. Previously in Chapter 3 and Taylor et al. (2013), the hydrodynamic properties of the scaled jacket such as drag area (A), frontal area (A_f), volume (V), and drag and inertia coefficients (C_d and C_m) were inferred from the experiments. These inferred properties are then used to calibrate the properties of the porous tower in this numerical simulations. We will demonstrate that a single value of $C_d = 0.9$ and $C_m = 2.0$ can be used consistently to reproduce the measured peak forces for regular waves with and without current over a wide range of wave heights and current speeds, as well as to provide the additional complete force time histories and the flow visualisation. We will also demonstrate that good agreement can be achieved between the numerical simulations and the measured data.

The force over the tower volume obtained by integrating the undisturbed wave field is denoted as F_{und}, i.e. when the porous tower is absent. This is equivalent to a standard Morison formulation, where the presence of the structure is assumed not to modify the undisturbed wave kinematics. On the other hand, the same Morison integral over the tower volume with the resistance switched on, i.e. using the disturbed kinematics within the flow, is denoted as F_{dist}, i.e. when the porous tower is present.

6.4.1 Steady current flow

Here, a steady uniform current through a porous tower is simulated and compared in terms of the probed velocity profile (u_c) between the numerical simulation and the simple current blockage model (SCB). The steady flow case serves as the first comparative test as it has uniform velocity across water depth and involves little free-surface fluctuation, hence the comparison between the two different flow representations is clear and straightforward. It is important to obtain good agreement in this steady flow case to justify the compatibility of the two flow representations (one by the actuator disc theory, the other by numerical approximation of the Navier–Stokes equations), in that they can be calibrated in terms of the hydrodynamic loading, $C_d A/A_f$ and the quadratic porous resistance, FL.

For steady flow case, the SCB model is used. The blocked current, u_s, can be expressed in terms of the free stream current, u_c, the total hydrodynamic area, $C_d A$, which we define as the product of the Morison drag coefficient, C_d, and the solid drag area of the scaled jacket, A, and the total frontal area of the jacket, A_f, as:

$$u_s = u_c \Big/ \left(1 + \frac{C_d A}{4A_f}\right) \tag{6.5}$$

The description and derivation of the model is provided in Chapter 3.2, Taylor (1991) and Taylor et al. (2013). For the purpose of comparison with the Allender and Petrauskas experimental data points, two steady current flow cases are simulated: u_c = 1.25 and 2.5 m/s.

Table 6.3 summarises the results for the two steady flow cases, presented in terms of the average current within the tower volume. The simulation result without the porous tower present (F_{und}) is to be compared with the input velocity profile at the inlet, while the simulation result with the porous tower present (F_{dist}) is to be compared with the SCB model. Good agreement is achieved between the F_{und} results and the input velocity, and a slight increase is observed in the F_{dist} results as compared to the SCB results. This slight increase could be due to side leakage through the lateral faces of the porous tower, which enhances the lateral mixing between the inner blocked flow and the outer free-field flow, as described in Santo et al. (2013a). The CFD simulation uses a 60 m × 60 m block whereas the analytical one-dimensional stick model uses a single disc of 60 m × 0 m, so a slightly higher effective current for the simulation result is expected. Thus, as previously demonstrated in the planar flow through a porous block simulation in Chapter 4 and Santo et al. (2013a), these two different flow representations are compatible with each other.

Table 6.3: Simulation results in terms of effective current velocity at the tower location for 1.25 m/s and 2.5 m/s steady flow cases.

Input current (m/s)	SCB result (m/s)	Effective average current at the tower position (m/s) – tower absent	– tower in place
1.25	1.03	1.24	1.05
2.5	2.05	2.48	2.09

The results in terms of peak drag forces for the simulated two steady current cases provide the points on the extreme left of Figures 6.17 and 6.18 for zero wave height in regular waves plus current flow simulations described in Section 6.4.3. The agreement between the numerical simulations and the measured peak forces is shown to be good.

Figure 6.8 shows three-dimensional flow visualisation at a vertical cut across the wake, and the surface flow beyond, looking upstream towards the porous tower for the case of 1.25 m/s steady current. The tower is indicated as white colour grid. The longitudinal flow is expressed as the difference between the disturbed velocity with the tower in-place minus that for the same current on the same computational grid but with the tower absent ($\mathbf{u}_{dist} - \mathbf{u}_{und}$). White colour corresponds to a fast flow perturbation of 0.1 m/s out of the page in a downstream direction, black to a reduced flow perturbation of -0.3 m/s into the page. A net flow retardation (black colour) in the form of steady wake region is clearly visible at immediate downstream of the tower, accompanied by faster flow divergence and shear layers along the edge of the tower (white colour). There is an expansion of the retarded flow region before it slowly diffuses out and recovers to close to the undisturbed flow at $\sim$ 250 m downstream the tower. Also shown is the vertical cut at 250 m downstream of the centre of the tower, which demonstrates relatively little vertical mixing between the blocked flow and the undisturbed flow as there are no significant free-surface effects occurring in this steady current simulation case. This flow retardation process reflects a current–structure interaction, which gives rise to simple current blockage.

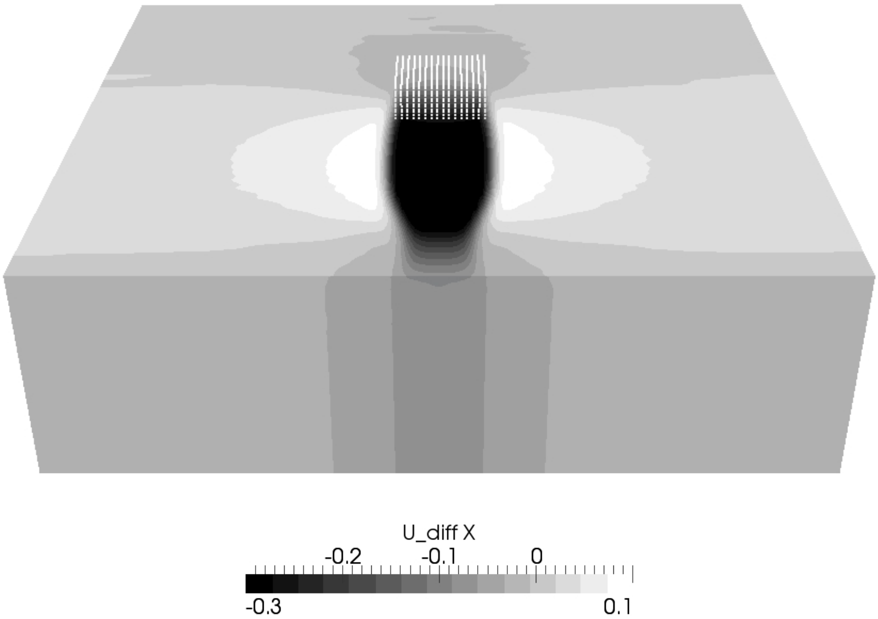

Figure 6.8: Three-dimensional flow visualisation at a vertical cut across the wake, and the surface flow beyond, looking upstream towards a porous tower for the case of 1.25 m/s steady current through the tower. The colour code follows $U_{diff}X$ colour legend, which is the difference between the disturbed and the undisturbed velocity, for the longitudinal flow towards the observer in the positive x-direction. White colour corresponds to a fast flow perturbation of 0.1 m/s out of the page in a downstream direction, black to a reduced flow perturbation of -0.3 m/s into the page. The same grey scale is used both for longitudinal flow in and out of the vertical slice and also for the horizontal downstream component of the velocity on the free-surface.

6.4.2 Regular waves

The case of regular waves with no current is simulated as the next comparative test between the numerical simulations and the physical experiments. It is important to obtain qualitatively and quantitatively good agreement in this case to justify the validity and feasibility of the assumptions undertaken in the simulations, as we move on to attempt to reproduce the experimental results for regular waves plus current.

It is worth mentioning that in this regular wave case without the presence of steady current, there is assumed to be no build up of a global mean wake effect, thus there is no occurrence of current blockage, and as a result the standard Morison theory with no blockage is applicable for comparison between the theory and the numerical simulations, apart from possible issues associated with Stokes drift and Keulegan–Carpenter (KC) number effects.

Table 6.4 provides the properties of all the regular waves simulated in this work. The associated wave numbers are obtained based on Stokes 3rd order deepwater wave dispersion theory (adequate because $kh \geq \pi$):

$$\omega^2 = gk[1 + (ka)^2] \tag{6.6}$$

where $\omega = 2\pi/T$ is the wave angular frequency, T is the wave period, $k = 2\pi/\lambda$ is the wave number, λ is the wavelength, and a is the linear wave amplitude. The water depth, h, is 135 m.

Table 6.4: Wave properties for regular wave simulations.

Wave height, H (m)	5	10	15	20	25
Wave number, k (m^{-1})	0.02449	0.02423	0.02383	0.02332	0.02275
Wave period, T (sec)	12.8	12.8	12.8	12.8	12.8

Each regular wave simulation is run for about 15 wave periods in order to reach a sufficiently periodic steady-state condition.

We note that the presence of the porous tower causes a slight phase-delay and smearing effect to the free-surface profile when compared with the free-field profile. Nevertheless, the observed effect is local. The presence of the porous tower introduces little disruption to the free-surface globally, which is consistent with the underlying assumption that the presence of cylinders in an array or group (or in a space-frame offshore structure) has little effect on the global surface elevation flow-field (little wave field distortion in terms of diffraction and reflection). A small surface disturbance on the wave crest is visible immediately downstream of the tower in Figure 6.2. In fact, much of the disruption occurs below free-surface level in terms of the mean vorticity of the wake, as visible from the flow visualisation in Section 6.5.

Full-scale drag (solid lines) and inertia (dashed lines) force time histories are illustrated in Figure 6.9 for 15 m regular waves with (F_{dist}, shown as black lines) and without (F_{und}, shown as grey lines) the porous tower present, which shows a force reduction in the drag term and negligible effect in the inertia term. There is a small effect of extra submergence of the porous tower (extra 15 m submerged at crest). It is obvious that the force reduction is larger at the force crests than at the force troughs. This force reduction might be attributed to a blockage effect perhaps due to Stokes drift downstream, particularly at the surface, and this drift will be blocked to some extent. Hence, the crest results are markedly different, while the trough results are close.

Table 6.5 shows the variation of peak drag forces for varying regular wave height (from 5 to 25 m). Generally, the relative reduction of the peak crest of the drag force

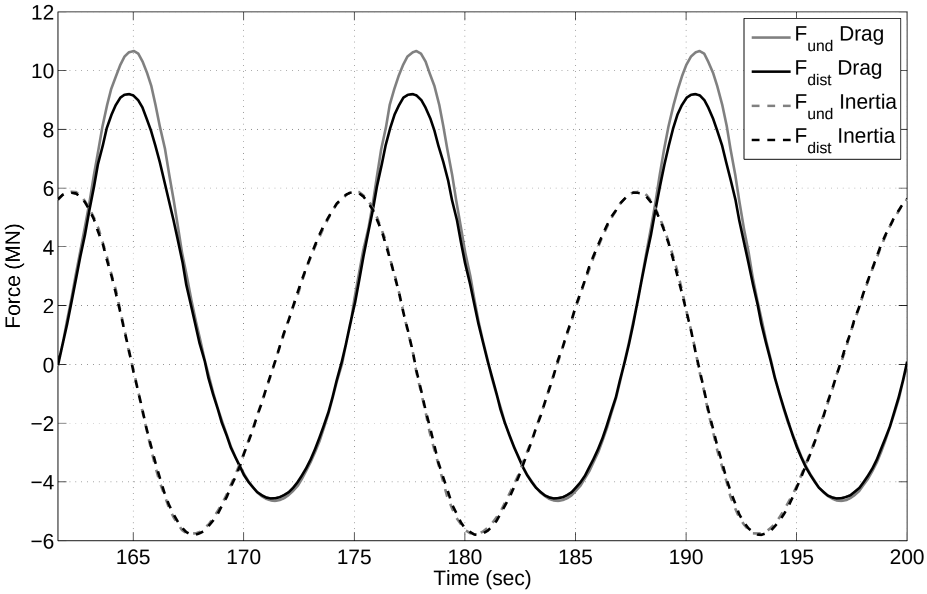

Figure 6.9: Force time histories for 15 m regular waves with (F_{dist}, shown as black lines) and without (F_{und}, shown as grey lines) the porous tower present. Drag forces are shown as solid lines, and inertia forces as dashed lines.

is close to independent of the wave height, so it is not related to Stokes drift. The average reduction over the entire simulated regular wave cases is about 12%. Overall, it can be observed that the peak drag force scales well with the wave height squared (H^2) as is to be expected.

Table 6.5: The variation of peak drag forces with and without the porous tower present due to various regular wave heights.

Wave height (m)	Peak drag force F_{und} (MN)	F_{dist} (MN)	Reduction (%)
5	1.05	0.95	10
10	4.52	4.00	12
15	10.66	9.20	14
20	19.18	17.02	11
25	34.64	30.03	13
		Average	12

Figure 6.10 summarises the key results from the simulations in terms of peak drag and peak total force (data points with solid trend lines) as a function of wave height, plotted on top of Allender and Petrauskas experimental data points as well as the analytical one-dimensional stick model based on the standard Morison (dashed black

line), which have been shown previously in Figure 3.15 in Chapter 3 (or in Figure 13 in Taylor et al. (2013)). It is noted that good agreement is obtained between the simulations and the physical experiments, which provides some support for the assumptions used in the numerical simulations, as well as in the theory.

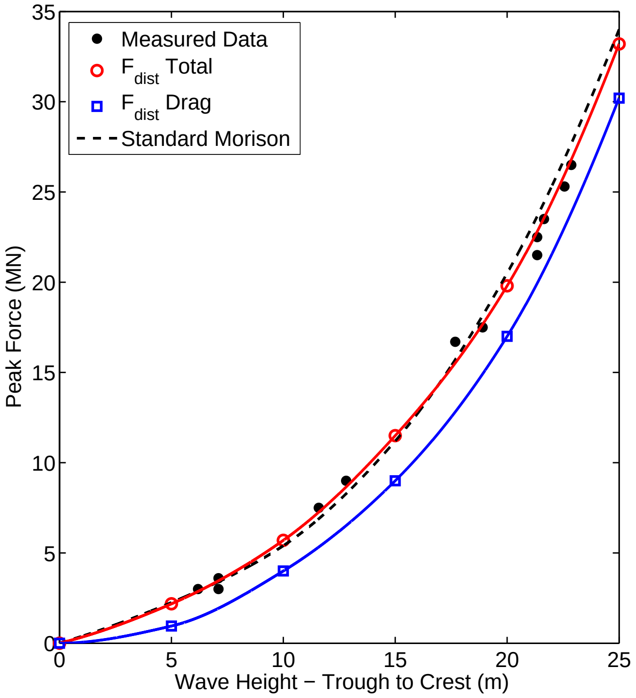

Figure 6.10: Comparison of the simulated and the measured peak drag and peak total forces on space-frame model with waves and zero current. The simulated peak drag forces is shown as solid (blue) line with hollow squares, the simulated peak total forces as solid (red) line with hollow circles, the measured forces from Allender and Petrauskas (1987) as solid black circles, and the standard Morison as dashed black line.

6.4.3 Regular waves plus current flow

Next, we are interested in modelling combined regular waves with an in-line current flow through a porous tower. This section attempts to reproduce the measured *peak* forces by Allender and Petrauskas with the same and consistent C_d and C_m values used previously for steady current and pure regular waves (with no current) simulations, but now with the force time histories as well as the peak values.

A full current blockage model has been introduced to account for the extra blockage resulting from the complete wave–current–structure interaction as described in Chapter 3 and Taylor et al. (2013) for peak force and Chapter 5 and Santo et al. (2014b) for force time history.

In the physical experiments, the scaled jacket model was towed by a carriage in the opposite direction to the wave propagation to simulate a uniform current profile on top of regular wave flow. The regular wave and its kinematics remain the same, with the period fixed at 12.8 sec. Thus, the scaled jacket model which moved with the current (or the carriage) would encounter the waves at a different frequency compared to when the model was stationary. This exact condition is reproduced in the numerical wave tank.

Instead of moving the porous tower as in the physical experiments, a uniform current profile is fluxed at the inlet boundary together with regular waves to produce regular waves with an in-line current. For regular waves with no current, the spatial surface elevation at the inlet (as well as at the tank when the waves propagate downstream) is $\eta = a\cos[\omega t - kx]$, where η is the surface elevation, a is the linear wave amplitude, t is the temporal and x is the spatial variable. With the presence of a uniform current u_c, the fixed space coordinate x of the waves viewed in a frame of reference which moves with the current is replaced by $x' = x - u_c t$. The spatial surface elevation can then be re-written as $\eta = a\cos[\omega t - k(x - u_c t)]$, so the effective frequency is now $\omega' = \omega + u_c k$, which defines the encounter frequency of the waves with the model which moves together with the current. Hence, relative to the porous tower, the wave induced fluid velocity at the wave crest is in the same direction as the waves are advancing and so is the current, but the encounter frequency of the waves with the tower is increased to ω'. Meanwhile, the standard wave dispersion relationship still holds for this case of waves and in-line current as a frame of reference which moves with the current u_c is adopted here.

The same set of regular waves is simulated, with two different current velocities, $u_c = 1.25$ and 2.5 m/s. Each regular wave plus current simulation is run for about 15 wave periods in order to reach a sufficiently steady-state condition.

Figures 6.11 and 6.12 show full-scale force time histories for 20 m regular waves of 12.8 sec period with 1.25 m/s and 2.5 m/s current in 135 m water depth with the tower present, whereby both the drag (solid black line) and the inertia (dashed black line) forces are obtained directly from the simulation and the total force (solid grey line) is the superposition of these two forces. A very slight above linear increase is observed in the simulated inertia force when current increases from 1.25 m/s to 2.5 m/s despite the same C'_m input. Nevertheless, the increase is rather small ($\sim$ 5% difference), and this may result from the time derivative term $((1 + C'_m)\partial\rho\mathbf{u}/\partial t)$ which is slightly modified due to the change in the encounter frequency.

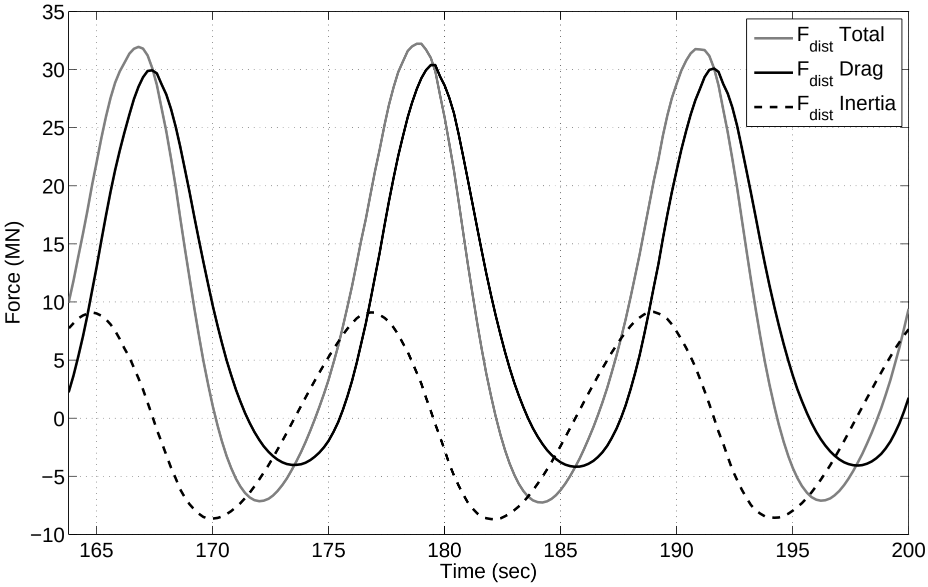

Figure 6.11: Full-scale total force, drag and inertia force time histories for 20 m regular waves of 12.8 sec period with an in-line 1.25 m/s current in 135 m water depth. The total force is shown as solid grey line, the drag force as solid black line, and the inertia force as dashed black line.

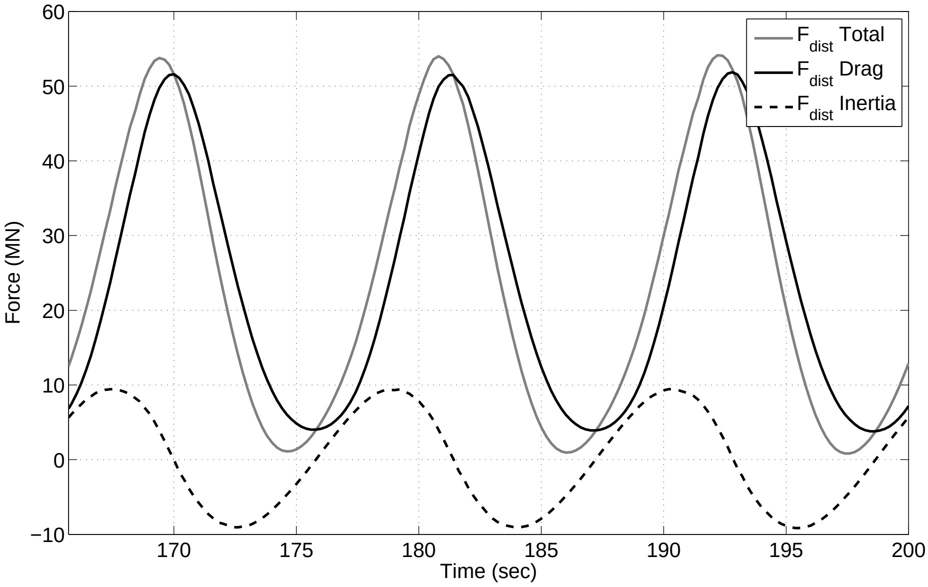

Figure 6.12: Full-scale total force, drag and inertia force time histories for 20 m regular waves of 12.8 sec period with an in-line 2.5 m/s current in 135 m water depth. The total force is shown as solid grey line, the drag force as solid black line, and the inertia force as dashed black line.

Figures 6.13 and 6.14 show the comparison of drag force time histories with (solid black lines - F_{dist}) and without (solid grey lines - F_{und}) the tower present for the same 20 m regular waves with 1.25 m/s and 2.5 m/s current. A significant reduction

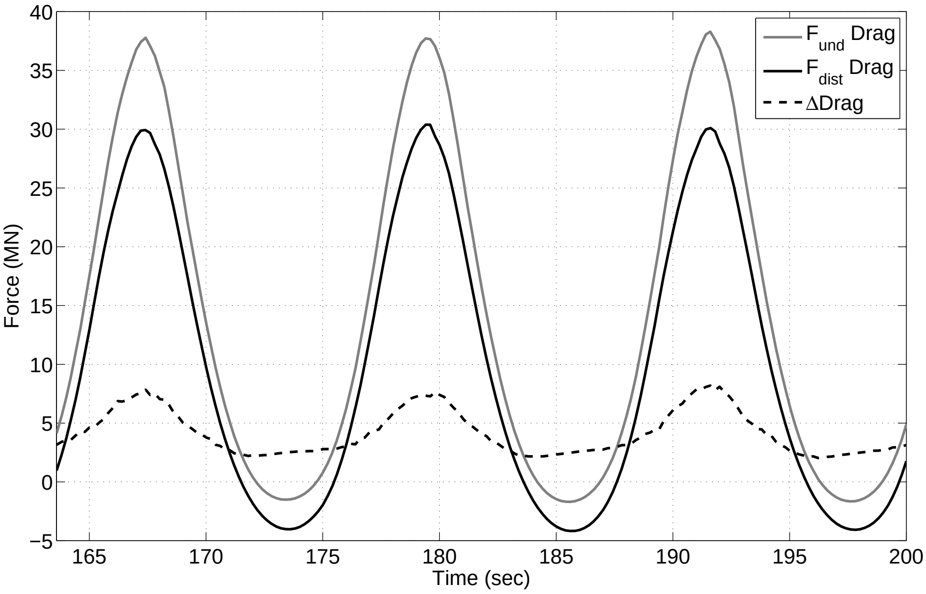

Figure 6.13: Comparison of drag force time histories with (F_{dist}, shown as solid black line) and without (F_{und}, shown as solid grey line) tower present for 20 m regular waves of 12.8 sec period with an in-line 1.25 m/s current in 135 m water depth. Also shown is the drag force reduction (ΔDrag) plotted as dashed black line.

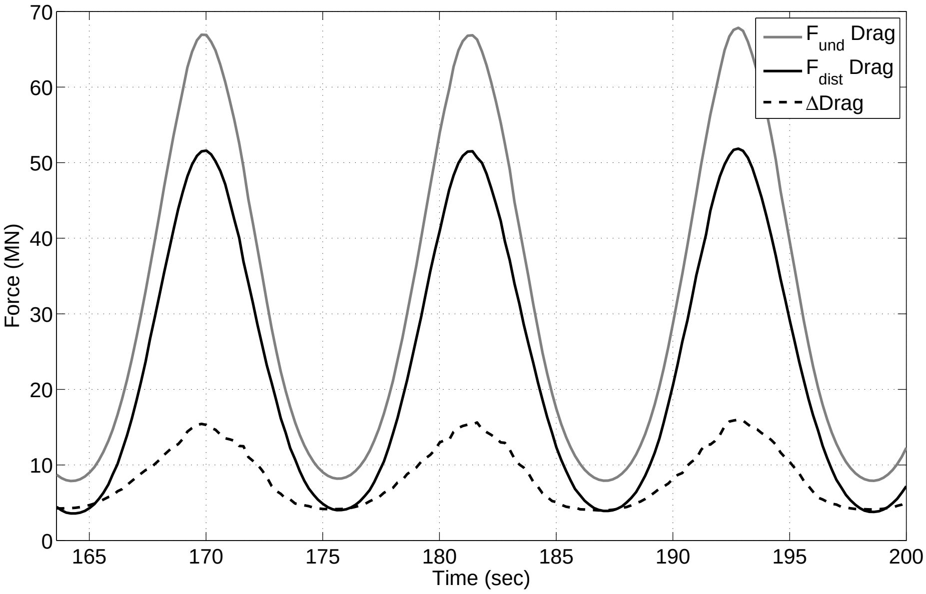

Figure 6.14: Comparison of drag force time histories with (F_{dist}, shown as solid black line) and without (F_{und}, shown as solid grey line) tower present for 20 m regular waves of 12.8 sec period with an in-line 2.5 m/s current in 135 m water depth. Also shown is the drag force reduction (ΔDrag) plotted as dashed black line.

in the drag force due to current blockage is observed, obtained by subtracting the drag force of F_{dist} from F_{und}. The amount of the drag force reduction is plotted as dashed black line and shown as ΔDrag, which shows that most of the reduction occur in phase with the wave crest (when the wave kinematics are in the same direction with the in-line current). The inertia term (not shown) is observed to be virtually completely unaffected by the presence of the porous tower, which is consistent with the formulation of the current blockage theory in which only the drag term is affected.

Figures 6.15 and 6.16 show the drag force reduction time histories for the simulated wave heights of 5 m, 10 m and 20 m, with 1.25 m/s and 2.5 m/s current, respectively. All the drag force reductions are smoothed by averaging cycle-by-cycle (in total five cycles) when the drag forces have reached sufficiently steady-state periodic conditions.

It is noted that the amount of force reduction for both 5 m regular waves with 1.25 m/s and 2.5 m/s current is comparable to the reduction due to simple current blockage model (SCB) as well as the full model (FCB), since the current velocity is of comparable magnitude with the wave kinematics. Beyond 5 m regular waves, all the reductions are due to the full current blockage effect (wave–current–structure interaction), which are considerably larger than the simple current blockage effect (current–structure interaction). The crest of the drag reduction occurs in phase with the passage of the wave crest for all wave heights, and it increases as the wave height increases. The trough of the reduction, on the other hand, generally exhibits a flat plateau during the passage of the wave trough (when the wave kinematics are in the opposite direction with the in-line current) except for the 20 m wave height (and 25 m wave height – not shown) with 1.25 m/s current where there is some force reduction at the force trough which increases as the wave height increases. This is presumably associated with energised reverse (backward) flow which occurs during the passage of wave trough. For regular waves with 2.5 m/s current, the flat plateau at the trough of the force reduction is found to be independent of the wave height, as the occurrence of the energised backward flow seems to be well counter-balanced by the stronger current. The magnitude of the trough of the reduction roughly quadruples from about 1 MN to 4 MN when the current velocity doubles from 1.25 m/s to 2.5 m/s.

All the simulation results can be summarised in terms of the peak total force as a function of wave height, and these are shown in Figure 6.17 for regular waves with 1.25 m/s current and Figure 6.18 for regular waves with 2.5 m/s current corresponding to Figures 3.16 and 3.17 in Chapter 3 (or Figures 15 and 14 in Taylor et al. (2013)). The simulations results are plotted as solid lines with square and circle data points, the experimental results as solid data points, while the analytical one-dimensional stick model results based on the full current blockage model (FCB) as dashed black lines.

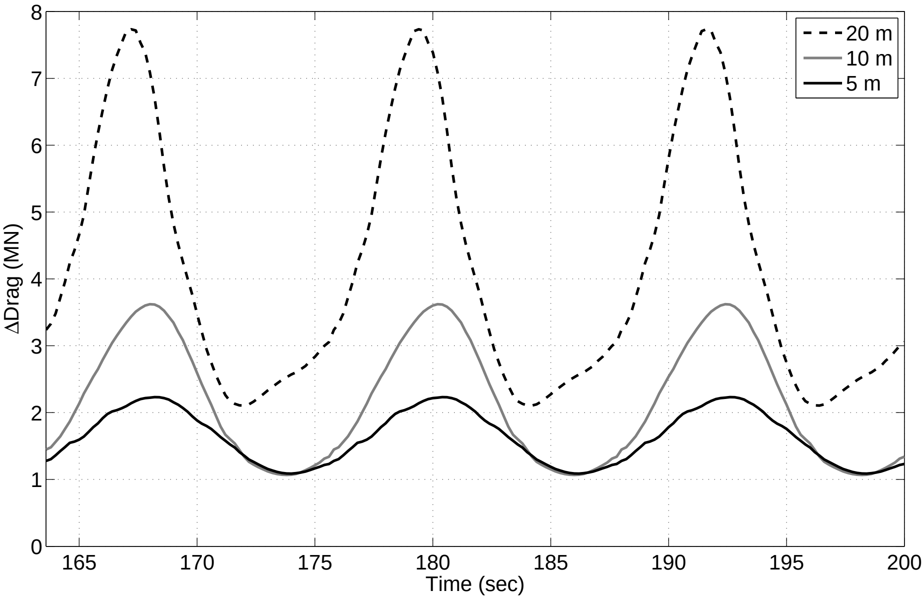

Figure 6.15: Summary of the drag force reduction time histories obtained from F_{und} - F_{dist} for ranges of regular waves with 1.25 m/s current. The drag force reduction for 20 m regular waves is shown as dashed black line, for 10 m regular waves as solid grey line, and for 5 m regular waves as solid black line.

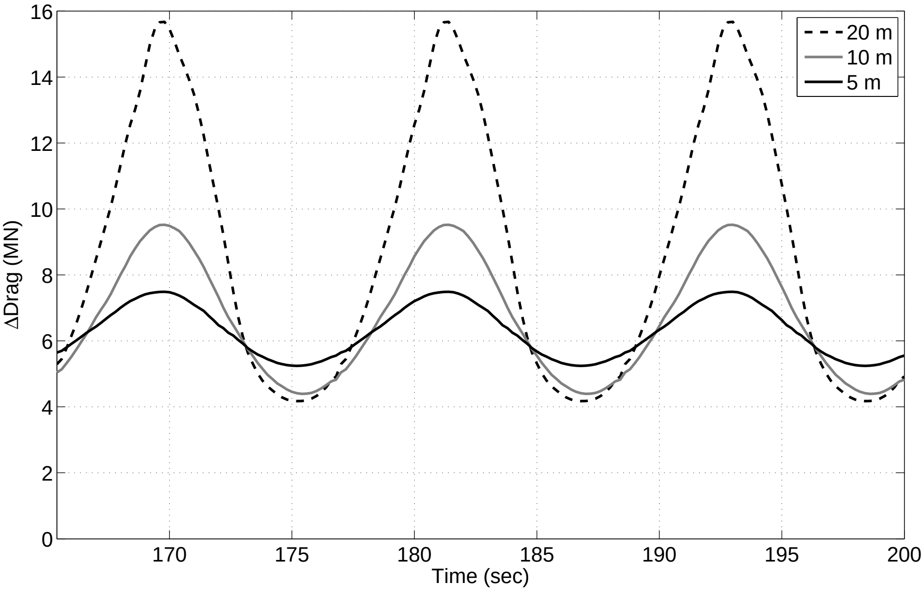

Figure 6.16: Summary of the drag force reduction time histories obtained from F_{und} - F_{dist} for ranges of regular waves with 2.5 m/s current. The drag force reduction for 20 m regular waves is shown as dashed black line, for 10 m regular waves as solid grey line, and for 5 m regular waves as solid black line.

It can be assumed that the discrepancy between the numerical results and the analytical results is largely attributed to the finite size effect of the volume averaging

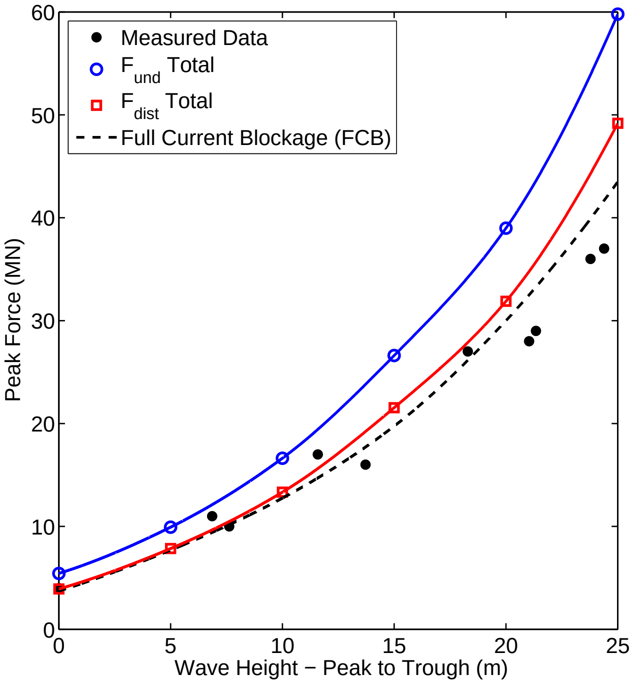

Figure 6.17: Comparison of the simulated and the measured forces on space-frame model with waves and 1.25 m/s in-line current. The simulated peak forces with the tower absent (F_{und}) is shown as solid (blue) line with hollow circles, the simulated peak forces with the tower present (F_{dist}) as solid (red) line with hollow squares, the measured forces from Allender and Petrauskas (1987) as solid black circles, and the full current blockage results as dashed black line.

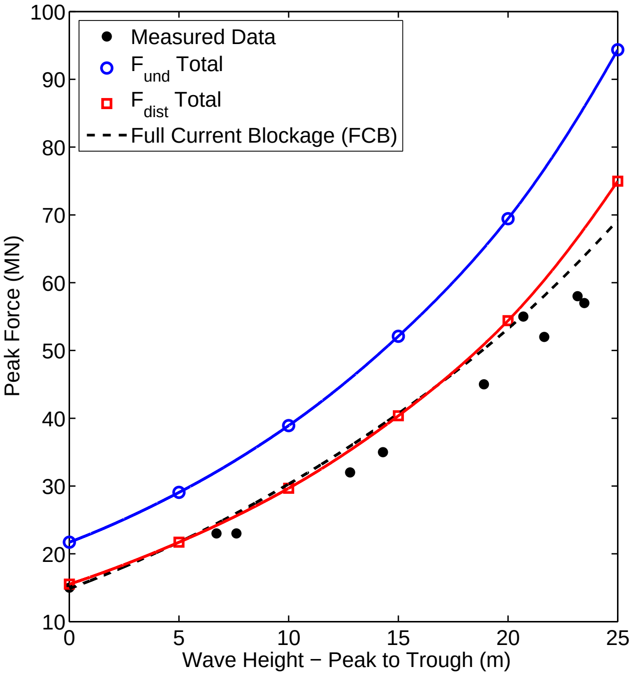

Figure 6.18: Comparison of the simulated and the measured forces on space-frame model with waves and 2.5 m/s in-line current. The caption follows that of Figure 6.17.

of the porous drag and inertia force components, and the effects of the lateral mixing. For both numerical results, the deviation from the analytical results when $H > 20$ m is probably due to the non-linear effects of the Stokes waves simulated in the numerical wave tank which increase with wave height - the analytical results were plotted based on Airy (linear) wave theory, with a rather crude approximation for the free-surface correction based on linear kinematics at mean sea level. The slight over-estimation of the peak forces for the largest waves may arise from the assumption in the numerical and analytical modelling that the volume distribution of the porous tower is spatially uniform. It is likely that for the Allender and Petrauskas model structure there were fewer structural elements (less resistance) in the wave action zone, particular at and above mean sea level, than below, as can be seen in Figure 6.1. Unfortunately, no detailed information on this issue was available to guide the modelling work.

Overall, it can be concluded that the simulation results match well with the peak forces measured by Allender and Petrauskas; all of these simulations for current only, waves only, and waves with in-line current are using identical C_d and C_m values. The results also match the FCB model. The good agreement between the simulation and the FCB model provides further support for the validity of the current blockage theory in representing the actual fluid loading after taking into account the full blockage effects for regular waves with an in-line current. The previous validation work was only applicable to regular planar oscillations with an in-line steady flow (see Chapter 4 and 5, or Santo et al. (2013a) and Santo et al. (2014b)).

6.5 Flow visualisation

Now, flow visualisations on the dynamical behaviour of the flow structures are presented. These comprise shielded flow through the porous tower, shear layer separations at the edge of the tower and jet flows emerging out from the tower towards the outer faster flow (side flow leakage which enhances lateral mixing).

6.5.1 General remarks on the nature of the flow field

Figures 6.19(*a*, *b*) show the longitudinal velocity flow field at a horizontal cut at -30 m below mean sea level within the central portion of the whole computational domain for 20 m regular waves with 1.25 m/s current with the tower in-place. The colour reflects the strength of the longitudinal flow through the tower, in which the dominant flow is from left (upstream) to right (downstream). Figure 6.19(*a*) shows an instant when a wave crest is at the centre of the tower, which clearly demonstrates flow distortion downstream of the tower as a mean wake at that particular slice. Red colour corresponds to instantaneous forward velocity of 4 m/s, blue to instantaneous reverse velocity of −2 m/s. Figure 6.19(*b*) shows a time-averaged longitudinal flow map over a complete wave cycle at the same slice, which demonstrates a global mean wake immediately downstream the tower as a result of the complete wave–current–structure interaction. The net flow and force reduction due to the combined waves and current is larger than due to the current alone. This can be observed from the width and strength of the mean wake, which are both much larger than that shown in Figure 6.8 for just steady current through the tower. This dramatic increase in the global mean wake is the motivation for the development of the full current blockage model (FCB) (Taylor et al., 2013).

General observations on the nature of the flow structures:

- The flow field is highly unsteady at the top of the porous tower, with the magnitude of the oscillatory in-line wave kinematics $\sim 4\times$ the mean current speed. Nevertheless, the bulk features of the flow field are apparently adequately resolved by the CFD simulations.
- Within and initially downstream of the porous tower, the flow structure is very 'blocky', with more mean flow reduction at the top of the tower and less further down the water depth, where simple blockage of the current dominates. This occurs despite the large oscillations in the flow velocity as the waves propagate through the tower in addition to the mean current.
- There is little disturbance to the position of the wave crests downstream of the tower, and what there is is complex, changing form with position downstream (as can be seen from Figure 6.2).
- Although the wake is fully three-dimensional and there is considerable wake structure well downstream of the tower, the wake remains very close to completely symmetric about the centre-plane in the downstream direction. As can be seen from Figure 6.19(*c*), there is considerable rearrangement of the wake structure, including apparent vortex 'breakdown' and rearrangement, but this occurs at least one surface wavelength downstream of the tower. The figure shows instantaneous streamtubes all originating in the top half of the water column from a vertical plane at 145 m downstream of the centre of the tower within the central portion of the whole computational domain. The streamtube

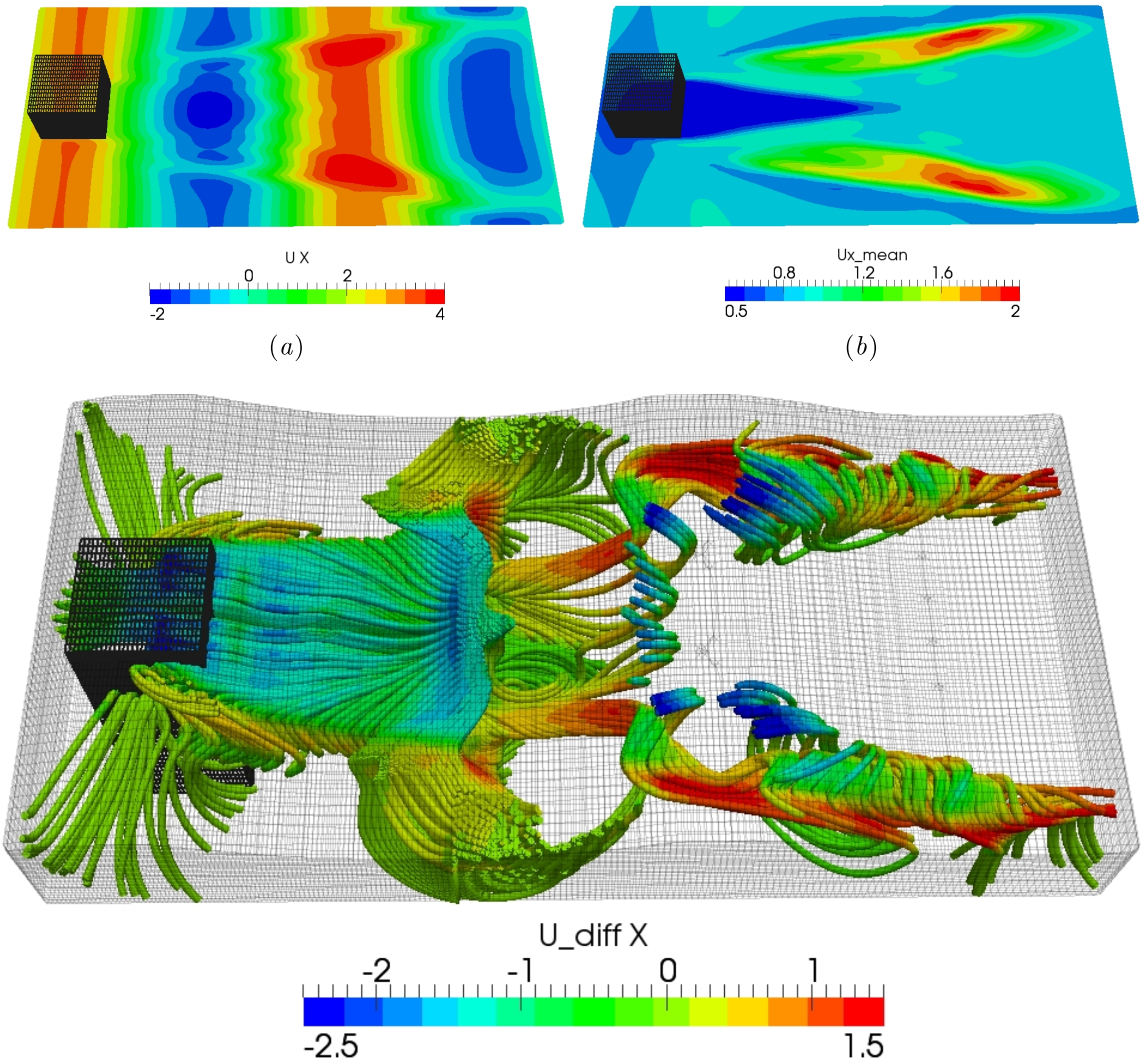

(*a*) (*b*)

(*c*)

Figure 6.19: Three-dimensional flow visualisation of the longitudinal flow structures within the central portion of the whole computational domain for the case of 20 m regular waves with 1.25 m/s current through a porous tower. Figures(*a*, *b*) show longitudinal velocity flow field at a horizontal cut at -30 m below mean sea level in which the dominant flow is from left (upstream) to right (downstream). Figure(*a*) shows a snapshot when a wave crest is at the centre of the tower, in which the colour reflects the instantaneous strength of the longitudinal velocity flow. Figure(*b*) shows a time-averaged longitudinal flow map over a complete wave cycle, in which the colour reflects the strength of the mean longitudinal velocity flow. Figure(*c*) shows instantaneous streamtubes all originating in the top half of the water column from a vertical plane at 145 m downstream of the centre of the tower, expressed as the difference between the disturbed velocity with the tower in-place and the undisturbed velocity with the tower absent ($\mathbf{u}_{dist} - \mathbf{u}_{und}$). The colour reflects the instantaneous strength difference in the longitudinal velocity flow component.

is drawn for the flow field corresponding to the difference between the disturbed velocity with the tower in-place and the undisturbed velocity with the tower absent ($\mathbf{u}_{dist} - \mathbf{u}_{und}$), and coloured as the instantaneous strength difference in the longitudinal velocity component. There is an extra (red) downstream velocity component evident from leakage through the sides of the tower and a retarded (blue) blocky wake just downstream of the tower. On the edges of the tower there are vortices at both sides, and when the vortices reach the next crest line, there is a vortex re-arrangement but prior to this there is a tightly wound core with fast axial flow (red). Downstream of the crest line after the re-arrangement, the axial cores are spreading further out but still localised. There is considerable vertical motion as well as complex horizontal flow structures evident in the figure.

- The flow structure through the porous block can be interpreted as 'base bleed', somewhat akin to the injection of fluid into the near wake immediately downstream of a bluff body in order to reduce the drag force (Bearman, 1967; Wood, 1967). The downstream displacement of the complex wake region for our wave–current–structure interaction is sufficient for close to completely symmetric flow close to the tower. In the far field we would might expect global wake instability to result in the characteristic side-to-side Karman street oscillation of the wake, but we see no evidence for this in the (admittedly) spatially compact flow domain.

- In the near field downstream of the tower, there is considerable axial flow along what are vortices either side of the central block of retarded flow. This flow is significant, remaining submerged below the free-surface and the shape of the vortices changes with downstream distance. But the presence of such vortices does act to constrain the wake flow and to modify the depth profile. On the free-surface behind the tower, we have regions of accelerated and decelerated flow as patches along the downstream direction. These are associated with the crest and trough phases of the flow through the tower being swept downstream by the combined effects of the mean current and Stokes drift in the wave, in the examples shown these mean flows are of comparable magnitude.

- One wavelength downstream of the tower, with a wave crest within the tower, the axial vortices seem to undergo a vortex 'breakdown' associated with the spread of a jet type axial flow pulse across the whole width of the wake, giving at the surface retarded flow, then the jet flow, and beneath both retarded flow with the remnants of the simple current blockage wake close to the bed. For a trough at the tower, this vortex 'breakdown' occurs an additional one half wavelengths downstream, showing that this is a highly mobile phenomenon consistent with the position of the wave crests.

- Although the simulations have been performed with a VOF-type code, where the free-surface is smeared out using cells where the averaged fluid density decreases dramatically in a relatively short distance vertically, the region where the average fluid density is 50% - 95% of that of water is well above the accelerated wake jet pulse as vortex 'bursting' starts, so we believe that this feature is unlikely to be a variable density artifact.

6.5.2 Commentary of the local structure of the flow field on a sequence of planes downstream of the porous tower

Now we examine the structure of the flows on vertical slices across the wake, comparing and contrasting these cross-sectional flow features when a regular wave crest (left) and trough (right) is located at the centre of the porous tower, as shown in Figure 6.20 for the case of 20 regular waves with 1.25 m/s in-line current. This shows a series of cuts across the wake, and the surface flow beyond, looking upstream towards the porous tower, visible in the centre of each image. Figures 6.20(*a*, *b*), (*c*, *d*), (*e*, *f*), (*g*, *h*), and (*i*, *j*) show cuts at 50 m, 150 m, 200 m, 250 m and 350 m downstream of the centre of the porous tower, respectively. The colours reflect the strength of the longitudinal flow towards the observer in the positive x-direction. This is expressed as the difference between the disturbed velocity with the tower in-place minus that for the same waves on the same computational grid but with the tower absent ($\mathbf{u}_{dist} - \mathbf{u}_{und}$). Red colour corresponds to a fast flow perturbation of 1.5 m/s out of the page in a downstream direction, blue to flow perturbations into the page of -2.5 m/s. The same colours are used both for longitudinal flow in and out of the vertical slice and also for the horizontal downstream component of the velocity on the free-surface. Further detailed description of the local flow structures is presented in Table 6.6.

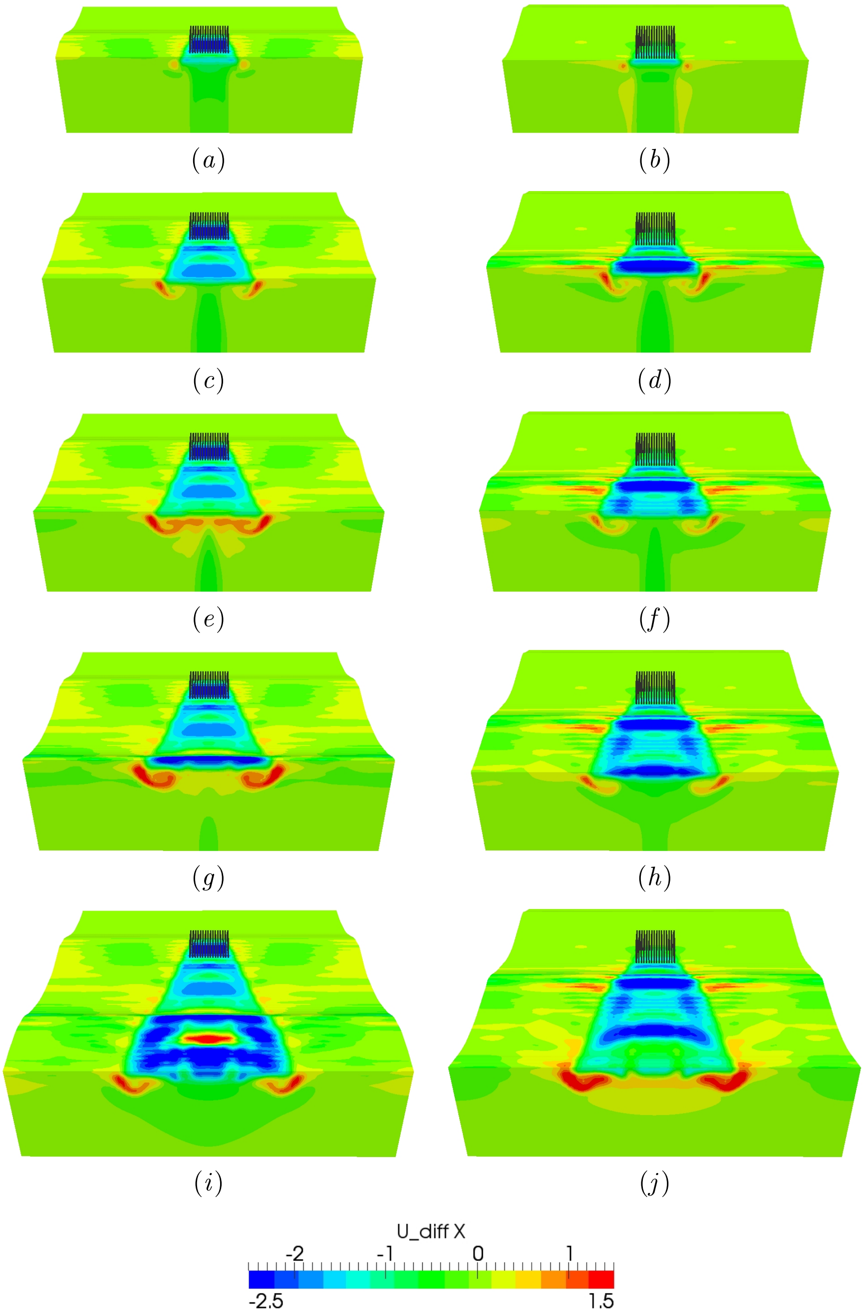

Figure 6.20: Three-dimensional flow visualisation of the flow structures for the case of 20 m regular waves with 1.25 m/s current through a porous tower. Left hand figures show a snapshot when a wave crest is at the centre of the tower, right hand figures when a wave trough is at the centre of the tower half a wave cycle later. Figures(a, b), (c, d), (e, f), (g, h), and (i, j) show a series of cuts at 50 m, 150 m, 200 m, 250 m and 350 m downstream of the centre of the porous tower, respectively. The colour code follows $U_{diff}X$ colour legend, which is the difference between the disturbed and the undisturbed velocity, for the longitudinal flow towards the observer in the positive x-direction. Red colour corresponds to a fast flow perturbation of 1.5 m/s out of the page in a downstream direction, blue to flow perturbations into the page of -2.5 m/s. The same colours are used both for longitudinal flow in and out of the vertical slice and also for the horizontal downstream component of the velocity on the free-surface.

Table 6.6: Description of the local structure of the flow field on a sequence of planes downstream of the porous tower.

Downstream distance from the centre of the porous tower	Crest	Trough
50 m	- axial flow is weak in cores downstream of the tower, and highly retarded within and across the tower at the free-surface, - vertical gradient is smooth down the tower.	- axial core flow is stronger downstream compared to the crest at the tower case, - vortices are much more visible, - there is slightly more necking of the simple sheared wake profile, - surface layer is weakly retarded at the tower, and the axial flow velocity is increased the deeper the position.
150 m	- roll-up of the vortices is now starting, inwards at the bottom, - there is a slight pinching of central wake deficit region.	- there is more roll-up and stretching, - axial flow increment is still slightly larger, as is pinching, but the basic structure is very similar.
200 m	- we are now approaching the next crest line across the flow, - there is a rather sudden spread and magnification of axial flow increase across the whole wake below the surface, giving in the vertical direction weak retardation of the axial flow on the surface, then acceleration in a layer with relatively undisturbed retardation beneath.	- axial flows in cores is now weaker, with no spreading across the main wake, which is very different from the crest at the tower case case.

250 m	- axial flows are re-established in two cores, - layered jet in the centre of the wake is weaker but still clear, - this re-arrangement of the axial flow structure is associated with passing through the wave crest one wavelength downstream of the tower.	- edge core flows are still much weaker, - patterns of flow perturbation on the free-surface downstream of the tower are clear.
350 m	- some uneven axial flow retardation is still visible below the surface on the centre-line, - still two core flows at either side cut are weakening downstream as we approach the next trough, - the deep blockage current wake is no longer visible, - much stronger free-surface pattern is visible on the free-surface upstream of the vertical cut, a reflection of the vortex ‘burst’ at $\sim$ 250 m.	- there is an intensification of the axial flow cores as we are approaching the next wave crest, - there is a generation of a submerged downstream jet, which is a somewhat similar flow structure to crest case at 200 m, and associated with the start of a vortex ‘burst’, but now at an additional one half surface wavelength downstream compared to the crest at the tower case.

In summary, the wake flow behind the porous tower is strongly unsteady as it reflects the modulation by the waves. The wake itself remains well separated and distinct from the surrounding bypass flow. There is interesting and significant unsteady fully three-dimensional wake dynamics, but all of this appears to occur well downstream. The flow within the tower is relatively simple, and as a consequence, the Morison-type forces are also relatively simple in form.

In short, the flow visualisation has been helpful in providing insights into the global flow behaviour. It is worth noting that the flow visualisation has been performed assuming uniform resistance in all flow direction as a first approximation to the Allender and Petrauskas type of jacket model, while the actual structure could possibly have a non-uniformly distributed resistance and this might affect local and/or global flow structures – a problem left for future work. It is also worth mentioning that no visualisation of the local flow disruption within the porous tower of the order of the width of individual cylinders is attempted as the local flow structure modelling is not accounted for in such porous tower simulations. The observed flow structures from this flow visualisation are the global flow structures (in the form of the mean vorticity of the wakes), which are mostly due to shear flow separation, and to some extent side flow leakage. These global mean wakes are the product of the complete fluid–structure interaction process, and they are responsible for the global flow and force reduction on statically-responding fixed space-frame offshore structures.

6.6 Chapter summary & conclusions

This chapter demonstrates that the use of a porous tower in a full CFD numerical simulation as a model for an offshore jacket structure is a viable approach for Morison-type loading in general, and for investigating the current blockage effects in particular. The Morison drag and inertia contributions are treated directly by inserting resistance elements into the Navier–Stokes equations, and this process only requires calibration of the resistance parameters as the effective Morison C_d and C_m coefficients.

Little wave reflection is observed from the downstream wave absorption zone showing that the numerical wave tank is working well. There is little wave diffraction from the porous tower, as shown by the localised distortions of the crest lines downstream of the tower. Various numerical studies have been conducted to investigate the length of the tank domain, to achieve grid independent simulation results, and to assess the two different Morison drag formulations. In general, the numerical wave tank with the free-surface capturing VOF technique works reasonably well in simulating regular waves with no current, steady current and combined regular waves with an in-line current.

This chapter proceeds with numerical reproduction of the Allender and Petrauskas experimental peak forces: all cases are well predicted using the same values of C_d and C_m. And of course the numerical simulations provide predictions of the complete force time history as well as the peak values reported by Allender and Petrauskas. The forces from the simulated steady current flow compare well with the simple current blockage model (SCB), with a slight increase in the net shielded current and the corresponding drag force due to side leakage which is consistent with the findings from the planar flow simulation presented in Chapter 4 and Santo et al.

(2013a). The forces from the simulated regular waves agree well with the peak force measurements by Allender and Petrauskas as well as the standard Morison theory with no blockage. For the case of regular waves plus current, the simulated forces also compare reasonably well with their measurements as well as the full current blockage model (FCB) presented in Chapter 3 and Taylor et al. (2013). It has been demonstrated numerically that the force reduction on space-frame structures due to current blockage effect is real and significant.

Apart from the additional information on force time history, flow visualisation is also attainable numerically. Flow visualisation is helpful in providing insights into the flow behaviour of the global mean wake, which is responsible for the global flow and force reduction. The wake flow behind the porous tower is strongly unsteady as it is modulated by the waves, and remains well separated and distinct from the surrounding bypass flow. There is interesting and significant unsteady fully three-dimensional wake dynamics, but all of this appears to occur well downstream. Thus, the flow within the tower is relatively simple, and as a consequence, the Morison-type forces are also relatively simple in form.

This chapter provides further evidence for the validity of the full current blockage model (FCB). It also demonstrates the novel use of the porous block as a simple representation for the complex geometry of real jacket structures when exposed to combined large waves and significant in-line current, which could be of significance for possible incorporation into a standard offshore design practice. Given the present state of development, both the analytical and the numerical models of current blockage are valid for statically-responding space-frame offshore structures, such as jackets, in regular wave applications.

This chapter has been submitted to the Journal of Fluids Mechanics as Santo et al. (2014a).

Chapter 7

Conclusions and recommendations for future work

7.1 Conclusions

- The analytical model of current blockage is derived from actuator disc theory, and is suitable for steady current (for simple current blockage or SCB) and regular waves with an in-line current (for full current blockage or FCB).
- The SCB model has been used as a part of the standard design method after it was incorporated in the API design guidelines in 1994 (American Petroleum Institute, 2000), but it only takes into account current–structure interaction.
- As there is strong evidence showing a much larger blockage for a structure subjected to combined waves and current, the FCB model has been developed, and this model takes into account a complete wave–current–structure interaction.
- The asymptotic limit of the FCB reveals clear separation in the drag components, i.e. no wave times current coupled term. This is in direct contrast to the standard Morison and the present API practice (or SCB), which demonstrates the fundamental difference in the governing principles and the underlying assumptions.
- The FCB model agrees well with a range of the published experimental data on drag forces on a model jacket, both for steady flow and for regular wave with an in-line steady flow, with fixed Morison coefficients (C_d).
- The FCB model also agrees well with a range of CFD numerical simulations in planar flow through grids, where individual cylinders are not modelled, but

the global drag resistance is represented by Morison-type quadratic resistance porous block, with a single calibration on C_d value. The replacement of a full and complex geometry by a calibrated porous block is itself a novel and useful development.

- The FCB model is further developed to include a full time–dependent force time history, and it is demonstrated to agree well with a series of experiments performed at Cornell University for regular oscillations plus mean flow both in terms of the peak values as well as the shape in force time history. The asymptotic limit of the complete FCB model is shown to consist of a summation of the wave drag and the current drag components. The shape of the wave drag component is proportional to $\cos\omega t|\cos\omega t|$, while that of the current drag component to $|\cos\omega t|$, i.e. it is phase-locked to the oscillatory wave crests.
- The FCB model agrees well with a range of numerical simulations in 3D flow of regular waves and current, where Morison-type inertia is now incorporated directly into the simulation, with calibration on both C_d and C_m coefficients. The numerical results also match well with the Allender & Petrauskas experimental data with a single value of C_d and C_m coefficients. And of course the numerical simulations provide additional predictions of the complete force time history and the flow visualisation as well as the peak values reported by Allender & Petrauskas.
- The use of a porous block in CFD numerical simulations to simulate full jacket models under combined waves and current is a genuine approach in offshore engineering and of significance to a possible incorporation into a standard offshore design practice.
- The FCB model and the novel use of porous block in CFD numerical simulations to account for the complete current blockage effect in general work very well for regular waves. The force reduction is real and significant. This thesis has a direct implication and application to new-builds and reassessment of space–frame offshore structures. The present offshore design guidelines (API, DNV and ISO) should be regarded as seriously inadequate for combined regular waves and an in-line steady current acting on offshore structures.
- Overall, this thesis demonstrates that the analytical and numerical current blockage models work remarkably well for statically-responding fixed space–frame structures (such as jackets) in regular waves application.

7.2 Recommendations for future work

- To formulate a complete current blockage model for regular waves taking into account free surface effects and the nonlinear wave kinematics above mean sea level, as the previous proposed form described in Chapter 5 is valid for planar oscillations only. A preliminary form for a more complete current blockage model is presented in Appendix D.

- To further investigate current blockage in random waves by both experiments and numerical simulations, by use of focused wave (NewWave) and embedded focused wave in a regular wave background. Previous studies have shown and confirmed that NewWave is a good representation of the largest waves both in extra-tropical (winter) and tropical storms, see Jonathan and Taylor (1997), Taylor and Williams (2004) and Santo, Taylor, Eatock Taylor, and Choo (2013b). An academic collaboration with the University of Strathclyde to conduct experiments is being carried out at the time of writing, and the first series of test in a large towing tank in the Kelvin Hydrodynamics Laboratory in Glasgow has been conducted for a jacket model subjected to regular waves. The second series of test is being planned which will involve focussed waves. The jacket model is shown in Figure 7.1.

- To formulate an extended analytical model of current blockage suited for random waves for offshore engineering application. The extended full model ought to incorporate the time–distance scales needed for global wake and mean vorticity to build up to produce complete blockage effects and then the subsequent decay as an extreme event encounters and passes by a space-frame offshore structure.

- To assess variations in waves and current. The effects of wave spreading, shallow water waves, non-aligned waves and currents (in contrast to the present modelling of waves with an in-line current), sheared current, current over a finite portion of the water depth, etc. would also be valuable to investigate for a range of realistic structures.

- To account for a tapered porous tower to represent a typically-tapered jacket, and also non-spatially-uniform and anisotropic drag resistance, for instance where a higher resistance is skewed to one side of a structure to account for a closely spaced group of conductors commonly found in a real jacket.

- To investigate the current blockage effects in dynamically-responding structures, such as jackets and compliant towers in deep water, and jack-up legs in shallow water. The relative velocity formulation is not as straightforward as the standard design practice due to the complexity of the current drag component which is phase-locked to the oscillatory wave crests (as predicted by the FCB model). More experiments and numerical simulations (by dynamic or moving mesh) are required.

- To obtain and analyse, if possible, field measurement data in the future in the form of joint industry project (JIP) with industry collaborators. The effects of Reynolds number, and turbulence in the open sea in a storm (presumably high towards the free-surface), are definitely areas worth investigating if suitable field data were to be available.

- To investigate the possibility of having a relatively straightforward methodology to implement the full blockage recipe into the present industry design practice such as the offshore blockage factor (from simple current blockage model) presently being adopted by the API, DNV and ISO. Some discussions with Prof. Peter Marshall reveal that one possibility for the practical application of this study is to have a reduced global load factor after accounting for full blockage, which will be fed into the USFOS®-type of software as part of the standard procedure to assess structural reliability, of which the local stress and strength design of the local structural members can be performed and checked.

- To investigate how best to implement the improved understanding of current blockage into commercial offshore analysis softwares, such as MicroSAS® and USFOS®. If it is found that only porous block-type simulations by OpenFOAM® or others can accurately capture the details of the reduced fluid loading on space-frame structures, it will be necessary to tightly couple the flow simulation software with structural analysis packages.

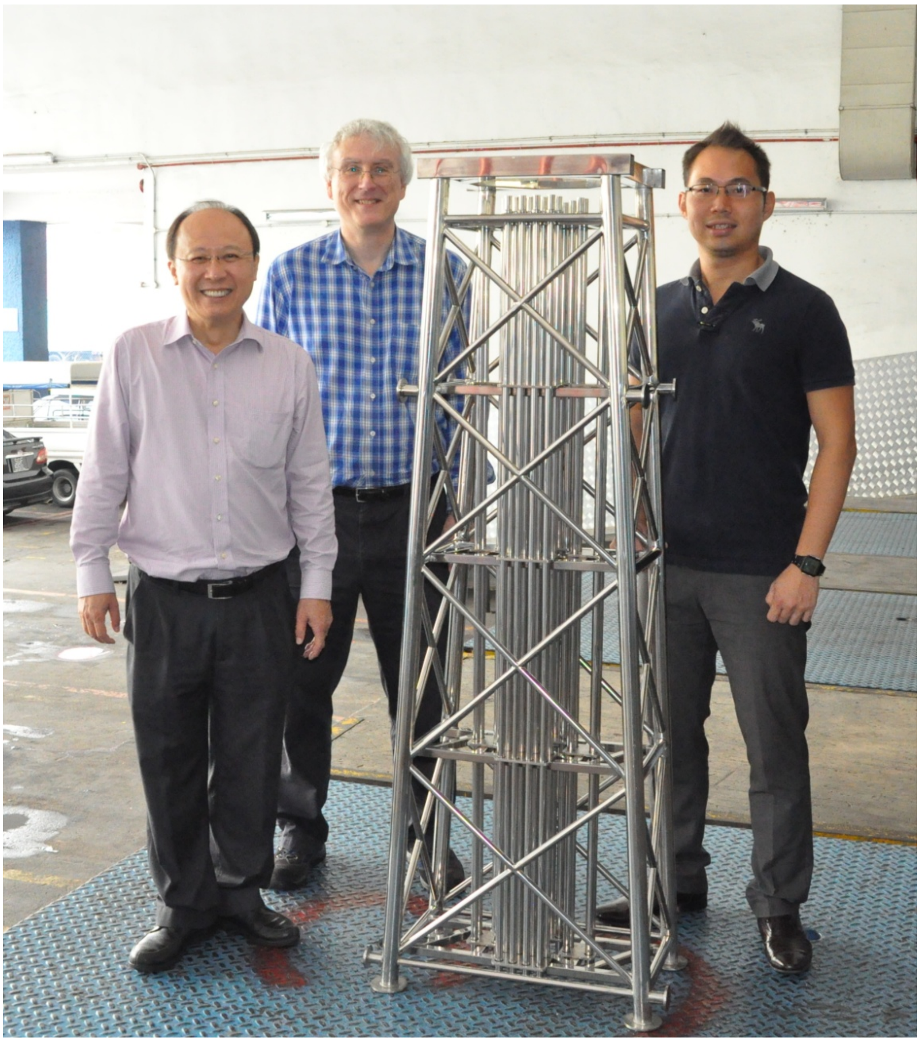

Figure 7.1: From left to right: Prof. Choo, Prof. Taylor, the NUS jacket model, and the author.

Bibliography

Allender, J., Petrauskas, C., 1987. Measured and predicted wave plus current loading on a laboratory-scale, space frame structure. In: Offshore Technology Conference, OTC 5371.

American Petroleum Institute, 2000. Recommended practice for planning, designing, and constructing fixed offshore platforms–working stress design. API RP2A-WSD 21st Edition with Erratas and Supplements 1, 130–132.

Bea, R. G., Pawsey, S. F., Litton, R. W., 1988. Measured and predicted wave forces on offshore platforms. In: Offshore Technology Conference, OTC 5787.

Bearman, P. W., 1967. The effect of base bleed on the flow behind a two-dimensional model with a blunt trailing edge. Aeronautical Quarterly 18, 207–224.

Berberović, E., van Hinsberg, N. P., Jakirlić, S., Roisman, I. V., Tropea, C., 2009. Drop impact onto a liquid layer of finite thickness: Dynamics of the cavity evolution. Physical Review E – Statistical, Nonlinear, and Soft Matter Physics 79 (3), 036306.

Brackbill, J. U., Kothe, D. B., Zemach, C., 1992. A continuum method for modeling surface tension. Journal of Computational Physics 100 (2), 335–354.

Efthymiou, M., Graham, C. G., 1990. Environmental loading on fixed offshore platforms. In: Environmental Forces on Offshore Structures and Their Predictions: Proceedings of an International Conference.

Ferziger, J. H., Perić, M., 2002. Computational Methods for Fluid Dynamics, 3rd Edition. Springer: Berlin.

Finnigan, T. D., 1992. Current blockage effects on model-scale offshore platform. In: Civil Engineering in the Oceans V. ASCE, pp. 294–310.

Forristall, G. Z., 1996. Measurements of current blockage by the Bullwinkle platform. Journal of Atmospheric and Oceanic Technology 13 (6), 1247–1266.

Fureby, C., Tabor, G., Weller, H., Gosman, A., 1997. A comparative study of subgrid scale models in homogeneous isotropic turbulence. Physics of Fluids 9, 1416.

Garrison, C. J., 1985. Comments on cross-flow principle and Morison's equation. Journal of Waterway, Port, Coastal, and Ocean Engineering 111 (6), 1075–1079.

Georgiou, P. N., Vickery, B. J., 1980. Wind loads on building frames. In: Wind Engineering: Proceedings of the Fifth International Conference on Wind Engineering, Colorado, USA, 8-13 July 1979. Vol. 1. Pergamon, p. 421.

Glauert, H., 1983. The Elements of Aerofoil and Airscrew Theory. Cambridge University Press, Cambridge.

Hirt, C. W., Nichols, B. D., 1981. Volume of fluid (VOF) method for the dynamics of free boundaries. Journal of Computational Physics 39 (1), 201–225.

Issa, R. I., 1986. Solution of the implicitly discretised fluid flow equations by operator-splitting. Journal of Computational Physics 62 (1), 40–65.

Jacobsen, N. G., Fuhrman, D. R., Fredsøe, J., 2012. A wave generation toolbox for the open-source CFD library: OpenFoam®. International Journal for Numerical Methods in Fluids 70 (9), 1073–1088.

Jonathan, P., Taylor, P. H., 1997. On irregular, nonlinear waves in a spread sea. Journal of Offshore Mechanics and Arctic Engineering 119, 37.

Lambrakos, K. F., Beckmann, H., 1992. Shielding and blockage model for offshore platforms. In: Proceedings of the Conference on the Behaviour of Offshore Structures (BOSS 92).

Lock, C. N. H., 1930. The interference of a wind tunnel on a symmetrical body. HM Stationery Office.

Mendes, A. C., Kishev, R., Chaplin, J. R., Tomchev, S., 2000. Experimental determination of the hydrodynamic loading on a model of offshore platform in waves and current. In: Proceedings of the International Society of Offshore and Polar Engineering Conference. Vol. 1. International Society of Offshore and Polar Engineers, pp. 196–203.

Milne-Thomson, L. M., 1968. Theoretical Hydrodynamics. Macmillan, New York.

Monopolis, G., Danaczko, M., 1989. Installation model tests of a Gulf of Mexico compliant tower. In: Offshore Technology Conference, OTC 5911.

Morison, J., O'Brien, M., Johnson, J., Schaaf, S., 1950. The force exerted by surface waves on piles. Journal of Petroleum Technology 2 (5), 149–154.

Nicolle, A., Eames, I., 2011. Numerical study of flow through and around a circular array of cylinders. Journal of Fluid Mechanics 679 (1), 1–31.

Nishino, T., Willden, R. H. J., 2012. Effects of 3-d channel blockage and turbulent wake mixing on the limit of power extraction by tidal turbines. International Journal of Heat and Fluid Flow 37, 123–135.

OpenCFD, 2011. Foundation Training Notes. OpenCFD Ltd.

Patankar, S. V., 1980. Numerical Heat Transfer and Fluid Flow. Taylor & Francis Group.

Patankar, S. V., Spalding, D. B., 1972. A calculation procedure for heat, mass and momentum transfer in three-dimensional parabolic flows. International Journal of Heat and Mass Transfer 15 (10), 1787–1806.

Reed, K., Aarsnes, J. V., Beltrand, O., Andersen, E., 1990. Wave and current forces on conductor pipe groups. In: Environmental Forces on Offshore Structures and Their Predictions: Proceedings of an International Conference.

Santo, H., Taylor, P. H., Bai, W., Choo, Y. S., 2013a. Blockage effects in wave and current: 2D planar simulations of combined regular oscillations and steady flow through porous blocks. Ocean Engineering (submitted).

Santo, H., Taylor, P. H., Bai, W., Choo, Y. S., 2014a. Current blockage in a numerical wave tank: 3D simulations of regular waves and current through a porous tower. Journal of Fluids Mechanics (submitted).

Santo, H., Taylor, P. H., Eatock Taylor, R., Choo, Y. S., 2013b. Average properties of the largest waves in Hurricane Camille. Journal of Offshore Mechanics and Arctic Engineering 135, 011602.

Santo, H., Taylor, P. H., Williamson, C. H. K., Choo, Y. S., 2014b. Current blockage experiments: Force time histories on obstacle arrays in combined steady and oscillatory motion. Journal of Fluid Mechanics 739, 143–178.

Schlichting, H., 1979. Boundary Layer Theory. McGraw-Hill.

Stallard, T., Taylor, P., Williamson, C., Borthwick, A., 2009. Cylinder loading in transient motion representing flow under a wave group. Proceedings of the Royal Society A: Mathematical, Physical and Engineering Science 465 (2105), 1467–1488.

Standing, R. G., House, O., 1997. Review of current blockage effects on space-frame structures. Offshore Technology Report - Health and Safety Executive, OTH 481.

Steele, K., 1986. Performance of the Lena guyed tower. In: Offshore Technology Conference, OTC 5255.

Sterndorff, M. J., Velk, P. J., Klinting, P. J., 1990. Coupled experimental and analytical investigation of hydrodynamic forces on a jacket in waves. In: Environmental Forces on Offshore Structures and Their Predictions: Proceedings of an International Conference.

Sykes, D. M., 1981. Lattice frames in turbulent airflow. Journal of Wind Engineering and Industrial Aerodynamics 7 (2), 203–214.

Taylor, P. H., 1991. Current blockage: Reduced forces on offshore space-frame structures. In: Offshore Technology Conference, OTC 6519.

Taylor, P. H., Santo, H., Choo, Y. S., 2013. Current blockage: Reduced Morison forces on space frame structures with high hydrodynamic area, and in regular waves and current. Ocean Engineering 57, 11–24.

Taylor, P. H., Williams, B. A., 2004. Wave statistics for intermediate depth water NewWaves and symmetry. Journal of Offshore Mechanics and Arctic Engineering 126, 54.

Tennekes, H., Lumley, J. L., 1972. A First Course in Turbulence. MIT Press, Cambridge, MA.

Wilcox, D. C., 1988. Reassessment of the scale-determining equation for advanced turbulence models. AIAA journal 26 (11), 1299–1310.

Wood, C. J., 1964. The effect of base bleed on a periodic wake. The Journal of the Royal Aeronautical Society 68, 477–482.

Wood, C. J., 1967. Visualization of an incompressible wake with base bleed. Journal of Fluid Mechanics 29 (2), 259–272.

Appendix A

Derivation for the total drag formulation for many sparse discs

For the case of a switching model for high hydrodynamic loading, consider a long array of obstacle discs aligned inline with a uniform flow. Assume that the spacing between any two discs is sparse enough so that the upstream discs affect those downstream but those downstream discs do not affect the upstream ones, in terms of reduced flow velocity. Further assume that the mixing out of the wakes downstream of each disc can be neglected. Taking the free stream velocity $u_c = 1$, and the hydrodynamic loading on each disc as $\phi = \frac{C_d A}{4A_f}$, the mean flow velocity profile at each disc can be written as:

$$\begin{aligned}
u_1 &= 1 - \phi u_1 \\
u_2 &= 1 - 2\phi u_1 - \phi u_2 \\
u_3 &= 1 - 2\phi u_1 - 2\phi u_2 - \phi u_3 \\
u_n &= 1 - 2\phi u_1 - ... - 2\phi u_{n-1} - \phi u_n
\end{aligned}$$

Again, the flow velocity at the first disc is only affected by its own upstream divergence (no effect from the downstream). The second disc is immersed in the fully expanded wake region of the first disc together with its own upstream divergence. The third disc is immersed in the fully expanded wake region of the two upstream discs, and so on.

After some algebraic manipulation, the above simple relations between the mean velocities at successive discs can be simplified to an expression valid for each disc:

$$u_n = \frac{1}{(1+\phi)} \left(\frac{1-\phi}{1+\phi} \right)^{n-1}$$

The total drag on the whole array of N discs requires taking a sum of the velocities squared:

$$\begin{aligned}\sum_{n=1}^{N} u_n^2 &= u_1^2 + u_2^2 + u_3^2 + ... + u_N^2 \\ &= \frac{1}{(1+\phi)^2} + \frac{1}{(1+\phi)^2}\left(\frac{1-\phi}{1+\phi}\right)^2 + \frac{1}{(1+\phi)^2}\cdot \\ &\quad \left(\frac{1-\phi}{1+\phi}\right)^4 + ... + \frac{1}{(1+\phi)^2}\left(\frac{1-\phi}{1+\phi}\right)^{2N-2}\end{aligned}$$

The expression above is a geometric series which can be further simplified into:

$$\sum_{n=1}^{N} u_n^2 = \frac{1}{4\phi}\left[1 - \left(\frac{1-\phi}{1+\phi}\right)^{2N}\right]$$

Further assume the number of discs to be large ($N \rightarrow \infty$), and the loading on each disc becomes small ($\phi \rightarrow 0$), yet their products $N\phi$ remains finite, which is one quarter for the total hydrodynamic loading of the whole array:

$$N\phi = \frac{C_d A}{4A_f}$$

The summation can now be expressed exactly in terms of a simple exponential, applying the binomial series theorem:

$$\begin{aligned}\lim_{N\rightarrow\infty,\phi\rightarrow 0} \sum_{n=1}^{N} u_n^2 &= \lim_{N\rightarrow\infty,\phi\rightarrow 0} \frac{1}{4\phi}\left[1 - \left(\frac{1-\phi}{1+\phi}\right)^{2N}\right] \\ &= 1 - \exp\left[-\left(\frac{C_d A}{A_f}\right)\right]\end{aligned}$$

Appendix B

Table of inferred C_d and C_m

Table B.1: Calibrated C_d coefficients for 1 grid steady flow case.

Blockage Ratio, A/A_f	C_d
0.15	1.80
0.30	2.00
0.45	2.85
0.60	6.70

Table B.2: Inferred Morison coefficients for $A/A_f = 0.15$.

		C_d					C_m			
u_c/u_w	$[u_w,\, u_c]$	1	2A	2B	3	Average	1	2A	2B	3
2	[5 , 10]	1.75	1.66	1.59	1.64	1.66	24.03	13.42	13.65	9.76
1	[10 , 10]	1.86	1.86	1.82	1.94	1.87	25.11	13.34	14.14	10.68
1	[5 , 5]	1.94	1.82	1.79	2.04	1.90	24.30	13.09	13.93	10.54
1/2	[10 , 5]	1.92	1.92	1.91	1.98	1.93	27.07	15.86	16.57	12.74
1/3	[15 , 5]	1.87	1.91	1.92	1.90	1.90	26.69	17.08	16.61	14.35
1/3	[12 , 4]	1.85	1.86	1.87	1.85	1.86	26.57	17.39	17.34	14.65
1/4	[16 , 4]	1.83	1.82	1.83	1.79	1.82	26.99	17.74	18.40	15.73

Table B.3: Inferred Morison coefficients for $A/A_f = 0.30$.

		C_d					C_m			
u_c/u_w	$[u_w,\, u_c]$	1	2A	2B	3	Average	1	2A	2B	3
2	[5 , 10]	2.55	2.76	2.82	3.56	2.92	16.60	12.41	10.83	10.17
1	[10 , 10]	2.74	3.64	3.64	3.63	3.41	17.58	12.84	12.29	11.18
1	[5 , 5]	2.78	3.32	3.29	3.36	3.19	19.93	14.09	13.61	12.86
1/2	[10 , 5]	2.89	2.76	2.78	2.71	2.79	21.33	17.24	16.97	15.99
1/3	[15 , 5]	2.54	2.49	2.52	2.46	2.50	22.54	20.19	19.30	19.50
1/3	[12 , 4]	2.50	2.44	2.47	2.39	2.45	23.48	20.63	19.90	20.07
1/4	[16 , 4]	2.37	2.31	2.37	2.26	2.33	24.90	24.09	21.81	24.27

Table B.4: Inferred Morison coefficients for $A/A_f = 0.45$.

		C_d					C_m			
u_c/u_w	$[u_w,\, u_c]$	1	2A	2B	3	Average	1	2A	2B	3
2	[5 , 10]	4.02	5.61	5.90	5.97	5.38	13.96	12.36	12.03	11.75
1	[10 , 10]	5.00	5.04	5.13	4.98	5.04	13.62	13.21	12.48	13.88
1	[5 , 5]	4.56	4.51	4.59	4.44	4.53	18.29	16.77	16.22	16.71
1/2	[10 , 5]	3.95	3.77	3.87	3.71	3.83	21.78	22.34	21.71	23.21
1/3	[15 , 5]	3.68	3.49	3.63	3.39	3.55	27.11	30.86	28.13	31.77
1/3	[12 , 4]	3.54	3.33	3.48	3.21	3.39	28.18	32.57	29.81	33.39
1/4	[16 , 4]	3.34	3.08	3.29	2.92	3.16	36.42	42.46	37.84	44.20

Table B.5: Inferred Morison coefficients for $u_c/u_w = 0$, 2B grid configuration.

		C_d			C_m		
$[u_w,\, u_c]$	T (sec)	0.15	0.30	0.45	0.15	0.30	0.45
[10 , 0]	1.8	2.29	3.27	5.18	15.98	14.32	17.37
[10 , 0]	3.6	1.95	2.63	3.87	18.36	19.55	27.26
[15 , 0]	3.6	1.87	2.51	3.63	19.75	23.92	35.38
[16 , 0]	4.5	1.77	2.37	3.27	21.39	27.29	43.50

Appendix C

C++ source code excerpts for OpenFOAM®

Code modification at *porousZoneTemplates.C* to account for 2D Morison in quasi-steady flow in regular oscillations plus current:

```
template<class RhoFieldType>
void Foam::porousZone::addViscousInertialResistance
(
    scalarField& Udiag,
    vectorField& Usource,
    const labelList& cells,
    const scalarField& V,
    const RhoFieldType& rho,
    const scalarField& mu,
    const vectorField& U
) const
{
    const tensor& D = D_.value();
    const tensor& F = F_.value();
    const scalar Uw = Uw_;

    forAll (cells, i)
    {

    label N = 20; // Number of grid points

    scalar PHI[N-1];

    scalar Ucs = U[cells[i]].x();
    scalar Uv = U[cells[i]].y();

    for (label j=0; j<= N-1; j++)
    {
         PHI[j] = (j*((3.142857)/(N-1)));
    }

    scalar sumX = 0;
```

```
    scalar sumY = 0;

    sumX = (Uw*cos(PHI[0]) + Ucs)*sqrt(sqr(Uw*cos(PHI[0])+Ucs) + sqr(Uv))
            + (Uw*cos(PHI[N-1]) + Ucs)*sqrt(sqr(Uw*cos(PHI[N-1])+Ucs) + sqr(Uv));

    sumY = (Uv)*sqrt(sqr(Uw*cos(PHI[0])+Ucs) + sqr(Uv))
            + (Uv)*sqrt(sqr(Uw*cos(PHI[N-1])+Ucs) + sqr(Uv));


    for (label j=1; j< N-1; j++)
    {
         sumX = sumX + 2*(Uw*cos(PHI[j]) + Ucs)*sqrt(sqr(Uw*cos(PHI[j])+Ucs) + sqr(Uv));
         sumY = sumY + 2*(Uv)*sqrt(sqr(Uw*cos(PHI[j])+Ucs) + sqr(Uv));
    }

    sumX = sumX/(2*(N-1));
    sumY = sumY/(2*(N-1));

    vector axis(1, 0, 0);
    vector axis1(0, 1, 0);

    Usource[cells[i]] -= (((V[cells[i]]*rho[cells[i]])*sumX*F) & axis);
    Usource[cells[i]] -= (((V[cells[i]]*rho[cells[i]])*sumY*F) & axis1);

    }
}
```

Code *wavePorousFoam.C* to account for 3D Morison porous resistance (drag and inertia) for free-surface two-phase flow:

```
#include "fvCFD.H"
#include "MULES.H"
#include "subCycle.H"
#include "interfaceProperties.H"
#include "twoPhaseMixture.H"
#include "turbulenceModel.H"
#include "interpolationTable.H"
#include "relaxationZone.H"
#include "porousZones.H"
#include "OFstream.H"

// * * * * * * * * * * * * * * * * * * * * * * * * * * * * * * * * * * * * * //

int main(int argc, char *argv[])
{
    #include "setRootCase.H"
    #include "createTime.H"
    #include "createMesh.H"
    #include "readPISOControls.H"
    #include "initContinuityErrs.H"
    #include "readGravitationalAcceleration.H"
    #include "readWaveProperties.H"
    #include "createFields.H"
    #include "readTimeControls.H"
    #include "correctPhi.H"
    #include "CourantNo.H"
    #include "setInitialDeltaT.H"

    // * * * * * * * * * * * * * * * * * * * * * * * * * * * * * * * * * * * //

    Info<< "\nStarting time loop\n" << endl;

    label masterIndex = 0;

    scalar Ubarx[9999], UmodUbarx[9999], timeName[9999], ddtbarx[9999];

    while (runTime.run())
    {
        #include "readPISOControls.H"
        #include "readTimeControls.H"
        #include "CourantNo.H"
        #include "alphaCourantNo.H"
        #include "setDeltaT.H"

        runTime++;

        Info<< "Time = " << runTime.timeName() << nl << endl;

        twoPhaseProperties.correct();

        #include "alphaEqnSubCycle.H"
```

```
relaxing.correct();

#include "UEqn.H"

// --- PISO loop
for (int corr=0; corr<nCorr; corr++)
{
    #include "pEqn.H"
}

turbulence->correct();

runTime.write();

if ( runTime.value() >= scalar(0.2*(masterIndex + 1)) )
{

     label zoneId = mesh.cellZones().findZoneID("porosity1");

     scalar sumUx = 0; scalar sumSqUx = 0; scalar sumDdt = 0;
     scalar sumVolume = 0; scalar counter = 0; Ubarx[masterIndex] = 0;
     UmodUbarx[masterIndex] = 0; timeName[masterIndex] = 0;

     if (zoneId != -1)
     {
         const labelList& cellIds = mesh.cellZones()[zoneId];

         forAll (cellIds, i)
         {
            if ( alpha1[cellIds[i]] >= scalar(0.5) )
            {
               sumUx = sumUx + U[cellIds[i]].x() * mesh.V()[cellIds[i]];
               sumSqUx = sumSqUx + U[cellIds[i]].x() * mag(U[cellIds[i]])
                         * mesh.V()[cellIds[i]];
               sumDdt = sumDdt + ddt[cellIds[i]].x() * mesh.V()[cellIds[i]];
               sumVolume = sumVolume + mesh.V()[cellIds[i]];
               counter = counter+1;
            }
          }

          if (Pstream::parRun())
          {
             reduce(sumUx, sumOp<scalar>());
             reduce(sumSqUx, sumOp<scalar>());
             reduce(sumVolume, sumOp<scalar>());
             reduce(sumDdt, sumOp<scalar>());
             reduce(counter, sumOp<scalar>());
          }

          Ubarx[masterIndex] = sumUx/sumVolume;
          UmodUbarx[masterIndex] = sumSqUx/sumVolume;
          ddtbarx[masterIndex] = sumDdt/sumVolume;
          timeName[masterIndex] = runTime.value();
```

```
             }

             masterIndex = masterIndex + 1;

        }

        Info<< "ExecutionTime = " << runTime.elapsedCpuTime() << " s"
            << "  ClockTime = " << runTime.elapsedClockTime() << " s"
            << nl << endl;
    }

    OFstream dataOutput("sumDragAndInertia.dat");

    for (label i=0; i<masterIndex; i++)
    {
        dataOutput << timeName[i] << "  " << Ubarx[i] << "   "
                   << UmodUbarx[i] << "   " << ddtbarx[i] << endl;
    }

    dataOutput();

    Info<< "End\n" << endl;

    return 0;
}
```

Choice of numerical schemes and solution solver for three-dimensional free-surface two-phase flow simulation.

Each simulation is run with an adjustable time step, in which the minimum time interval (*deltaT*) is kept at 0.001 sec. The Courant number (*maxCo*) is kept at maximum of 0.5, and the interface Courant number (*maxAlphaCo*) is limited to 0.25.

Some of the key numerical schemes listed in *fvSchemes* used for the simulation are as follows:

```
gradSchemes
{
    default cellLimited leastSquares 1.0;
}

divSchemes
{
    div(rho*phi,U)  Gauss limitedLinearV 1;
    div(phi,alpha)  Gauss MUSCL;
    div((nuEff*dev(grad(U).T()))) Gauss linear;
    div(phi,k)      Gauss limitedLinear 1;
}

laplacianSchemes
{
    default         Gauss linear corrected;
}
```

The algebraic equation solver used for pressure, p, is *GAMG DICGaussSeidel*, while for velocity, u, and kinetic energy, k, is *smoothSolver DILUGaussSeidel*. The entry for the PISO dictionary in *fvSolution* is as follows:

```
PISO
{
    pdRefCell 0;
    pdRefValue 0;
    momentumPredictor yes;
    nOuterCorrectors 2;
    nCorrectors     3;
```

```
    nNonOrthogonalCorrectors 1;
    nAlphaCorr      1;
    nAlphaSubCycles 1;
    cAlpha          1;
}
```

Appendix D

Proposed full current blockage model for regular waves

Previously in Chapter 5, the drag–time history of the asymptotic model of the full current blockage model for regular waves with an in-line current has been validated, with the form reproduced as follows:

$$\text{Drag } = \frac{1}{2}\rho C_d A u_w^2 \cos\omega t|\cos\omega t| + \frac{\pi}{4}\rho A_f u_c^2|\cos\omega t| \tag{D.1}$$

The proposed form of the asymptotic model is simple and thus easy to implement in commercial software codes, such as USFOS® (www.usfos.no) and MicroSAS® (www.mcdermott.com). However, the form is valid for planar oscillations assuming the wave kinematics are exactly sinusoidal with steady flow, when $u_w > u_c$. When the depth-variation of the wave kinematics is taken into account in real ocean waves, and in the numerical study presented previously in Chapter 6, there are regions where $u_w < u_c$ which pose incompatibility to the proposed planar model. Thus, a switching model, which takes into account the wave kinematics depth-variation and switches between the full asymptotic model and a submodel depending on the relative magnitude of the wave kinematics to the current velocity, is proposed as follows:

$$\begin{aligned}
\text{if}\quad & (u_w > u_{cs}) \\
& \text{Drag } = \frac{1}{2}\rho C_d A u_w^2 \cos\omega t|\cos\omega t| + \frac{\pi}{4}\rho A_f u_c^2|\cos\omega t| \\
\text{else}\quad & \\
& \text{Drag } = \frac{1}{2}\rho C_d A(u_w\cos\omega t + u_{cs})|u_w\cos\omega t + u_{cs}|
\end{aligned} \tag{D.2}$$

where u_{cs} is the blocked current velocity from Equation 3.22 in Chapter 3 for case

(iii) and it is reproduced below:

$$u_{cs} = \frac{u_c + \sqrt{u_c^2 - 2\left(1 + \dfrac{C_d A}{4A_f}\right)\left(\dfrac{C_d A}{4A_f}\right) u_w^2}}{2\left(1 + \dfrac{C_d A}{4A_f}\right)} \tag{D.3}$$

with an imposed requirement that $u_{cs} > u_c/2$. It is worth noting that the value of u_{cs} here is always smaller than the u_{cs} obtained from the current API practice (the simple current blockage model, SCB). This switching model becomes the complete proposed full current blockage model for regular waves plus current.

A comparison of the full model, the asymptotic model, and the numerical result for 25 m regular waves in 1.25 m/s current is illustrated in Figure D.1.

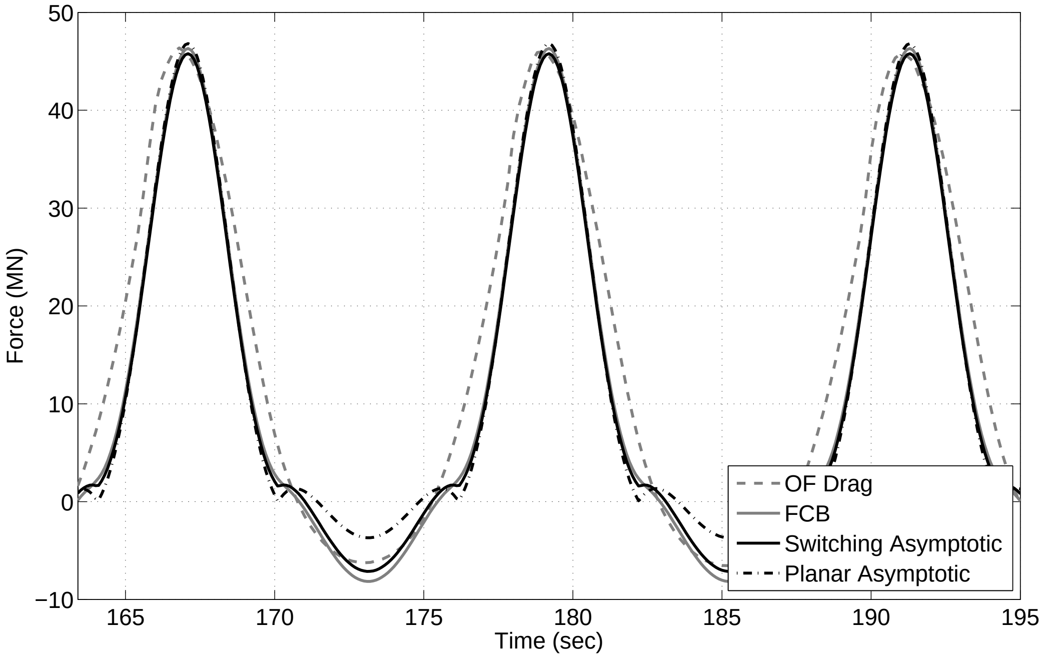

Figure D.1: Comparison of the full current blockage model, the proposed switching asymptotic model and the numerical result for $H = 25$ m regular waves with $u_c = 1.25$ m/s.